Exploring the Physicochemical Properties of Coacervate Droplets toward Sensing, Catalysis, and Biomedical Applications

Ph.D. Thesis

By

BHAWNA

DEPARTMENT OF CHEMISTRY

INDIAN INSTITUTE OF TECHNOLOGY INDORE

MAY 2023

Exploring the Physicochemical Properties of Coacervate Droplets toward Sensing, Catalysis, and Biomedical Applications

A THESIS

Submitted in partial fulfillment of the

requirements for the award of the degree

of

DOCTOR OF PHILOSOPHY

By

BHAWNA

DEPARTMENT OF CHEMISTRY

INDIAN INSTITUTE OF TECHNOLOGY INDORE

MAY 2023

INDIAN INSTITUTE OF TECHNOLOGY INDORE

I hereby certify that the work which is being presented in the thesis entitled **Exploring the Physicochemical Properties of Coacervate Droplets toward Sensing, Catalysis, and Biomedical Applications** in the partial fulfillment of the requirements for the award of the degree of **DOCTOR OF PHILOSOPHY** and submitted in the **DEPARTMENT OF CHEMISTRY, Indian Institute of Technology Indore**, is an authentic record of my own work carried out during the time period from **JULY 2018** to **MAY 2023** under the supervision of **Dr. Tushar Kanti Mukherjee**, Professor and Head, Department of Chemistry, IIT Indore.

The matter presented in this thesis has not been submitted by me for the award of any other degree of this or any other institute.

Bhawna
24-05-2023

signature of the student with date
(BHAWNA)

This is to certify that the above statement made by the candidate is correct to the best of my knowledge.

24/05/2023

Signature of Thesis Supervisor with date
(Dr. TUSHAR KANTI MUKHERJEE)

BHAWNA has successfully given his/her Ph.D. Oral Examination held on 08/08/2023

08/08/2023

Signature of Thesis Supervisor with date
(Dr. TUSHAR KANTI MUKHERJEE)

Acknowledgements

i

Dedicated to

My Parents (Mr. Mohan Lal & Mrs. Kanta),

my brother (Hardik), my husband (Dr. Gaurav Pandey), and

my supervisor Dr. Tushar Kanti Mukherjee

Abstract

With the recent advancement in nanotechnology in the field of interdisciplinary nanoscience, there is a growing interest in the development of new multifunctional self-assembled artificial cells. Artificial or synthetic cell is defined as a closed entity that mimics one or more functions of natural cell and sequesters biologically active substances. To understand the various biological pathways happening inside the living system, extensive efforts have been made to fabricate and optimize the physicochemical properties of a diverse range of artificial cells such as hybrid liposomes, polymersomes, plasmonic vesicles, dendrimer nanoparticles, hydrogels, metal-organic frameworks, polymeric nanoparticles, and coacervate droplets.

Among them, coacervate droplets offer unique advantages over other protocellular systems due to their inherent membrane-free structure and preferential sequestration of a wide range of solutes including dyes, sugars, proteins, enzymes, nucleic acids, and nanoparticles. Moreover, the physicochemical properties of coacervate droplets can be tuned by modulating the stochiometric ratio of polyelectrolytes, equilibration time, pH, and ionic strength of the medium. While the self-assembled coacervation process and their potential application as a model protocell system have been reported in the literature, a very few reports are available on their active role as a nanocarrier for biomedical applications. In addition, it would become more advantageous to design inherently luminescent biocompatible coacervate droplets as a luminescent marker for biomedical applications. In this thesis, we have fabricated a unique class of biocompatible luminescent synthetic hybrid coacervates from the mixture of carbon dots (CDs) and poly(diallyldimethylammonium chloride) (PDADMAC) in an aqueous medium and further subjected to theranostic applications. Subsequently, to understand the target-specific delivery of hydrophobic drugs via nanocarrier,

the physicochemical properties of synthetic ATP-coacervates have been compared with different nanoassemblies such as micelles, and liposomes.

On the other hand, the scope of synthetic nanoreactors or bioreactor towards catalysis is limited by their inherent structural constraints such as fixed pore or cavity size, limited scope for free diffusion of substrates and products as well as lacking of multiple catalytic centers. Therefore, it is highly desirable to design an efficient synthetic nanoreactor or bioreactor to understand various catalytic transformations in a confined environment. In this thesis, we have examined the rates of various catalytic transformations such as redox catalysis and enzyme catalysis inside synthetic coacervates and further explored their potential application for glucose sensing. Moreover, it has been reported that ~40% of the total volume of the cell is occupied by biomacromolecules. Irrespective of its highly crowded interior environment, the rate of biochemical reactions is very fast and highly selective. To mimic the cellular environment, the enzyme kinetics in the presence of inert macromolecular crowders have been well documented in the literature but the influence of inert crowders on the physicochemical properties of enzymes is highly overlooked. Moreover, the fundamental mechanism behind the enhanced activity upon crowding is still not clear. Therefore, it is important to examine the reaction kinetics in vitro in the presence of macromolecular crowders to address the mechanism of fast biochemical reactions. In this thesis, we have explored the formation process of biomolecular condensates of enzymes in the presence of various macromolecular crowders such as PEG, Ficoll, dextran, and BSA and further investigated the reaction rates of enzymatic reactions inside these biomolecular condensates.

The contents of each chapter included in the thesis are discussed as follows:

1. Introduction

In this chapter, the functional role of confined environment of membraneless compartments or coacervate droplets over different artificial cells have been discussed in detail. In addition, the effect of macromolecular crowders on enzyme activity have been explained briefly. Finally, applicability of coacervate droplets in various domains along with different kinetic models have been provided.

2. Materials, sample preparation and experimental techniques

This chapter contains the details of all the materials employed for the work described in the thesis. The complete synthesis procedures of carbon dots (CDs), quantum dots (QDs), (*p*-cymene)Ru (curcuminato)Cl] (Ru-Cur), small unilamellar vesicles (SUVs), giant unilamellar vesicles (GUVs), multilamellar vesicles (MLVs) and fabrication processes of CD-, ATP-, and QD-coacervates have been discussed along with their detailed characterization. This chapter also covers the details of various experimental procedures and techniques utilized for the work described in this thesis.

3. Biocompatible pH-responsive luminescent coacervate nanodroplets from carbon dots and poly(diallyldimethylammonium chloride) toward theranostic applications

In this chapter, the fabrication of pH-responsive luminescent CD-coacervate nanodroplet (ND) from biocompatible CD and PDADMAC has been demonstrated. Equilibrating the binary mixture of CD and PDADMAC for different time intervals result in the formation of smaller and larger nanodroplets (SNDs and LNDs). These droplets are found to be stable over a broad range of composition, pH, and ionic strength of the medium. In addition,

high partitioning of neutral, cationic, and anionic solutes is observed inside droplets. The cell viability assay shows the excellent biocompatibility of SNDs for BHK-21 cell lines. Time-dependent cellular uptake experiment shows the disassembled SNDs after internalization due to lower acidic pH of lysosomes. Our findings highlight the potential of these biocompatible luminescent pH-responsive NDs toward theranostic applications.

4. Specific loading and in vitro controlled release of a Ru-based hydrophobically encapsulated model anticancer drug inside nanoassemblies toward stimuli-responsive drug delivery

The loading of a hydrophobic model anticancer drug, [(p-cymene)Ru(curcuminato)Cl] (Ru-Cur), inside the hydrophobic compartments of different nanoassemblies, namely, micelles, liposomes, and coacervate nanodroplets along with their in-vitro pH-and temperature-dependent controlled release has been explored in this chapter. It is observed that coacervate nanodroplets showed efficient loading and sustained release of the hydrophobic drug which makes them an ideal nanocarriers over other conventional nanoassemblies. The release profile shows that the mechanism is diffusion-and swelling-controlled in the pH range between 7.4 to 6 and diffusion- and erosion-controlled at pH 5. In addition, it has been also found that the temperature has a profound influence on the drug release profiles. Therefore, the present study provides fundamental insight into the pH-responsive disassembly mechanism and highlights the potential importance of these Ru-Cur-loaded coacervates toward various theranostic applications.

5. Nanocatalysis under nanoconfinement: A metal-free hybrid coacervate nanodroplet as a catalytic nanoreactor for efficient redox reactions

Designing of active artificial nanoreactors with multiple catalytic centers find

tremendous importance for efficient catalytic transformations in recent times. In this chapter, we report a unique blend of nanoscience and chemical catalysis using a metal-free hybrid synthetic protocell as a catalytic nanoreactor for redox transformations, which are otherwise incompatible in bulk medium (Scheme 3). Hybrid coacervate NDs were fabricated from 2.5 nm-sized CDs and PDADAMC and then utilized further for reductive hydrogenation of nitroarenes in the presence of NaBH4 (Scheme 3). These NDs show excellent recyclability without any compromise on reaction kinetics and conversion yield. In addition, spatiotemporal control over the hydrogenation reaction has been successfully achieved using mixed population of coacervates.

6. Synthetic protocell as efficient bioreactor: enzymatic superactivity and ultrasensitive Glucose sensing in urine

In this chapter, the fabrication of a high-performance integrated cascade bioplatform based on synthetic droplets have been explored. At first, liquid-like membrane-less droplets have been prepared via multivalent electrostatic interactions between negatively charged ATP and positively charged PDADMAC in an aqueous medium. The compartmentalized enzymes inside synthetic hybrid droplets show high encapsulation efficiency, low leakage, prolong retention of activity, and exceptional stability toward protease digestion (Scheme 4). Our findings show that the enzymatic reaction inside droplets follow Michaelis-Menten model and exhibit remarkable enhancement in the catalytic activity of up to 100- and 51-fold for HRP@Droplet and GOx/HRP@Droplet, respectively (Scheme 4). These enhanced activities have been explained on the basis of increased local concentration of enzymes and substrates, along with altered conformations of sequestered enzymes. In addition, we have utilized highly efficient and recyclable GOx/HRP@Droplet composite to demonstrate ultrasensitive glucose sensing with a limit of

detection of 228 nM. Finally, the composite platform has been exploited to detect glucose in spiked urine samples in solution and filter paper (Scheme 4). Our present study illustrates the unprecedented activity of the compartmentalized enzymes and paves the way for next-generation composite bioreactors for a wide range of applications.

7. Biomolecular condensates regulate enzymatic activity under a crowded milieu: synchronization of liquid–liquid phase separation and enzymatic transformation

Enzymes drive a wide range of complex metabolic reactions with high efficiency and selectivity under extremely heterogenous and crowded cellular environments. The molecular interpretation behind the enhanced enzymatic reactivity under crowded milieu is described in this chapter. We first time demonstrate the macromolecular crowding induced homotypic liquid-liquid phase separation (LLPS) via the formation of liquid-like condensates of both HRP and GOx. These condensates are enthalpically driven by multivalent electrostatic as well as hydrophobic interactions. Our findings reveal an unprecedented enhancement (91- to 205-fold) in the catalytic efficiency (k_{cat}/K_m) of HRP at pH 4.0 within the droplet phase relative to that in the bulk aqueous phase in the presence of different crowders. In addition, other enzymes also undergo spontaneous LLPS under macromolecular crowding, signifying the generality of this phenomenon. Coalescence driven highly regulated GOx/HRP cascade reactions within the fused droplets have demonstrated with enhanced activity and specificity under the crowded environments. The present discovery highlights the active role of membraneless condensates in regulating the enzymatic efficacy for complex metabolic reactions under the crowded cellular environments and may find significant importance in the field of biocatalysis.

8. Conclusions:

The conclusions of the thesis can be described as follows:

1) The study revealed that self-assembly between negatively charged CDs and cationic polymer PDADMAC leads to the formation of biocompatible inherently luminescent coacervate droplets and illustrated their potential application toward cell imaging and pH-triggered intracellular disassembly characteristics.

2) The physicochemical properties and release behavior of an encapsulated drug are found to be far superior in synthetic coacervates as compared to other nanoassemblies.

3) The unique metal-free CD-embedded hybrid coacervates showed efficient redox hydrogenation transformation which is otherwise not possible in the presence of bare CDs in bulk aqueous medium.

4) The enhancement in enzymatic activity upto 100-fold is observed inside synthetic ATP droplets. It has been shown that the robust, stable, and cost-effective integrated GOx/HRP@Droplet composite sense glucose in spiked urine sample within few seconds.

5) It has been shown that macromolecular crowding results in the enhancement of enzymatic activity via homotypic LLPS of HRP and GOx.

List of Publications

❖ **Publications included in this Thesis:**

1) <u>**Saini, B.**</u>; Singh, R. R.; Nayak, D.; Mukherjee, T. K. (2020), Biocompatible pH-responsive luminescent coacervate nanodroplets from carbon dots and poly(diallyldimethylammonium chloride) toward theranostic applications. ACS Appl. Nano Mater., 3, 5826−5837. (DOI: 10.1021/acsanm.0c00995)

2) <u>**Saini, B.**</u>; Singh, R.; Mukhopadhyay, S.; Mukherjee, T. K. (2021), Specific loading and in vitro controlled release of a Ru-Based hydrophobically encapsulated model anticancer drug inside nano-assemblies toward stimuli-responsive drug delivery. ACS Appl. Nano Mater., 4, 2037−2051. (DOI: 10.1021/acsanm.0c03356)

3) <u>**Saini, B.**</u>; Singh, S.; Mukherjee, T. K. (2021), Nanocatalysis under nanoconfinement: a metal-free hybrid coacervate nanodroplet as a catalytic nanoreactor for efficient redox and photocatalytic reactions. ACS Appl. Mater. Interfaces, 13, 51117−51131. (DOI: 10.1021/acsami.1c17106)

4) <u>**Saini, B.**</u>; Mukherjee, T. K. (2022), Synthetic protocell as efficient bioreactor: enzymatic superactivity and ultrasensitive glucose sensing in urine. ACS Appl. Mater. Interfaces, 14, 53462−53474. (DOI: 10.1021/acsami.2c13112)

5) <u>**Saini, B.**</u>; Mukherjee, T. K. (2022), Biomolecular condensates regulate enzymatic activity under crowded milieu: Synchronization of liquid-liquid phase separation and enzymatic transformation. J. Phys. Chem. B, 127, 180−193. (DOI: 10.1021/acs.jpcb.2c07684)

❖ **Publications apart from this Thesis:**

6) Patel, C. K.; Singh, S.; **Saini, B.**; Mukherjee, T. K. **(2022)**, Macromolecular crowding-induced unusual liquid-liquid phase separation of human serum albumin via soft protein-protein interactions. J. Phys. Chem. Lett., 13, 3636–3644. (DOI: 10.1021/acs.jpclett.2c00307)

7) **Saini, B.**; Khamari, L.; Mukherjee, T. K. (2022), Kinetic and mechanistic insight into the surfactant-induced aggregation of gold nanoparticles and their catalytic efficacy: importance of surface restructuring. J. Phys. Chem. B, 126, 2130−2141. (DOI: 10.1021/acs.jpcb.2c00702)

Table of Contents

Chapter 2: Materials, Sample Preparation, and Experimental Techniques

Chapter 3: Biocompatible pH-Responsive Luminescent Coacervate Nanodroplets toward Theranostic Applications

Chapter 4: Specific Loading and In Vitro Controlled Release of a Ru-Based Hydrophobically Encapsulated Model Anticancer Drug inside Nanoassemblies toward Stimuli-Responsive Drug Delivery

Chapter 5: Nanocatalysis under Nanoconfinement: A Metal-Free Hybrid Coacervate Nanodroplet as a Catalytic Nanoreactor for Efficient Redox Reactions

Chapter 6: Synthetic Protocell as Efficient Bioreactor: Enzymatic Superactivity and Ultrasensitive Glucose Sensing in Urine

Chapter 7: Biomolecular Condensates Regulate Enzymatic Activity under a Crowded Milieu: Synchronization of Liquid−Liquid Phase Separation and Enzymatic Transformation

Chapter 8: Conclusions and Future Scopes

List of Schemes

Chapter 7

xxx

List of Figures

Chapter 3

and (D) confocal images of ND dispersion at pH 4.5 showing disassembled structures. (E) Changes in the turbidity of ND dispersion at 600 nm as a function of NaCl concentrations. (F) Changes in the PL intensity of aqueous dispersions of CDs and NDs as a function of time. The inset shows the photographs of aqueous dispersions of CD and ND under UV light illumination (λ_{ex} = 365 nm).

ATP nanodroplets. (C) Fluorescence enhancement factors of Ru-Cur in the presence of liposomes and ATP nanodroplets. The inset shows the daylight and UV-light (λ_{ex} = 365 nm) photographs of Ru-Cur aqueous dispersions in the presence of ATP nanodroplets. (D) Fluorescence decay trace (λ_{ex} = 405 nm) of Ru-Cur in the presence of ATP-nanodroplets.

Chapter 5

embedded NDs. (H) Size distribution histogram of NDs with mean size.

mM) in the presence of CDs (half-filled circle) and CD-embedded NDs (solid filled circle). Plot of $-\ln(C_t/C_0)$ vs reaction time for the reduction of 20 μM (I) 4-NP and (J) 4-NA by different concentrations of NaBH$_4$ (red: 2 mM; green: 4 mM; and blue: 10 mM) in the presence of CD-embedded NDs. (L) Confocal DIC images of CD-embedded NDs before and after the reduction reaction of 20 μM 4-NP and 4-NA in the presence of 10 mM NaBH$_4$. All the measurements were performed at 298 K in pH 10 aqueous medium.

Chapter 6

(***) P value < 0.001 and not significant (NS; P = 0.84). All the measurements were performed in pH 6.0 phosphate buffer.

Figure 6.6. (A) Changes in the absorbance ($\lambda = 650$ nm) of ox-TMB as a function of time with different concentrations ($0-100$ μM) of glucose in pH 6.0 phosphate buffer. (B) Linearized plot of absorbance at 650 nm of ox-TMB as a function of glucose concentrations in pH 6.0 phosphate buffer. The inset shows the linearized plot at lower concentrations of glucose. (C) Photographs of colorimetric response of aqueous mixtures (upper panel) and filter papers (lower panel) upon increase in the concentrations of glucose in pH 6.0 phosphate buffer. (D) Photograph of bare GOx/HRP-loaded filter paper. (E) Schematics showing the glucose sensing in spiked urine samples in solution and filter paper using GOx/HRP@ Droplet. (F) Changes in the UV-vis absorption spectra of the unspiked and spiked urine samples in the presence of GOx/HRP@Droplet composite. (G) Comparison of the colorimetric response of commercial strips and GOx/HRP@Droplet-loaded filter papers in the absence and presence of glucose. 226

Chapter 7

mean ± SEM for three (n = 3) independent experiments. Statistical significance was assessed by a two-tailed, unpaired Student's t-test with ***, P value < 0.001; **, P value < 0.01; and not significant (NS), P > 0.05.

Figure 7.8. (A) Schematic illustration showing the enzymatic reaction after the LLPS in the presence of crowder. (B) Michaelis-Menten plots of HRP as a function of TMB concentrations in the absence and presence of different crowders after the LLPS in pH 4.0 acetate buffer at 37 °C. (C) Michaelis-Menten plots of GOx as a function of glucose concentrations in the absence and presence of different crowders after the LLPS in pH 7.4 PBS at 37 °C. (D) Estimated V_{max} values of HRP and GOx in the absence and presence of 10% PEG, 10% dextran, 12.5% Ficoll, and 20 mg/mL BSA. (E) Estimated V_{max} values of HRP in the presence of 1% PEG, 1% dextran, 1% Ficoll, and 1 mg/mL BSA. The data represent the mean ± SEM for three (n = 3) independent experiments. 253

Figure 7.9. (A) Illustration of enzymatic reaction after the LLPS of enzyme in a time-dependent manner. Michaelis−Menten plots of HRP as a function of TMB concentrations at different time intervals after the LLPS in (B) 10% PEG, (C) 10% dextran, (D) 12.5% Ficoll, and (E) 20 mg/mL BSA. (F) Estimated V_{max} values of HRP in the absence and 254

and after the cascade reactions with different substrates. CLSM images of (F) FITC-labeled trypsin, and (G) RBITC-labeled alcohol dehydrogenase in the presence of 10% PEG in pH 7.4 PBS. The scale bars correspond to 5 μm.

List of Tables

Chapter 6

Chapter 7

Acronyms

NDs	Nanodroplets
CD	Carbon dot
PDADMAC	Poly(diallyldimethylammonium chloride)
PL	Photoluminescence
UV	Ultraviolet
Vis	Visible
AFM	Atomic force microscopy
FTIR	Fourier transform infrared
PXRD	Powder X-ray diffraction
QY	Quantum yield
OD	Optical density
SNDs	Smaller nanodroplets
LNDs	Larger nanodroplets
NaOH	Sodium hydroxide
FESEM	Field-emission scanning electron microscopy
CLSM	Confocal laser scanning microscopy
NaCl	Sodium chloride
DIC	Differential Interference Contrast
NR	Nile red
DOX	Doxorubicin
RB	Rose bengal
EtBr	Ethidium bromide
FITC	Fluorescein isothiocyanate

MTT	3-(4,5-dimethylthiazol-2-yl)-2,5-diphenyl tetrazolium bromide
BHK-21	Baby hamster kidney fibroblast cells
NPs	Nanoparticles
Ru-Cur	(p-cymene)Ru-(curcuminato)Cl]
SUV	Small unilamellar vesicle
GUV	Giant unilamellar vesicle
MLV	Multilamellar vesicle
ATP	Adenosine triphosphate
NMR	Nuclear magnetic resonance
ESI-MS	Electrospray ionization-mass spectrometry
$CDCl_3$	Deuterated chloroform
MeOH	Methanol
CTAB	Cetyltrimethylammonium bromide
TX-100	Triton X-100
SDS	Sodium dodecyl sulfate
Fwhm	Full width at half-maximum
CMC	Critical micelle concentration
TCSPC	Time correlated single-photon-counting technique
IRF	Instrument response function
TEM	Transmission electron microscopy
DPPC	Dipalmitoylphosphatidylcholine
PBS	Phosphate buffer saline
LC	Loading content
EE	Encapsulation efficiency
XPS	X-ray photoelectron spectroscopy

MSA	Mercaptosuccinic acid
QD	Quantum dot
PLys	Poly-L-lysine
4-NP	4-Nitrophenol
4-NA	4-Nitroaniline
4-AP	4-Aminophenol
4-AA	4-Aminoaniline
N_2	Nitrogen
$NaBH_4$	Sodium borohydride
L-H	Langmuir–Hinshelwood
GC-MS	Gas chromatography-mass spectrometry
DMSO-d^6	Deuterated dimethyl sulfoxide
Rh6G	Rhodamine 6G
PEG	polyethylene glycol
r-CD	Reduced carbon dot
Ox	Oxidized
GOx	Glucose oxidase
HRP	Horseradish peroxidase
DAPI	4',6-diamidino-2-phenylindole
OPD	o-Phenylenediamine
ABTS	2,2'-azino-bis(3-ethylbenzothiazoline-6-sulfonic acid)
TMB	3,3′,5,5′-Tetramethylbenzidine
H_2O_2	Hydrogen peroxide
CD	Circular dichroism
O_2	Oxygen
s.e.m.	Standard error of the mean
LOD	Limit of detection

BSA	Bovine serum albumin
RBITC	Rhodamine B isothiocyanate
LLPS	Liquid-liquid phase separation
mPEGNH$_2$	Methoxy polyethylene glycol
IDRs	Intrinsically disordered regions
LCDs	Low complexity domains
SMART	Simple Molecular Architecture Research Tool
LCST	Lower critical solution temperature
UCST	Upper critical solution temperature
MB	methylene blue
NaSCN	Sodium thiocyanate

Nomenclature

nm	Nanometer
cm	Centimeter
η	Refractive index
θ	Diffraction angle
d	Interplanar spacing
ζ	Zeta
mV	Millivolt
pH	The negative logarithm of hydronium-ion concentration
h	Hour
mg	Milligram
mL	Milliliter
μM	Micromolar
pK_a	Dissociation constant of an acid in ground state
mM	Millimolar
rpm	Rotation per minute
min	Minute
K	Partition coefficient
μg	Microgram
μM	Micromolar
I	Intensity
ns	Nanosecond
τ	Life time
T_m	Transition temperature
°C	Degree Celsius

T	Turbidity
A	Absorbance
M	Absolute cumulative release
E_r	Cumulative release
eV	Electronvolt
nM	Nanomolar
C	Concentration
K	Kelvin
k_{app}	Apparent rate constant
k	Reaction rate constant
M	Molar
t	Time
T	Temperature
ΔG	Gibbs free energy of activation
ΔH	Enthalpy of activation
ΔS	Entropy of activation
k_B	Boltzmann's constant
h	Planck's constant
E_a	Activation energy
A	Pre-exponential factor
KJ	Kilojoule
mol	Mole
ppm	Parts per million
δ	Chemical shift
λ	Wavelength
RT	Room temperature
s	Second
µm	Micrometer

pM	Picomolar
ε	Molar absorption coefficient
V_0	initial velocity
[S]	molar concentration of substrate
k_{cat}	catalytic rate constant
K_m	Michaelis constant
V_{max}	Maximum velocity
P	Probability
NS	Not significant
λ_{em}	Emission wavelength
λ_{max}	Absorption wavelength
SD	Standard deviation
μL	Microliter
ng	Nanogram
g	Gram
pI	Isoelectric point
α	Alpha

Chapter 1

Introduction

Chapter 1

1.1.   Preface

Cells are considered as the fundamental unit of a living system with a micro-confined space encircled by an outer cell membrane and comprised of multiple internal organelles. The critical characteristics of a cellular system are compartmentalization, metabolism, replication, and adaptation *[1–3]*. Out of these characteristics, compartmentalization is the basal property of a living system and therefore eukaryotic cell is mainly composed of membrane-bound and membrane-less compartments or organelles (Scheme 1.1). For instance, membrane-bound compartments such as mitochondria and lysosomes are closely associated with ATP production *[4]*, and macromolecule destruction *[5]*, respectively. However, intracellular membrane-less compartments like nucleoli *[6]*, Cajal bodies *[7]*, centrosomes *[8]*, stress granules, and P bodies *[9, 10]* are widely linked to intracellular environmental sensing *[11]*, regulation of RNA processing and transportation *[12, 13]*, congenital immunity *[14]*, DNA repairing *[15]*, neurotransmitter reservoir *[16],* and the events of neurodegenerative diseases *[17]*. More importantly, cell directs many of their biochemical reactions in membrane-less compartments found in the cytoplasm as well as in the nucleus compared to membrane-bound compartments *[18, 19]*. The membrane-less compartment and its interior contents collectively serve as a stable protocell and this whole protocell is totally separated by an interface from the environment *[7, 20]*. Recent evidences have shown that the membrane-less compartments or organelles inside the cells are known as liquid-like droplets that are formed by the liquid-liquid phase separation (LLPS) from the cytoplasm *[2,9,21–29]*. These droplets in the cell show fusion, surface wetting, and dripping characteristics highlighting the liquid-like behavior of droplets *[19, 21]*. In addition, the inner microenvironment of liquid-like droplets generates a distinct transient barrier between the

membrane-less compartment and cytoplasm and thence creates a microenvironment with different pH, ionic strength, and polarity for adequate biocatalysis *[2, 19, 22, 23]*. The spatiotemporal arrangement of encapsulated enzymes inside dense compartments, namely mitochondria *[24, 25]*, peroxisomes *[26]*, carboxysomes *[27]*, vacuoles *[28]*, lysosomes *[29]*, etc. expeditiously work for multi cascade reactions inside the cell toward energy production, remotion of ROS, CO_2 sequestration, osmotic control, and intracellular digestion. Therefore, the fast diffusion within these compartments makes them an efficient microreactor for entire biochemical pathways *[30]*.
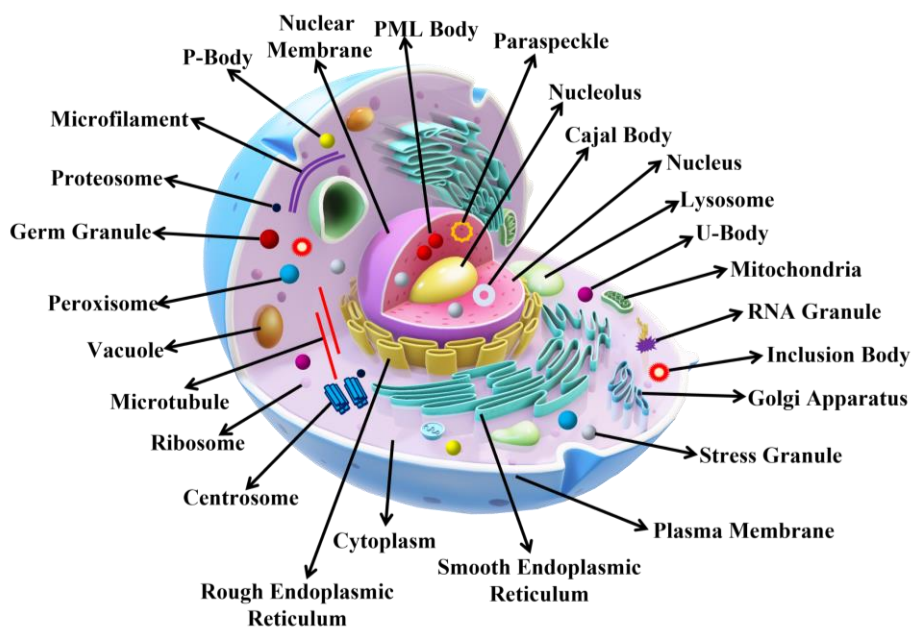
Scheme 1.1. Structure of eukaryotic cell with various membrane-less and membrane-bound organelles.

However, the enigma behind the evolution of cells from simple chemical compounds to modern cells is still unresolved *[31]*. Scientific communities have directed a lot of efforts to delineate the autopoietic nature of the living system and to understand the long-standing mystery of the origin of cellular

life after Oparin theory *[32, 33]*. Oparin proposed that life is an outcome of lifeless molecules, and hypothesized that physiochemical conditions on the early favored various chemical reactions to generate simple water-soluble organic compounds from inorganic precursors *[34]*. These organic compounds were further utilized in various reactions that finally produced novel and complex structures with distinct properties. Therefore, to understand the diverse functionalities or physiological aspects of cellular metabolism, the creation of an artificial cells or biomimetic compartments are highly demandable.

1.2. Artificial cells

The key challenge to explore the biochemical pathways of natural cell is the inherent complex-cum-fragile nature of cellular system that circuitously strike down the functionalities of various organelles inside the cell *[35]*. This complexity of natural cells has inspired scientists to design a wide range of artificial or synthetic cells with cell-like properties via bottom-up approach responding how the primitive cells evolved from the lifeless matter *[36]*. The concept of artificial cell was first proposed by Dr. Thomas Ming Swi Chang in 1957 *[37]*. He had developed stable microcapsules similar to cell-like compartments of 1-100 μm in diameter with semipermeable properties and showed that encapsulated enzymes could work efficiently inside these microcapsules in compare to free solution *[38]*. An artificial or synthetic or minimal cell is defined as a closed entity that mimics one or more functions of natural cell and encapsulates biologically active substances such as enzymes, drugs, hormones, proteins, and genes *[1, 39]*. Artificial cells have been defined in many different ways such as Tian *et al.* stated artificial cell as a micro-compartmentalized system which can mimic potential biochemical reactions *[40]*. Similarly, Jeong *et al.* described that for the development of compartmentalized artificial cell,

optimal conditions of reproducible giant unilamellar vesicles (GUV) are required *[41]*. Moreover, the product formed from artificial scaffold is completely different from the product formed from the cell engineering method as both products are formulated via different approaches. Therefore, the mode of designing of different artificial or synthetic cells from scratch is more important and are described below in brief.

1.2.1. Formulation of artificial cells

The fabrication of an artificial cell is classified into two categories based on their internal characteristics, namely typical artificial cells and non-typical artificial cells (Scheme 1.2). The typical artificial cells have structure similar to live natural cells and exhibit one or more key features of living biological cells such as evolution, self-growth, metabolism, reproduction etc. *[42, 43]*. However, the non-typical artificial cells have no morphological or structural restrictions and imitate some of the characteristics of natural cells such as surface properties, cellular functions, shapes and even morphology *[44]*. Artificial cells are also categorized into two types of approaches based on their construction method, namely top-down approach and bottom-up approach (Scheme 1.2) *[45]*.
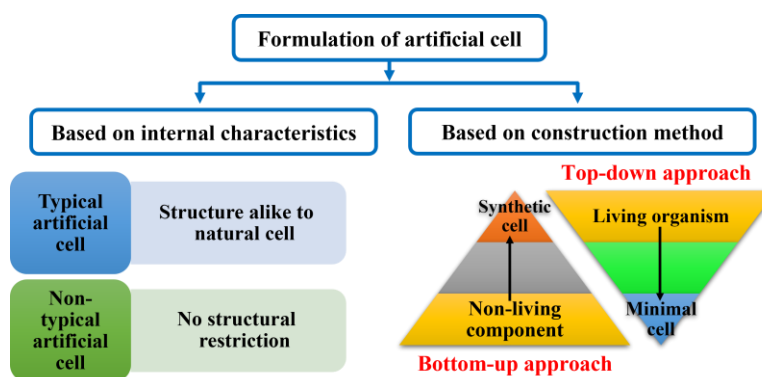
Scheme 1.2. *Schematic representation of synthetic routes of artificial cell.*

The top-down approach works likewise as cell engineering approach where the unnecessary genomes are completely replaced by synthetic one

or highest number of genomes striked down to the lowest number of genes that are required for essential biological functions and survival of cellular system *[46, 47]*. In 1995, Fraser *et al.* first time discovered a total of 517 genes as smallest genome of simplest living organism named Mycoplasma genitalium *[48]*, and further identified that only 382 out of 482 protein-coding and 43 RNA-coding genes are essential for life *[46, 49]*. Furthermore, unnecessary genes were striked down from 350 to ~150 genes with all necessary information required for the sustainability of life *[50, 51]*. It has been found that genome content may be vary in different organisms due to the differences in their physiology and metabolic capacity *[48]*. In addition, the existence of minimal cell was found to be strongly dependent on the resources present in the surroundings and cell permeability because knocking out of some of the essential component may lose self-reproducibility of the cell *[35]*. Upon considering these factors, the first synthetic cell governed by genome editing was created in 2010 from scratch named as *M. mycoides* cells *[52]*. However, the applicability of top-down method is limited due to its high cost, inaccuracy, unfriendly, and inherent toxic behavior *[35]*. Therefore, to overcome these limitations and to understand the origin of life, bottom-up approach for the creation of an artificial cell creates a link between the non-living and living world. In this complementary approach, non-biotic components such as biomacromolecules or inorganic materials stacked together to create *de novo* an artificial cell mimic to biological cell that have permeability, and self-replicability *[32, 53]*.
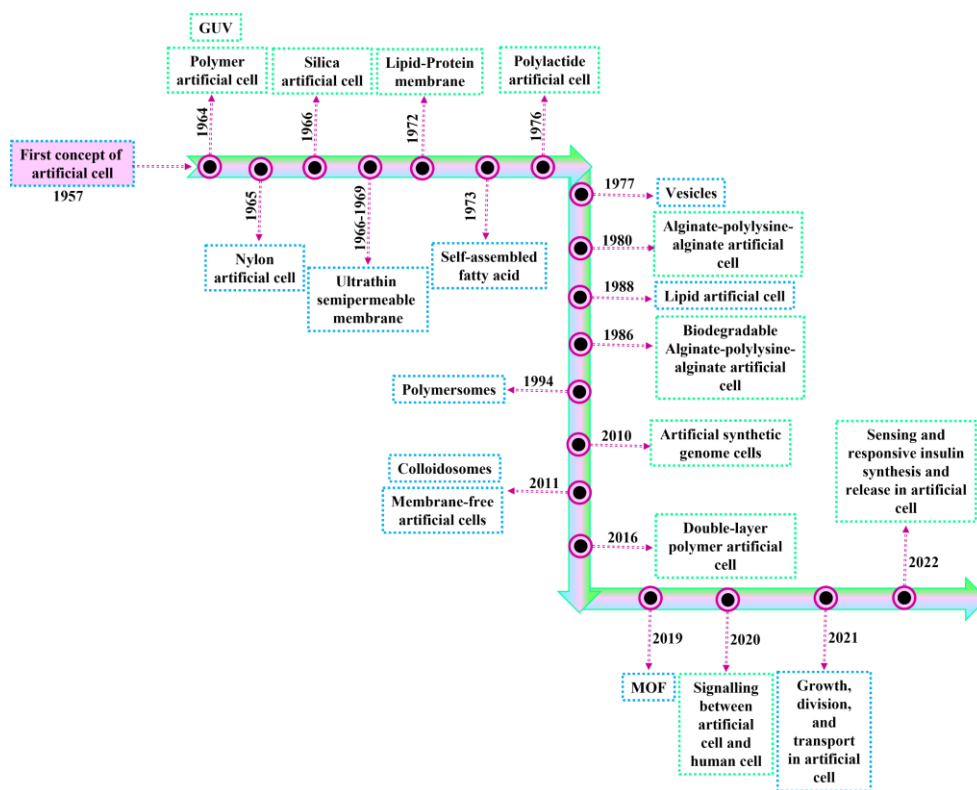
Scheme 1.3. *Schematic illustration of development in artificial cell.*

The milestone for constructing the artificial cells started since 1957 after the successful creation of lipid vesicles by Chang (Scheme 1.3) *[35].* Afterwards, many researchers have used bottom-up approach to design a wide range of artificial cells with versatile functional response which are discussed below in brief.

1.2.2. Type of artificial cells

A series of artificial or synthetic cells have been constructed as a protocell model to demonstrate the cell-like properties ranging from liposomes, polymersomes, proteinosomes, colloidosomes, dendrimers to coacervates (Scheme 1.4).

7

1.2.2.1. Liposomes

Liposomes are the first described synthetic analog for biomimetic system which are formulated by different techniques such as thin-film hydration, solvent injection, electro-formation, high-pressure extrusion, reverse-phase evaporation, and microfluidics *[54]*. Monolayer vesicles such as small unilamellar vesicles (SUVs; < 100 nm), large unilamellar vesicles (LUVs; 100 nm-1 µm), and giant unilamellar vesicles (GUVs; > 1 µm) along with multilayered vesicles (MLVs) have been used to understand the organization, functions, and dynamics of lipid membrane with specific peptide chains *[55]*. The size and morphology of GUVs were found to be similar to natural cells and thence used for studying the properties of cell membrane. For instance, Picon *et al*. fabricated phospholipid-based GUVs and then encapsulated with cyprosins, a proteolytic enzyme *[56]*. Here, they have observed the accelerated cheese production and enhanced flavor intensity along with shortened ripening time. Similarly, Lee *et al*. designed a protocellular system or biomimetic vesicle regulating two ATP-dependent reactions, carbon fixation, and actin polymerization reaction *[57]*. Furthermore, distinct and efficient cell-like bioreactors with modified lipid composition have been created and utilized for selective permeability of nutrients *[58]*, intracellular signaling cascade *[59]*, intercellular communication *[60]*, translation of chemical messages or sensing *[61]*, and evolutionary mechanisms *[62]*. Despite of these favorable applications, liposomes exist in metastable state that induces low physical stability, high membrane permeability, low chemical versatility, and high sensitivity toward their fabrication.

1.2.2.2. Polymersomes

Fatty acids, the simplest form of lipids, are the single chain amphiphilic molecules that can form stable spherical structures like vesicles, and micelles in an aqueous medium *[63]*. In comparison to liposomes, polymersomes shows enhanced cell membrane properties and thereof act as primitive cellular model *[64]*. However, the use of organic solvents during their formulation, limited diffusion of molecules via hydrophobic membrane, chemical incompatibility, and harsh chemical modifications of lipid materials further limit their development and applicability *[65]*.
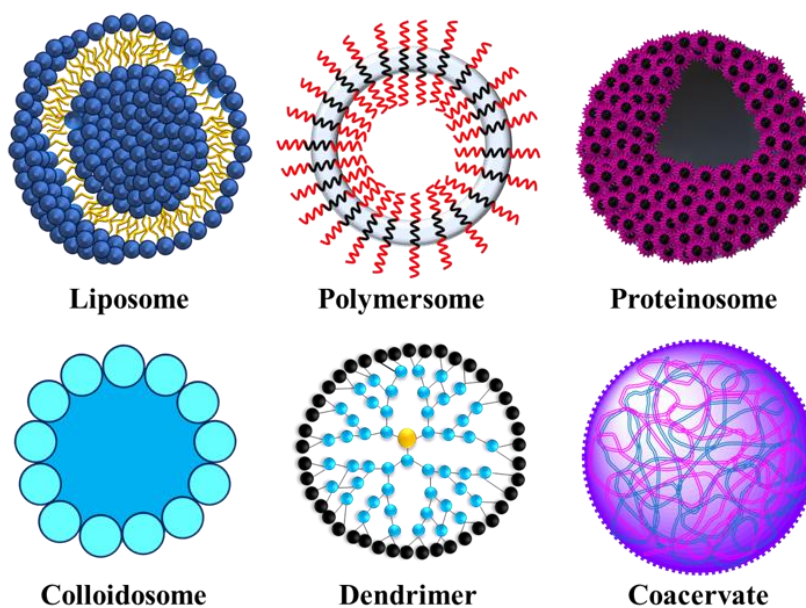
Scheme 1.4. Structure of different type of artificial cells.

On the other hand, polymersomes formed from amphiphilic block copolymers as lipid substituents show lower leakage, higher stability, lower mobility, controlled membrane permeability, and excellent chemical versatility which makes them a good candidate for the construction of biomimetic system *[66, 67]*. For instance, Chang showed that

semipermeable membranes of polymersomes could be able to pass small molecules such as nutrients, metabolites etc. *[68]* and can also encapsulate cells, microorganisms, enzymes, hormones, short peptides, hemoglobin, adsorbents, and bioactive substances *[68–74]*. Similarly, O'Shea *et al.* fabricated sodium-alginate-polylysine-sodium alginate membrane as protocell model evidencing the prolonged xenograft survival rate *[75]*. Anraku *et al.* designed injectable enzyme-loaded polymersomes as nanoreactor for activating prodrugs at the tumor site that can be utilized for enzyme/prodrug therapies (EPT) and enzyme-replacement therapies *[76]*.

Furthermore, hybrid vesicles or advanced vesicles fabricated from lipid and copolymers such as poly(dimethylsiloxane)-graft-poly(ethylene oxide) (PDMS-g-PEO), polyethylene glycol (PEG), polycaprolactone (PCL), and polylactide (PLA) have been designed by adjusting the lipid/polymer ratio for showing their applicabilities toward surface mechanism, drug delivery, encapsulation, and selective permeability *[77, 78]*. However, the artificial cells fabricated from lipid and amphiphilic polymer show high stability, and high chemical versatility but also possesses low molecular permeability.

1.2.2.3. Proteinosomes

Proteinosomes are delineated as permeable, biocompatible, and bifunctional compartment which are consisted by monolayer of conjugated protein-polymer building blocks and encloses by hydrophilic lumen. Protein-based versatile protocells exhibit high encapsulation efficiency, selective membrane permeability, multi-compartmentalization, and cytoskeleton-like matrix formation.

For example, Huang *et al.* developed first proteinosomes formed by bovine serum albumin-poly(N-isopropylacrylamide) (BSA-NH$_2$/PNIPAM) at the oil/water interface and demonstrated its properties toward selective

permeability, encapsulation, targeted delivery, stimuli-responsiveness, and gene-directed protein synthesis *[79]*. Similarly, Cai *et al.* fabricated proteinosomes by using electrostatic interaction between negatively-charged BSA-PNIPAM and positively charged enzymes, lysozymes, and trypsin and further highlighted the importance of structural and functional integrity of enzymes *[80]*. Moreover, different types of enzyme-polymers nanoconjugates have been fabricated and utilized for multi-step membrane-mediated cascade reaction *[81]*, and spatiotemporal release of different components *[82, 83]*. Apart from simple preparation method, biocompatibility, and semi-permeable properties of listed polymersomes, the development of polymersomes have some shortcomings associated with structural instability, high sensitivity, and uncontrolled size formulation.

1.2.2.4. Colloidosomes

Colloidosomes are interiorly hollow elastic shells and are formed by self-assembly of colloid particles at the interface of liquid/liquid biphasic system which can be inorganic, organic, or both *[84–86]*. The high chemical versatility, and good physiochemical properties of colloidosomes exemplify its importance as microreactor for catalysis, photoreactions, oscillation reactions, and theranostic applications *[84, 85, 87]*. For example, Pan *et al.* designed a hybrid catalytic reactor from hemoglobin-modified silica nanoparticles and demonstrated its good biocatalytic stability, enhanced cascade reaction rates along with good functional response toward biological computing *[88]*. Also, Liu *et al.* fabricated a dual-enzyme colloidosome reactors (DECRs) by silica nanoparticles and encapsulated water-soluble glucose oxidase (GOx) inside the colloidosomes *[89]*. The fabricated microreactor showed high performance of biphasic cascade reactions of *N*-heteroaromatic compounds without any decrease in yield even after four cycles. Similarly, Rodríguez *et al.* utilized catalase, lipase,

or alkaline phosphatase-loaded colloidosomes to understand the dynamics of protocellular community for artificial phagocytosis response *[90]*. Furthermore, Sun *et al.* prepared a lipase-encapsulated hollow colloidosomes by green methodology and demonstrated good encapsulation rate, better biocompatibility, enhanced catalytic rate and excellent reusability over ten catalytic cycles *[91]*. Therefore, it has been found that colloidosomes provide adequate enzyme active sites at the organic phase-water interface which arises due to the high surface area of the nanoparticles present over the structure. However, the complex synthetic procedure and harsh crosslinked-enzyme immobilization process limit their advancement as biomimetic system *[92]*.

1.2.2.5. Dendrimersomes

Dendrimersomes are the stable, homogenous, monodispersed uni- or multilamellar vesicles self-assembled in water from amphiphilic Janus dendrimers (AJDs). They exhibit an ability to self-assemble into chemically versatile uniform structures such as vesicles, micelles, tubular, cubosomes along with incorporation of transmembrane channels which make them an alternate model to polymersomes and liposomes *[93]*. Different dendrimersomes have been utilized in chemical catalysis *[94]*, drug delivery carrier *[95]*, targeting delivery *[96]*, solubility enhancement *[97]*, and as therapeutic agents *[98]*. For example, Gitsov *et al.* designed a special type of nanoreactors through adsorption of different copolymers onto the laccase enzyme in an aqueous medium and displayed amended catalytic performances under green chemistry conditions *[99]*. Similarly, Perli *et al.* constructed triazolylferrocenyl dendrimersomes in water containing nontraditional green fluorescence (NTIL) for nanotheranostic devices *[100]*. However, low encapsulation efficiency, and special condition for their synthesis further limits their advancement.

All these above-mentioned examples of synthetic cell have their own beneficial structural features and displays various functionalities but are often constructed using complicated, multi-step processes involving specialized techniques *[101]*. Therefore, the spontaneous liquid-liquid phase separation of coacervates in an aqueous medium offers an alternative driving force for compartmentalization.

1.3. Membrane-less coacervates

Inspired from membrane-less organelles formed inside many living cells, condensates or coacervates have become a popular candidate as synthetic compartment, as they have been found to concentrate nucleic acids, nucleotides, peptides and many types of small molecules *[102, 103]*. Membrane-less coacervates are dense liquid droplets formed by liquid-liquid phase separation (LLPS) in an aqueous medium through a process of coacervation *[102]*. Coacervation is a phenomenon in which a colloidal solution gets separated into colloid-rich and colloid-poor phases. The colloid-rich phase bearing larger content of colloidal components are known as coacervate droplets and this phase remains in equilibrium with the dilute phase, both present in the single medium. As coacervate droplets exhibits the sponge-like structure, so it is also called as sponge phase, or anomalous phase, or L_3 phase *[104]*. The term coacervate came from two Latin words "co" (jointly) and "acerv" (a mound) and this term was coined by Bungenberg de Jong and Kruyt in 1929 while examining the coacervation process in the gum Arabic and gelatin *[105]*.

1.3.1. Types of coacervation process

Generally, coacervation process is classified into two categories, namely simple-/self-coacervation and complex coacervation (Scheme 1.5). In simple coacervation, only one type of polymer such as polyelectrolytes, proteins, surfactants, along with additives are used to form coacervates

whereas in complex coacervation, two oppositively charged polyelectrolytes, proteins, surfactants, with or without additives interact with each other *[106]*.
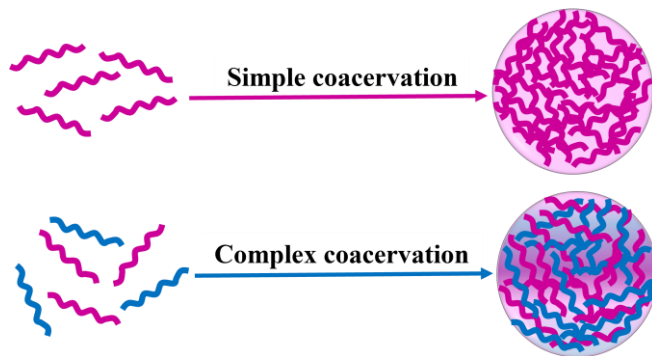
Scheme 1.5. *Schematic illustration of coacervation.*

The phase separation driven by electrostatic attraction between two oppositely charged polyions in synthetic polyelectrolytes along with an additional interactions like hydrogen bonding and hydrophobic interactions in biopolymers are referred as complex coacervation *[107–109]*. This type of coacervation occurs through associative phase separation. In contrary, nonassociative phase separation is also known as an aqueous two-phase system (ATPS) that occurs in between the nonionic macromolecules such as poly(ethylene glycol) (PEG)/dextran system *[110]*. In addition, the phenomena of phase separation could also be possible without any additives in case of some zwitterionic or ionic/nonionic polymers when the temperature reaches above the lower critical solution temperature (LCST) *[111]*. This type of simple coacervation process mostly occurs in biopolymers where 'clouding' term is used for this phenomenon and 'cloud point' is for critical temperature.

Importantly, it has been observed that the coacervate formation is impelled by two factors, the first one is the release of counterions that leads to an increase in entropy and another one is the electrostatic interactions that

directs the decrease in enthalpy *[112]*. Significantly, complex coacervation is entropically favorable and is driven by the gain in the translational entropy of small ions when they released from being bound or condensed to the polyelectrolytes *[113]*. Also, the process of coacervate formation is exclusively pointed their importance towards bio compartmentalization strategy as they can exchange materials dynamically with intracellular cytosol, sequester various macromolecules, and preserve structural integrity *[114, 115]*. Therefore, the scope of formation of coacervates has been expanded from proteins and polysaccharides to synthetic polymers *[116]*, polynucleotides *[101, 117, 118]*, nanoparticles *[119]*, surfactants *[120]*, and other self-assembled structures *[121–123]*. Hence, the applicability of coacervates extended into various domains of cellular biology *[124]*, food science *[125]*, personal care products *[126]*, medicine as drug delivery *[117, 127]*, sensing *[128]*, adhesives *[129]*, nano/bioreactors *[76, 116, 130]*, additives *[131]*, emulsifier *[131]*, and viscosity modifiers *[132]* etc.

1.3.2. Features of membrane-less coacervates

The fabrication procedure of membrane-less condensates is very facile in water *[101]*. The interior crowded environment helps to preserve the bioactivity of various bioactive molecules pointed its usefulness toward various enzymatic reactions *[133]*. Moreover, the uniform or homogenous spherical structure with lower dielectric constant of coacervates favors the preferential sequestration of dye molecules, proteins such as green fluorescent proteins, hemoglobin, myoglobin, and metal nanoparticles inside its cavity *[101]*. These condensates also show high viscoelasticity, varying fluidity, controlled assembly and disassembly, and dynamic environmental response *[19, 21]*. Moreover, easy diffusion and immobilization of solutes inside the confined environment of coacervates

15

extends the shelf life of solutes. Subsequently, spatiotemporal control over reaction kinetics increases their importance toward enzymatic reactions due to increased effective local concentration inside it *[134, 135]*. In addition, condensates enable the stimuli-responsive controlled release of cargo *[118, 136]*. All these features make membrane-less coacervates a promising protocell model alternative to earlier developed artificial cells.

1.3.3. Factors influencing coacervation

The process of coacervate formation is a result of subtle balance of various interactions such as electrostatic, hydrogen bonding, hydrophobic, van der Waal forces, cation-π interaction, and π-π interaction etc. *[137–140]* (Scheme 1.6).
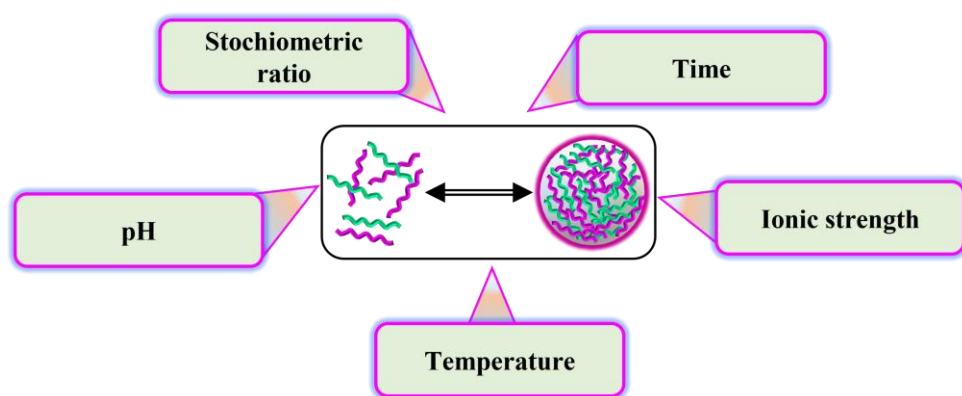
Scheme 1.6. *Factors influencing coacervate formation.*

Once this balance of weak interactions is disturbed, the coacervates may convert into either single phase or precipitate. Therefore, the process of coacervate formation is strongly dependent on the different factors such as stoichiometric ratio, pH, temperature, ionic strength, and time *[108, 109, 141–144]*.

(A) Effect of stoichiometric ratio

The ratio between the number of positive and negative charges present in the simple polyelectrolyte mixture is defined as the charge stochiometric ratio. This ratio is the first most decisive parameter associated with the complex coacervation process. In general, electroneutrality need to be focused to accomplish the coacervate formation which occurs in very narrow range of stochiometric compositions (Scheme 1.7).
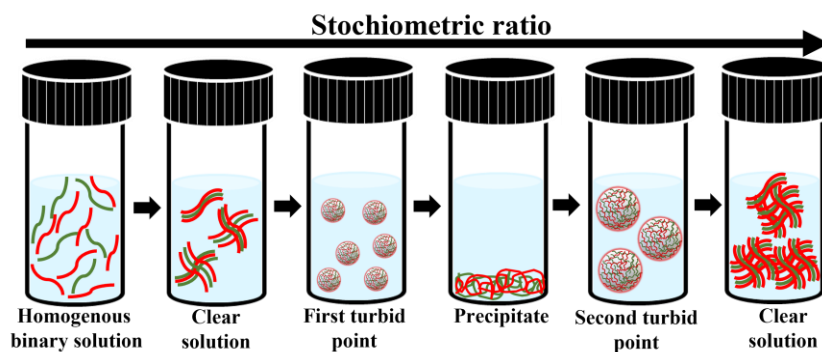
Scheme 1.7. Schematic illustration showing effect of stochiometric ratio. This narrow range can be broadened upon addition of different concentrations of salt *[145]*. But in case of complex molecules like proteins, the driving force for coacervation process comes from the specific charge patches present on the protein surface, not from the overall charge of the macromolecules. Moreover, the stochiometric ratio not only influence the formation of coacervate droplets but their morphology also *[107]*.

(B)   Effect of pH

Alteration in pH can tune the degree of ionization of typically small molecule ions or weak polyelectrolytes, which further affects the electrostatic interactions between molecules and hence this property varies as a function of pH. The pH response of singly charged acidic group can be defined by the negative logarithm of the acid dissociation constant or pK_a value. When the pH of the solution becomes equal to the pK_a value, half of the molecules will be neutralized and half will be charged inside the

solution. For the acidic groups like carboxylates, the number of charged groups will increase upon increase the pH value above pK_a. Similarly, for the basic groups like amines, the number of charged groups will increase upon decrease the pH value below pK_a. Similar approach can also be applicable for the base dissociation constant or pK_b. In case of complex macromolecules, no single pK_a value can be used to explain the effect of pH on whole molecule. Therefore, the apparent pK_a value comes into picture and it varies as a function of solution pH. To define the electroneutrality of multiple charged protein, isoelectric point or pI is the best parameter. When the pH of the solution is above or below the pI, a protein bears a net negative or positive charge, respectively.

For instance, Nicholas *et al.* fabricated pH-responsive coacervate droplets using poly(diallyldimethylammonium)chloride and dipeptide *N*-fluorenyl-9-methoxy-carbonyl-*D*-alanine-*D*-alanine and found that upon decreasing the pH of the medium, coacervate droplets converted into the supramolecular hydrogel *[146]*. Similarly, Huang *et al.* examined the pH-dependent morphological changes of *O*-carboxymethyl chitosan and gum Arabic droplets and noticed that upon increase in pH of the solution, network structure become more regular and shows smaller pore sizes *[147]*. Joshi *et al.* explored the phases of gelatin A/pectin binary mixture via light scattering, turbidimetry, and zeta potential measurements *[148]*. Here, they have observed that at pH<pI, electrostatic interactions were found to be dominant whereas at pH>pI, no such interactions were found.

(C)   Effect of ionic strength

The formation or dissociation of coacervates is strongly influenced by the ionic strength of the medium (Scheme 1.8). The presence of low salt concentration in the system can facilitate the formation of coacervates by modulating the extent of electrostatic attraction between the

polyelectrolytes and allow extrinsic charge compensation to trigger the molecular rearrangement.
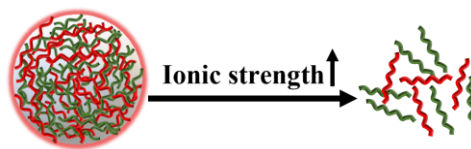
Scheme 1.8. *Schematic illustration showing effect of ionic strength on coacervation.*

However, the high salt concentration inhibits the coacervate formation and disfavors the entropic release of bound counterions. The interpretation of these trends comes from the turbidimetric experiment that explains the critical salt concentration effectively. The critical salt concentration is the concentration of optimum salt at which the liquid-liquid phase separation is diminished. For instance, divalent salts such as $CaCl_2$, Na_2SO_4 etc. have lower critical salt concentration than the monovalent salt NaCl. Subsequently, more significant decrease in critical salt concentration is observed for the divalent cations like Ca^{2+} in compare to divalent anions like SO_4^{2-} [109, 149, 150]. These differences in critical salt concentration may be attributed due to the differences in the hardness of constituent ions, chaotropic or kosmotropic Hofmeister behavior of ions.

For instance, Chollakup *et al.* utilized a poly(acrylic acid/poly(allylamine) (PAA/PAH) system to explore the effect of ionic strength on coacervation process *[142]*. Here, at low concentration of PAA and PAH in the presence of 100 mM NaCl, no coacervate formation is observed. However, at higher concentration precipitation occurred. Subsequently, a limited amount of precipitate and coacervate regions were obtained at 400 mM NaCl. While increasing the NaCl concentration upto 1500 mM, coacervation is observed without precipitation.

(D) Effect of temperature

The influence of temperature on the coacervation process can be described by number of pathways. The increased electrostatic dissociation and increased hydrophobic interactions are closely associated to temperature which is affected by changing the degree of ionization *[131]*. The strong effect of temperature on the coacervate formation only depends on the nature of individual molecules, not on the self-assembly process (Scheme 1.9). The electrostatic interaction between polyelectrolytes decreases with increasing temperature. On the other hand, the thermoresponsive polymers can either show lower critical solution temperature (LCST) or an upper critical solution temperature (UCST). In the LCST region, polymer is completely soluble at lower temperature and phase separation occurs upon heating and generally driven by entropic factor. However, in UCST region, polymer is completely soluble at higher temperature and phase separation occurs upon cooling where the interaction between polymer-polymer and solvent-solvent gets dominated.
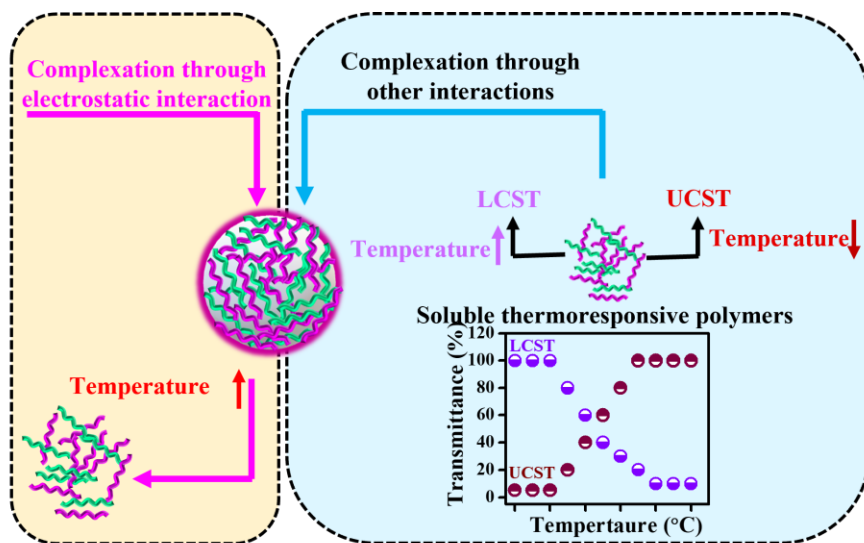
Scheme 1.9. *Schematic illustration showing effect of temperature on coacervation.*

For instance, Zhang *et al.* reported thermoresponsive polymer formed from poly(*N*-(2-hydroxypropyl) methacrylamide-glycolamide) (poly(HPMA-GA)) *[151]*. This polymer showed coacervation at lower temperature due to the dominating hydrogen bonding and hydrophobic interactions and upon increasing the temperature, coacervation stops due to the decreasing hydrogen bonding. Similarly, Nishida *et al.* designed a pH- and temperature-responsive coacervate system based on LCST-type polymer *β*-cyclodextrin-threaded polyrotaxane and encapsulated model proteins such as albumin protein (BSA), lysozyme, and galactosidases *[152]*. Here, they have observed the temperature induced coacervate formation and while decreasing the pH from physiological condition to 5, polymer readily degrades and thence release ~80% proteins without any loss in activity after 24 h. Subsequently, Aumiller *et al.* fabricated thermoresponsive polyU/polyamine coacervate droplets and found that polyU forms soluble complexes with polyamines at low temperature due to intramolecular secondary structure and base-stacking interactions whereas upon heating, the secondary structure gets broken and converted into a random coil conformation which favors the coacervation process *[153]*.

(E) Effect of aging

The liquid coacervates have the potential to show coalescence phenomenon over time as coacervates are considered as metastable phase *[154]*. The smaller droplets fuse to form larger droplets or turns into a bulk/macroscopic coacervate phase over time (Scheme 1.10).
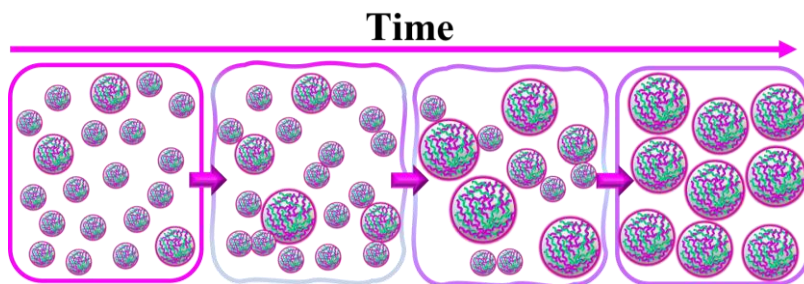
Time

Scheme 1.10. *Schematic representation showing effect of time on coacervation.*

This type of coalescence can also be accelerated by centrifugation at high rotation per minute *[155]*. Moreover, the coacervation between oppositively charged polyelectrolytes sometime form hydrogel.

The stability of coacervates influenced by all-above-mentioned factors are examined via turbidimetry and optical microscopy.

1.3.4. Type of membrane-less coacervates

There are mainly three types of membrane-less coacervates listed in this thesis, namely synthetic organic coacervates, synthetic hybrid coacervates, and biomolecular condensates (Scheme 1.11).

1.3.4.1. Synthetic organic coacervates

Synthetic organic coacervates are commonly formed by the organic macroions including polyelectrolytes, biopolymers, amphiphilic polymers, surfactants, and dendrimers. For example, Vitorazi *et al.* reported a complexation between PDADMAC and sodium polyacrylate (PANa) that is composed by two-step process *[156]*. Further they have demonstrated that coacervates generally shows two-step behavior in thermodynamic titration and it is a kinetically controlled process that starts only after the formation of polyelectrolyte complex (PEC). In another work, Li *et al.* reported a comparative structural difference of two systems named as

PDADMAC/PSSNa and PDADMAC/PANs *[157]*. Here, they have observed that those system which are formed by highly electrostatic interaction like PDADMAC/PSSNa shows formation of solid aggregates via liquid to solid phase transition whereas weakly interacting system like PDADMAC/PANa went through liquid-liquid phase separation resulting as coacervate droplet formation. Moreover, van Swaay *et al.* designed narrow size distributed coacervate droplets from PDADMAC with either adenosine triphosphate (ATP) or carboxymethyl-dextran by using microfluidic flow-focusing system and compared their improved stability with conventional vortex dispersion technique [*158*].
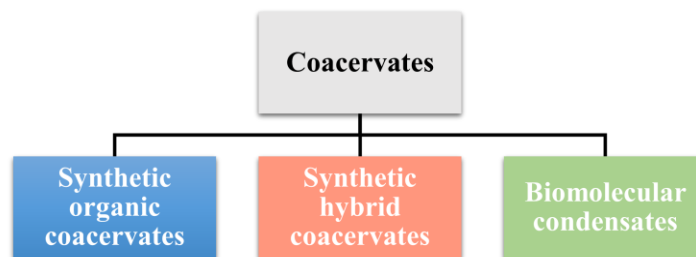
Scheme 1.11. *Type of coacervates.*

Cruz *et al.* designed coacervate droplets using poly(sodium L-glutamate) (PGNa) and poly(amido amine) dendrimer (PAAD) in the presence of 250 mM sodium chloride (NaCl) at pH 9.1 and explained the formation of microgel from colloid aggregation via interpolyelectrolyte complex (IPEC) *[159]*. Yang *et al.* explained the role and position of co- and counter ions in the formation of poly(diallyldimethylammonium) (PDADMA) and poly(styrene sulfonate) (PSS) coacervate droplets *[160]*. In an elegant work, Narayanan *et al.* reported a new class of thermoresponsive biodegradable polyester forming coacervate droplets which could be utilized as an injectable scaffold, adhesive, and delivery carrier of sensitive therapeutics like drug or protein *[161]*. Priftis *et al.* synthesized ternary coacervates by combining

poly(allylamine)hydrochloride (PAH) or branched poly(ethyleneimine) (PEI) with poly(acrylic acid) (PAA) and poly(*N,N*-dimethylaminoethyl methacrylate) (PDMAEMA) *[162]*. Here, the ternary coacervates showed the enhanced salt resistance compared to the binary PAA/PDMAEMA system.

Moreover, Dubin *et al.* studied the complex coacervation between cationic polyelectrolyte PDADMAC and mixed micelles of anionic surfactant sodium dodecyl sulfate (SDS)-neutral surfactant Triton X-100 (TX-100) and explored the three diffusional modes in the dilute-phase and coacervate-phase *[163]*. Moulik *et al.* formed coacervates of amphiphilic sodium N-Dodecanoylsarcosinate (SDDS) with polycationic hydroxyethyl celluloses and studied the nature of interactions between different species and subsequently examined the concentration-dependent phase transition from complexation to aggregation to coacervation *[164]*. Miyake *et al.* constructed polymer/detergent coacervate droplets driven by electrostatic interaction to explain the role of molecular structures and concentration on the coacervation process in shampoos and body washes *[165]*. Keshavarzi *et al*. fabricated biopolymers/surfactants membrane complexes in solution and explained the effect of surfactant hydrophobicity and concentration to drive the coacervate formulation *[166]*. In addition, Douliez *et al.* explained the ability of droplet formation of cationic surfactants like cetylpyridinium chloride (CPCl) or cetyltrimethylammonium bromide (CTAB) with decanoic acid in the pH range of 4.0 to 8.0 in the presence of different salts *[167]*. Also, they have showed the possibility of their utilization for encapsulation of biomolecules such as enzymes and DNA. Kumar *et al*. fabricated complex coacervates by using fluroenylmethoxycarbonyl (Fmoc)-protected D-Ala-D-Ala dipeptide with PDADMAC at pH 8 and explained the conversion of coacervate to fibril formation upon decreasing

the pH *[168]*. Similarly, Bartosz *et al.* reported tunable phase separation of histidine-rich squid beak proteins (HBPs) from microdroplets to hydrogels where the multiple events promoted hydrophobic collapses and further showed its utilization for stimuli-responsive smart drug delivery systems *[169]*. Exploring the dynamic assembly of coacervates, Koga *et al.* demonstrated reversible growth and disassembly of poly-L-lysine/ATP coacervate microdroplets in response to change in pH *[118]*. Further, exploiting the high concentration of ATP in the microdroplet, they achieved an enhanced rate of glucose phosphorylation and dehydrogenation process. Apart from these, Valley *et al.* reported that coacervates formed from high-density inorganic polyoxometalate (POM) shows faster phase-separation rate, low volume fraction, and high loading capacity for methylene blue *[170]*.

However, the inhomogeneous charge distribution over these polymeric macroions along with variance in charges based on solution conditions often leads to inaccurate description of their intermolecular interactions. Also, the quantification of enthalpy contribution from independent macroions to complexation resulted due to the hydrophobic attraction between non-polar groups of organic molecules is quite difficult *[171]*. To understate these complications and for substantial applications, a new class of synthetic hybrid coacervates with enhanced materialistic properties and integrated functions came into picture.

1.3.4.2. Synthetic hybrid coacervates

Synthetic hybrid coacervates are formed via the binary mixture of organic and inorganic molecules such as inorganic cluster, and nanoparticles etc. where the multivalent charges and charge distribution is well known in the aqueous medium. For instance, Jing *et al.* examined the complexation between zwitterionic poly(sulfobetaine methacrylate) (PSBMA) and

25

inorganic polyoxometalate (POM) polyanions in LiCl aqueous solutions and showed its importance toward green catalysis to nanomedicine *[171]*. Pablo *et al.* developed a scaling theory to understand the structure and dynamics of hybrid coacervates from linear polyelectrolytes and spherical colloids such as globular proteins, solid nanoparticle (NPs), or ionic spherical micelles *[172]*. Similarly, Berret *et al.* reported CeO_2-based core-shell hybrid coacervates with efficient absorption and their strong stability on various substrates for coating and anti-biofouling applications *[173]*.

Recently, Vaishnav *et al.* fabricated a new class of organic-inorganic hybrid coacervates by utilizing anionic CdTe quantum dots (QDs) and cationic PDADMAC *[174]*. These droplets were found to be colloidally stable over a broad range of composition, pH, and ionic strength. Moreover, these droplets were further utilized for Hg^{2+} detection, photocatalysis, and dye degradation application *[128, 175]*. As these hybrid droplets are formed from Cd and Te heavy metals, therefore their applicability is restricted for biomedical applications due to their cytotoxicity. Here, in the present thesis, biocompatible negatively charged carbon-dots (CDs) have been firstly synthesized and further utilized for the fabrication of hybrid CDs-embedded coacervates in the presence of cationic polymer PDADMAC for theranostic applications.

Carbon-dots (CDs) are a special type of fluorescent carbon-based nanomaterial with particle size less than 10 nm and also known as carbon quantum dots (CQDs) *[176]*. CDs are fabricated very efficiently via bottom-up approaches, mainly by hydrothermal and microwave method. Generally, CDs are amorphous in nature and exhibits aromatic sp^2 hybridized carbon core along with aliphatic carbon atoms *[177, 178]*. CDs shows strong absorption peak in the UV region and intense photoluminescence without photobleaching. Due to their excellent and

tunable PL holdings, small size, excellent water solubility, cost-effectiveness, amenable surface functionalization, and biocompatibility, CDs have been utilized for wide applications such as drug delivery, bioimaging, biosensing, optoelectronics, catalysis, anticounterfeiting *[176, 179, 180]*.

In continuation, poly(diallyldimethylammonium chloride) (PDADMAC) is the most commonly used water-soluble cationic polyelectrolyte possesses quaternary ammonium group in the penta-cyclic ring of the polymeric backbone. The positive charge on PDADMAC remains constant throughout at all pH values of the solution and hence, it is widely used in biopharmaceutical industry for an acceptable concentration (Scheme 1.12) *[181]*.
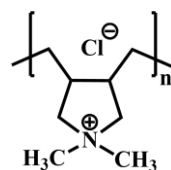
Scheme 1.12. *Structure of PDADMAC.*

1.3.4.3. Biomolecular condensates

Biomolecular condensates are a distinct class of membrane-less intracellular organelles which carry out specialized functions within the cells. P granules, a type of membrane-less compartment found in the *Caenorhabditis elegans*, were the first biomolecular condensate observed to form via LLPS *[21]*. The term biomolecular condensate refers to biological polymers that undergo self-assembly via clustering to increase the local concentration of the assembling components. In addition, biomolecular condensate represents coalescence of biomolecules like RNA, DNA, and proteins; however, are functional, nonstoichiometric, and dynamic assemblies like membrane-bound organelles but lacking any enclosed membrane *[182]*. These condensates are involved in diverse

processes including RNA metabolism, ribosome biogenesis, DNA damage response, and signal transduction etc. Moreover, the presence of intrinsically disordered regions (IDRs) in proteins and multivalent macromolecular interactions between proteins or between proteins and nucleic acids, lead to liquid demixing and their phase separation *[183]*. Also, it supports compartmentalization and spatiotemporal regulation of biochemical activities inside the cell.

Most importantly, phase separation of biopolymers can impact reaction kinetics and free-energy changes associated with substrate binding, transition state, product release, and turn over number. Within this framework, biological enzymes are particularly good candidate to stabilize the transition state *[184]*. But how the crowded cellular environment regulates various biochemical reactions so efficiently in the presence of enzymes is a fundamental question of cell biology and is a hot topic to address now a days. Earlier studies have demonstrated that instant addition of macromolecular crowders, enzymatic activities either decreased or increased or remain unaltered *[185–187]*. But the contrasting effects of macromolecular crowding on kinetic parameters is still not clear. Also, the physiological behavior of enzymes under crowding is highly neglected. Therefore, it is utmost important to identify the physiological behavior of enzymes and fundamental mechanism associated with the reaction kinetics in the presence of macromolecular crowders.

1.3.4.3.1. Macromolecular crowders and their role

Macromolecular crowders are the inert, non-charged polymers that occupy more volume inside the cell in compare to other solvent but do not interact with target proteins. This excluded volume effect increases the effective concentration of macromolecules which basically alters the rates and equilibrium constants of the reaction *[187, 188]*. Also, it affects the

protein's structure and stability, enzyme's activity, diffusion, protein-protein interactions, protein-nucleic acid interactions, and pathological aggregation etc. *[187–193]*. Macromolecular crowding effect alters the behavior of molecules inside the cell which is radically different than the test-tube measurement reflected that the in vitro metabolic rate in dilute condition is totally different by many orders of magnitude from the actual values observed in the living system (in vivo) *[194]*. Therefore, the study of biochemical reactions under crowded environment is very important. Here, in the present thesis, the in vitro macromolecular crowding effects are mimicked by using high concentration of synthetic and polymeric crowders such as polyethylene glycol (PEG), ficoll, dextran, and bovine serum albumin (BSA) (Scheme 1.13).

Polyethylene glycol (PEG) or polyethylene oxide (PEO) or polyoxyethylene (POE) or macrogol is a flexible water-soluble synthetic polyether compound which is prepared by polymerization of ethylene oxide *[195]*. It forms hydrogen bonds in a ratio of 100 water molecules per one PEG molecule PEG is commercially available with wide molecular weight in the range of 300 g/mL to 10,000,000 g/mL and are liquids or low-melting solids based on their molecular weights. PEGs are liquid when molecular weights are < 1000 and it turns into waxy solids upon increasing molecular weights >1000. The chemical properties of almost all PEG are nearly identical but their physical properties are different from each other due to their differences in chain lengths *[196]*. In addition, ficoll is a neutral, highly branched, water-soluble polysaccharide with high-mass and of 5 nm in radius *[197]*. It is formed by copolymerization reaction of sucrose with epichlorohydrin. Ficoll do not contain any ionized functional groups, therefore it is stable in neutral and basic solutions but instantly hydrolyzed

in very acidic condition *[198]*. Ficoll is characterized as lowest shape asymmetry of known nonglobular polymers *[199]*.
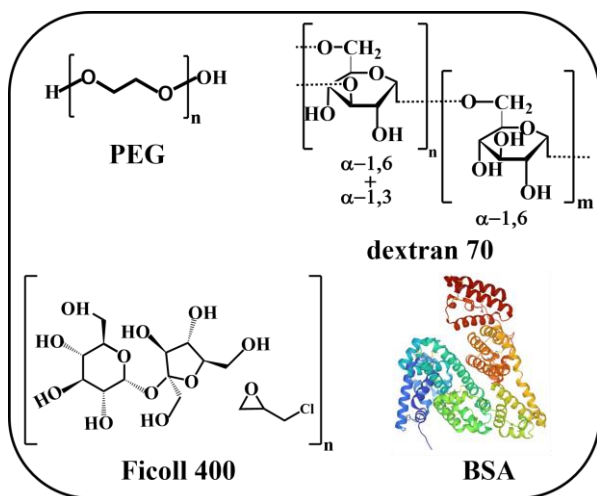
Scheme 1.13. *Structure of macromolecular crowders.*

On the other hand, dextran is a flexible, water-soluble linear polymer of glucose monomer. It behaves as a random coil structure *[200]*. Bovine serum albumin (BSA) is a stable, non-reactive, globular non-glycosylated serum albumin protein consists of 583 amino acids of single polypeptide chain cross-linked with 17 cystine residues with molecular weight of 66 kDa. BSA has three homologous but structurally different domains, named as I, II, and III which are further divided into two subdomains A and B *[201]*. Subdomains IIA and IIIA contains site-I and site-II that shows prominent binding to small molecules with selective specificities. While site-I markers include dansylamide, warfarin, iodipamide, and phenylbutazone, site-II allows binding of ibuprofen, flufenamic acid, and diazepam *[202]*. BSA has less tryptophan, glycine, methionine, and isoleucine whereas it is abundant in ionic amino acids such as glutamic acid and lysine. Also, the secondary structure of BSA contains 74% α-helical component and due to its negative charge, it plays a dominant role in transportation of various ligands (salts, fatty acids, vitamins, hormones) to target site *[202]*. Generally,

macromolecular crowders are used in food industry, cosmetics, pharmaceutical industry, and for bio medicinal applications etc. *[187, 189, 203–205]*. The enzymatic reactions often understood in terms of confinement-induced and crowding-induced alteration in enzyme conformation. For this, the chemically different substrates can also be affected by interior confined environment of protocell and also by the macromolecular crowding. Here, in the present thesis, the validation of these referred consideration has been analyzed for HRP by taking hydrophilic (OPD, ABTS) and hydrophobic (TMB) substrates (Scheme 1.14) with different chemical reactivity in the presence of H_2O_2. Similarly, the enzymatic rate of GOx was examined by taking glucose, sucrose, maltose, lactose, and mannose substrates.
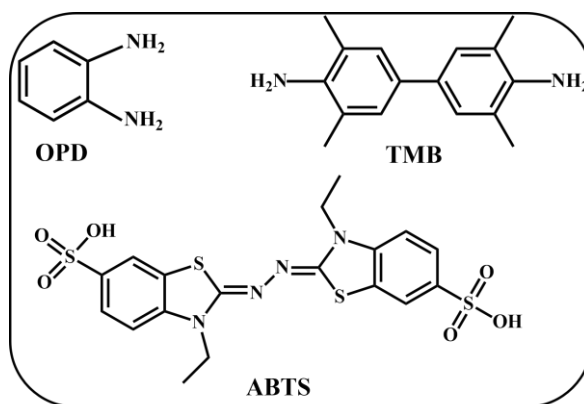
Scheme 1.14. *Structure of different substrates used for peroxidase activity.*

1.4. Applications of membrane-less coacervates

Coacervates are a promising class of protocellular compartments that are capable of concentrating reagents with high encapsulation efficiency, hosting chemical reactions, and protecting sequestered molecules from the outside environment and thence extensively utilized in biomedical, agriculture, food, cosmetic, and textile domains (Scheme 1.15) *[206, 207]*.

31

More important, coacervate-based systems are widely used for the extraction of compounds from the aqueous medium. For example, Zhao *et al.* developed a system from cationic gemini surfactant hexamethylene-1,6-bis (dodecyl dimethylammonium bromide) and 10% hydrolyzed polyacrylamide (HPAM) in neutral conditions *[208]*. These coacervates preferably adsorbed anionic dye (methyl orange) compared to cationic dye (methylene blue) with an extraction efficiency of >95% due to synergistic interactions.
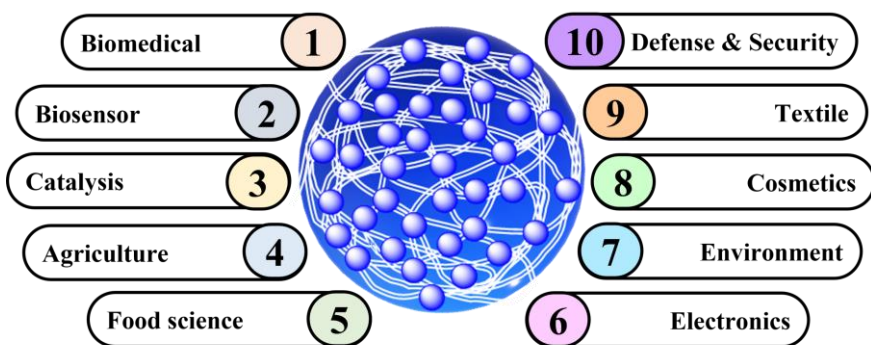
***Scheme 1.15.** Applications of membrane-less coacervates.*

Similarly, Chiappisi *et al.* showed the sensitivity of pH-sensitive chitosan/surfactant coacervates toward the removal of different pollutants such as organic molecules or metal ions/ligands from aqueous solutions *[209]*. Zhao and Zacharia used different sets of cationic and anionic polyelectrolytes to generate various complex coacervates and then compared their sequestration efficiency for methylene blue (MB) *[210]*. Only PEI/SPS system showed excellent extraction efficiency >80% over a range of MB concentrations at acidic pH whereas the other systems showed poor extraction efficiency. This system indicated the need of introducing strong π-π interactions inside the coacervate phase along with electrostatic and hydrophobic interactions to extract targeted compounds from the mixture solution. Liu *et al*. utilized cationic surfactant and anionic

polyelectrolyte coacervate for the efficient removal of organic pollutants via versatile approach *[211]*.

In addition, various type of self-assembled structures has been formulated and utilized for glucose monitoring. For example, Costantini *et al.* designed microfluidic glass chips from poly(2-hydroxyethyl methacrylate) polymer brushes and immobilized glucose-oxidase (GOx) and horseradish peroxidase (HRP) enzymes over it *[212]*. The limit of detection (LOD) was found to be 60 µM in human blood samples within 20 s that showed its capabilities towards extremely efficient glucose sensor with high selectivity, and repeatability. Kim *et al.* developed RBC membrane (RBCM)-coated enzymatic glucose sensor that showed LOD value of 0.66 mM despite of existence of interfering molecule *[213]*. Han *et al.* synthesized one-pot tandem non-enzyme MnO_2 nanoflakes as nanomaterial for colorimetric detection of glucose *[214]*. Similarly, Gayathri *et al.* designed flower-like CoNi-HN/GO hybrid nanomaterial that acts as a glucose sensor *[215]*. This glucose sensor showed excellent stability, good sensitivity with 28.5 µM LOD. Moreover, Zeng *et al.* formulated simple, robust, and cost-effective catalytic nanoconjugates by coupling gold nanoparticles with HRP at proper stochiometric mixing and utilized it for glucose detection *[216]*. Liu *et al.* fabricated graphdiyne (GDY)-based composite material by immobilizing ferrous ions and GOx onto GDY sheet that showed LOD value of 0.89 µM for glucose *[217]*. Similarly, non-enzymatic glucose sensor like Zero-dimensional Au_xPd_{100-x} nanocomposites also showed LOD in the same range ~0.85 µM for glucose *[218]*. Also, the as-synthesized metal-free nanozyme of modified carbon nitride as biomimetic catalyst showed oxidase-peroxidase activity for detection of glucose with a LOD of 0.8 µM within 30 s *[219]*. The synthetic procedure for most of the above-mentioned self-assembled biomimetic systems are somehow complicated along with high LOD and high

response time. Therefore, it is important to examine the utility of facile fabricated membrane-less coacervates as glucose sensor for selective glucose detection. Here, in the present thesis, we have fabricated the ATP-coacervates in the presence of polyelectrolyte PDADMAC and further utilized this bioreactor as glucose sensor.

In continuation, adenosine triphosphate (ATP) is an organic compound that are composed by three components, an adenine nitrogenous base, a ribose sugar, and three consecutively bonded phosphate groups (Scheme 1.16). ATP is found in all living forms inside the mitochondria and known as energy currency of cell *[220]*. It is implied mainly in three cellular pathways, glycolysis, citric acid cycle, and beta-oxidation and involved in different biochemical functions such as intracellular and extracellular signal transduction, DNA/RNA synthesis, transportation, and protein synthesis *[221, 222]*. ATP is stable in the aqueous solutions at pH range between 6.8 to 7.4 and further hydrolyses into adenosine diphosphate (ADP) and inorganic phosphate at extreme pH values. However, it possesses negative charge at physiological pH due to the presence of three phosphate groups.
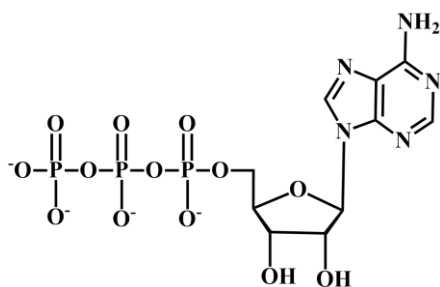
Scheme 1.16. *Structure of ATP molecule.*

Compared with other reported drug delivery systems, coacervates show many promising advantages. The unique structural feature of coacervates with hydrophilic interface and hydrophobic core enables it to encapsulate a wide range of hydrophilic and hydrophobic solutes including

biomacromolecules with high encapsulation efficiency *[101, 117, 223, 224]*. Moreover, it enhances the stabilization of the encapsulated solutes from external denaturants. A large number of synthesized drugs exhibit poor water solubility. These coacervates enhances the solubility of water-insoluble drugs which finally facilitates their delivery to cells *[225]*.

For instance, Rauck *et al.* fabricated novel coacervate delivery system from poly(ethylene argininylaspartate diglyceride) (PEAD) and heparin *[226]*. These targeted coacervates showed high biocompatibility, and high efficacy in the damaged spinal cord along with its potential to deliver therapeutic proteins to the injured nervous system. Armstrong *et al.* presented a new approach of delivering biomolecular payloads like proteins, oligonucleotides, and molecular dyes to specific position of stem cell membranes using ATP/PDDA microdroplets *[227]*. Here, they have demonstrated the role of dynamic holographic assembler to optically-manipulate loaded microdroplets for precisely target bioactive species present on the selected area of cellular membrane. Subsequently, they have also fabricated biodegradable amylose-based coacervate microvectors for the delivery of protein payloads to cells regardless of their affinity to the cell membrane *[228]*. Duo *et al.* developed near-infrared fluorescent and magnetic resonance dual-imaging coacervates for trypsin mapping and targeted payload delivery for malignant tumors *[229]*. Miserez *et al.* constructed pH- and redox-responsive coacervate microdroplets and encapsulated small peptides, enzymes, and messenger RNA (mRNAs) *[230]*. These therapeutic-loaded droplets showed endocytic cellular internalization along with glutathione-mediated release of payload which further highlight its importance as an efficient delivery carrier for treating various diseases. Moreover, they have also utilized glucose-responsive peptide coacervates for controlled release of insulin *[231]*. Similarly,

Nishida *et al.* also utilized pH-responsive coacervate droplets for in vivo delivery of proteins *[152]*. Zhao *et al.* designed nanoparticle-assembled coacervate system based on hydrogen bonding-driven self-assembly *[232]*. These coacervates showed its excellent results as high potent drug delivery vehicle and bioadhesive along with sustained drug release in rat acute colitis model as compared with the oral administration of the same amount of drug in solution form. In another work, Silva *et al.* used polycationic poly(allylamine hydrochloride) (PAH) and multivalent anion tripolyphosphate (TPP) to form coacervate droplets having gel-like properties and encapsulated anionic drug, ibuprofen with ~30% loading capacity *[233]*. The loading capacity and release was further tuned by adding strong amphiphilic solute such as sodium dodecyl sulfate. Barthold *et al.* synthesized starch nanoparticles by coacervation process and utilized it for the pulmonary delivery of proteins such as insulin, IgG1, RNAse, etc. *[234]*. It has been observed by Park *et al.* that Heparin formed coacervate droplets with biodegradable polycation poly(ethylene argininylaspartatediglyceride) (PEAD) that acts a good carrier for growth factor (GF) *[235]*. This study highlights the >90% loading efficiency, good biocompatibility, and sustained release of therapeutic growth factors showing its importance toward wound healing, heart repair, and bone regeneration. Also, Sun *et al.* explored phase-separating peptides for cytosolic delivery, and redox-mediated release of macromolecular therapeutics such as macromolecules, small peptides, messenger RNA etc. *[230]*. Jing *et al.* fabricated carboxymethyl chitosan (CMCS)-based coacervates near its *p*I value for oral drug delivery *[236]*. These coacervates showed pH-responsive behavior and found to be stable over a broad range of ionic medium. The encapsulation efficiency and loading capacity was found to be $94.79 \pm 0.49\%$ and $26.29 \pm 0.52\%$, respectively. Moreover,

Martin *et al.* constructed a light-responsive coacervate droplets from double-stranded DNA and *trans*-azobenzene trimethyl ammonium bromide *[237]*. These droplets undergo disassembled upon UV light irradiation while assembled under blue light due to the trans/cis photoisomerization behavior of azobenzene under light exposure and the faster transformation rate of trans to cis conversion was found at high temperature. Here, in the present thesis, we have quantitatively compared the loading content, encapsulation efficiency, and release profile of hydrophobic Ru-Cur drug inside various nanoassemblies such as micelles, liposomes, and coacervates. As of now, Ru(II)-based metal complexes have gained tremendous attention for theranostic applications because of their ligand-exchange kinetics similar to Pt(II) complexes, versatile oxidation states, lower cytotoxicity, tumor cell selectivity, and high therapeutic activity *[238]*. In addition, the physicochemical properties of curcumin do not change after binding with Ru metal which significantly enhances its importance toward photochemotherapy *[239]*.

Furthermore, spatial localization and up-concentration of specific solutes inside the core makes coacervates as cellular analog or protocell model to gain more insights into metabolic pathways, disease mechanism, and prebiotic evolution of cells *[240]*. However, the understanding of enzymatic pathways or enzymatic reactions inside any bioreactor is still challenging as the enzymatic activity could be degraded due to diffusion processes, limited encapsulation efficiency, and pH variation *[241]*. In addition, the sensitive nature of enzymes requires stable and highly efficient synthetic mimic for their preservation for more prolonged time *[242–245]*. Therefore, coacervates provide a stable platform for enzyme catalysis via enhancing the enzyme number inside densed network of polyelectrolytes *[246, 247]* and acts as a center for different catalytic reactions, storage, and

synthesis of proteins *[248, 249]*. For example, McCall *et al.* used polypeptide coacervates to examine the partitioning of cytoskeleton protein (actin) inside the droplets *[250]*. The enrichment of actin and actin filament assembly rate was found to be ~30-fold and ~50-fold, respectively inside coacervate droplets which further highlight the effect of localization and enrichment of biomolecules inside densed phase. In addition, Toor *et al.* constructed simple coacervates as an enzymatic reactor from ampholyte polymer chains stabilized with agar and studied the enzymatic cascade reaction of glucose oxidase, and catalase within these coacervate *[251]*. This study highlights the active role of proximity, and confinement for efficient biocatalysis. Similarly, Liu *et al.* fabricated catalase-containing coacervate microdroplets and further integrated this system into living cells to scavenge intracellular reactive oxygen species (ROS) and recovered cell viability *[252]*. Drobot *et al.*, fabricated a synthetic protocell from carboxymethyl dextran sodium salt and poly-*L*-lysine to examine the reaction rates of RNA catalysis and found that both ribozyme and RNA substrates are highly sequestered inside the coacervate phase *[253]*. Here, the cleavage rate was found to be faster in smaller sized droplets due to the enrichment of the effective local concentration of substrate inside its core. Moreover, Lim *et al.* designed a glucose-responsive biomimetic peptide coacervate system and encapsulated both insulin and glucose oxidase (GOx) with ~100% encapsulation efficiency *[254]*. When the whole system was exposed to glucose solution, glucose molecules diffused inside the droplets and converted into gluconic acid, that finally lead to coacervate degradation. The release rate of insulin from coacervate was determined by glucose level as performed by pancreatic β-cells. Moreover, Kojima *et al.* first constructed the coacervate droplets by using adenosine triphosphate (ATP) and PDDA polymer and placed these droplets in an aqueous two-

phase system of PEG and dextran to monitor the multi-step enzymatic cascade reaction *[255]*. Chenglong *et al.* fabricated a redox-responsive coacervate droplets from crosslinked cationic polymer and anionic gene plasmid and further studied the release and transfection of DNA by the expression of EGFP in 293T cells *[256]*. Qiao *et al.* reported a ternary protocell consortium to observe the response-retaliation pathways and hence utilized it as an example for population dynamics of interacting community of protocells empowered by antagonistic enzyme-mediated interactions *[257]*. Aumiller *et al.* fabricated a complex coacervates using negatively charged polyuridylic acid RNA and cationic peptide and finally checked the repeated on/off activity of phosphorylation/dephosphorylation enzymatic pathways which could be served as protocell model for nucleolar region *[258]*. In addition, Semenov *et al.* again formulated the same coacervates and showed that disassembly of these droplets can be triggered directly by an enzymatic reaction *[259]*. Also, Peeples and Rosen obtained 36-fold enhancement for SUMOylation enzyme cascade reaction into engineered condensates as compared to the surrounding bulk *[260]*. Koga *et al.* formed pH-responsive peptide-nucleotide coacervate droplets that can sequester a wide range of organic and inorganic molecules and promote the formation of secondary structures in peptide *[261]*. Drobot *et al.* performed RNA catalysis within coacervate droplets and showed their capabilities toward up-concentration of oligonucleotides *[262]*. In addition, Banerjee *et al.* designed a spatiotemporal controllable coacervate droplets based on single-stranded RNA and synthetic peptide and further analyzed the supramolecular dynamics of ribonucleoprotein granules via assembly/disassembly nature of system *[263]*. Despite of all these developments of different type of coacervates toward enzyme catalysis, it is important to establish its critical role for industrial applications as well.

Here, in the present thesis, we have studied the redox catalysis in CD-condensates and enzyme catalysis in ATP-condensates.

1.5. Catalysis

Catalysis is the process of accelerating the rate of a chemical reaction by adding a substance known as catalyst. Generally, catalyst interacts with reactant molecules to form intermediates that gives the final reaction product without consuming itself during the course of the reaction. Catalyst often follows different mechanistic pathway therefore it has no effect on chemical equilibrium of the reaction. Catalysis is mainly classified into two categories, namely homogenous and heterogenous catalysis *[264]*. In homogenous catalysis, components are dispersed in the same phase as reactant's molecule whereas in heterogenous catalysis, the reaction components are in different phases.

1.5.1. Redox catalysis

Redox catalysis is a type of heterogenous catalysis and redox reaction is a type of oxidation-reduction reaction which involves a transfer of electrons between two reacting species. There is different type of redox reactions such as decomposition reaction, combination reaction, displacement reaction, and disproportionation reaction *[265]*. Here, in the present thesis, we have examined the redox hydrogenation reaction inside CD-coacervate as a catalytic nanoreactor where we observed nitroarene to aminoarene conversion in the presence of sodium borohydride (NaBH4). It is previously reported that reductive hydrogenation of nitroarenes by NaBH4 follows Langmuir-Hinshelwood (L-H) mechanism *[266]*.

1.5.2. Langmuir-Hinshelwood (L-H) model

In the L-H model, one or more reactants such as nitroarene and BH_4^- strongly adsorbs on the metal surface and then BH_4^- transfer a hydride species to it (Scheme 1.17). These two steps are reversible in nature and can

be modelled by Langmuir isotherm. The adsorption-desorption steps on the metal surface are very fast, therefore the reduction of nitroarene by the surface hydrogen species becomes the rate determining step. The apparent rate constant of this mechanism is given by *[267]*,

$$k_{app} = kS\theta_{nitroarene}\,\theta_{BH_4^-} = \frac{kSK_{nitroarene}^n c_{nitroarene}^{n-1}(K_{BH_4^-}\,c_{BH_4^-})^m}{(1+(K_{nitroarene}c_{nitroarene})^n+(K_{BH_4^-}\,c_{BH_4^-})^m)^2} \quad (1)$$

where $\theta_{nitroarene}$ and $\theta_{BH_4^-}$ are the degree of surface coverage by reactant molecules, k is the molar rate constant per square meter of the catalyst, $K_{nitroarene}$ is the adsorption constant of nitroarene, $K_{BH_4^-}$ is the adsorption coefficient of borohydride, $c_{nitroarene}$ and $c_{BH_4^-}$ are the concentration of nitroarene and borohydride, respectively. The exponent n and m are related to the heterogeneity of the adsorbents.
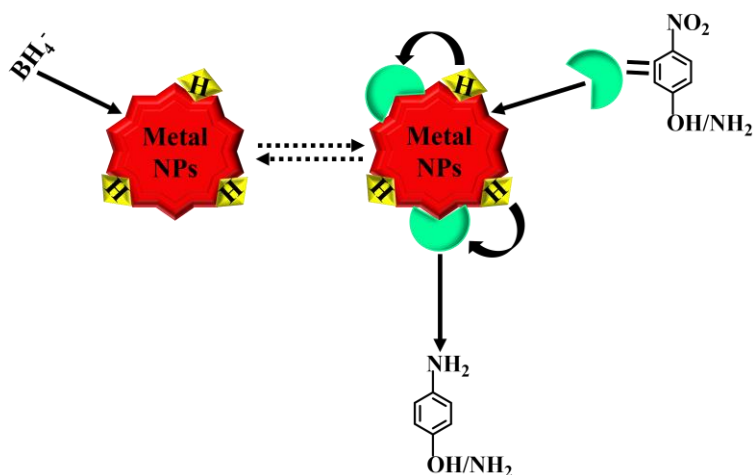
Scheme 1.17. *Schematic illustration of L-H mechanism for reduction of nitroarenes on metal surface.*

1.5.3. Enzyme catalysis

Enzymes are crucial proteins that act as a biological catalyst to accelerate the reaction rate of a chemical reaction by lowering its activation energy inside the cell. Enzymes neither consume in chemical reaction nor they do modulate the equilibrium of reaction. Almost all of the metabolic

pathways inside the cell demands enzyme catalysis in order to sustain life *[268]*. Generally, enzymes are globular proteins where the sequence of amino acids specifies its structure-function relationship. On an important note, enzymes activity can be affected by inhibitor molecules that decrease enzyme activity and activator molecules that increase the activity. In addition, enzymes have their functional responses at their optimal pH and temperature *[269–272]*. Any change in pH can modulate the ionization states while changes in temperature can disturb the intra- and intermolecular bonding of polypeptide chains. Therefore, enzyme's activity decreases significantly outside its optimal pH, and temperature, and most of them unfolded permanently when heated or exposed to chemical denaturants, and hence shedding their structure and functions. There are mainly two types of models who specifies the enzyme-substrate interactions; (1) Lock and key model, and (2) Induced fit model *[273]* (Scheme 1.18). In the lock and key model, the active site of an enzyme is a perfect fit to bind any substrate molecule and hence do not require any conformational changes for its binding. However, in induced fit model, the active site of an enzyme is complementary to the substrate molecule and therefore when substrate binds, the conformational changes in active site occurs to make it suitable for better fit for substrate binding. During evolution, some enzymes have dropped their ability to carry out biocatalysis, which is oftentimes speculated in their amino acid sequences featuring pseudocatalytic properties *[274]*. However, in some enzymes no amino acids are directly involved in enzyme catalysis, rather composed by specific sites to bind and orient catalytic cofactors.

These structures may also comprise by allosteric sites where the binding of substrate molecule results a decrease or increase in enzyme activity by conformational changes. Moreover, enzymes are very specific

about their binding pockets along with complementary shape, charge, and nature (hydrophilic/hydrophobic) of substrates *[275]*.
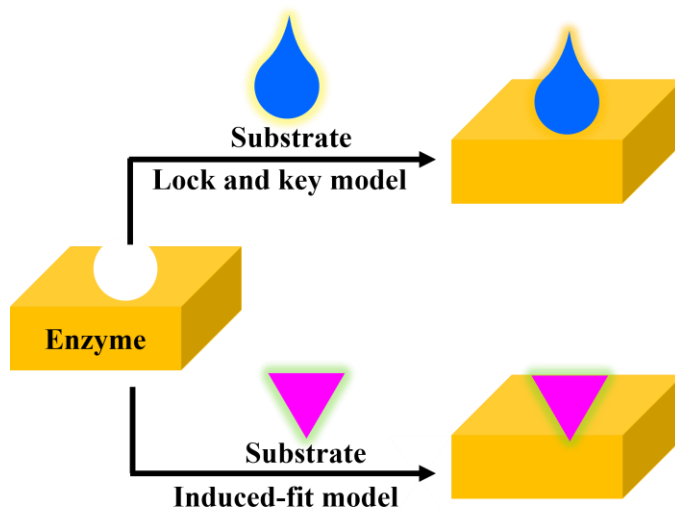
Scheme 1.18. Schematic representation of different models of substrate-enzyme binding.

In addition, many enzymatic cascade reactions have been observed for various metabolic pathways inside the cell suggesting the integrity of enzyme-catalyzed biomimetic pathways. Cascade reaction is a sequence of one-pot chemical reactions that comprises at least two consecutive reactions such that product of first reaction acts as a substrate for another reaction *[276]*. This reaction is also known as domino reaction or tandem reaction. Here in the cascade reaction, the isolation of intermediates is impossible and reaction conditions do not change among the consecutive steps. The usefulness of cascade reactions includes high atom economy, lesser waste generation as well as less time and work requirement. Therefore, it is important to understand the structure and function of enzymes in a crowded environment similar to biological cellular system where 40% of the total volume of cell is occupied by the biomacromolecules. Here, in this thesis, glucose oxidase, and horseradish peroxidase enzymes have been chosen to

examine the rate of catalytic reaction inside ATP-condensates and in presence of macromolecular crowders. Moreover, cascade reaction has also been performed by taking both of the enzymes simultaneously.

1.5.3.1. Structure and functions of enzymes

1.5.3.2. Glucose oxidase (GOx)

Glucose oxidase (GOx) is an oxidoreductase enzyme consists of 605 amino acid residues that catalyses the oxidation of glucose to gluconic acid and hydrogen peroxide (H_2O_2). This enzyme is considered as an "ideal enzyme" and is often addressed as oxidase "Ferrari" due to its fast mechanism, high stability, and specificity *[277]*. GOx is a member of the glucose-methanol-choline oxidoreductase superfamily having molecular weight of 160 kDa. It is a homodimeric glycoprotein comprised by two functional domains each weighing 80 kDa, N-terminal Flavinadenine dinucleotide (FAD)-binding domain which is buried ~1.5 nm inside the protein shell that acts as an initial electron acceptor, and glycosylated with 16% carbohydrate content (Scheme 1.19) *[277]*.
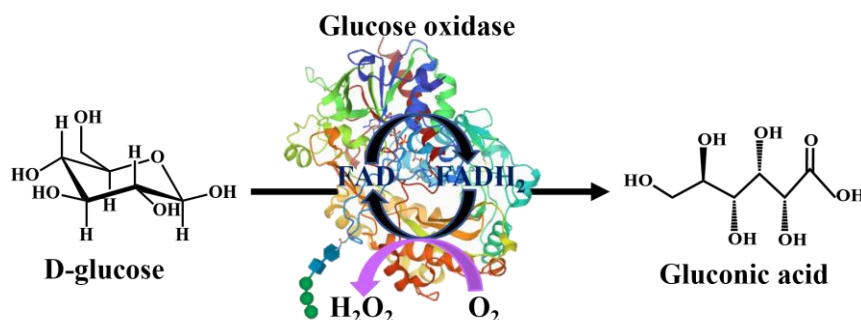
Scheme 1.19. Structure of GOx along with its enzymatic reaction.

The two identical domains are covalently linked by disulfide bonds and the FAD-binding domain is centered on a five-stranded parallel *β*-sheet

which is flanked by smaller three-stranded anti-parallel β-sheet on one side and three α-helices on the other side *[278]*. The extremely conserved part of the FAD motif is the $\beta\alpha\beta$ mononucleotide-binding motif. The majority of the binding site is constituted by residues from the N-terminal part of the amino acid sequence. The residues from the central realm render an additional support whereas most of the residues from C-terminal region frame the edges of the flavin binding pocket as well as contribute two of the three active site residues. Generally, GOx is mainly produced by fungi and insects that have significant industrial and medicinal applications *[279]*.

1.5.3.3. Horseradish peroxidase

Horseradish peroxidase (HRP) is a globular metalloenzyme consists of single polypeptide chain with 308 amino acid residues, 4 disulfide bridges between cysteine residues as well as heme group [iron(III)protoporphyrin IX] and two calcium atoms with predominant α-helical secondary structure and single exceptional β-sheet region (Scheme 1.20) *[280]*. Each calcium site is seven-coordinated with oxygen-donor ligands offered by different side chains of amino acids like carboxylates (Asp), hydroxyl groups (Ser, Thr), backbone carbonyls and a distal water molecule.
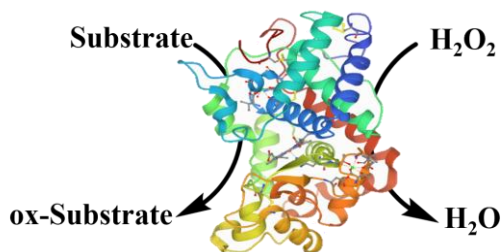
Scheme 1.20. Structure of HRP along with its enzymatic reaction.

On the other hand, the iron heme is the center of enzyme whereas two calcium atoms lie within the helical region of the enzyme with one is in distal region and one is in proximal region. The planar structure of heme group is composed by centered iron atom bound by four pyrrole molecules

45

of porphyrin ring *[281]*. Iron metal has two open bonding sites above and below of the heme group. The heme group has a proximal histidine residue attached below the heme group whereas the second histidine residue on the distal side is vacant in the relaxed state which is open for the attachment of H_2O_2 during redox reaction. The sixth position of this octahedral molecule bind by an oxygen atom of H_2O_2 while activation. Moreover, this glycoprotein with molecular weight of 44 kDa has ~18-22% carbohydrate content *[282]*. HRP catalyzes the oxidation of various organic substrates in the presence of oxidizing agent, H_2O_2. The different chromogenic substrates such as TMB, ABTS, and OPD gives colored product after oxidation which can be detected by spectrophotometry *[283]*. Generally, HRP is used in food, environment and biomedical fields *[284]*.

1.5.3.4. Michaelis-Menten kinetic model

Michaelis-Menten kinetics is a specific type of model that explains how the rate of enzyme-catalyzed reaction affected by varying the reaction conditions. Initially, an enzyme (E) binds to substrate (S) molecule to produce an enzyme-substrate complex (ES), and finally into product (P). The series of these following steps is known as mechanism and is represented by

$$\textbf{E + S} \rightleftarrows \textbf{ES} \longrightarrow \textbf{E + P} \tag{2}$$
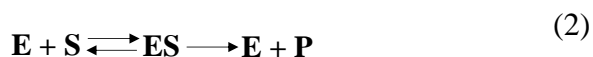
For a given enzyme concentration and low substrate concentration [S], the rate of reaction (v_0) increases linearly with substrate concentrations. In this condition, the enzyme molecules are majorly free to catalyze the reaction. While increasing substrate concentration, enzyme and substrate molecules encounter with each other and further at high substrate concentrations, the rate of reaction asymptotically approaches to saturation where almost all of the enzyme's active sites occupied by the substrate

molecules and no more enzymes are available for reacting with substrate. Here, the rate of reaction depends on the typically ES complex that describes the zero-order unimolecular reaction and rate determining-step with apparent rate constant, k_{cat}. The apparent unimolecular rate constant k_{cat} is also called as turnover number which defines the maximum number of enzymatic reactions catalyzed per second. Subsequently, the substrate concentration at which the reaction velocity is half of the maximum velocity is known as K_m and the efficiency of an enzyme is defined by k_{cat}/K_m. The Michaelis-Menten equation describing the reaction rate is as follows *[219]*,

$$v = \frac{V_{max}\,[S]}{K_m + [S]} \tag{3}$$

where, v is the initial velocity, [S] is the molar concentration of substrate, V_{max} ($V_{max} = k_{cat}[E]_{total}$) is the maximum velocity, and K_m ($K_m = \frac{k_2 + k_{-1}}{k_1}$) is the Michaelis constant.

The more useful representation of non-linear Michalies-Menten plot has been simplified into linear plot which is known as Lineweaver Burk plot or double reciprocal plot. The equation used to generate this plot is listed below and generated by taking the reciprocal of both sides of the Michaelis-Menten equation *[285, 286]*,

$$\frac{1}{v} = \frac{K_m}{V_{max}[S]} + \frac{1}{V_{max}} \tag{4}$$

The kinetic constants K_m and V_{max} are helpful to understand how enzymes work together inside the cell to control metabolism.

1.6. Organizations of the thesis

The overall objective of the work presented in the thesis is to explore the physicochemical properties of various biocompatible coacervate droplets for sensing, catalysis, and biomedical applications. Moreover, the impression of various molecular crowders on the enzymatic activity of HRP and GOx enzymes has also been illustrated.

Chapter 1 discusses the functional role of membrane-less compartments toward metabolic pathways inside the natural cell. A brief overview of the different types of earlier reported artificial cells along with their formulations have been discussed. In addition, the liquid-liquid phase separated membrane-less coacervates as prominent biomimetic system along with their features, types, and applications have also been discussed in detail. Thereafter, the influence of macromolecular crowders such as PEG, dextran, ficoll, and BSA on the catalytic rates of HRP and GOx has been illustrated. Finally, the mechanism of redox catalysis by L-H model and enzyme catalysis by Michalies-Menten model have been covered briefly.

Chapter 2 includes the details of all the chemicals used. The complete synthetic procedures of CDs, QDs, Ru-Cur, SUV, GUV, MLV along with different type of coacervates such as CD-, ATP-, QD-coacervates have been discussed. This chapter also covers the sample preparation, experimental procedures, and techniques used to complete the entire work of thesis.

Chapter 3 demonstrates the fabrication of biocompatible luminescent coacervates from CDs and PDADMAC. These coacervates have been utilized for MTT assay, and size-dependent cellular uptake in BHK-21 kidney fibroblast cells.

Chapter 4 explores the comparative study of loading content, encapsulation efficiency, in vitro pH-responsive release of Ru-Cur encapsulated self-assembled nanocarriers such as micelles, liposomes, and coacervates.

Chapter 5 investigates the role of confined environment of metal-free CD-coacervate for the redox catalysis and highlights its importance as a catalytic nanoreactor.

Chapter 6 demonstrates the role of ATP-coacervates as a bioreactor and illustrates the role of confinement on the enhanced enzymatic catalytic rates. The HRP/GOx immobilized coacervates have been utilized for glucose sensing in solution and solid support.

Chapter 7 explores the novel findings of biomolecular condensates of enzymes in the presence of macromolecular crowders and illustrates the enhancement in the catalytic rates inside these biomolecular condensates.

Chapter 8 concludes the work done in the entire thesis along with their scope for future applications.

1.7. References

1. Buddingh' B. C., van Hest J. C. M. (2017), Artificial cells: Synthetic compartments with life-like functionality and adaptivity, Acc. Chem. Res., 50(4), 769–777. (DOI:10.1021/acs.accounts.6b00512)

2. Tu Y., Peng F., Adawy A., Men Y., Abdelmohsen L. K. E. A., Wilson D. A. (2016), Mimicking the cell: Bio-inspired functions of supramolecular assemblies, Chem. Rev., 116(4), 2023–2078. (DOI:10.1021/acs.chemrev.5b00344)

3. Rasmussen S., Chen L., Nilsson M., Abe S. (2003), Bridging nonliving and living matter, Artificial Life, 9(3), 269–316. (DOI:10.1162/106454603322392479)

4. Friedman J. R., Nunnari J. (2014), Mitochondrial form and function, Nature, 505(7483), 335–343. (DOI:10.1038/nature12985)

5. Luzio J. P., Pryor P. R., Bright N. A. (2007), Lysosomes: fusion and function, Nat. Rev. Mol. Cell Biol., 8(8), 622–632. (DOI:10.1038/nrm2217)

6. Brangwynne C. P., Mitchison T. J., Hyman A. A. (2011), Active liquid-like behavior of nucleoli determines their size and shape in Xenopus laevis oocytes, Proc. Natl. Acad. Sci. U.S.A., 108(11), 4334–4339. (DOI:10.1073/pnas.1017150108)

7. Dubey N. C., Tripathi B. P. (2021), Nature inspired multienzyme immobilization: Strategies and concepts, ACS Appl. Bio Mater., 4(2), 1077–1114. (DOI:10.1021/acsabm.0c01293)

8. Mahen R., Venkitaraman A. R. (2012), Pattern formation in centrosome assembly, Curr. Opin. Cell Biol., 24(1), 14–23. (DOI:10.1016/j.ceb.2011.12.012)

9. Molliex A., Temirov J., Lee J., Coughlin M., Kanagaraj A. P., Kim H. J., et al. (2015), Phase separation by low complexity domains promotes stress granule assembly and drives pathological fibrillization, Cell, 163(1), 123–133. (DOI:10.1016/j.cell.2015.09.015)

10. Hennig S., Kong G., Mannen T., Sadowska A., Kobelke S., Blythe A., et al. (2015), Prion-like domains in RNA binding proteins are essential for building subnuclear paraspeckles, J. Cell Biol., 210(4), 529–539. (DOI:10.1083/jcb.201504117)

11. Franzmann T. M., Jahnel M., Pozniakovsky A., Mahamid J., Holehouse A. S., Nüske E., et al. (2018), Phase separation of a yeast prion protein promotes cellular fitness, Science, 359(6371), eaao5654. (DOI:10.1126/science.aao5654)

12. Sabari B. R., Dall'Agnese A., Boija A., Klein I. A., Coffey E. L., Shrinivas K., et al. (2018), Coactivator condensation at super-enhancers links phase separation and gene control, Science, 361(6400), eaar3958. (DOI:10.1126/science.aar3958)

13. Boija A., Klein I. A., Sabari B. R., Dall'Agnese A., Coffey E. L., Zamudio AV., et al. (2018), Transcription factors activate genes through the phase-separation capacity of their activation domains, Cell, 175(7), 1842-1855.e16. (DOI:10.1016/j.cell.2018.10.042)

14. Du M., Chen Z. J. (2018), DNA-induced liquid phase condensation of cGAS activates innate immune signaling, Science, 361(6403), 704–709. (DOI:10.1126/science.aat1022)

15. Kilic S., Lezaja A., Gatti M., Bianco E., Michelena J., Imhof R., et al. (2019), Phase separation of 53 BP 1 determines liquid-like behavior of DNA repair compartments, EMBO J., 38(16) (DOI:10.15252/embj.2018101379)

16. Milovanovic D., Wu Y., Bian X., De Camilli P. (2018), A liquid phase of synapsin and lipid vesicles, Science, 361(6402), 604–607. (DOI:10.1126/science.aat5671)

17. Zbinden A., Pérez-Berlanga M., De Rossi P., Polymenidou M. (2020), Phase separation and neurodegenerative diseases: A disturbance in the force, Dev. Cell, 55(1), 45–68. (DOI:10.1016/j.devcel.2020.09.014)

18. Gao Z., Zhang W., Chang R., Zhang S., Yang G., Zhao G. (2021), Liquid-liquid phase separation: Unraveling the enigma of biomolecular condensates in microbial cells, Front. Microbiol., 12, 751880. (DOI:10.3389/fmicb.2021.751880)

19. Hyman A. A., Weber C. A., Jülicher F. (2014), Liquid-liquid phase separation in biology, Annu. Rev. Cell Dev. Biol., 30(1), 39–58. (DOI:10.1146/annurev-cellbio-100913-013325)

20. Stubbe J., Tian J., He A., Sinskey A. J., Lawrence A. G., Liu P. (2005), Nontemplate-dependent polymerization processes: Polyhydroxyalkanoate synthases as a paradigm, Annu. Rev. Biochem., 74(1), 433–480. (DOI:10.1146/annurev.biochem.74.082803.133013)

21. Brangwynne C. P., Eckmann C. R., Courson D. S., Rybarska A., Hoege C., Gharakhani J., et al. (2009), Germline P granules are liquid droplets that localize by controlled dissolution/condensation, Science, 324(5935), 1729–1732. (DOI:10.1126/science.1172046)

22. Agapakis C. M., Boyle P. M., Silver P. A. (2012), Natural strategies for the spatial optimization of metabolism in synthetic biology, Nat. Chem. Biol., 8(6), 527–535. (DOI:10.1038/nchembio.975)

23. Alberti S., Hyman A. A. (2016), Are aberrant phase transitions a driver of cellular aging?, BioEssays, 38(10), 959–968. (DOI:10.1002/bies.201600042)

24. Gear A. R. L. (1970), Inner- and outer-membrane enzymes of mitochondria during liver regeneration, Biochem. J., 120(3), 577–587. (DOI:10.1042/bj1200577)

25. Igamberdiev A. U., Kleczkowski L. A. (2015), Optimization of ATP synthase function in mitochondria and chloroplasts via the adenylate kinase equilibrium, Front. Plant Sci., 6 (DOI:10.3389/fpls.2015.00010)

26. Che H., van Hest J. C. M. (2019), Adaptive polymersome nanoreactors, ChemNanoMat., 5(9), 1092–1109. (DOI:10.1002/cnma.201900245)

27. Kerfeld C. A., Aussignargues C., Zarzycki J., Cai F., Sutter M. (2018), Bacterial microcompartments, Nat. Rev. Microbiol., 16(5), 277–290. (DOI:10.1038/nrmicro.2018.10)

28. Dubey N. C., Tripathi B. P. (2021), Nature inspired multienzyme immobilization: Strategies and concepts, ACS Appl. Bio Mater., 4(2), 1077–1114. (DOI:10.1021/acsabm.0c01293)

29. Mason A. F., Yewdall N. A., Welzen P. L. W., Shao J., van Stevendaal M., van Hest J. C. M., et al. (2019), Mimicking cellular

compartmentalization in a hierarchical protocell through spontaneous spatial organization, ACS Cent. Sci., 5(8), 1360–1365. (DOI:10.1021/acscentsci.9b00345)

30. Alberti S. (2017), The wisdom of crowds: regulating cell function through condensed states of living matter, J. Cell Sc., 17, 2789-2796. (DOI:10.1242/jcs.200295)

31. Spoelstra W. K., Deshpande S., Dekker C. (2018), Tailoring the appearance: what will synthetic cells look like?, Curr. Opin. Biotechnol., 51, 47–56. (DOI:10.1016/j.copbio.2017.11.005)

32. Mann S. (2012), Systems of creation: The emergence of life from nonliving matter, Acc. Chem. Res., 45(12), 2131–2141. (DOI:10.1021/ar200281t)

33. Dzieciol A. J., Mann S. (2012), Designs for life: protocell models in the laboratory, Chem. Soc. Rev., 41(1), 79–85. (DOI:10.1039/C1CS15211D)

34. Luisi P. L. (2006), The Emergence of life: From chemical origins to synthetic biology, 1st ed. Cambridge University Press, ISBN: 978-0-521-82117-9. (DOI:10.1017/CBO9780511817540)

35. Xu C., Hu S., Chen X. (2016), Artificial cells: from basic science to applications, Mater. Today, 19(9), 516–532. (DOI:10.1016/j.mattod.2016.02.020)

36. Schwille P. (2011), Bottom-up synthetic biology: Engineering in a Tinkerer's World, Science, 333(6047), 1252–1254. (DOI:10.1126/science.1211701)

37. Ding Y., Wu F., Tan C. (2014), Synthetic biology: A bridge between artificial and natural cells, Life, 4(4), 1092-1116. (DOI:10.3390/life4041092)

38. Chang T. M. S. (1964), Semipermeable microcapsules, Science, 146(3643), 524–525. (DOI:10.1126/science.146.3643.524)

39. Hammer D. A., Kamat N. P. (2012), Towards an artificial cell, FEBS Lett., 586(18), 2882–2890. (DOI:10.1016/j.febslet.2012.07.044)

40. Tian L., Li M., Patil A. J., Drinkwater B. W., Mann S. (2019), Artificial morphogen-mediated differentiation in synthetic protocells, Nat. Commun, 10(1), 3321. (DOI:10.1038/s41467-019-11316-4)

41. Jeong S., Nguyen H. T., Kim C. H., Ly M. N., Shin K. (2020), Toward artificial cells: Novel advances in energy conversion and cellular motility, Adv. Funct. Mater., 30(11), 1907182. (DOI:10.1002/adfm.201907182)

42. Szostak J. W., Bartel D. P., Luisi P. L. (2001), Synthesizing life, Nature, 409(6818), 387–390. (DOI:10.1038/35053176)

43. Saraniti M. (2008), Designing biomimetic nanomachines, Nat. Nanotech., 3(11), 647–648. (DOI:10.1038/nnano.2008.327)

44. Yoo J-W., Irvine D. J., Discher D. E., Mitragotri S. (2011), Bio-inspired, bioengineered and biomimetic drug delivery carriers, Nat. Rev. Drug Discov., 10(7), 521–535. (DOI:10.1038/nrd3499)

45. Blain J. C., Szostak J. W. (2014), Progress toward synthetic cells, Annu. Rev. Biochem., 83(1), 615–640. (DOI:10.1146/annurev-biochem-080411-124036)

46. Glass J. I., Assad-Garcia N., Alperovich N., Yooseph S., Lewis M. R., Maruf M., et al. (2006), Essential genes of a minimal bacterium, Proc. Natl. Acad. Sci. U.S.A., 103(2), 425–430. (DOI:10.1073/pnas.0510013103)

47. Lartigue C., Glass J. I., Alperovich N., Pieper R., Parmar P. P., Hutchison C. A., et al. (2007), Genome transplantation in bacteria:

Changing one species to another, Science, 317(5838), 632–638. (DOI:10.1126/science.1144622)

48. Fraser C. M., Gocayne J. D., White O., Adams M. D., Clayton R. A., Fleischmann R. D., et al. (1995), The minimal gene complement of Mycoplasma genitalium, Science, 270(5235), 397–404. (DOI:10.1126/science.270.5235.397)

49. Fookes M. C., Hadfield J., Harris S., Parmar S., Unemo M., Jensen J. S., et al. (2017), Mycoplasma genitalium: whole genome sequence analysis, recombination and population structure, BMC Genom., 18(1), 993. (DOI:10.1186/s12864-017-4399-6)

50. Gil R., Silva F. J., Peretó J., Moya A. (2004), Determination of the core of a minimal bacterial gene set, Microbiol. Mol. Biol. Rev, 68(3), 518–537. (DOI:10.1128/MMBR.68.3.518-537.2004)

51. Luisi P. L., Ferri F., Stano P. (2006), Approaches to semi-synthetic minimal cells: a review, Naturwissenschaften, 93(1), 1–13. (DOI:10.1007/s00114-005-0056-z)

52. Gibson D. G., Glass J. I., Lartigue C., Noskov V. N., Chuang R-Y., Algire M. A., et al. (2010), Creation of a bacterial cell controlled by a chemically synthesized genome, Science, 329(5987), 52–56. (DOI:10.1126/science.1190719)

53. Ivanov I., Castellanos S. L., Balasbas S., Otrin L., Marušič N., Vidaković-Koch T., et al. (2021), Bottom-up synthesis of artificial cells: Recent highlights and future challenges, Annu. Rev. Chem. Biomol. Eng., 12(1), 287–308. (DOI:10.1146/annurev-chembioeng-092220-085918)

54. Bangham A. D., Horne R. W. (1964), Negative staining of phospholipids and their structural modification by surface-active

agents as observed in the electron microscope, J. Mol. Biol., 8(5), 660-IN10. (DOI:10.1016/S0022-2836(64)80115-7)

55. Jelinek R., Kolusheva S. (2005), Membrane interactions of host-defense peptides studied in model systems, CPPS, 6(1), 103–114. (DOI:10.2174/1389203053027511)

56. Picon A., Serrano C., Gaya P., Medina M., Nuñez M. (1996), The effect of liposome-encapsulated cyprosins on Manchego cheese ripening, J. Dairy Sci., 79(10), 1699–1705. (DOI:10.3168/jds.S0022-0302(96)76535-9)

57. Lee K. Y., Park S-J., Lee K. A., Kim S-H., Kim H., Meroz Y., et al. (2018), Photosynthetic artificial organelles sustain and control ATP-dependent reactions in a protocellular system, Nat. Biotechnol., 36(6), 530–535. (DOI:10.1038/nbt.4140)

58. Noireaux V., Libchaber A. (2004), A vesicle bioreactor as a step toward an artificial cell assembly, Proc. Natl. Acad. Sci. U.S.A., 101(51), 17669–17674. (DOI:10.1073/pnas.0408236101)

59. Elani Y., Law R. V., Ces O. (2014), Vesicle-based artificial cells as chemical microreactors with spatially segregated reaction pathways, Nat. Commun., 5(1), 5305. (DOI:10.1038/ncomms6305)

60. Gardner P. M., Winzer K., Davis B. G. (2009), Sugar synthesis in a protocellular model leads to a cell signaling response in bacteria, Nat. Chem., 1(5), 377–383. (DOI:10.1038/nchem.296)

61. Lentini R., Santero S. P., Chizzolini F., Cecchi D., Fontana J., Marchioretto M., et al. (2014), Integrating artificial with natural cells to translate chemical messages that direct E. coli behaviour, Nat. Commun., 5(1), 4012. (DOI:10.1038/ncomms5012)

62. Adamala K., Szostak JW. (2013), Competition between model protocells driven by an encapsulated catalyst, Nat. Chem., 5(6), 495–501. (DOI:10.1038/nchem.1650)

63. Gebicki J. M., Hicks M. (1973), Ufasomes are stable particles surrounded by unsaturated fatty acid membranes, Nature, 243(5404), 232–234. (DOI:10.1038/243232a0)

64. Meierhenrich U. J., Filippi J-J., Meinert C., Vierling P., Dworkin J. P. (2010), On the origin of primitive cells: From nutrient intake to elongation of encapsulated nucleotides, Angew. Chem. Int. Ed., 49(22), 3738–3750. (DOI:10.1002/anie.200905465)

65. Claessens M. M. A. E., van Oort B. F., Leermakers F. A. M., Hoekstra F. A., Cohen Stuart M. A. (2004), Charged lipid vesicles: Effects of salts on bending Rigidity, Stability, and Size, Biophys. J., 87(6), 3882–3893. (DOI:10.1529/biophysj.103.036772)

66. Lu Y., Allegri G., Huskens J. (2022), Vesicle-based artificial cells: materials, construction methods and applications, Mater. Horiz., 9(3), 892–907. (DOI:10.1039/D1MH01431E)

67. Green J. J., Elisseeff J. H. (2016), Mimicking biological functionality with polymers for biomedical applications, Nature, 540(7633), 386–394. (DOI:10.1038/nature21005)

68. Chang T. M. S. (1964), Semipermeable microcapsules, Science, 146(3643), 524–525. (DOI:10.1126/science.146.3643.524)

69. Chang T. M. S. (2005), Therapeutic applications of polymeric artificial cells, Nat. Rev. Drug Discov., 4(3), 221–235. (DOI:10.1038/nrd1659)

70. Liu Z. C., Swi Chang T. M. (2010), Artificial cell microencapsulated stem cells in regenerative medicine, tissue engineering and cell therapy, Chapter: In Pedraz JL, Orive G (eds), Therapeutic

Applications of Cell Microencapsulation. New York, NY Springer New York, pp.68–79. (DOI:10.1007/978-1-4419-5786-3_7)

71. Orive G., Hernández R. M., Gascón A. R., Calafiore R., Chang T. M. S., Vos P. D., et al. (2003), Cell encapsulation: Promise and progress, Nat. Med., 9(1), 104–107. (DOI:10.1038/nm0103-104)

72. Chang T. M. S. (1969), Removal of endogenous and exogenous toxins by a microencapsulated absorbent, Can. J. Physiol. Pharmacol., 47(12), 1043–1045. (DOI:10.1139/y69-170)

73. Chang T. M. S. (1971), The in vivo Effects of semipermeable microcapsules containing L-Asparaginase on 6C3HED lymphosarcoma, Nature, 229(5280), 117–118. (DOI:10.1038/229117a0)

74. Chang T. M. S. (2004), Artificial cells for cell and organ replacements, Artif. Organs, 28(3), 265–270. (DOI:10.1111/j.1525-1594.2004.47343.x)

75. O'Shea G. M., Sun A. M. (1986), Encapsulation of rat islets of Langerhans prolongs xenograft survival in diabetic mice, Diabetes, 35(8), 943–946. (DOI:10.2337/diab.35.8.943)

76. Anraku Y., Kishimura A., Kamiya M., Tanaka S., Nomoto T., Toh K., et al. (2016), Systemically injectable enzyme-loaded polyion complex vesicles as in vivo nanoreactors functioning in tumors, Angew. Chem., 128(2), 570–575. (DOI:10.1002/ange.201508339)

77. Chemin M., Brun P-M., Lecommandoux S., Sandre O., Le Meins J-F. (2012), Hybrid polymer/lipid vesicles: fine control of the lipid and polymer distribution in the binary membrane, Soft Matter, 8(10), 2867. (DOI:10.1039/c2sm07188f)

78. Khan S., McCabe J., Hill K., Beales P. A. (2020), Biodegradable hybrid block copolymer–lipid vesicles as potential drug delivery

systems, J. Colloid Interface Sci., 562, 418–428. (DOI:10.1016/j.jcis.2019.11.101)

79. Huang X., Li M., Green D. C., Williams D. S., Patil A. J., Mann S. (2013), Interfacial assembly of protein–polymer nano-conjugates into stimulus-responsive biomimetic protocells, Nat. Commun., 4(1), 2239. (DOI:10.1038/ncomms3239)

80. Cai Y., Yu Q., Zhao H. (2020), Electrostatic assisted fabrication and dissociation of multi-component proteinosomes, J. Colloid Interface Sci., 576, 90–98. (DOI:10.1016/j.jcis.2020.05.013)

81. Huang X., Li M., Mann S. (2014), Membrane-mediated cascade reactions by enzyme–polymer proteinosomes, Chem. Commun., 50(47), 6278–6280. (DOI:10.1039/C4CC02256D)

82. Liu X., Zhou P., Huang Y., Li M., Huang X., Mann S. (2016), Hierarchical proteinosomes for programmed release of multiple components, Angew. Chem. Int. Ed., 55(25), 7095–7100. (DOI:10.1002/anie.201601427)

83. Liu L., Su D., Liu X., Wang L., Zhan J., Xie H., et al. (2017), Construction of biological hybrid microcapsules with defined permeability towards programmed release of biomacromolecules, Chem. Commun., 53(85), 11678–11681. (DOI:10.1039/C7CC06243E)

84. Li M., Green D. C., Anderson J. L. R., Binks B. P., Mann S. (2011), In vitro gene expression and enzyme catalysis in bio-inorganic protocells, Chem. Sci., 2(9), 1739. (DOI:10.1039/c1sc00183c)

85. Dinsmore A. D., Hsu M. F., Nikolaides M. G., Marquez M., Bausch A. R., Weitz D. A. (2002), Colloidosomes: Selectively permeable capsules composed of colloidal particles, Science, 298(5595), 1006–1009. (DOI:10.1126/science.1074868)

86. Wang C., Liu H., Gao Q., Liu X., Tong Z. (2007), Facile fabrication of hybrid colloidosomes with alginate gel cores and shells of porous CaCO$_3$ microparticles, ChemPhysChem, 8(8), 1157–1160. (DOI:10.1002/cphc.200700147)

87. Li S., Moosa B. A., Croissant J. G., Khashab N. M. (2015), Electrostatic assembly/disassembly of nanoscaled colloidosomes for light-triggered cargo release, Angew. Chem. Int. Ed., 54(23), 6804–6808. (DOI:10.1002/anie.201501615)

88. Pan Y., Qiu W., Li Q., Zhu S., Lin C., Zeng W., et al. (2019), Assembling two-phase enzymatic cascade pathways in pickering emulsion, ChemCatChem, 11(7), 1878–1883. (DOI:10.1002/cctc.201900098)

89. Liu Z., Wang B., Jin S., Wang Z., Wang L., Liang S. (2018), Bioinspired dual-enzyme colloidosome reactors for high-performance biphasic catalysis, ACS Appl. Mater. Interfaces, 10(48), 41504–41511. (DOI:10.1021/acsami.8b14321)

90. Rodríguez-Arco L., Kumar B. V. V. S. P., Li M., Patil A. J., Mann S. (2019), Modulation of higher-order behaviour in model protocell communities by artificial phagocytosis, Angew. Chem. Int. Ed., 58(19), 6333–6337. (DOI:10.1002/anie.201901469)

91. Sun M., Yin W., Chen J., Wang W., Guo T., Meng T. (2021), Hollow colloidosomes with an enzyme confined in a porous shell as Pickering interfacial biocatalysts for efficient bioconversions, Green Chem., 23(2), 740–744. (DOI:10.1039/D0GC02999H)

92. Li M., Harbron R. L., Weaver J. V. M., Binks B. P., Mann S. (2013), Electrostatically gated membrane permeability in inorganic protocells, Nat. Chem., 5(6), 529–536. (DOI:10.1038/nchem.1644)

93. Percec V., Wilson D. A., Leowanawat P., Wilson C. J., Hughes A. D., Kaucher M. S., et al. (2010), Self-Assembly of Janus dendrimers into uniform dendrimersomes and other complex architectures, Science, 328(5981), 1009–1014. (DOI:10.1126/science.1185547)

94. Wu L., Li B-L., Huang Y-Y., Zhou H-F., He Y-M., Fan Q-H. (2006), Phosphine dendrimer-stabilized palladium nanoparticles, a highly active and recyclable catalyst for the Suzuki−Miyaura Reaction and Hydrogenation, Org. Lett., 8(16), 3605–3608. (DOI:10.1021/ol0614424)

95. Patri A. K., Majoros I. J., Baker J. R. (2002), Dendritic polymer macromolecular carriers for drug delivery, Curr. Opin. Chem. Biol., 6(4), 466–471. (DOI:10.1016/S1367-5931(02)00347-2)

96. Patri A., Kukowskalatallo J., Bakerjr J. (2005), Targeted drug delivery with dendrimers: Comparison of the release kinetics of covalently conjugated drug and non-covalent drug inclusion complex, Adv. Drug Deliv. Rev., 57(15), 2203–2214. (DOI:10.1016/j.addr.2005.09.014)

97. Gupta U., Agashe H. B., Asthana A., Jain N. K. (2006), Dendrimers: Novel polymeric nanoarchitectures for solubility enhancement, Biomacromolecules, 7(3), 649–658. (DOI:10.1021/bm050802s)

98. Gajbhiye V., Palanirajan V. K., Tekade R. K., Jain N. K. (2010), Dendrimers as therapeutic agents: a systematic review, J. Pharm. Pharmacol., 61(8), 989–1003. (DOI:10.1211/jpp.61.08.0002)

99. Gitsov I., Hamzik J., Ryan J., Simonyan A., Nakas J. P., Omori S., et al. (2008), Enzymatic nanoreactors for environmentally benign biotransformations. 1. Formation and catalytic activity of supramolecular complexes of laccase and linear−dendritic block copolymers, Biomacromolecules, 9(3), 804–811. (DOI:10.1021/bm701081m)

100. Perli G., Wang Q., Braga C. B., Bertuzzi D. L., Fontana L. A., Soares MCP., et al. (2021), Self-Assembly of a triazolylferrocenyl dendrimer in water yields nontraditional intrinsic green fluorescent vesosomes for Nanotheranostic Applications, J. Am. Chem. Soc., 143(33), 12948–12954. (DOI:10.1021/jacs.1c05551)

101. Williams D. S., Koga S., Hak C. R. C., Majrekar A., Patil A. J., Perriman A. W., et al. (2012), Polymer/nucleotide droplets as bio-inspired functional micro-compartments, Soft Matter, 8(22), 6004. (DOI:10.1039/c2sm25184a)

102. Koga S., Williams D. S., Perriman A. W., Mann S. (2011), Peptide–nucleotide microdroplets as a step towards a membrane-free protocell model, Nat. Chem., 3(9), 720–724. (DOI:10.1038/nchem.1110)

103. Abbas M., Lipiński W. P., Nakashima K. K., Huck W. T. S., Spruijt E. (2021), A short peptide synthon for liquid–liquid phase separation, Nat. Chem., 13(11), 1046–1054. (DOI:10.1038/s41557-021-00788-x)

104. Menger F. M., Peresypkin A. V., Caran K. L., Apkarian R. P. (2000), A sponge morphology in an elementary coacervate, Langmuir, 16(24), 9113–9116. (DOI:10.1021/la0010626)

105. Booij H. L., Bungenberg de Jong H. G. (1956), Colloid systems, Chapter: In biocolloids and their Interactions. Vienna Springer Vienna, pp.8–14. (DOI:10.1007/978-3-7091-5456-4_2)

106. Veis A. (2011), A review of the early development of the thermodynamics of the complex coacervation phase separation, Adv. Colloid Interface Sci., 167(1–2), 2–11. (DOI:10.1016/j.cis.2011.01.007)

107. Zhou L., Shi H., Li Z., He C. (2020), Recent Advances in complex coacervation design from macromolecular assemblies and emerging

applications, Macromol. Rapid Commun., 41(21), 2000149. (DOI:10.1002/marc.202000149)

108. Gucht J van der., Spruijt E., Lemmers M., Cohen Stuart M. A. (2011), Polyelectrolyte complexes: Bulk phases and colloidal systems, J. Colloid Interface Sci., 361(2), 407–422. (DOI:10.1016/j.jcis.2011.05.080)

109. Perry S., Li Y., Priftis D., Leon L., Tirrell M. (2014), The Effect of Salt on the complex coacervation of vinyl polyelectrolytes, Polymers, 6(6), 1756–1772. (DOI:10.3390/polym6061756)

110. Douliez J., Perro A., Béven L. (2019), Stabilization of all-in-water emulsions to form capsules as artificial cells, ChemBioChem, 20(20), 2546–2552. (DOI:10.1002/cbic.201900196)

111. Mukherjee P., Padhan S. K., Dash S., Patel S., Mishra B. K. (2011), Clouding behaviour in surfactant systems, Adv. Colloid Interface Sci., 162(1–2), 59–79. (DOI:10.1016/j.cis.2010.12.005)

112. van Stevendaal M. H. M. E., Vasiukas L., Yewdall N. A., Mason A. F., van Hest J. C. M. (2021), Engineering of biocompatible coacervate-based synthetic cells, ACS Appl. Mater. Interfaces, 13(7), 7879–7889. (DOI:10.1021/acsami.0c19052)

113. Rathee V. S., Sidky H., Sikora B. J., Whitmer J. K. (2018), Role of associative charging in the entropy–energy balance of polyelectrolyte complexes, J. Am. Chem. Soc., 140(45), 15319–15328. (DOI:10.1021/jacs.8b08649)

114. Orti F., Navarro A. M., Rabinovich A., Wodak S. J., Marino-Buslje C. (2021), Insight into membraneless organelles and their associated proteins: Drivers, clients and regulators, Comput. Struct. Biotechnol. J., 19, 3964–3977. (DOI:10.1016/j.csbj.2021.06.042)

115. Crowe C. D., Keating C. D. (2018), Liquid–liquid phase separation in artificial cells, Interface Focus, 8(5), 20180032. (DOI:10.1098/rsfs.2018.0032)

116. Kawamura A., Harada A., Kono K., Kataoka K. (2007), Self-assembled nano-bioreactor from block ionomers with elevated and stabilized enzymatic function, Bioconjug. Chem., 18(5), 1555–1559. (DOI:10.1021/bc070029t)

117. Frankel E. A., Bevilacqua P. C., Keating C. D. (2016), Polyamine/nucleotide coacervates provide strong compartmentalization of Mg^{2+}, nucleotides, and RNA, Langmuir, 32(8), 2041–2049. (DOI:10.1021/acs.langmuir.5b04462)

118. Koga S., Williams D. S., Perriman A. W., Mann S. (2011), Peptide–nucleotide microdroplets as a step towards a membrane-free protocell model, Nat. Chem, 3(9), 720–724. (DOI:10.1038/nchem.1110)

119. Pawar N., Bohidar H. B. (2011), Anisotropic domain growth and complex coacervation in nanoclay-polyelectrolyte solutions, Adv. Colloid Interface Sci., 167(1–2), 12–23. (DOI:10.1016/j.cis.2011.06.007)

120. Voets I. K., de Keizer A., Cohen Stuart M. A. (2009), Complex coacervate core micelles, Adv. Colloid Interface Sci., 147–148, 300–318. (DOI:10.1016/j.cis.2008.09.012)

121. Krogstad D. V., Lynd N. A., Choi S-H., Spruell J. M., Hawker C. J., Kramer E. J., et al. (2013), Effects of polymer and salt concentration on the structure and properties of triblock copolymer coacervate hydrogels, Macromolecules, 46(4), 1512–1518. (DOI:10.1021/ma302299r)

122. Hunt J. N., Feldman K. E., Lynd N. A., Deek J., Campos L. M., Spruell J. M., et al. (2011), Tunable, high modulus hydrogels driven by ionic

coacervation, Adv. Mater., 23(20), 2327–2331. (DOI:10.1002/adma.201004230)

123. Kim B., Lam C. N., Olsen B. D. (2012), Nanopatterned protein films directed by ionic complexation with water-soluble diblock copolymers, Macromolecules, 45(11), 4572–4580. (DOI:10.1021/ma2024914)

124. Fromm S. A., Kamenz J., Nöldeke E. R., Neu A., Zocher G., Sprangers R. (2014), In vitro reconstitution of a cellular phase-transition process that involves the mRNA decapping machinery, Angew. Chem. Int. Ed., 53(28), 7354–7359. (DOI:10.1002/anie.201402885)

125. Schmitt C., Turgeon S. L. (2011), Protein/polysaccharide complexes and coacervates in food systems, Adv. Colloid Interface Sci., 167(1–2), 63–70. (DOI:10.1016/j.cis.2010.10.001)

126. Pir Cakmak F., Grigas A. T., Keating C. D. (2019), Lipid vesicle-coated complex coacervates, Langmuir, 35(24), 7830–7840. (DOI:10.1021/acs.langmuir.9b00213)

127. Chen W. C. W., Lee B. G., Park D. W., Kim K., Chu H., Kim K., et al. (2015), Controlled dual delivery of fibroblast growth factor-2 and Interleukin-10 by heparin-based coacervate synergistically enhances ischemic heart repair, Biomater., 72, 138–151. (DOI:10.1016/j.biomaterials.2015.08.050)

128. Singh S., Vaishnav J. K., Mukherjee T. K. (2020), Quantum dot-based hybrid coacervate nanodroplets for ultrasensitive detection of Hg^{2+}, ACS Appl. Nano Mater., 3(4), 3604–3612. (DOI:10.1021/acsanm.0c00317)

129. Ivinova O. N., Izumrudov V. A., Muronetz V. I., Galaev I. Yu., Mattiasson B. (2003), Influence of complexing polyanions on the

thermostability of basic proteins, Macromol. Biosci., 3(34), 210–215. (DOI:10.1002/mabi.200390024)

130. Schoonen L., van Hest J. C. M. (2016), Compartmentalization approaches in soft matter science: From nanoreactor development to organelle mimics, Adv. Mater., 28(6), 1109–1128. (DOI:10.1002/adma.201502389)

131. Moulik S. P., Rakshit A. K., Pan A., Naskar B. (2022), An overview of coacervates: The special disperse state of amphiphilic and polymeric materials in solution, Colloids Interfaces, 6(3), 45. (DOI:10.3390/colloids6030045)

132. Hwang D. S., Zeng H., Srivastava A., Krogstad D. V., Tirrell M., Israelachvili J. N., et al. (2010), Viscosity and interfacial properties in a mussel-inspired adhesive coacervate, Soft Matter, 6(14), 3232. (DOI:10.1039/c002632h)

133. Ma Q., Song Y., Baier G., Holtze C., Shum H. C. (2016), Osmo-solidification of all-aqueous emulsion with enhanced preservation of protein activity, J. Mater. Chem. B, 4(7), 1213–1218. (DOI:10.1039/C5TB02187A)

134. Chen Y., Yuan M., Zhang Y., Liu S., Yang X., Wang K., et al. (2020), Construction of coacervate-in-coacervate multi-compartment protocells for spatial organization of enzymatic reactions, Chem. Sci., 11(32), 8617–8625. (DOI:10.1039/D0SC03849K)

135. Kojima T., Takayama S. (2018), Membraneless compartmentalization facilitates enzymatic cascade reactions and reduces substrate inhibition, ACS Appl. Mater. Interfaces, 10(38), 32782–32791. (DOI:10.1021/acsami.8b07573)

136. Love C., Steinkühler J., Gonzales D. T., Yandrapalli N., Robinson T., Dimova R., et al. (2020), Reversible pH-Responsive coacervate

formation in lipid vesicles activates dormant enzymatic reactions, Angew. Chem. Int. Ed., 59(15), 5950–5957. (DOI:10.1002/anie.201914893)

137. Molliex A., Temirov J., Lee J., Coughlin M., Kanagaraj A. P., Kim H. J., et al. (2015), Phase separation by low complexity domains promotes stress granule assembly and drives pathological fibrillization, Cell, 163(1), 123–133. (DOI:10.1016/j.cell.2015.09.015)

138. Wegmann S., Eftekharzadeh B., Tepper K., Zoltowska K. M., Bennett R. E., Dujardin S., et al. (2018), Tau protein liquid–liquid phase separation can initiate tau aggregation, EMBO J., 37(7) (DOI:10.15252/embj.201798049)

139. Ray S., Singh N., Kumar R., Patel K., Pandey S., Datta D., et al. (2020), α-Synuclein aggregation nucleates through liquid–liquid phase separation, Nat. Chem., 12(8), 705–716. (DOI:10.1038/s41557-020-0465-9)

140. Poudyal M., Patel K., Sawner A. S., Gadhe L., Kadu P., Datta D., et al. (2022), Liquid condensate is a common state of proteins and polypeptides at the regime of high intermolecular interactions, Biophysics, preprint. (DOI:10.1101/2021.12.31.474648)

141. Priftis D., Tirrell M. (2012), Phase behaviour and complex coacervation of aqueous polypeptide solutions, Soft Matter, 8(36), 9396–9405. (DOI:10.1039/C2SM25604E)

142. Chollakup R., Smitthipong W., Eisenbach C. D., Tirrell M. (2010), Phase behavior and coacervation of aqueous poly(acrylic acid)−poly(allylamine) solutions, Macromolecules, 43(5), 2518–2528. (DOI:10.1021/ma902144k)

143. Liu Y., Winter H. H., Perry S. L. (2017), Linear viscoelasticity of complex coacervates, Adv. Colloid Interface Sci., 239, 46–60. (DOI:10.1016/j.cis.2016.08.010)

144. Ali S., Bleuel M., Prabhu V. M. (2019), Lower critical solution temperature in polyelectrolyte complex coacervates, ACS Macro Lett., 8(3), 289–293. (DOI:10.1021/acsmacrolett.8b00952)

145. Perry S., Li Y., Priftis D., Leon L., Tirrell M. (2014), The effect of salt on the complex coacervation of vinyl polyelectrolytes, Polymers, 6(6), 1756–1772. (DOI:10.3390/polym6061756)

146. Nichols M. K., Kumar R. K., Bassindale P. G., Tian L., Barnes A. C., Drinkwater B. W., et al. (2018), Fabrication of micropatterned dipeptide hydrogels by acoustic trapping of stimulus-responsive coacervate droplets, Small, 14(26), 1800739. (DOI:10.1002/smll.201800739)

147. Huang G-Q., Han X-N., Xiao J-X. (2017), Glutaraldehyde-crosslinked O-carboxymethyl chitosan–gum arabic coacervates: Characteristics versus complexation acidity, J. Dispers. Sci. Technol., 38(11), 1607–1612. (DOI:10.1080/01932691.2016.1265454)

148. Joshi N., Rawat K., Bohidar H. B. (2018), pH and ionic strength induced complex coacervation of pectin and gelatin A, Food Hydrocoll., 74, 132–138. (DOI:10.1016/j.foodhyd.2017.08.011)

149. Fares H. M., Ghoussoub Y. E., Delgado J. D., Fu J., Urban V. S., Schlenoff J. B. (2018), Scattering neutrons along the polyelectrolyte complex/coacervate continuum, Macromolecules, 51(13), 4945–4955. (DOI:10.1021/acs.macromol.8b00699)

150. Priftis D., Laugel N., Tirrell M. (2012), Thermodynamic characterization of polypeptide complex coacervation, Langmuir, 28(45), 15947–15957. (DOI:10.1021/la302729r)

151. Zhang Z., Li H., Kasmi S., Van Herck S., Deswarte K., Lambrecht BN., et al. (2019), A synthetic, transiently thermoresponsive homopolymer with UCST behaviour within a physiologically relevant window, Angew. Chem. Int. Ed., 58(23), 7866–7872. (DOI:10.1002/anie.201900224)

152. Nishida K., Tamura A., Yui N. (2018), pH-Responsive coacervate droplets formed from acid-labile methylated polyrotaxanes as an injectable protein carrier, Biomacromolecules, 19(6), 2238–2247. (DOI:10.1021/acs.biomac.8b00301)

153. Aumiller W. M., Pir Cakmak F., Davis B. W., Keating C. D. (2016), RNA-Based coacervates as a model for membraneless organelles: Formation, properties, and interfacial liposome assembly, Langmuir, 32(39), 10042–10053. (DOI:10.1021/acs.langmuir.6b02499)

154. Douliez J., Perro A., Béven L. (2019), Stabilization of all-in-water emulsions to form capsules as artificial cells, ChemBioChem, 20(20), 2546–2552. (DOI:10.1002/cbic.201900196)

155. Chollakup R., Beck J. B., Dirnberger K., Tirrell M., Eisenbach C. D. (2013), Polyelectrolyte molecular weight and salt effects on the phase behavior and coacervation of aqueous solutions of poly(acrylic acid) sodium salt and poly(allylamine) hydrochloride, Macromolecules, 46(6), 2376–2390. (DOI:10.1021/ma202172q)

156. Vitorazi L., Ould-Moussa N., Sekar S., Fresnais J., Loh W., Chapel J-P., et al. (2014), Evidence of a two-step process and pathway dependency in the thermodynamics of poly(diallyldimethylammonium chloride)/poly(sodium acrylate) complexation, Soft Matter, 10(47), 9496–9505. (DOI:10.1039/C4SM01461H)

157. Li H., Fauquignon M., Haddou M., Schatz C., Chapel J-P. (2021), Interfacial behavior of solid- and liquid-like polyelectrolyte complexes as a function of charge stoichiometry, Polymers, 13(21), 3848. (DOI:10.3390/polym13213848)

158. van Swaay D., Tang T-YD., Mann S., de Mello A. (2015), Microfluidic formation of membrane-free aqueous coacervate droplets in water, Angew. Chem. Int. Ed., 54(29), 8398–8401. (DOI:10.1002/anie.201502886)

159. Cruz M. A., Morris D. L., Swanson J. P., Kundu M., Mankoci S. G., Leeper T. C., et al. (2018), Efficient protein encapsulation within thermoresponsive coacervate-forming biodegradable polyesters, ACS Macro Lett., 7(4), 477–481. (DOI:10.1021/acsmacrolett.8b00118)

160. Yang M., Digby Z. A., Schlenoff J. B. (2020), Precision doping of polyelectrolyte complexes: Insight on the role of ions, Macromolecules, 53(13), 5465–5474. (DOI:10.1021/acs.macromol.0c00965)

161. Narayanan A., Menefee J. R., Liu Q., Dhinojwala A., Joy A. (2020), Lower critical solution temperature-driven self-coacervation of nonionic polyester underwater adhesives, ACS Nano, 14(7), 8359–8367. (DOI:10.1021/acsnano.0c02396)

162. Priftis D., Xia X., Margossian K. O., Perry S. L., Leon L., Qin J., et al. (2014), Ternary, tunable polyelectrolyte complex fluids driven by complex coacervation, Macromolecules, 47(9), 3076–3085. (DOI:10.1021/ma500245j)

163. Kizilay E., Dinsmore A. D., Hoagland D. A., Sun L., Dubin P. L. (2013), Evolution of hierarchical structures in polyelectrolyte–micelle coacervates, Soft Matter, 9(30), 7320. (DOI:10.1039/c3sm50591j)

164. Dan A., Ghosh S., Moulik S. P. (2009), Physiochemistry of the interaction between inulin and alkyltrimethylammonium bromides in aqueous medium and the formed coacervates, J. Phys. Chem. B, 113(25), 8505–8513. (DOI:10.1021/jp902641d)

165. Kakizawa Y., Miyake M. (2019), Creation of new functions by combination of surfactant and polymer - complex coacervation with oppositely charged polymer and surfactant for shampoo and body wash , J. Oleo Sci., 68(6), 525–539. (DOI:10.5650/jos.ess19081)

166. Keshavarzi B., Schwarzenberger K., Huang M., Javadi A., Eckert K. (2019), Formation of structured membranes by coacervation of xanthan gum with C_nTAB surfactants, Langmuir, 35(42), 13624–13635. (DOI:10.1021/acs.langmuir.9b02220)

167. Douliez J-P., Martin N., Gaillard C., Beneyton T., Baret J-C., Mann S., et al. (2017), Catanionic coacervate droplets as a surfactant-based membrane-free protocell model, Angew. Chem. Int. Ed., 56(44), 13689–13693. (DOI:10.1002/anie.201707139)

168. Krishna Kumar R., Harniman R. L., Patil AJ., Mann S. (2016), Self-transformation and structural reconfiguration in coacervate-based protocells, Chem. Sci., 7(9), 5879–5887. (DOI:10.1039/C6SC00205F)

169. Gabryelczyk B., Cai H., Shi X., Sun Y., Swinkels P. J. M., Salentinig S., et al. (2019), Hydrogen bond guidance and aromatic stacking drive liquid-liquid phase separation of intrinsically disordered histidine-rich peptides, Nat. Commun., 10(1), 5465. (DOI:10.1038/s41467-019-13469-8)

170. Valley B., Jing B., Ferreira M., Zhu Y. (2019), Rapid and efficient coacervate extraction of cationic industrial dyes from wastewater,

ACS Appl. Mater. Interfaces, 11(7), 7472–7478. (DOI:10.1021/acsami.8b21674)

171. Jing B., Qiu J., Zhu Y. (2017), Organic–inorganic macroion coacervate complexation, Soft Matter, 13(28), 4881–4889. (DOI:10.1039/C7SM00955K)

172. Rumyantsev A. M., Borisov O. V., de Pablo J. J. (2023), Structure and dynamics of hybrid colloid–polyelectrolyte coacervates, Macromolecules, 56(4), 1713–1730. (DOI:10.1021/acs.macromol.2c02464)

173. Qi L., Chapel J-P., Castaing J-C., Fresnais J., Berret J-F. (2008), Organic versus hybrid coacervate complexes: co-assembly and adsorption properties, Soft Matter, 4(3), 577. (DOI:10.1039/b716178f)

174. Vaishnav J. K., Mukherjee T. K. (2019), Highly photostable and two-photon active quantum dot–Polymer multicolor hybrid coacervate droplets, Langmuir, 35(36), 11764–11773. (DOI:10.1021/acs.langmuir.9b01783)

175. Singh S., Rao C., Nandi C. K., Mukherjee T. K. (2022), Quantum dot-embedded hybrid photocatalytic nanoreactors for visible light photocatalysis and dye degradation, ACS Appl. Nano Mater., 5(5), 7427–7439. (DOI:10.1021/acsanm.2c01446)

176. Liu J., Li R., Yang B. (2020), Carbon dots: A new type of carbon-based nanomaterial with wide applications, ACS Cent. Sci., 6(12), 2179–2195. (DOI:10.1021/acscentsci.0c01306)

177. Bhattacharya A., Chatterjee S., Prajapati R., Mukherjee T. K. (2015), Size-dependent penetration of carbon dots inside the ferritin nanocages: evidence for the quantum confinement effect in carbon

dots, Phys. Chem. Chem. Phys., 17(19), 12833–12840. (DOI:10.1039/C5CP00543D)

178. Bhattacharya A., Chatterjee S., Khorwal V., Mukherjee T. K. (2016), Luminescence turn-on/off sensing of biological iron by carbon dots in transferrin, Phys. Chem. Chem. Phys., 18(7), 5148–5158. (DOI:10.1039/C5CP05890B)

179. Karakoçak B. B., Liang J., Kavadiya S., Berezin M. Y., Biswas P., Ravi N. (2018), Optimizing the synthesis of red-emissive nitrogen-doped carbon dots for use in bioimaging, ACS Appl. Nano Mater., 1(7), 3682–3692. (DOI:10.1021/acsanm.8b00799)

180. Du J., Xu N., Fan J., Sun W., Peng X. (2019), Carbon dots for in vivo bioimaging and theranostics, Small, 15(32), 1805087. (DOI:10.1002/smll.201805087)

181. Khodadadian M., Ghassemi M., Behrouz H., Maleknia S., Mahboudi F. (2019), Determination of residual poly diallyldimethylammonium chloride (PDADMAC) in monoclonal antibody formulations by size exclusion chromatography and evaporative light scattering detector, Biologicals, 57, 21–28. (DOI:10.1016/j.biologicals.2018.11.002)

182. Banani S. F., Lee H. O., Hyman A. A., Rosen M. K. (2017), Biomolecular condensates: organizers of cellular biochemistry, Nat. Rev. Mol. Cell Biol., 18(5), 285–298. (DOI:10.1038/nrm.2017.7)

183. Uversky V. N. (2021), Recent Developments in the field of intrinsically disordered proteins: Intrinsic disorder–based emergence in cellular biology in light of the physiological and pathological liquid–liquid phase transitions, Annu. Rev. Biophys., 50(1), 135–156. (DOI:10.1146/annurev-biophys-062920-063704)

184. Zhang Y., Narlikar G. J., Kutateladze T. G. (2021), Enzymatic reactions inside biological condensates, J. Mol. Biol., 433(12), 166624. (DOI:10.1016/j.jmb.2020.08.009)

185. Asaad N., Engberts J. B. F. N. (2003), Cytosol-mimetic chemistry: Kinetics of the trypsin-catalyzed hydrolysis of p- nitrophenyl acetate upon addition of polyethylene glycol and N-tert-butyl acetoacetamide, J. Am. Chem. Soc., 125(23), 6874–6875. (DOI:10.1021/ja034298f)

186. Aumiller W. M., Davis B. W., Hashemian N., Maranas C., Armaou A., Keating C. D. (2014), Coupled enzyme reactions performed in heterogeneous reaction media: Experiments and modeling for glucose oxidase and horseradish peroxidase in a PEG/Citrate aqueous two-phase system, J. Phys. Chem. B, 118(9), 2506–2517. (DOI:10.1021/jp501126v)

187. Jiang M., Guo Z. (2007), Effects of macromolecular crowding on the intrinsic catalytic efficiency and structure of enterobactin-specific isochorismate synthase, J. Am. Chem. Soc., 129(4), 730–731. (DOI:10.1021/ja065064)

188. Gomez D., Huber K., Klumpp S. (2019), On protein folding in crowded conditions, J. Phys. Chem. Lett., 10(24), 7650–7656. (DOI:10.1021/acs.jpclett.9b02642)

189. Kuznetsova I., Turoverov K., Uversky V. (2014), What macromolecular crowding can do to a protein, IJMS, 15(12), 23090–23140. (DOI:10.3390/ijms151223090)

190. White D. A., Buell A. K., Knowles T. P. J., Welland M. E., Dobson C. M. (2010), Protein aggregation in crowded environments, J. Am. Chem. Soc., 132(14), 5170–5175. (DOI:10.1021/ja909997e)

191. Pastor I., Vilaseca E., Madurga S., Garcés J. L., Cascante M., Mas F. (2010), Diffusion of α-chymotrypsin in solution-crowded media. A

fluorescence recovery after photobleaching study, J. Phys. Chem. B, 114(11), 4028–4034. (DOI:10.1021/jp910811j)

192. Wilcox X. E., Ariola A., Jackson J. R., Slade K. M. (2020), Overlap concentration and the effect of macromolecular crowding on citrate synthase activity, Biochem., 59(18), 1737–1746. (DOI:10.1021/acs.biochem.0c00073)

193. Nakano S., Karimata H. T., Kitagawa Y., Sugimoto N. (2009), Facilitation of RNA enzyme activity in the molecular crowding media of cosolutes, J. Am. Chem. Soc., 131(46), 16881–16888. (DOI:10.1021/ja9066628)

194. Minton A. P. (2006), How can biochemical reactions within cells differ from those in test tubes?, J. Cell Sci., 119(14), 2863–2869. (DOI:10.1242/jcs.03063)

195. Bailey F. E., Koleske J. V. (2000), Polyoxyalkylenes, Chapter: In Wiley-VCH Verlag GmbH & Co. KGaA (ed), Ullmann's encyclopedia of industrial chemistry. Weinheim, Germany Wiley-VCH Verlag GmbH & Co. KGaA, p.a21_579. (DOI:10.1002/14356007.a21_579)

196. Bhattacharya S., Shunmugam R. (2020), Unraveling the effect of PEG chain length on the physical properties and toxicant removal capacities of cross-Linked network synthesized by thiol–norbornene photoclick chemistry, ACS Omega, 5(6), 2800–2810. (DOI:10.1021/acsomega.9b03554)

197. Lee C. F., Bird S., Shaw M., Jean L., Vaux D. J. (2012), Combined effects of agitation, macromolecular crowding, and interfaces on amyloidogenesis, J. Biol. Chem., 287(45), 38006–38019. (DOI:10.1074/jbc.M112.400580)

198. Cozzolino S., Graziano G. (2021), The magnitude of macromolecular crowding caused by dextran and ficoll for the conformational stability of globular proteins, J. Mol. Liq., 322, 114969. (DOI:10.1016/j.molliq.2020.114969)

199. Lavrenko P. N., Mikriukova O. I., Okatova O. V. (1987), On the separation ability of various ficoll gradient solutions in zonal centrifugation, Anal. Biochem., 166(2), 287–297. (DOI:10.1016/0003-2697(87)90577-X)

200. Venturoli D., Rippe B. (2005), Ficoll and dextran vs. globular proteins as probes for testing glomerular permselectivity: effects of molecular size, shape, charge, and deformability, Am. J. Physiol. Renal Physiol., 288(4), F605–F613. (DOI:10.1152/ajprenal.00171.2004)

201. Majorek K. A., Porebski P. J., Dayal A., Zimmerman M. D., Jablonska K., Stewart A. J., et al. (2012), Structural and immunologic characterization of bovine, horse, and rabbit serum albumins, Mol. Immunol., 52(3–4), 174–182. (DOI:10.1016/j.molimm.2012.05.011)

202. Topală T., Bodoki A., Oprean L., Oprean R. (2014), Bovine serum albumin interactions with metal complexes, Med. Pharm. Rep., 87(4), 215–219. (DOI:10.15386/cjmed-357)

203. Shahid S., Hasan I., Ahmad F., Hassan Md. I., Islam A. (2019), Carbohydrate-based macromolecular crowding-induced stabilization of proteins: Towards understanding the significance of the size of the crowder, Biomolecules, 9(9), 477. (DOI:10.3390/biom9090477)

204. Poggi C. G., Slade K. M. (2015), Macromolecular crowding and the steady-state kinetics of malate dehydrogenase, Biochem., 54(2), 260–267. (DOI:10.1021/bi5011255)

205. Biswas S., Kundu J., Mukherjee S. K., Chowdhury P. K. (2018), Mixed macromolecular crowding: A protein and solvent perspective, ACS Omega, 3(4), 4316–4330. (DOI:10.1021/acsomega.7b01864)

206. Nakashima K. K., Vibhute M. A., Spruijt E. (2019), Biomolecular chemistry in liquid phase separated compartments, Front. Mol. Biosci., 6, 21. (DOI:10.3389/fmolb.2019.00021)

207. van Haren M. H., Nakashima K. K., Sprujit E. (2020), Coacervate-based protocells: Integration of life-like properties in a droplets, J. Syst. Chem., 8, 107-120.

208. Zhao W., Fan Y., Wang H., Wang Y. (2017), Coacervate of polyacrylamide and cationic gemini surfactant for the extraction of methyl orange from aqueous solution, Langmuir, 33(27), 6846–6856. (DOI:10.1021/acs.langmuir.7b01421)

209. Chiappisi L., Simon M., Gradzielski M. (2015), Toward bioderived intelligent nanocarriers for controlled pollutant recovery and pH-sensitive binding, ACS Appl. Mater. Interfaces, 7(11), 6139–6145. (DOI:10.1021/am508846r)

210. Zhao M., Zacharia N. S. (2016), Sequestration of methylene blue into polyelectrolyte complex coacervates, Macromol. Rapid Commun., 37(15), 1249–1255. (DOI:10.1002/marc.201600244)

211. Liu B., Zhao W., Shen Y., Fan Y., Wang Y. (2021), Trimeric cationic surfactant coacervation as a versatile approach for removing organic pollutants, Langmuir, 37(19), 5993–6001. (DOI:10.1021/acs.langmuir.1c00557)

212. Costantini F., Tiggelaar R., Sennato S., Mura F., Schlautmann S., Bordi F., et al. (2013), Glucose level determination with a multi-enzymatic cascade reaction in a functionalized glass chip, Analyst, 138(17), 5019. (DOI:10.1039/c3an00806a)

213. Kim I., Kim C., Lee D., Lee S. W., Lee G., Yoon D. S. (2020), A bio-inspired highly selective enzymatic glucose sensor using a red blood cell membrane, Analyst, 145(6), 2125–2132. (DOI:10.1039/C9AN02421B)

214. Han L., Zhang H., Chen D., Li F. (2018), Protein-directed metal oxide nanoflakes with tandem enzyme-like characteristics: Colorimetric glucose sensing based on one-pot enzyme-free cascade catalysis, Adv. Funct. Mater., 28(17), 1800018. (DOI:10.1002/adfm.201800018)

215. Gayathri S., Arunkumar P., Kim J., Han J. H. (2022), Bimetallic layered hydroxide nitrate@graphene oxide as an electrocatalyst for efficient non-enzymatic glucose sensors: Tuning sensitivity by hydroxide-regulated $M_2(OH)_{4-n}(A^{n-})$ phases derived from solvent engineering, ACS Sustain. Chem. Eng., 10(4), 1689–1701. (DOI:10.1021/acssuschemeng.1c07644)

216. Zeng D., Luo W., Li J., Liu H., Ma H., Huang Q., et al. (2012), Gold nanoparticles-based nanoconjugates for enhanced enzyme cascade and glucose sensing, Analyst, 137(19), 4435. (DOI:10.1039/c2an35900f)

217. Liu J., Shen X., Baimanov D., Wang L., Xiao Y., Liu H., et al. (2019), Immobilized ferrous ion and glucose oxidase on graphdiyne and its application on one-step glucose detection, ACS Appl. Mater. Interfaces, 11(3), 2647–2654. (DOI:10.1021/acsami.8b03118)

218. Cai S., Fu Z., Xiao W., Xiong Y., Wang C., Yang R. (2020), Zero-dimensional/two-dimensional Au_xPd_{100-x} nanocomposites with enhanced nanozyme catalysis for sensitive glucose detection, ACS Appl. Mater. Interfaces, 12(10), 11616–11624. (DOI:10.1021/acsami.9b21621)

219. Zhang P., Sun D., Cho A., Weon S., Lee S., Lee J., et al. (2019), Modified carbon nitride nanozyme as bifunctional glucose oxidase-

peroxidase for metal-free bioinspired cascade photocatalysis, Nat. Commun., 10(1), 940. (DOI:10.1038/s41467-019-08731-y)

220. Fan H., Li K., Tu T., Zhu X., Zhang L., Liu M. (2022), ATP-induced emergent circularly polarized luminescence and encryption, Angew. Chem. Int. Ed., 61(19) (DOI:10.1002/anie.202200727)

221. Prieß M., Göddeke H., Groenhof G., Schäfer L. V. (2018), Molecular mechanism of ATP hydrolysis in an ABC transporter, ACS Cent. Sci., 4(10), 1334–1343. (DOI:10.1021/acscentsci.8b00369)

222. Sridharan S., Kurzawa N., Werner T., Günthner I., Helm D., Huber W., et al. (2019), Proteome-wide solubility and thermal stability profiling reveals distinct regulatory roles for ATP, Nat. Commun., 10(1), 1155. (DOI:10.1038/s41467-019-09107-y)

223. Keating C. D. (2012), Aqueous phase separation as a possible route to compartmentalization of biological molecules, Acc. Chem. Res., 45(12), 2114–2124. (DOI:10.1021/ar200294y)

224. Martin N., Li M., Mann S. (2016), Selective uptake and refolding of globular proteins in coacervate microdroplets, Langmuir, 32(23), 5881–5889. (DOI:10.1021/acs.langmuir.6b01271)

225. Timilsena Y. P., Akanbi T. O., Khalid N., Adhikari B., Barrow C. J. (2019), Complex coacervation: Principles, mechanisms and applications in microencapsulation, Int. J. Biol. Macromol., 121, 1276–1286. (DOI:10.1016/j.ijbiomac.2018.10.144)

226. Rauck B. M., Novosat T. L., Oudega M., Wang Y. (2015), Biocompatibility of a coacervate-based controlled release system for protein delivery to the injured spinal cord, Acta Biomater., 11, 204–211. (DOI:10.1016/j.actbio.2014.09.037)

227. Armstrong J. P. K., Olof S. N., Jakimowicz M. D., Hollander A. P., Mann S., Davis S. A., et al. (2015), Cell paintballing using optically

targeted coacervate microdroplets, Chem. Sci., 6(11), 6106–6111. (DOI:10.1039/C5SC02266E)

228. Xiao W., Jakimowicz M. D., Zampetakis I., Neely S., Scarpa F., Davis S. A., et al. (2020), Biopolymeric coacervate microvectors for the delivery of functional proteins to cells, Adv. Biosys., 4(11), 2000101. (DOI:10.1002/adbi.202000101)

229. Guo H., Song S., Dai T., Sun K., Zhou G., Li M., et al. (2020), Near-infrared fluorescent and magnetic resonance dual-imaging coacervate nanoprobes for trypsin mapping and targeted payload delivery of malignant tumors, ACS Appl. Mater. Interfaces, 12(15), 17302–17313. (DOI:10.1021/acsami.0c03433)

230. Sun Y., Lau S. Y., Lim Z. W., Chang S. C., Ghadessy F., Partridge A., et al. (2022), Phase-separating peptides for direct cytosolic delivery and redox-activated release of macromolecular therapeutics, Nat. Chem., 14(3), 274–283. (DOI:10.1038/s41557-021-00854-4)

231. Lim Z. W., Ping Y., Miserez A. (2018), Glucose-responsive peptide coacervates with high encapsulation efficiency for controlled release of insulin, Bioconj. Chem., 29(7), 2176–2180. (DOI:10.1021/acs.bioconjchem.8b00369)

232. Zhao P., Xia X., Xu X., Leung K. K. C., Rai A., Deng Y., et al. (2021), Nanoparticle-assembled bioadhesive coacervate coating with prolonged gastrointestinal retention for inflammatory bowel disease therapy, Nat. Commun., 12(1), 7162. (DOI:10.1038/s41467-021-27463-6)

233. de Silva U. K., Brown J. L., Lapitsky Y. (2018), Poly(allylamine)/tripolyphosphate coacervates enable high loading and multiple-month release of weakly amphiphilic anionic drugs: an

in vitro study with ibuprofen, RSC Adv., 8(35), 19409–19419. (DOI:10.1039/C8RA02588F)

234. Barthold S., Kletting S., Taffner J., de Souza Carvalho-Wodarz C., Lepeltier E., Loretz B., et al. (2016), Preparation of nanosized coacervates of positive and negative starch derivatives intended for pulmonary delivery of proteins, J. Mater. Chem. B, 4(13), 2377–2386. (DOI:10.1039/C6TB00178E)

235. Park U., Lee M. S., Jeon J., Lee S., Hwang M. P., Wang Y., et al. (2019), Coacervate-mediated exogenous growth factor delivery for scarless skin regeneration, Acta Biomater., 90, 179–191. (DOI:10.1016/j.actbio.2019.03.052)

236. Jing H., Du X., Mo L., Wang H. (2021), Self-coacervation of carboxymethyl chitosan as a pH-responsive encapsulation and delivery strategy, Int. J. Biol. Macromol., 192, 1169–1177. (DOI:10.1016/j.ijbiomac.2021.10.072)

237. Martin N., Tian L., Spencer D., Coutable-Pennarun A., Anderson JLR., Mann S. (2019), Photoswitchable phase separation and oligonucleotide trafficking in DNA coacervate microdroplets, Angew. Chem. Int. Ed., 58(41), 14594–14598. (DOI:10.1002/anie.201909228)

238. Shen J., Kim H-C., Wolfram J., Mu C., Zhang W., Liu H., et al. (2017), A liposome encapsulated ruthenium polypyridine complex as a theranostic platform for triple-negative breast cancer, Nano Lett., 17(5), 2913–2920. (DOI:10.1021/acs.nanolett.7b00132)

239. Pettinari R., Marchetti F., Condello F., Pettinari C., Lupidi G., Scopelliti R., et al. (2014), Ruthenium(II)–arene RAPTA type complexes containing curcumin and bisdemethoxycurcumin display potent and selective anticancer activity, Organometallics, 33(14), 3709–3715. (DOI:10.1021/om500317b)

240. Uversky V. N. (2017), Protein intrinsic disorder-based liquid–liquid phase transitions in biological systems: Complex coacervates and membrane-less organelles, Adv. Colloid Interface Sci., 239, 97–114. (DOI:10.1016/j.cis.2016.05.012)

241. Tsitkov S., Hess H. (2019), Design principles for a compartmentalized enzyme cascade reaction, ACS Catal., 9(3), 2432–2439. (DOI:10.1021/acscatal.8b04419)

242. Dubey N. C., Tripathi B. P., Müller M., Stamm M., Ionov L. (2015), Enhanced activity of acetyl CoA synthetase adsorbed on smart microgel: an implication for precursor biosynthesis, ACS Appl. Mater. Interfaces, 7(3), 1500–1507. (DOI:10.1021/am5063376)

243. Dubey N. C., Tripathi B. P., Stamm M., Ionov L. (2014), Smart core–shell microgel support for acetyl coenzyme A synthetase: A step toward efficient synthesis of polypetide-based drugs, Biomacromolecules, 15(7), 2776–2783. (DOI:10.1021/bm5006382)

244. Tacias-Pascacio V. G., Ortiz C., Rueda N., Berenguer-Murcia A., Acosta N., Aranaz I., et al. (2019), Dextran aldehyde in biocatalysis: More than a mere immobilization system, Catal., 9(7), 622. (DOI:10.3390/catal9070622)

245. Rodrigues R. C., Virgen-Ortíz J. J., dos Santos J. C. S., Berenguer-Murcia Á., Alcantara A. R., Barbosa O., et al. (2019), Immobilization of lipases on hydrophobic supports: immobilization mechanism, advantages, problems, and solutions, Biotechnol. Adv. 37(5), 746–770. (DOI:10.1016/j.biotechadv.2019.04.003)

246. André A. A. M., Spruijt E. (2020), Liquid–liquid phase separation in crowded environments, IJMS, 21(16), 5908. (DOI:10.3390/ijms21165908)

247. Lin Y., Protter D. S. W., Rosen M. K., Parker R. (2015), Formation and maturation of phase-separated liquid droplets by RNA-binding proteins, Mol. Cell, 60(2), 208–219. (DOI:10.1016/j.molcel.2015.08.018)

248. Shin Y., Brangwynne C. P. (2017), Liquid phase condensation in cell physiology and disease, Science, 357(6357), eaaf4382. (DOI:10.1126/science.aaf4382)

249. Woodruff J. B., Hyman A. A., Boke E. (2018), Organization and function of non-dynamic biomolecular condensates, Trends Biochem. Sci., 43(2), 81–94. (DOI:10.1016/j.tibs.2017.11.005)

250. McCall P. M., Srivastava S., Perry S. L., Kovar D. R., Gardel M. L., Tirrell M. V. (2018), Partitioning and enhanced self-assembly of actin in polypeptide coacervates, Biophys. J., 114(7), 1636–1645. (DOI:10.1016/j.bpj.2018.02.020)

251. Toor R., Hourdin L., Shanmugathasan S., Lefrançois P., Arbault S., Lapeyre V., et al. (2023), Enzymatic cascade reaction in simple-coacervates, J. Colloid and Interface Sci., 629, 46–54. (DOI:10.1016/j.jcis.2022.09.019)

252. Chen Y., Yuan M., Zhang Y., Zhou S., Wang K., Wu Z., et al. (2022), Enzyme-active liquid coacervate microdroplets as artificial membraneless organelles for intracellular ROS scavenging, Biomater. Sci., 10(16), 4588–4595. (DOI:10.1039/D2BM00713D)

253. Drobot B., Iglesias-Artola J. M., Le Vay K., Mayr V., Kar M., Kreysing M., et al. (2018), Compartmentalized RNA catalysis in membrane-free coacervate protocells, Nat. Commun., 9(1), 3643. (DOI:10.1038/s41467-018-06072-w)

254. Lim ZW., Ping Y., Miserez A. (2018), Glucose-responsive peptide coacervates with high encapsulation efficiency for controlled release

of insulin, Bioconj. Chem., 29(7), 2176–2180. (DOI:10.1021/acs.bioconjchem.8b00369)

255. Kojima T., Takayama S. (2018), Membraneless compartmentalization facilitates enzymatic cascade reactions and reduces substrate inhibition, ACS Appl. Mater. Interfaces, 10(38), 32782–32791. (DOI:10.1021/acsami.8b07573)

256. Chenglong W., Shuhan X., Jiayi Y., Wencai G., Guoxiong X., Hongjing D. (2020), Dextran-based coacervate nanodroplets as potential gene carriers for efficient cancer therapy, Carbohydrate Polymers, 231, 115687. (DOI:10.1016/j.carbpol.2019.115687)

257. Qiao Y., Li M., Qiu D., Mann S. (2019), Response-retaliation behavior in synthetic protocell communities, Angew. Chem. Int. Ed., 58(49), 17758–17763. (DOI:10.1002/anie.201909313)

258. Aumiller W. M., Keating C. D. (2016), Phosphorylation-mediated RNA/peptide complex coacervation as a model for intracellular liquid organelles, Nat. Chem., 8(2), 129–137. (DOI:10.1038/nchem.2414)

259. Semenov S. N., Wong A. S. Y., van der Made R. M., Postma S. G. J., Groen J., van Roekel H. W. H., et al. (2015), Rational design of functional and tunable oscillating enzymatic networks, Nat. Chem, 7(2), 160–165. (DOI:10.1038/nchem.2142)

260. Peeples W., Rosen M. K. (2021), Mechanistic dissection of increased enzymatic rate in a phase-separated compartment, Nat. Chem. Biol., 17(6), 693–702. (DOI:10.1038/s41589-021-00801-x)

261. Koga S., Williams D. S., Perriman A. W., Mann S. (2011), Peptide–nucleotide microdroplets as a step towards a membrane-free protocell model, Nat. Chem., 3(9), 720–724. (DOI:10.1038/nchem.1110)

262. Drobot B., Iglesias-Artola J. M., Le Vay K., Mayr V., Kar M., Kreysing M., et al. (2018), Compartmentalised RNA catalysis in

membrane-free coacervate protocells, Nat. Commun., 9(1), 3643. (DOI:10.1038/s41467-018-06072-w)

263. Banerjee P. R., Milin A. N., Moosa M. M., Onuchic P. L., Deniz A. A. (2017), Reentrant phase transition drives dynamic substructure formation in ribonucleoprotein droplets, Angew. Chem. Int. Ed., 56(38), 11354–11359. (DOI:10.1002/anie.201703191)

264. Yansaneh O. Y., Zein S. H. (2022), Latest advances in waste plastic pyrolytic catalysis, Processes, 10(4), 683. (DOI:10.3390/pr10040683)

265. Francke R., Little R. D. (2014), Redox catalysis in organic electrosynthesis: basic principles and recent developments, Chem. Soc. Rev., 43(8), 2492. (DOI:10.1039/c3cs60464k)

266. Liu L., Corma A. (2018), Metal catalysts for heterogeneous catalysis: From single atoms to nanoclusters and nanoparticles, Chem. Rev., 118(10), 4981–5079. (DOI:10.1021/acs.chemrev.7b00776)

267. Hervés P., Pérez-Lorenzo M., Liz-Marzán L. M., Dzubiella J., Lu Y., Ballauff M. (2012), Catalysis by metallic nanoparticles in aqueous solution: model reactions, Chem. Soc. Rev., 41(17), 5577. (DOI:10.1039/c2cs35029g)

268. Agarwal P. K. (2006), Enzymes: An integrated view of structure, dynamics and function, Microb. Cell Factories, 5(1), 2. (DOI:10.1186/1475-2859-5-2)

269. Lindberg D., de la Fuente Revenga M., Widersten M. (2010), Temperature and pH dependence of enzyme-catalyzed hydrolysis of trans -methylstyrene oxide. A unifying kinetic model for observed hysteresis, cooperativity, and regioselectivity, Biochem., 49(10), 2297–2304. (DOI:10.1021/bi902157b)

270. Prentice E. J., Hicks J., Ballerstedt H., Blank L. M., Liáng L. L., Schipper L. A., et al. (2020), The inflection point hypothesis: The

relationship between the temperature dependence of enzyme-catalyzed reaction rates and microbial growth rates, Biochem., 59(38), 3562–3569. (DOI:10.1021/acs.biochem.0c00530)

271. Kim S. H., Kim K-R., Ahn D-R., Lee J. E., Yang E. G., Kim S. Y. (2017), Reversible regulation of enzyme activity by pH-responsive encapsulation in DNA nanocages, ACS Nano, 11(9), 9352–9359. (DOI:10.1021/acsnano.7b04766)

272. Iannuzzelli J. A., Bacik J-P., Moore E. J., Shen Z., Irving E. M., Vargas D. A., et al. (2022), Tuning enzyme thermostability via computationally guided covalent stapling and structural basis of enhanced stabilization, Biochem., 61(11), 1041–1054. (DOI:10.1021/acs.biochem.2c00033)

273. Espinosa-Cantú A., Cruz-Bonilla E., Noda-Garcia L., DeLuna A. (2020), Multiple forms of multifunctional proteins in health and disease, Front. Cell Dev. Biol., 8, 451. (DOI:10.3389/fcell.2020.00451)

274. Wiltschi B., Cernava T., Dennig A., Galindo Casas M., Geier M., Gruber S., et al. (2020), Enzymes revolutionize the bioproduction of value-added compounds: From enzyme discovery to special applications, Biotechnol. Adv., 40, 107520. (DOI:10.1016/j.biotechadv.2020.107520)

275. Kingsley L. J., Lill M. A. (2015), Substrate tunnels in enzymes: Structure-function relationships and computational methodology: Protein tunnel structure-function relationship, Proteins, 83(4), 599–611. (DOI:10.1002/prot.24772)

276. Li Y., Yang G., Ren Y., Shi L., Ma R., van der Mei H. C., et al. (2020), Applications and perspectives of cascade reactions in bacterial

infection control, Front. Chem., 7, 861. (DOI:10.3389/fchem.2019.00861)

277. Bauer J. A., Zámocká M., Majtán J., Bauerová-Hlinková V. (2022), Glucose oxidase, an enzyme "Ferrari": Its structure, function, production and properties in the light of various industrial and biotechnological applications, Biomolecules, 12(3), 472. (DOI:10.3390/biom12030472)

278. Hecht H. J., Kalisz H. M., Hendle J., Schmid R. D., Schomburg D. (1993), Crystal structure of glucose oxidase from aspergillus niger refined at 2·3 Å reslution, J. Mol. Biol., 229(1), 153–172. (DOI:10.1006/jmbi.1993.1015)

279. Ślusarczyk J., Adamska E., Czerwik-Marcinkowska J. (2021), Fungi and algae as sources of medicinal and other biologically active compounds: A review, Nutrients, 13(9), 3178. (DOI:10.3390/nu13093178)

280. Veitch N. C. (2004), Horseradish peroxidase: a modern view of a classic enzyme, Phytochem., 65(3), 249–259. (DOI:10.1016/j.phytochem.2003.10.022)

281. Chattopadhyay K., Mazumdar S. (2000), Structural and conformational stability of horseradish peroxidase: Effect of temperature and pH, Biochem., 39(1), 263–270. (DOI:10.1021/bi990729o)

282. Lopes G. R., Pinto D. C. G. A., Silva A. M. S. (2014), Horseradish peroxidase (HRP) as a tool in green chemistry, RSC Adv., 4(70), 37244–37265. (DOI:10.1039/C4RA06094F)

283. Harpaz D., Eltzov E., Ng T. S. E., Marks R. S., Tok A. I. Y. (2020), Enhanced colorimetric signal for accurate signal detection in paper-

based biosensors, Diagnostics, 10(1), 28. (DOI:10.3390/diagnostics10010028)

284. Walters S. (2021), Horseradish: A Neglected and underutilized plant species for improving human health, Horticulturae, 7(7), 167. (DOI:10.3390/horticulturae7070167)

285. Rodriguez J-M. G., Hux N. P., Philips S. J., Towns M. H. (2019), Michaelis–menten graphs, lineweaver–burk plots, and reaction schemes: Investigating introductory biochemistry students' conceptions of representations in enzyme kinetics, J. Chem. Educ., 96(9), 1833–1845. (DOI:10.1021/acs.jchemed.9b00396)

286. Choi B., Rempala G. A., Kim J. K. (2017), Beyond the Michaelis-Menten equation: Accurate and efficient estimation of enzyme kinetic parameters, Sci. Rep., 7(1), 17018. (DOI:10.1038/s41598-017-17072-z)

Chapter 2

Materials, Sample Preparation, and Experimental Techniques

2.1. Introduction

This chapter contains the details of all the chemicals used in the thesis. The complete synthetic procedures of CDs, Ru-Cur, SUV, GUV, MLV, and QDs along with the different types of coacervates such as CD-, ATP-, QD-coacervate droplets have been discussed here. This chapter also covers the detailed sample preparation, experimental procedures, and techniques involved to complete the entire work of thesis.

2.2. Chemicals

Citric acid monohydrate (99.5%), sodium dihydrogen phosphate monohydrate ($NaH_2PO_4 \cdot H_2O$), disodium hydrogen phosphate (Na_2HPO_4), disodium hydrogen phosphate heptahydrate ($Na_2HPO_4 \cdot 7H_2O$), sodium acetate trihydrate ($CH_3COONa \cdot 3H_2O$), sodium bicarbonate ($NaHCO_3$), sodium carbonate anhydrous (Na_2CO_3), acetic acid (CH_3COOH), ethanol (EtOH), methanol (MeOH), o-phenylenediamine (OPD), and deuterated dimethyl sulfoxide (DMSO-d^6) were purchased from Merck. Ethylenediamine (EDA, 99.5%), poly-(diallyldimethylammonium chloride) (PDADMAC, MW =100000-200000), sodium hydroxide (NaOH), hydrochloric acid (HCl), sodium chloride (NaCl), nile red (NR), rose bengal (RB), fluorescein isothiocyanate (FITC), ethidium dibromide (EtBr), yeast alcohol dehydrogenase, ficoll 400, dextran 70, methoxy polyethylene glycol amine (mPEG-NH$_2$ 5000), sodium thiocyanate (NaSCN), 1,6-hexanediol, bovine serum albumin (BSA, ≥99%, essentially fatty acid-free), sodium citrate tribasic dihydrate, potassium chloride (KCl), cadmium chloride ($CdCl_2$), sodium tellurite (Na_2TeO_3), mercaptosuccinic acid (MSA), trisodium citrate dihydrate, dichloro(*p*-cymene)ruthenium(II) dimer ($[Ru(\eta^6\text{-pcymene})Cl_2]_2$) , Tris buffer, diethyl ether, alcohols, acetone, acetonitrile, dimethyl sulfoxide (DMSO), chlorohydrocarbon, sodium

methoxide (NaOMe), Hellmanex III, 3-(4,5-dimethylthiazol-2-yl)-2,5 diphenyltetrazolium bromide (MTT), and the Pur-A-Lyzert dialysis kit (molecular weight cutoff 3.5 kDa) were purchased from Sigma-Aldrich. Doxorubicin hydrochloride (>95.0%), horseradish peroxidase (HRP), glucose oxidase (GOx), rhodamine B isothiocyanate (RBITC), 4′,6-diamidino-2-phenylindole (DAPI), glucose, sucrose, maltose, lactose, mannose, hexane, trypsin, 3,3′,5,5′-tetramethylbenzidine (TMB), 2,2′-azino-bis(3-ethylbenzothiazoline-6-sulfonic acid)-diammonium salt (ABTS), and Whatman filter paper (pore size = 0.2 μm) were procured from TCI. 4-Nitrophenol (4-NP), 4-Nitroaniline (4-NA), sodium borohydride (NaBH$_4$), ethylacetate, polyethylene glycol (PEG-8000), poly-L-lysine hydrobromide (PLys), rhodamine 6G (Rh 6G), potassium bromide (KBr), and hydrogen peroxide (H$_2$O$_2$) were purchased from Loba Chemie (India). Hexadecyltrimethylammonium bromide (CTAB), sodium dodecyl sulfate (SDS), triton X-100 (TX-100), dipalmitoyl phosphatidylcholine (DPPC), adenosine triphosphate (ATP), chloroform (CHCl$_3$), phosphotungstic acid (PTA) were purchased from Alfa Aesar (India). Potassium phosphate monobasic (KH$_2$PO$_4$) was procured from Rankem (India). T-25 flasks were purchased from Corning. Minimum essential medium with Earle's balanced salt solution (MEM/EBSS), and fetal bovine serum (FBS) were procured from Hyclone. Penicillin-streptomycin, trypsin-1 mM EDTA, and glutamax were purchased from Gibco. The 96-well plates were obtained from Eppendorf. The urine sample was collected from a nondiabetic volunteer. Milli-Q water was obtained from a Millipore water purifier system (Milli-Q integral).

2.3. Synthetic procedures

2.3.1. Synthesis of CDs and PL quantum yield (QY)

Colloidal CDs were synthesized according to the previously reported hydrothermal method *[1].* In brief, 1.015 g of citric acid was first dissolved in 10 mL of Milli-Q water via sonication. After complete dissolution, 335 μL of ethylenediamine was added to it and again sonicated for 5 min (Scheme 2.1.).
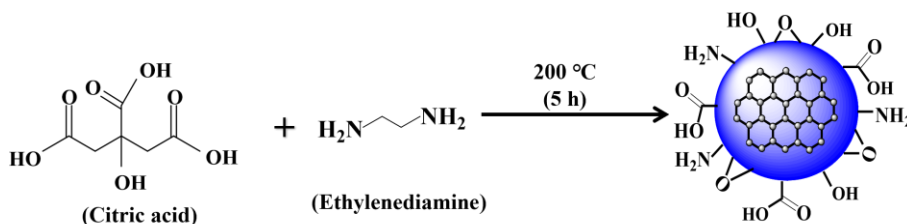
Scheme 2.1. *Synthesis of CDs.*

Then the solution was transferred to a 25 mL Teflon-padded autoclave and heated at 200 °C for 5 h. Subsequently, the reactor was cooled down to room temperature naturally, and the solution was dialyzed by using a Pur-A-Lyzer dialysis kit (MWCO 3.5 kDa) to remove excess free reactants from the reaction mixture.

The PL QY of CD was estimated by using quinine sulfate (0.1 M H_2SO_4, QY = 0.54) as a reference according to the equation;

$$\phi_{CD} = \phi_R \left(\frac{I_{CD}}{I_R}\right)\left(\frac{\eta_{QD}^2}{\eta_R^2}\right)\left(\frac{OD_R}{OD_{CD}}\right) \qquad (1)$$

Here ϕ, I, η, and OD stand for the quantum yield (QY), integrated PL intensity, refractive index of the solvent, and optical density, respectively. The subscripts "R" and "CD" stand for the reference and carbon dot sample.

2.3.2. Synthesis of [(p-cymene)Ru-(curcuminato)Cl] (Ru-Cur)

Ru-Cur was synthesized as reported previously *[2]*. The ligand HCurCI (0.1998 g, 0.504 mmol) was dissolved in MeOH (20 mL), and then NaOMe was added. The mixture was stirred for 1 h at room temperature, and further [Ru(η^6-pcymene)Cl$_2$]$_2$ (0.1543 g, 0.252 mmol) was added. The resulting solution was refluxed and stirred for 24 h.
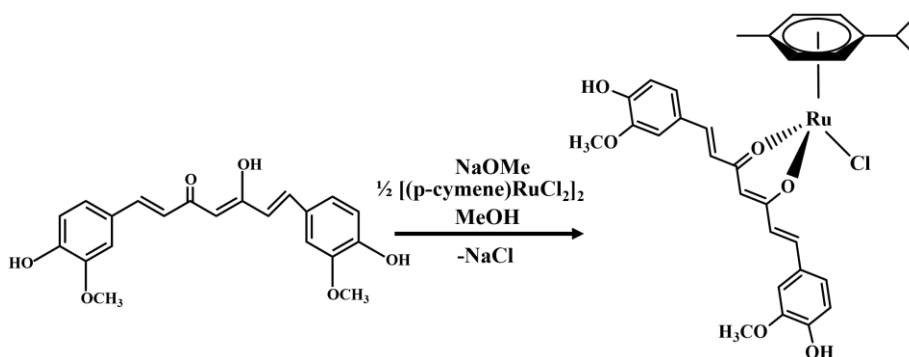
Scheme 2.2. *Synthesis of Ru-Cur.*

The solution was concentrated to a volume of ~2 mL and finally stored at 4 °C for future use. The obtained red color compound (0.3150 g, 0.473 mmol; yield 93%) was soluble in diethyl ether, alcohols, acetone, acetonitrile, dimethyl sulfoxide (DMSO), and chlorohydrocarbon solvents.

2.3.3. Synthesis of Ru-Cur-loaded small unilamellar vesicle (SUV)

SUVs were prepared by a well-known EtOH injection method, as reported previously *[3]*. In brief, 3.6 mg of DPPC was first dissolved in EtOH and injected rapidly into the pH 7.4 phosphate buffer solution, which was kept above the phase transition temperature ($T_m = 42$ °C) of the lipid for 1 h. The concentration of the lipid in the final liposome solution was 0.5 mM, and the injected EtOH was less than 1% (v/v) of the solution. The liposomal

solution was equilibrated with 5 µM Ru-Cur stock solution (1 mM) in Milli-Q water for 1 h to obtain Ru-Cur-loaded SUVs.

2.3.4. Synthesis of Ru-Cur-loaded giant unilamellar vesicle (GUV)

GUVs were prepared by an earlier-reported method with minor modification *[4]*. At first, 3.6 mg of DPPC in $CHCl_3$ and 3.2 mg of Ru-Cur in MeOH were dissolved in a 50 mL round-bottom flask. The final solvent composition was $CHCl_3$/MeOH (volume ratio 4:1). Then, the solvent was evaporated via rotary evaporation under low pressure for about 20 min to obtain a solid-matrix thin film. The residual solvent in the film was completely removed under vacuum overnight. Finally, the film was hydrated with 500 µL of buffered water (pH 7.4) in an ultrasonic bath for 15 min, with the temperature ranging from 40 to 45 °C.

2.3.5. Synthesis of Ru-Cur-loaded multilamellar vesicle (MLV)

MLVs were prepared according to an earlier-reported thin-layer evaporation technique *[5]*. Briefly, the DPPC lipid was first dissolved in $CHCl_3$ and then subsequently removed under low pressure in a rotary evaporator at 60 °C, obtaining a thin film of dry lipid on the flask wall. Evaporation was carried out for 2 h to completely remove all traces of the organic solvent. Afterwards, the film was hydrated by adding 1 mL of a $MeOH/H_2O$ mixture containing 5 µM Ru-Cur under vigorous stirring in order to favour MLV formation.

2.3.6. Synthesis of MSA-capped CdTe QDs

MSA-capped CdTe QDs were prepared according to the reported literature *[6]*. In a typical synthesis, $CdCl_2$ (0.04 M in 4 mL) was diluted to 50 mL in a one-necked flask at constant stirring. Subsequently, $C_6H_5Na_3O_7.2H_2O$ (100 mg), Na_2TeO_3 (0.01 M, 1 mL), MSA (50 mg), and $NaBH_4$ (100 mg) were added to the above mixture at room temperature. The mixture was stirred to dissolve properly for 5 minutes.
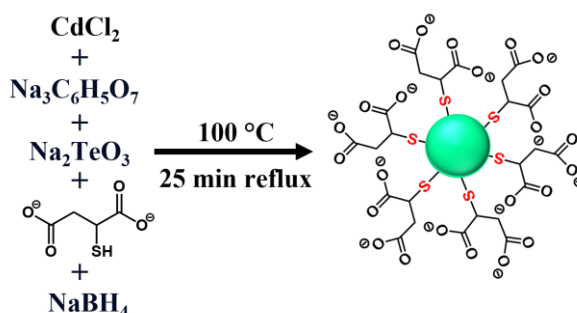
Scheme 2.3. Synthesis of CdTe QDs.

When the color of the solution changed to green, the flask was attached to a condenser and refluxed under open-air condition for 30 min in order to obtain green emissive QDs. The resulting CdTe QDs were then purified by dialysis for 24 h. The final product was stored at 4 °C in the dark for further use.

2.4. Sample preparations and experimental procedures

2.4.1. Preparation of buffer solutions

Buffer solutions with different pH values of 2, 4, 6, 7.4, 9, and 10 were prepared using Milli-Q water. The strength of each buffer solution was kept fixed at 10 mM. Hydrochloride acid potassium chloride buffer (pH 2), sodium acetate buffer (pH 4), phosphate buffer (pH 6 & 7.4), tris buffer (pH

9), and carbonate-bicarbonate buffer (pH 10) were used individually in the presence of 50 mM NaCl.

2.4.2. Preparation of Ru-Cur-loaded CTAB, TX-100, and SDS micelles

A stock solution of 1 mM Ru-Cur was prepared in a MeOH/H_2O mixture [0.1% (v/v)]. First, 3.2 mg of powdered Ru-Cur was dissolved in 500 µL of MeOH and then marked up to 5 mL with Milli-Q water. Subsequently, 5 µM Ru-Cur solution was equilibrated with different concentrations of CTAB (0-10 mM), TX-100 (0-1 mM), and SDS (0-30 mM) in Milli-Q water for 1 h before any spectroscopic and microscopic measurements.

2.4.3. Preparation of different types of coacervate droplets and turbidity measurements

2.4.3.1. CD-PDADMAC coacervate droplets

CD-PDADMAC coacervate nanodroplets (NDs) were prepared from the aqueous binary mixture of CD and PDADMAC at room temperature. The small nanodroplets (SNDs), and large nanodroplets (LNDs) were fabricated by equilibrating the aqueous mixture of 0.06 mg/mL CDs and 32 µM PDADMAC at pH 10 for 1 and 18 h, respectively. The pH was adjusted with 0.1 M NaOH. Subsequently, for turbidity measurements, the binary mixture of higher concentrations of CDs (0.12 mg/mL) and PDADMAC (64 µM) were equilibrated for 18 h. The equilibrated coacervate dispersion was purified from free CDs and PDADMAC by centrifugation (10000 rpm, 30 min). Finally, the purified droplets were further redispersed by pH 10 aqueous medium.

2.4.3.2. ATP-PDADAMAC coacervate droplets

ATP-PDADMAC coacervate droplets were prepared by equilibrating the aqueous binary mixture of 16.5 µM adenosine 5′-triphosphate (ATP) and 50 µM PDADMAC for 1 h at room temperature in Milli-Q water. After this, the coacervated phase was collected by centrifugation at 10000 rpm for 15 min and further redispersed by Milli-Q water. Similarly for another set of experiment, droplets were prepared by equilibrating the aqueous binary mixture of 8 μM ATP and 1-50 μM PDADMAC for 1 h at room temperature in aqueous buffer without and with (100, 250, 400, 600, and 750 rpm) stirring.

2.4.3.3. QD-PDADAMAC coacervate droplets

QD-PDADMAC coacervate droplets were prepared by equilibrated 170 nM of QDs and 65 µM of PDADMAC in Milli-Q water at room temperature for 3 h. The equilibrated coacervate dispersion was purified from free QDs and PDADMAC by centrifugation (10000 rpm, 30 min). Finally, the purified droplets were further redispersed in Milli-Q.

2.4.3.4. CD-PLys coacervate droplets

CD-PLys coacervate droplets were fabricated by equilibrating the aqueous binary mixture of 60 µg/mL CDs and 166.7 µM PLys for 12 h at room temperature in Milli-Q water. The coacervated phase was purified from free CDs and PDADMAC by centrifugation (10000 rpm, 30 min). Finally, the purified coacervates were further redispersed in pH 10 aqueous medium.

The turbidity of the equilibrated binary mixtures was calculated via the following equation:

$$T = 100 - (100 \times 10^{-A}) \qquad (2)$$

where T is the turbidity, and A is the absorbance at 450 or 600 nm.

2.4.4. Partitioning of solutes (dyes/drugs/enzymes) in coacervates and liposomes

Different stock solutions of 1 mM of each NR, RB, DOX, EtBr, FITC, DAPI and 5 mM of 4-NP, 4-NA were prepared in Milli-Q water. Subsequently, stock solution of 1 mM Ru-Cur was prepared in MeOH/H$_2$O mixture. Also, stock solutions of 1 mg/mL of each HRP and GOx were prepared in pH 4.0 acetate buffer and pH 7.4 phosphate buffer, respectively.

Next, 3.0 µM NR, 4.9 µM RB, 19.5 µM DOX, 87 µM EtBr, 2.6 µM FITC, 5.0 µM Ru-Cur, 20.0 µM 4-NP, and 20.0 µM 4-NA were added to the CD-coacervates separately and equilibrated overnight at room temperature. Similarly, 5 µM of each of Ru-Cur, DAPI, FITC, NR and 25 pM of HRP, GOx were added to the ATP-coacervates individually and equilibrated for 1 h at room temperature. After incubation, each of the equilibrated mixtures were centrifuged at 10000 rpm for 30 min to separate the supernatant from the coacervated phase.

Finally, the concentration of nonencapsulated solutes in the supernatant was estimated using UV-vis spectroscopy. The equilibrium partition coefficient (K) was estimated via the following equation;

$$K = \frac{[\text{Solute}]_{\text{coacervate}}}{[\text{Solute}]_{\text{Supernatant}}} \qquad (3)$$

2.4.5. Strategy for biocompatibility assay and cellular uptake

A monolayer of kidney fibroblast (BHK-21) cells was maintained in a T-25 flask using MEM/EBSS medium supplemented with 5% fetal bovine serum, 1% glutamax, and 1% penicillin-streptomycin solution. These cells were

kept in a humidified incubator at 37 °C and 5% CO_2 culture condition. After 24 h, the cells were washed twice with PBS, and fresh medium was added to the flask. On reaching 80% confluency, the cells were trypsinized with 0.25% trypsin-1mM EDTA solution and reseeded at a density of 5×10^3 cells per well in a 96 well plate for cytotoxicity assay.

The cytotoxicity of CDs, PDADMAC, and NDs was performed in triplicates by conventional MTT assay. Typically, the cultured BHK-21 cells (~5,000) were dispersed by culture medium in 96-well microtiter plates and then allowed to proliferate for the next 24 h incubated at 37 °C and 5% CO_2. After 24 h, old media was aspirated, and fresh media containing different doses of CDs, PDADMAC, and NDs were added and incubated for another 24 h. Next, 20 µL of freshly prepared 5 mg/mL MTT solution was added to each well. The cells were again incubated for 3 h followed by careful removing of media containing unreduced MTT, and the resulting insoluble violet-coloured formazan crystals were dissolved by adding 100 µL DMSO/well with shaking for 10 min at room temperature.

The absorbance value of the samples was measured at 590 nm wavelength and the cell viability were estimated according to the following equation;

$$\text{Cell viability (\%)} = \left(\frac{A_{\text{Treated}}}{A_{\text{Control}}}\right) \times 100 \qquad (4)$$

where A_{Treated} is the absorbance in the presence of sample, and A_{Control} is the absorbance in the absence of sample.

Furthermore, about 8×10^4 BHK-21 cells were seeded on a coverslip in a 6-well plate and incubated for 24 h at 37 °C and 5% CO_2 for cells to proliferate. Prior to cell seeding, coverslips were properly sterilized by

placing them in 90% ethyl alcohol for 3 h, followed by UV sterilization for 1 h. After 24 h incubation, the culture medium was aspirated, and the cells were washed twice with PBS. Next, the fresh culture medium was added, followed by the addition of different concentrations of CDs, NDs, and EtBr-loaded NDs and incubated for another 4 and 24 h. Prior to the fixation of cells on slides, the culture medium was removed, and the cells were again washed twice with PBS to remove CDs and ND residues. Thereafter, the cells were subjected to alcoholic fixation by adding 1 mL/well ice-cold methanol and kept for 10 min in -20 °C. The samples were then analyzed by using confocal laser scanning microscopy with 20 and100X objectives.

2.4.6. Estimation of loading content (LC%) and encapsulation efficiency (EE%)

For the calculation of the loading content (LC%), the Ru-Cur loaded liposomes and Ru-Cur loaded ATP-coacervates were first lyophilized separately and subsequently, their amounts were measured. The LC% was calculated using the following equation;

$$LC\ (\%) = \left(\frac{W_t}{W_m}\right) \times 100\% \qquad (5)$$

Similarly, for the estimation of encapsulation efficiency (EE%), the concentration of nonencapsulated Ru-Cur or enzymes were measured spectroscopically at their respective absorption maxima. The EE% was calculated using the following equation;

$$EE\ (\%) = \left(\frac{W_t}{W_i}\right) \times 100\% \qquad (6)$$

where W_t is the amount of loaded Ru-Cur or enzymes in liposomes or coacervates, W_m is the amount of Ru-Cur-loaded liposomes or Ru-Cur

loaded ATP-coacervates, and W_i is the amount of the initially added Ru-Cur or enzymes.

2.4.7. Release of Ru-Cur from liposomes and ATP-Coacervates

The release profiles of Ru-Cur from SUV of DPPC liposomes and ATP-coacervates were studied at different pH values of 7.4, 6.5, 6, and 5 at 37 °C in 10 mM phosphate-buffered saline (PBS). Aqueous dispersions (5 mL) of loaded liposomes and coacervates were sealed in dialysis bags (MWCO = 3.5 kDa). These dialysis bags were placed in beakers containing 45 mL of a PBS solution of different pH values and kept in a water bath at particular temperature with constant stirring (200 rpm). Aliquots (1 mL) from each sample were periodically removed for spectrophotometric analysis ($\lambda_{abs} = 425$ nm) and replenished with 1 mL of PBS of the same pH.

The cumulative release percentage (E_r) was calculated by using the following equation;

$$E_r = \frac{5 \times \sum_1^{n-1} C_i + 50 \times C_n}{m_{Ru-cur}} \times 100\% \qquad (7)$$

where $m_{Ru\text{-}Cur}$ is the amount of loaded Ru-Cur in the liposomes or ATP-coacervates, C_i is the concentration of Ru-Cur in the ith sample, and C_n is the concentration of Ru-Cur in the PBS solution.

2.4.8. Catalytic activity of CD, CD-NDs, ATP-NDs and mixed NDs toward redox reactions

All the reduction kinetics were performed in a 4 mL quartz cuvette using Varian Cary UV-vis spectrophotometer. To study the catalytic efficacy, CD and both the coacervates were first incubated with the desired substrate for 1 h separately in order to obtain the substrate-loaded nanoreactor at room temperature. The equilibrated coacervate dispersions were purified from the

free substrate using centrifugation at 10000 rpm for 30 min and then redispersed in pH 10 aqueous medium. Each of the reaction mixture was then transferred into the glass cuvette and then purged with N_2 gas for 15 min. Time-resolved UV-vis spectra were recorded immediately after the addition of freshly prepared $NaBH_4$ solution to monitor the progress of reaction in case of 4-NP and 4-NA.

2.4.8.1. 4-NP reduction

 The time-dependent reduction of 4-NP was performed inside the compartmentalized environment of CD-NDs. 20 µM of 4-NP was loaded inside the CD- NDs ([CD] =1 µg/mL) followed by N_2 purging. The reaction progress was tracked using UV-vis spectrophotometer as a function of time just after the addition of 10 mM $NaBH_4$ inside the reaction mixture. The total volume of the reaction mixture was 3 mL and the color of the solution changed gradually from yellow to colorless, indicating the completion of reduction reaction. A control experiment was also carried out with CD and ATP-NDs by following the same procedure as used for CD-NDs.

2.4.8.2. 4-NA reduction

The catalytic reduction of 4-NA was also performed by following the above-mentioned procedure as used for 4-NA. In brief, 20 µM 4-NA was loaded inside the CD-NDs ([CD] = 2 µg/mL) followed by N_2 purging, and then 10 mM $NaBH_4$ was added immediately to start the reaction. The reaction progress was tracked by monitoring the reaction mixture in UV-vis spectrophotometer as a function of time. Subsequently, a control experiment was also carried out with the bare CD.

2.4.8.3. Mixed population of NDs

To illustrate the spatiotemporal control of the reduction kinetics, ATP-NDs were first loaded with 20 µM 4-NP and then mixed with equal volume (1.5 mL) of CD-embedded hybrid NDs. The progress of reaction was monitored using UV-vis signal at 400 nm in two-time regimes, just after the mixing of ATP-NDs with CD-NDs and after equilibrating the mixed coacervate phase for 12 h. For confocal microscopy experiment, ATP-NDs were first labeled with Rh 6G and then mixed with CD-embedded NDs.

2.4.9. Recyclability test for CD-NDs

For the recyclability experiment, the fabricated CD-NDs were examined for six consecutive cycles by taking CD concentration of 2 µg/mL. After the completion of the reaction during first cycle, the coacervate phase having 4-AP-loaded NDs was separated from the bulk aqueous phase via centrifugation (10,000 rpm, 30 min). After centrifugation, the coacervate phase was re-dispersed with equal volume (3 mL) of Milli-Q water (pH 10) and subjected to solvent extraction with ethylacetate in a separating funnel. Afterwards, the separated ethylacetate phase was evaporated to yield 4-AP and the bulk phase having bare NDs was utilized for next cycle. The same procedure was followed for subsequent cycles. The k_{app} and conversion yield (%) were calculated for each cycle which are discussed in section 2.4.10.

2.4.10. Estimation of k_{app} and conversion yield (%)

The apparent rate constants were calculated by following the decrease in the absorbance value of substrates at their respective peak positions (λ_{max}). The λ_{max} for 4-NP, and 4-NA is 400 nm, and 380 nm respectively. The

concentration (C) vs. time (t) plot was fitted according to the first order kinetics whose equation is as follows;

$$C_t = C_0(1 - e^{-kt}) \qquad (8)$$

Taking $\log_e$ on both sides and rearranging *[7]*,

$$-\ln\left(\frac{C_t}{C_0}\right) = kt \qquad (9)$$

where C_0 is the initial concentration of substrate, C_t is the concentration of substrate at any time t during the reduction process, and k is the first-order reaction rate constant.

Conversion yield (%) was calculated by monitoring the percentage of decrease in the absorption of substrate at λ_{max} after completion of the reduction reaction and the equation is as follows;

$$\text{Conversion yield} = \left(\frac{C_0 - C_t}{C_0}\right) \times 100\% \qquad (10)$$

where C_0 is the concentration of substrate at initial time $t = 0$ and C_t is the concentration of substrate at any time t during the reduction reaction.

2.4.11. Variation in the concentrations of 4-NP, NaBH₄, hybrid NDs, and temperature effect

The progress of 4-NP reduction reaction was monitored by measuring the UV-vis changes at 400 nm with time.

2.4.11.1. Variation in 4-NP concentration

Time-dependent variation in reduction processes were observed by varying the concentration of 4-NP (5, 10, 20, 40, 60 and 200 µM) in the presence of

same concentration of CD-NDs ([CD] = 1 µg/mL) and NaBH$_4$ (10 mM) for each spectroscopic measurement.

2.4.11.2. Variation in NaBH$_4$ concentration

Time-dependent variation in reduction processes were observed by varying the concentration of NaBH$_4$ (2, 4 & 10 mM for both 4-NP & 4-NA) in the presence of CD-NDs ([CD] = 1 µg/mL for 4-NP & [CD] = 2 µg/mL for 4-NA) and nitroarenes (20 µM) for each spectroscopic measurement.

2.4.11.3. Variation in hybrid NDs concentration

Time-dependent variation in reduction processes were also observed by varying the concentration of coacervate NDs ([CD] = 1, 2, and 4 µg/mL) in the presence of same concentration of 4-NP (20 µM) and NaBH$_4$ (10 mM) for each spectroscopic measurement.

2.4.11.4. Variation in temperature and calculation of thermodynamic parameters

Temperature-dependent kinetic measurements were performed at four different temperatures (T = 290, 298, 303, 308) via keeping the reaction temperature constant by thermostatically controlled water bath inside CD-NDs ([CD] = 1 µg/mL) in the presence of 4-NP (20 µM), and NaBH$_4$ (10 mM).

The relationship between reaction rate constant *k* and temperature, *T* is given by the Eyring equation as follows;

$$\ln\left(\frac{k}{T}\right) = \frac{-\Delta H}{R}\left(\frac{1}{T}\right) + \ln\frac{k_B}{h} + \frac{\Delta S}{R} \qquad (11)$$

where k is the reaction rate constant, ΔG is the Gibbs free energy of activation, ΔH is the enthalpy of activation, ΔS is the entropy of activation, k_B is the Boltzmann's constant, and h is the Planck's constant.

We first plotted $\ln(k/T)$ versus $(1/T)$, where the slope is $-\Delta H/R$. The activation enthalpy, ΔH was calculated as $-(\text{slope} \times R)$ in units of J mol^{-1} ($R = 8.31451$ J K^{-1} mol^{-1}). The activation entropy, ΔS was calculated from the intercept of the plot $\ln(k/T)$ versus $(1/T)$ using the following equation;

$$\Delta S = \left(intercept - ln\left(\frac{k_B}{h}\right)\right) \times R \qquad (12)$$

and Gibbs free energy of activation, ΔG was calculated using the thermodynamic equation;

$$\Delta G = \Delta H - T\Delta S \qquad (13)$$

Activation energy, E_a and pre-exponential factor, A were calculated using the Arrhenius equation;

$$k = Ae^{(-Ea/_{RT})} \qquad (14)$$

2.4.12. Preparation of crowder and substrate solutions

10% (w/v) PEG, 10% (w/v) dextran, and 12.5% (w/v) Ficoll were prepared from a stock solution of 40% (w/v) PEG 8000, 40% (w/v) dextran 70, and 40% (w/v) Ficoll 400, respectively. 20 mg/mL BSA was prepared from the stock solution of 332 mg/mL BSA.

Stock solution of 20 mM TMB was prepared in DMSO, while the stock solutions of 20 mM OPD and 20 mM ABTS were prepared in Milli-Q water. The stock solutions of these substrates were used immediately after preparation.

2.4.13. Prediction of LCDs and IDRs of HRP and GOx

To predict the low complexity domains (LCDs) in the HRP and GOx, we used Simple Molecular Architecture Research Tool (SMART) (http://smart.embl-heidelberg.de/) *[8]* and for disorder regions (IDRs) IUPred2 (https://iupred2a.elte.hu/) *[9]* were used. IUPred2 data were then plotted using the OriginPro 8.1 software.

2.4.14. Labeling of enzymes and crowders with fluorescent dyes

The concentration of enzymes was estimated spectrophotometrically using the reported extinction coefficients of 1.02×10^5 M^{-1} cm^{-1} ($\lambda = 403$ nm) for HRP, 4.41×10^4 M^{-1} cm^{-1} ($\lambda = 280$ nm) for GOx, 8.80×10^2 M^{-1} cm^{-1} ($\lambda = 253$ nm) for trypsin, and 1.89×10^5 M^{-1} cm^{-1} ($\lambda = 280$ nm) for alcohol dehydrogenase. HRP and alcohol dehydrogenase were labeled with RBITC, whereas GOx and trypsin were labeled with FITC according to an earlier reported method *[10]*. In brief, 25 pM or 0.5 μM of each HRP and GOx were mixed with RBITC and FITC, respectively, in a molar ratio of 1:10 ([Enzyme]:[Dye]). Similarly, 60 nM alcohol dehydrogenase and 42 nM trypsin were mixed with RBITC and FITC, respectively in a molar ratio of 1:10 ([Enzyme]:[Dye]). These enzyme-dye mixtures were incubated for 4 h at room temperature followed by 6 h at 4 °C with constant stirring (500 rpm). After completion of the reaction, the excess dye was removed by dialysis (molecular weight cutoff 3.5 kDa) against 10 mM PBS at 4 °C for 12 h. Finally, the labeled enzymes were stored at 4 °C. The estimated labeling efficiency of HRP and GOx is found to be 77.3 and 84.1%, respectively. The same procedure was followed for the labeling of mPEGNH$_2$ and BSA with RBITC.

2.4.15. Phase separation assays in the presence of crowders

0.5 µM HRP and 0.5 µM GOx were incubated individually with 10% PEG, 12.5% Ficoll 400, 10% dextran 70, and 20 mg/mL BSA at 37 °C for 1 h. The effect of incubation time on droplet formation was monitored by varying the equilibration time (5, 15, 30, and 60 min) after the mixing of 10% PEG with the fluorescently labeled HRP and GOx. Also, the droplet formation in the presence of 10% PEG was monitored under different conditions by varying temperature (4, 37, 70, 80, and 90 °C), pH (4, 7.4, 9, and 10), NaCl concentration (50, 500, 1000, 2000, and 3000 mM), NaSCN concentration (0.5, 1, 2, and 3 M), and 1,6-hexanediol concentration (1, 3, 6, and 10%) upon 1 h of incubation.

2.4.16. Enzymatic assays

2.4.16.1. pH-dependent enzymatic activity of HRP and GOx in aqueous buffer

The concentration of HRP and GOx was kept fixed at 25 pM for all the kinetic experiments. All the enzymatic assays were performed in triplicates ($n = 3$) at 37 °C. The optimum activity of HRP and GOx was estimated in the aqueous buffer as a function of pH in the range of 2-10 at 37 °C with TMB (0-1000 μM) and glucose (0-300 mM) as substrate, respectively. HRP catalyzed reactions were monitored using UV-vis spectrophotometer immediately just after the addition of 8.8 mM H_2O_2 via recording the absorbance of oxidized TMB at 650 nm. GOx activity was measured according to the earlier report *[11]*. After purging O_2 gas for 15 min into the reaction mixtures, the kinetics were monitored immediately after the addition of different concentrations of glucose. The final product, gluconic acid, was assayed by reaction with hydroxylamine and subsequent

complexation with Fe^{3+}, which led to a red colored complex, hydroxamate-Fe^{3+} (λ_{max} = 505 nm).

2.4.16.2. Enzymatic assay of HRP at optimum pH

HRP shows optimum activity at pH 4.0 *[12]*. Therefore, all of the enzymatic assays of HRP were performed in pH 4 acetate buffer. At first, droplets were prepared by equilibrating the aqueous binary mixture of 8 μM ATP and 25 μM PDADMAC for 1 h in pH 4 acetate buffer with constant stirring (250 rpm) at 37 °C. Next, 25 pM of HRP was added into the droplet and incubated for 1 h at 37 °C. Afterwards, varying concentrations of substrates TMB (0-1000 μM), ABTS (0-1000 μM), and OPD (0-1000 μM) were added separately and further incubated for 1 h at 37 °C. Finally, the reaction kinetics corresponds to each substrate was monitored via UV-vis spectroscopy immediately after the addition of 8 mM H_2O_2. Control experiments were also performed in the absence of droplet by following the same procedure.

2.4.16.3. Enzymatic assays before phase separation in the presence of crowders

Enzyme kinetics before the phase separation were followed instantly after the addition of enzymes into the aqueous solution of substrate and different crowders (10% PEG, 10% dextran, 12.5% Ficoll, and 20 mg/mL BSA). The kinetics of HRP and GOx were monitored at their optimum pH values of 4 and 7.4, respectively. All the data points were analysed as mean ± s.e.m. Statistical analyses were performed via a two-tailed, unpaired Student's *t*-test with ***, *P* value < 0.001; **, *P* value < 0.01, and not significant (NS), *P* > 0.05, using Excel software.

2.4.16.4. Enzymatic assays after phase separation

Enzyme kinetics after the phase separation were performed in three different sets. In the first set, enzymes were allowed to undergo phase separation in the presence of different crowders for 1 h. Subsequently, HRP and GOx kinetics were monitored instantly after the addition of respective substrates. In the second set, the kinetics of phase separated HRP were monitored after the addition of TMB (0-1000 μM) in a time-dependent manner. Reactions were initiated after the addition of 8.8 mM H_2O_2 at a definite time interval (5-120 min). The enzymatic activity of HRP in the presence of 10% PEG was also monitored with OPD (0-1000 μM) and ABTS (0-1000 μM) in pH 4 acetate buffer via recording the absorbance at 420 and 450 nm, respectively. In the third set, HRP was first allowed to bind with TMB (0-1000 μM) in pH 4 aqueous buffer at 37 °C for 30 min. Subsequently, substrate bound HRP was mixed with 10% PEG and incubated further for 15 min at 37 °C. Finally, reaction was initiated after the addition of 8.8 mM H_2O_2 into the reaction mixture.

2.4.16.5. Cascade reaction in the presence of crowders

25 pM HRP and 25 pM GOx were incubated individually with either 10% PEG or 20 mg/mL BSA for 1 h at 37 °C in pH 4 acetate buffer and pH 7.4 phosphate buffer, respectively. Subsequently, both the solutions were mixed by taking equal volumes from each solution. Next, 1 mM of a substrate either TMB, OPD, or ABTS was added and further allowed to equilibrate for 1 h at 37 °C. Afterwards, the reaction mixture was purged with O_2 gas for 15 min. Finally, the absorbance values of oxidized substrates were recorded immediately after the addition of 1 mM glucose. Similarly, control experiments without crowders were performed under the same experimental conditions.

2.4.16.6. Cascade assay in ATP-coacervates

Cascade assays were performed at an optimum pH value of 6 in phosphate buffer *[12]*. 25 pM GOx, 25 pM HRP, and 1 mM TMB were added into the aqueous dispersion of droplets in pH 6 phosphate buffer and incubated for 1 h at 37 °C. Next, the reaction mixture was purged with oxygen (O_2) gas for 15 min. Finally, the absorbance of oxidized TMB (ox-TMB) was recorded at 650 nm immediately after the addition of 1 mM glucose. Control experiments were also performed in the absence of droplet, glucose, GOx, O_2, HRP, and TMB. Similarly, control experiments with 1 mM sucrose, 1 mM maltose, 1 mM lactose, and 1 mM mannose were also performed inside the droplets.

2.4.16.7. Estimation of enzyme activity

The enzyme activity was estimated by using the following equation *[13]*;

$$\text{Enzyme activity } (\mu\text{mol } min^{-1}\text{mL}^{-1}) = \frac{(\Delta A)\times(\text{Volume of reaction})\times 1000}{\varepsilon\times t\times V} \quad (15)$$

Here, ΔA is the difference in absorbance of test and blank sample at 650 nm, ε is the molar absorption coefficient of TMB at 650 nm (39 000 M^{-1} cm^{-1}), t is the total time taken for completion of the reaction (15 min), and V is the volume of enzyme taken (3 μL).

2.4.17. Glucose sensing and estimation of limit of detection (LOD)

2.4.17.1. In solution phase

To test the colorimetric response of GOx/HRP@Droplet toward glucose sensing in solution, 1 mM TMB was loaded inside the enzyme-sequestered droplet (25 pM GOx and 25 pM HRP) in pH 6 phosphate buffer. The aqueous droplet mixtures were equilibrated for 1 h at 37 °C and then purged

with O_2 gas for 15 min. Subsequently, the absorbance of ox-TMB was monitored at 650 nm immediately after the addition of different concentrations of glucose (0-100 μM).

2.4.17.2. In Whatman filter paper and commercial strip

Droplets loaded with 25 pM GOx, 25 pM HRP, and 1 mM TMB were deposited on Whatman filter papers and dried at 37 °C. Subsequently, the composite-loaded filter papers were soaked in glucose solutions (purged with O_2 gas for 15 min) of different concentrations. A commercial strip was dipped inside the spiked urine sample for 5 min and then photographs were taken.

2.4.17.3. In spiked urine samples

The collected urine sample was first centrifuged at 20000 rpm for 30 min and then the supernatant was diluted 10 times using pH 7.4 phosphate buffer. Droplets were loaded with 25 pM GOx, 25 pM HRP, and 1 mM TMB. The reaction mixture was purged with O_2 gas for 15 min and then 50 μL of spiked urine sample (0.2- and 0.5-mM glucose) was added inside the reaction mixture. Finally, the UV-vis absorption spectra were recorded. Control experiments were performed in the absence of droplets.

For glucose sensing on filter paper, composite-loaded filter papers were dipped inside the purged unspiked and spiked urine samples and then dried at 37 °C for 2-3 min. Finally, the photographs of dried filter papers were captured. Similarly, the composite-loaded filter paper was kept at room temperature for 7 days to check the colorimetric response.

LOD for glucose sensing was estimated using the following equation:

$$\text{LOD} = 3\left(\frac{\text{SD}}{\text{Slope}}\right) \qquad\qquad (16)$$

Here, SD is the standard deviation of blank droplet solution over three independent measurements, and the slope was estimated from the linearized plot between absorbance versus glucose concentrations. The SD value was estimated to be 0.000163.

2.4.18. Stability of enzymes

25 pM GOx and 25 pM HRP was added into the aqueous dispersion of droplets in pH 6 phosphate buffer and incubated for 1 or 50 days at 37 °C. Next, 1 mM TMB was added and allowed to equilibrate for 1 h at 37 °C. Finally, the reaction mixture was purged with O_2 gas for 15 min and the absorbance of ox-TMB was recorded at 650 nm immediately after the addition of 1 mM glucose. The GOx/HRP cascade activity was compared in bulk solution and within the droplets upon 50 days of storage. Similarly, to examine the biological stability, 5 ng/mL trypsin was added to the GOx/HRP-sequestered droplets (pH 6 phosphate buffer) and allowed to react for 48 h. Afterwards, 1 mM TMB was added and equilibrated for 1 h at 37 °C. Finally, the reaction mixture was purged with O_2 gas for 15 min and the absorbance of ox-TMB was recorded at 650 nm immediately after the addition of 1 mM glucose. A control experiment was also performed in bulk aqueous medium to evaluate the activity of GOx/HRP cascade pair in the presence of the same amount of trypsin.

2.4.19. Recyclability test for ATP-coacervates

To check the recyclability of the present bioplatform, reactions were monitored for five consecutive cycles. For the first cycle, droplets were equilibrated with 25 pM GOx, 25 pM HRP, and 1 mM TMB for 1 h at 37

°C. The reaction mixture was purged with O_2 gas for 15 min. Next, 1 mM glucose was added and kept for 15 min at 37 °C. After 15 min, the UV-vis absorption spectrum was recorded, and the activity was calculated. The coacervate phase containing ox-TMB was separated from the bulk aqueous phase via centrifugation (10000 rpm; 30 min). After centrifugation, the coacervate phase was redispersed with equal volume (3 mL) of pH 4 acetate buffer and subjected to solvent extraction with hexane in a separating funnel to remove ox-TMB. Afterwards, the aqueous phase containing bare droplets was utilized for the next cycle. The same procedure was followed for the subsequent cycles.

2.4.20. Estimation of Michaelis-Menten parameters

The absorbance values obtained from UV-vis spectrometer were plotted as a function of time using OriginPro 8.1 software, and then the data were linearly fitted for each concentration. The initial rates were calculated by considering the molar extinction coefficient of oxidized TMB ($\varepsilon_{650 \text{ nm}} = 39000 \text{ M}^{-1} \text{ cm}^{-1}$), ABTS ($\varepsilon_{420 \text{ nm}} = 36000 \text{ M}^{-1} \text{ cm}^{-1}$), and OPD ($\varepsilon_{420 \text{ nm}} = 18700 \text{ M}^{-1} \text{ cm}^{-1}$). The extinction coefficients were assumed to be same in different crowder solutions under dilute conditions *[14]*. The estimated initial rates were plotted against substrate concentrations. These data were finally fitted with the Michaelis-Menten equation according to the following expression:

$$V_0 = \frac{V_{max}\,[S]}{K_m + [S]} \qquad (17)$$

where V_0 is the initial velocity, [S] is the molar concentration of substrate, V_{max} is the maximum velocity, and K_m is the Michaelis constant. We used nonlinear curve fit analysis in OriginPro 8.1 software to estimate the fitted parameters V_{max} and K_m. Finally, the catalytic rate constant (k_{cat}) was calculated by dividing V_{max} by the total enzyme concentration used.

2.5. Instrumentations

2.5.1. Ultraviolet-visible (UV-vis) spectroscopy

Absorption spectra and reaction kinetics were monitored in a quartz cuvette (1 cm × 1 cm) using Varian UV-vis spectrophotometer (Cary 100 Bio) and PerkinElmer UV/vis/NIR spectrometer. The concentration of analyte with known molar extinction coefficient at a particular wavelength was determined using Beer-Lambert law as given below,

$$A = log\frac{I_0}{I} = \varepsilon cl \qquad (18)$$

where, A is absorption, I_0 is the intensity of incident light, I is the intensity of transmitted light, ε is the molar extinction coefficient, c is the molar concentration of the sample, l is the optical path length of the sample cell.

2.5.2. Photoluminescence (PL) spectroscopy

The emission spectra were recorded in a quartz cuvette (1 cm × 1 cm) using Fluoromax-4 spectrofluorometer (Horiba Jobin Yvon, model FM-100) with excitation and emission slit widths at 5 nm.

2.5.3. Time correlated single-photon-counting technique (TCSPC)

TCSPC was used for the estimation of PL lifetime. For the lifetime measurements, fluorescence decay traces were recorded on a Horiba Jobin Yvon picosecond time correlated single-photon-counting (TCSPC) spectrometer (model Fluorocube-01-NL). The samples were excited at 405 nm by a picosecond diode laser (DD-450L). The decay traces were collected with the emission polarizer at a magic angle 54.7° by a photomultiplier tube (TBX-07C). The instrument response function [IRF; full width at half-maximum (fwhm) ~140 ps] was recorded using a dilute Ludox solution.

The PL decay traces were analyzed using IBH DAS 6.0 software by the iterative reconvolution method, and the goodness of fit was judged by the iterative reconvolution method, and the goodness of the fit was judged by reduced χ-square (χ^2) value. All the decays wee fitted as a sum of n-exponential function,

$$F\,(t) = \sum_{i=1}^{n} a_i \exp(-t/\tau_i) \tag{19}$$

where $F(t)$ denotes normalized PL decay, τ_i and a_i are the ith lifetime and the corresponding pre-exponential factor, respectively. The average lifetime was obtained from the equation,

$$\tau_{avg} = \sum_{i=1}^{n} a_i \tau_i \tag{20}$$

The decay profiles were fitted with a multiexponential function according to the earlier-reported literature *[15]*.

2.5.4. Confocal laser scanning microscopy (CLSM)

The CLSM images were captured with an inverted confocal microscope (Olympus fluoView, model FV1200MPE, IX-83) using an oil immersion objective (20X and 100X). Diode laser sources at 405, 488, and 559 nm were used to excite the samples using appropriate dichroic and emission filters (blue channel: 410-480 nm; green channel: 490-550 nm; and red channel: 560-650 nm) in the optical path. A 20 µL aliquot of the sample solution was drop-cast onto cleaned glass slides and sandwiched with Blue Star coverslip. Finally, the sides of the coverslips were sealed with commercially available nail paint, and then images were captured.

2.5.5. Field-emission scanning electron microscopy (FESEM)

The FESEM images were captured using Supra 55 Zeiss field-emission scanning electron microscope. For FESEM measurements, samples were drop-casted on a cleaned glass slide and overnight in a desiccator. The dried samples were initially coated with gold prior to use.

2.5.6. Energy-dispersive X-ray analysis (EDX)

EDX analysis were performed using a Supra 55 Zeiss field emission scanning electron microscope.

2.5.7. Circular dichroism (CD) spectroscopy

CD spectra of various enzymes with very low concentration were recorded by a JASCO J-815 CD spectropolarimeter using a quartz cell of 1 mm path length. Scans were recorded from 190 to 260 nm and 380 to 430 nm at 37 °C with a slit width of 1 mm and a speed of 50 nm/min.

2.5.8. Atomic force microscopy (AFM)

AFM images were captured on a cleaned glass coverslip and mica surface in a noncontact mode using a scanning probe AIST-NT microscope (model SmartSPM-1000). The samples were deposited on the coverslip by spin-coating at 750 rpm for 3 minutes.

2.5.9. Transmission electron microscopy (TEM)

TEM measurements were performed using a 200 kV UHR FEG-TEM, JEOL JEM 2100F and 300 kV UHR FEG-TEM, FEI Tecnai G2, F30 field-emission scanning electron microscopes. For diluted SUVs, the sample was drop-casted on carbon-coated copper grid and the excess sample was removed by filter paper. Subsequently, sample was negatively stained with

one drop of 1% (w/v) PTA for 2 min. Finally, the excess staining agent was removed by washing with Milli-Q water and the sample was air dried at room temperature.

2.5.10. Zeta-potential (ζ) measurements

All the samples for ζ-potential experiments were prepared in Milli-Q water, which was filtered through a 0.22 μm syringe filter. The ζ-potential measurements were performed on particle analyzer (model-Litesizer 500 and Nanoplus-3).

2.5.11. Liquid chromatography-mass spectrometry (LC-MS)

Mass spectrum was recorded using an electrospray ionization (ESI) quadrupole time-of-flight liquid chromatography-mass spectrometer (Bruker Daltonik) in MeOH as the solvent by positive-ion mode ESI.

2.5.12. Gas chromatography-mass spectrometry (GC-MS)

GC-MS spectra of different samples were recorded using a Shimadzu GC-MS, QP2010 mass spectrometer.

2.5.13. Fourier transform infrared (FTIR) spectroscopy

FTIR technique was used for the confirmation of different functional groups present on the surfaces of nanoparticles. All spectra were recorded in a KBr pellet using a Bruker spectrometer (Tensor-27) in the range of 800 to 4000 cm^{-1}.

2.5.14. Powder X-ray diffraction (PXRD)

PXRD pattern was recorded on a Rigaku SmartLab, an automated multipurpose X-ray diffractometer with a Cu Kα source (the wavelength of X-rays was 0.154 nm).

2.5.15. X-ray photoelectron spectroscopy (XPS)

XPS measurements were performed using an Al Kα surface analysis ESCA+ omicron nano technology-based X-ray photoelectron spectrophotometer. The chamber pressure during the XPS measurements was 1×10^{-8} Torr.

2.5.16. Raman spectrometer

Raman spectrum was recorded by using the LabRam HR Evolution spectrometer (HORIBA Scientific) with an excitation wavelength of 633 nm.

2.5.17. Nuclear magnetic resonance (NMR)

NMR spectra of different samples were recorded using an AV III 400 Ascend Bruker BioSpin machine taking DMSO-d^6 as a solvent at ambient temperature.

2.6. References

1. Bhattacharya A., Chatterjee S., Prajapati R., Mukherjee T. K. (2015), Size-dependent penetration of carbon dots inside the ferritin nanocages: evidence for the quantum confinement effect in carbon dots, Phys. Chem. Chem. Phys., 17(19), 12833–12840. (DOI:10.1039/C5CP00543D)

2. Caruso F., Pettinari R., Rossi M., Monti E., Gariboldi M. B., Marchetti F., et al. (2016), The in vitro antitumor activity of arene-ruthenium(II) curcuminoid complexes improves when decreasing curcumin polarity, J. Inorg. Biochem., 162, 44–51. (DOI:10.1016/j.jinorgbio.2016.06.002)

3. Mohapatra M., Mishra A. K. (2011), Photophysical behavior of fisetin in dimyristoylphosphatidylcholine liposome membrane, J. Phys. Chem. B, 115(33), 9962–9970. (DOI:10.1021/jp1123212)

4. Parigoris E., Dunkelmann D. L., Murphy A., Wili N., Kaech A., Dumrese C., et al. (2020), Facile generation of giant unilamellar vesicles using polyacrylamide gels, Sci. Rep., 10(1), 4824. (DOI:10.1038/s41598-020-61655-2)

5. Maestrelli F., González-Rodríguez M. L., Rabasco A. M., Mura P. (2006), Effect of preparation technique on the properties of liposomes encapsulating ketoprofen–cyclodextrin complexes aimed for transdermal delivery, Int. J. Pharm., 312(1–2), 53–60. (DOI:10.1016/j.ijpharm.2005.12.047)

6. Zhang L., Zou X., Ying E., Dong S. (2008), Quantum dot electrochemiluminescence in aqueous solution at lower potential and its sensing application, J. Phys. Chem. C, 112(12), 4451–4454. (DOI:10.1021/jp7097944)

7. Zhang J., Wang L., Shao Y., Wang Y., Gates BC., Xiao F. (2017), A Pd@Zeolite Catalyst for nitroarene hydrogenation with high product selectivity by sterically controlled adsorption in the zeolite micropores, Angew. Chem. Int. Ed., 56(33), 9747–9751. (DOI:10.1002/anie.201703938)

8. Schultz J., Milpetz F., Bork P., Ponting C. P. (1998), SMART, a simple modular architecture research tool: Identification of signaling domains, Proc. Natl. Acad. Sci. U.S.A., 95(11), 5857–5864. (DOI:10.1073/pnas.95.11.5857)

9. Erdős G., Dosztányi Z. (2020), Analyzing protein disorder with IUPred2A, Curr. Protoc. Bioinform., 70(1) (DOI:10.1002/cpbi.99)

10. Ray S., Singh N., Kumar R., Patel K., Pandey S., Datta D., et al. (2020), α-Synuclein aggregation nucleates through liquid–liquid phase separation, Nat. Chem., 12(8), 705–716. (DOI:10.1038/s41557-020-0465-9)

11. Luo W., Zhu C., Su S., Li D., He Y., Huang Q., et al. (2010), Self-catalyzed, Self-limiting growth of glucose oxidase-mimicking gold nanoparticles, ACS Nano, 4(12), 7451–7458. (DOI:10.1021/nn102592h)

12. Saini B., Mukherjee T. K. (2023), Biomolecular condensates regulate enzymatic activity under a crowded milieu: Synchronization of liquid–liquid phase separation and enzymatic transformation, J. Phys. Chem. B, 127(1), 180–193. (DOI:10.1021/acs.jpcb.2c07684)

13. Weiß R., Gritsch S., Brader G., Nikolic B., Spiller M., Santolin J., et al. (2021), A biobased, bioactive, low CO_2 impact coating for soil improvers, Green Chem., 23(17), 6501–6514. (DOI:10.1039/D1GC02221K)

14. Aumiller W. M., Davis B. W., Hatzakis E., Keating C. D. (2014), Interactions of macromolecular crowding agents and cosolutes with small-molecule substrates: Effect on horseradish peroxidase activity with two different substrates, J. Phys. Chem. B, 118(36), 10624–10632. (DOI:10.1021/jp506594f)

15. Vaishnav J. K., Mukherjee T. K. (2017), Tuning of resonance energy transfer from 4′,6-diamidino-2-phenylindole to an ultrasmall silver nanocluster across the lipid bilayer, Phys. Chem. Chem. Phys., 19(40), 27305–27312. (DOI:10.1039/C7CP05225A)

Chapter 3

> ***Biocompatible pH-Responsive Luminescent Coacervate Nanodroplets toward Theranostic Applications***

Chapter 3

3.1. Introduction

The fabrication of multifunctional inherently luminescent robust self-assembled nanocomposites has gained tremendous importance due to their vast potential in various biomedical research fields *[1, 2]*. In this context, a diverse range of self-assembled composite nanomaterials such as hybrid liposomes *[3]*, polymersomes *[4]*, plasmonic vesicles *[5]*, dendrimer nanoparticles (NPs) *[6]*, hydrogels *[7]*, metal−organic frameworks (MOFs) *[8]*, polymeric nanoparticles (PNPs) *[9]*, and coacervate droplets *[10]* has been designed. Among these, conventional liposome-based nanocarriers has made a significant advancement due to their simple phospholipid containing flexible and dynamic bilayer structure, which mimic the cell membrane *[11]*. Although they can encapsulate hydrophilic, hydrophobic, and amphiphilic drug molecules, they often show poor drug loading, short retention time, and immediate leakage of encapsulated drugs *[6, 11]*. In this context, coacervate droplets offer unique advantages over others due to their inherent membrane-free crowded environment and preferential sequestration of a wide range of solutes including proteins, enzymes, and deoxyribonucleic acid (DNA) and may find tremendous importance in protein and DNA-based therapeutics *[12, 13]*.

In the recent past, extensive efforts have been made to understand the self-assembly mechanism between a diverse range of oppositely charged molecules such as fatty acids, synthetic and natural polymers, poly- or oligopeptides, biological macromolecules, and small surfactants and mono-nucleotides *[14–29]*. While the potential applications of coacervate droplets toward bioreactors and model protocell systems have been well documented, very less is known about their role as nanocarrier in theranostic applications. Moreover, it is always advantageous to have

inherently luminescent biocompatible coacervate droplets for bioimaging applications to avoid interference from excess external fluorescent markers. Therefore, to fill these gaps, our main objective in the present study is to fabricate a unique class of self-assembled inherently-luminescent biocompatible coacervate nanodroplets (NDs) toward theranostic applications. In this study, we have used negatively charged carbon dot (CD) and positively charged poly(diallyldimethylammonium chloride) (PDADMAC) in an aqueous medium to fabricate CD-based NDs. Notably, CDs are biocompatible in nature and exhibit fascinating physicochemical and optoelectronic properties *[30]*. It has been observed that the self-assembly of fabricated nanocomposite leads to the formation of biocompatible luminescent pH-responsive hybrid coacervate droplets. The physicochemical and photoluminescence (PL) properties of these CD-based NDs have been explored thoroughly by using various spectroscopic and microscopic techniques. Finally, these NDs are found to be biocompatible and have been utilized toward cellular uptake experiments.

3.2. Results and discussion

3.2.1. Characterization of CDs

The structure and morphology of as-synthesized CDs are characterized by UV−vis, PL, AFM, FTIR, PXRD, and Raman spectroscopy. Figure 3.1A shows the normalized absorption and emission spectra (λ_{ex} = 340 nm) of CDs in water. A prominent absorption peak at 340 nm is observed due to the n−π^* transitions from the C=O groups on the surface of CDs and a weak shoulder near 250 nm appears due to π−π^* transitions of aromatic sp^2 carbons within the core of CDs.

The synthesized CDs display a prominent PL band centered at 442 nm upon excitation at 340 nm with 0.60 PL QY (Figure 3.1A). The inset shows the photograph of aqueous dispersion of CDs upon UV light illumination ($\lambda_{ex} =$ 365 nm). Figure 3.1B shows the excitation-independent PL spectra of CDs upon excitation in the range from 300 to 390 nm, signifies the formation of colloidally stable CDs with uniform chemical composition and/or size distribution *[31]*.
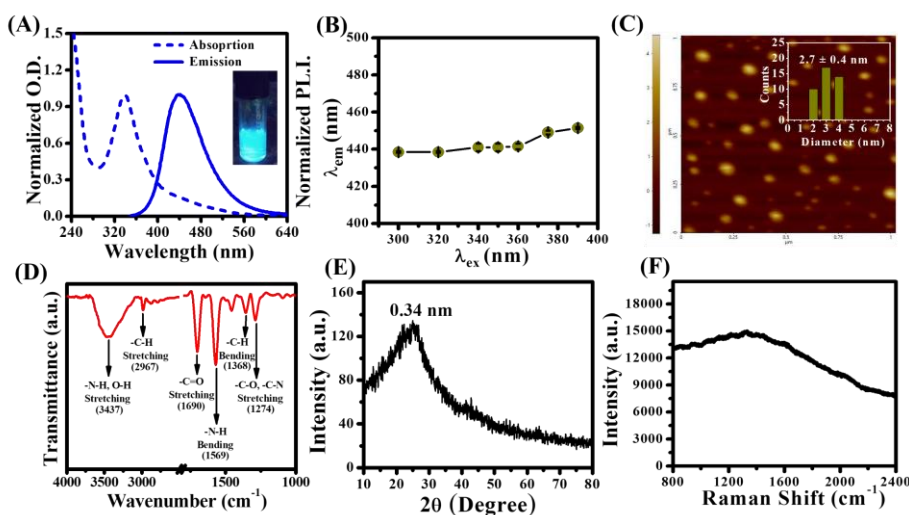
Figure 3.1. (A) Normalized absorption (dashed line) and PL spectra ($\lambda_{ex} =$ 340 nm, solid line) of CDs. (B) Changes in the PL wavelength of CDs at different excitation wavelengths. (C) AFM image of synthesized CDs. The inset shows the size distribution histogram with their mean size. (D) FTIR spectrum of synthesized CDs. (E) Powder XRD spectrum of CDs. (F) Raman spectrum of CDs. (Saini *et al. ACS Appl. Nano Mater.* **2020**, *3*, 5826-5837)

Figure 3.1C displays the AFM image of well-dispersed spherical CDs with a mean size of 2.7 ± 0.4 nm. Figure 3.1D shows the FTIR spectrum of CDs with a peak near 3437 cm^{-1} arises due to the stretching vibrations of O−H/N−H moieties. Two characteristic peaks at 2967 and

1368 cm^{-1} are assigned to the stretching and bending vibrations of C−H moieties, while two distinct peaks at 1690 and 1569 cm^{-1} arises due to the stretching and bending vibrations of C=O and N−H functional groups, respectively. The peak at 1274 cm^{-1} arises due to the stretching vibrations of C−O and C−N moieties. The PXRD spectrum shows a broad peak at 2θ = 25° (d = 0.34 nm) suggests the amorphous nature of these CDs (Figure 3.1E). Also, the Raman spectrum reveals a broad structureless feature without any characteristic G and D bands, indicating the low content of carbon lattice structure (Figure 3.1F). Moreover, it has been observed that the PL intensity of CDs depends on the solution pH (Figure 3.2A). The estimated ζ-potential for CDs at pH 10 and 4.5 is −31.3 ± 1.8 mV, and +15.4 ± 0.7 mV indicating the deprotonation and protonation of surface functionalized groups (Figure 3.2B). Taken together, these results reveal the formation of well-dispersed stable spherical luminescent CDs.
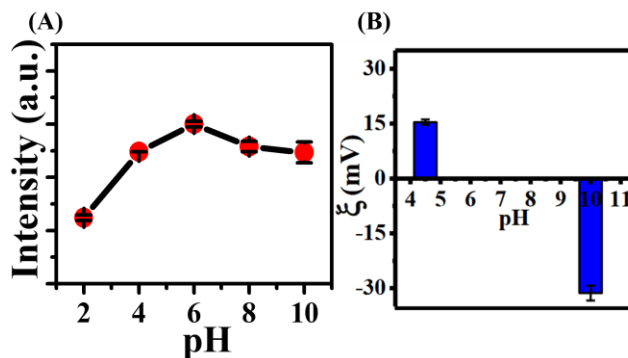
Figure 3.2. (A) Changes in the PL intensity of CDs (λ_{ex} = 340 nm) as a function of pH of the medium. (B) Estimated zeta potential of CDs at pH 4.5 and 10. (Saini *et al. ACS Appl. Nano Mater.* **2020**, *3*, 5826-5837)

3.2.2. Characterization of coacervate NDs

The aqueous binary mixtures of CDs and PDADMAC were equilibrated in an appropriate proportion for 1 and 18 h to get smaller and larger sized NDs (SNDs and LNDs), respectively. Figure 3.3A shows the AFM image of

well-dispersed spherical SNDs. The mean size estimated from AFM height profile is 73 ± 2.3 nm (Figure 3.3B).

Interestingly, equilibrating the same binary mixture for 18 h results in the formation of LNDs. AFM and FESEM measurements reveal the presence of individual LND with mean size of 418.5 ± 12.8 and 460.0 ± 16.0 nm, respectively (Figure 3.3C, D, & E). This increase in the size of NDs with equilibration time is due to the characteristic coalescence phenomenon [32].

Notably, the estimated negative ζ-potential value of CDs (-31.3 ± 1.8 mV) decreases to -17.0 ± 0.5 mV upon formation of NDs in the presence of positively charged PDADMAC (Figure 3.3F). This is expected as PDADMAC mainly binds with the surface carboxylate groups of CDs via electrostatic interactions [33]. Next, we have explored the colloidal and PL stability of these NDs as a function of various physiological parameters.
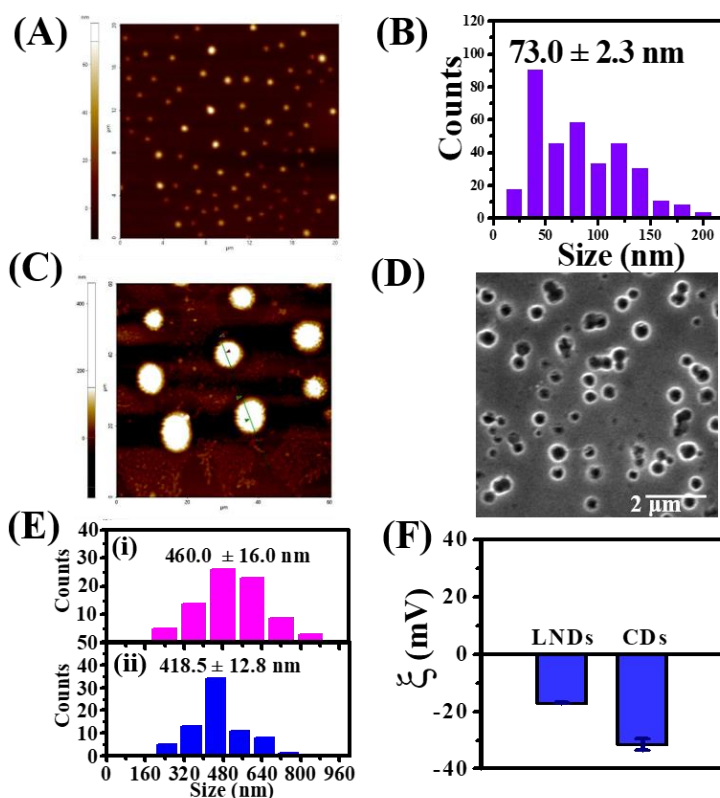
Figure 3.3. (A) AFM image of SNDs. (B) Size distribution histogram and mean size estimated from AFM height profile of SNDs. (C) AFM image of LNDs. (D) FESEM image of LNDs. (E) Size distribution histogram with their mean sizes estimated from (i) FESEM image, and (ii) AFM height profile. (F) Estimated ζ-potentials of CDs and LNDs. (Saini *et al. ACS Appl. Nano Mater.* **2020**, *3*, 5826-5837)

3.2.3. Colloidal and PL stability of coacervate NDs

The colloidal and PL stability of coacervate NDs were performed by taking higher concentrations of CD (0.12 mg/mL) and PDADMAC (64 μM) mixture by keeping the molar ratio same and incubated for 18 h.
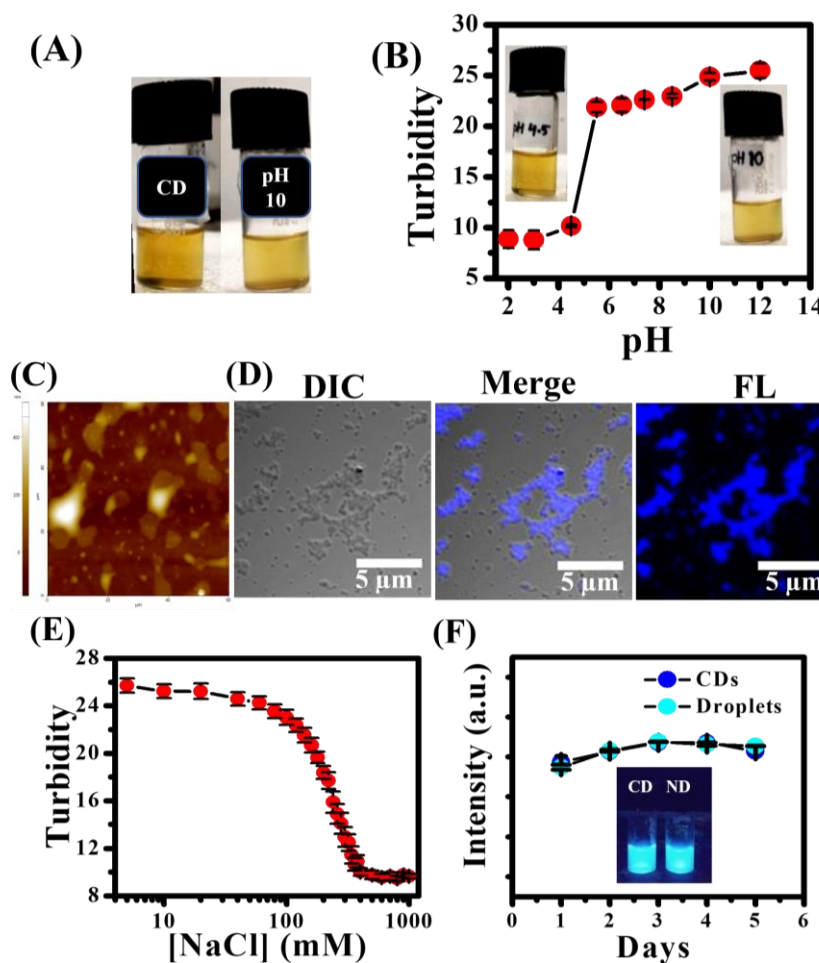
Figure 3.4. (A) Daylight photograph of aqueous dispersions of CDs and NDs. (B) Changes in the turbidity of ND dispersion at 600 nm as a function of pH. The inset shows the daylight photographs of ND dispersions at pH 10 and 4.5. (C) AFM image, and (D) confocal images of ND dispersion at pH 4.5 showing disassembled structures. (E) Changes in the turbidity of ND dispersion at 600 nm as a function of NaCl concentrations. (F) Changes in the PL intensity of aqueous dispersions of CDs and NDs as a function of time. The inset shows the photographs of aqueous dispersions of CD and ND under UV light illumination (λ_{ex} = 365 nm). (Saini *et al. ACS Appl. Nano Mater.* **2020**, *3*, 5826-5837)

Figure 3.4A shows the daylight photographs of transparent CDs dispersion and opaque binary mixture of CD and PDADMAC at pH 10 aqueous medium. This observed opaqueness can be explained by considering the presence of larger-sized fused NDs in the binary mixture at high concentration. The effect of pH on the stability of these self-assembled NDs were examined by turbidity profile plotted as a function of solution pH. Figure 3.4B displays the turbidity profile at 600 nm of the opaque binary mixture as a function of pH. It is evident that the turbidity remains opaque in the pH range between 5.5 and 12, decreases sharply below pH 5.5 and disappears completely in the pH range between 4.8 and 2.0 (Figure 3.4B). The observed pH-dependent phase transition indicates the disassembly of NDs at lower acidic pH which is due to the protonation of carboxylate groups (pK_a = 4.7) at the surface of CDs, results in weaken the electrostatic interaction between CDs and PDADMAC *[33]*. Further, to support this argument, we have visualized the binary mixture at pH 4.5 under AFM and confocal microscope. Both AFM and confocal images reveal disassembled polymeric networks without any spherical NDs (Figure 3.4C & D). Similar pH-dependent phase transitions and disassembly have

been observed earlier for various self-assembled nanostructures *[33, 34]*. Moreover, the turbidity of the binary mixture depends strongly on the ionic strength of the medium. The turbidity of the binary mixture decreases slowly beyond 200 mM NaCl, and completely disappears at and beyond 400 mM NaCl, substantiate the effective electrostatic screening between CD and PDADMAC (Figure 3.4E). Next, the PL stability of CD and ND was observed as a function of time and no change in PL intensity was observed even after 1 week of storage at room temperature (Figure 3.4F). Notably, the inset of figure 3.4F shows no change in the blue emission (λ_{ex} = 365 nm) of CD dispersion upon formation of NDs in the presence of PDADMAC. Their unique inherent PL properties along with colloidal stability makes them a suitable candidate for theranostic approach as luminescence markers.

3.2.4. Confocal laser scanning microscopy (CLSM) of NDs and dye sequestration

The luminescence properties of individual ND were explored by using CLSM. Figure 3.5 displays the CLSM images of well-dispersed spherical SNDs and LNDs. The fluorescence and merged images reveal distinct blue emission exclusively from SNDs and LNDs suggesting the uniform distribution of luminescent CDs inside these NDs (Figure 3.5A & B).
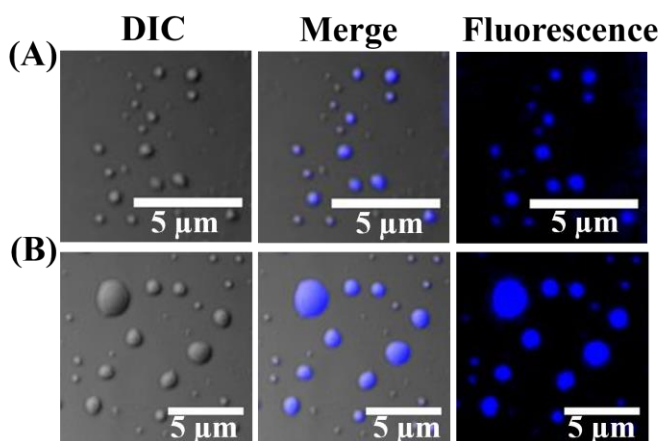
Figure 3.5. Confocal images (DIC, fluorescence, merge) of (A) SNDs, and (B) LNDs. (Saini *et al. ACS Appl. Nano Mater.* **2020**, *3*, 5826-5837)

Coacervates are known to sequester a variety of organic and inorganic molecules inside their membrane-less porous structure *[14–16, 33]*. To explore the sequestration behavior of our present system, we equilibrated LNDs with different dyes such as fluorescein isothiocyanate (FITC), Nile red (NR), rose bengal (RB), and ethidium bromide (EtBr) along with an anticancer drug doxorubicin (DOX) for 12 h. The equilibrated mixtures were centrifuged at 10000 rpm for 30 min to separate the supernatant from the coacervate phase. The equilibrium partition coefficients (K) for different solutes were estimated by using UV−vis spectroscopy and are listed in Table 3.1. These high values of K irrespective of charge indicate preferential sequestration inside the less polar crowded environment of LNDs via hydrophobic as well as electrostatic interactions *[33]*.

Table 3.1. Estimated equilibrium partition coefficients (K) of different solutes in the presence of LNDs.

Solutes	Initial concentration (µM)	K
Nile red	3.0	6.1 ± 0.5
Rose bengal	4.9	8.8 ± 1.1
Doxorubicin hydrochloride	19.5	10.6 ± 1.1
Ethidium bromide	87.0	15.9 ± 3.7
Fluorescein isothiocyanate	19.8	13.4 ± 0.2

Moreover, the preferential partitioning of DOX inside these NDs may open up a new avenue for their subsequent utilization in stimuli-responsive controlled drug release. Next, the complexes of LNDs

containing FITC, NR, RB, EtBr, and DOX were visualized directly under a confocal microscope (Figure 3.6). All the DIC images reveal the presence of well-dispersed intact spherical LNDs without any unwanted aggregation or disassembly even after sequestration, indicating the structural robustness of these NDs. Well-dispersed blue emission from individual LNDs in all blue channels signify the presence of CDs inside LNDs.
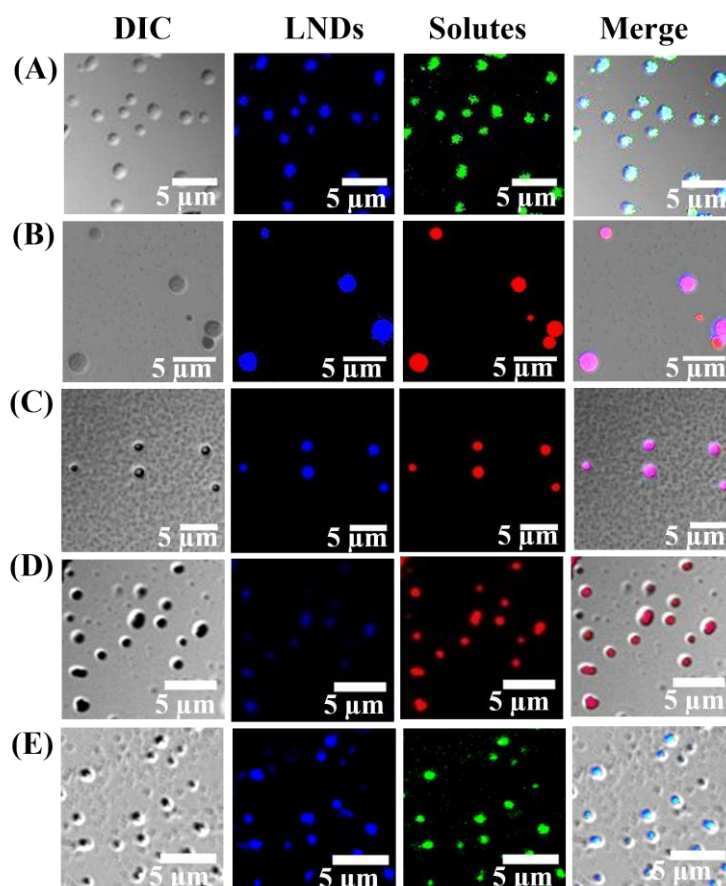
Figure 3.6. Confocal microscopy images of LNDs showing sequestration of (A) FITC, (B) NR, (C) RB, (D) EtBr, and (E) DOX. (Saini *et al. ACS Appl. Nano Mater.* **2020**, *3*, 5826-5837)

The green channel (490−565 nm) reveals localized green emission from FITC-loaded LNDs and DOX-loaded LNDs while merged image of both shows distinct cyan emission suggesting preferential sequestration of

solutes inside these LNDs (Figure 3.6A & E). Similarly, the sequestration of NR, RB, and EtBr results in uniform magenta emission exclusively from the LNDs (Figure 3.6B, C & D). However, the sequestration of EtBr results in weaker blue and red signals in the blue and red channels, respectively (Figure 3.6D). Control steady-state PL measurement reveals that sequestration of EtBr results in PL quenching of CDs inside these LNDs (Figure 3.7). The possible mechanism behind the observed PL quenching might be due to the photoinduced electron transfer from photoexcited CDs to EtBr dyes *[35]*.
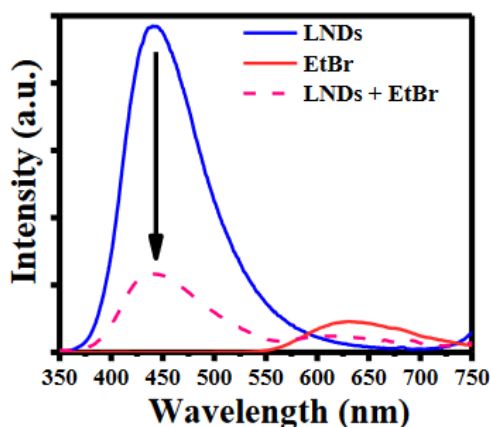
Figure 3.7. Steady-state PL spectra (λ_{ex} = 340 nm) of LNDs, EtBr, and their complex. (Saini *et al. ACS Appl. Nano Mater.* **2020**, *3*, 5826-5837)

3.2.5. Cytotoxicity and cellular uptake study

To know the cytotoxicity effect of the present NDs, cell viability experiments were performed on BHK-21 cells by taking SNDs (73 ± 2.3 nm) via standard MTT assay. The dose-dependent MTT assay (μg/mL) of CD, PDADMAC, and ND was performed at a fix incubation time of 24 h. The MTT assay reveals ~82.4% (230 μg/mL), ~95% (60 μg/mL), and ~78% (42.7 μg/mL) cell viability values correspond to SNDs, bare CD and PDADMAC concentrations, respectively (Figure 3.8A, B & C). The low cell viability of positively charged PDADMAC may arise due to the strong

binding with the cell membrane which ultimately causes membrane disruption and cell death *[36]*. Nevertheless, our findings reveal that intact SNDs are nontoxic in nature and can be utilized further toward various biomedical applications.

Next, we performed cellular uptake experiments with BHK-21 cell line at a fixed dose of 115 μg/mL of SNDs to understand the interaction of SNDs with cell membrane and subsequent internalization process along with intracellular trafficking with EtBr-loaded SNDs. The reason behind choosing EtBr-loaded SNDs is that EtBr is a well-known nucleus staining intercalating dye with characteristic highly intense red emission, which is well-separated from the blue emission of SNDs and enhanced after binding with DNA *[37]*. Initially, we checked the stability of these NDs in control cell culture that reveals the well-dispersed intact spherical LNDs with characteristic blue emission Figure 3.8D.
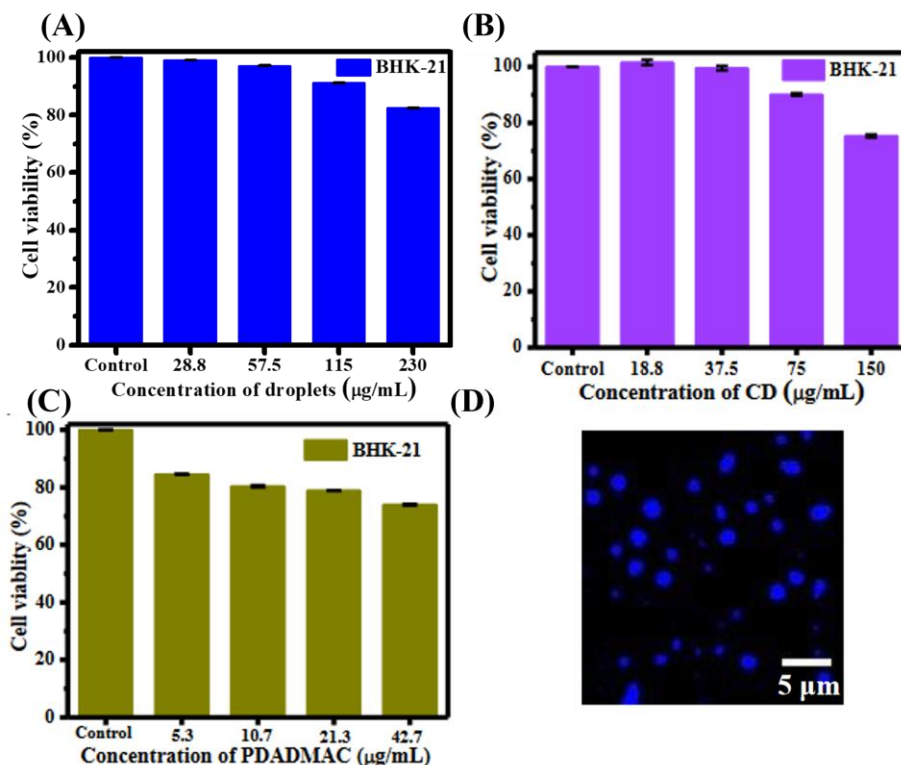
Figure 3.8. MTT cell viability assays of (A) SNDs, (B) CDs, and (C) PDADMAC in BHK-21 cells at 24 h of incubation. (Saini *et al. ACS Appl. Nano Mater.* **2020**, *3*, 5826-5837)

Figure 3.9 shows the time-dependent (4 and 24 h) cell imaging experiments along with control experiment without SND. The DIC image in the absence of SNDs reveals healthy cells with no visible fluorescence (Figure 3.9 (i)). However, cells incubated with SNDs for 4 h show distinct uniform blue fluorescence throughout the cells without any cytosol and nucleus specificity (Figure 3.9 (ii)). The appearance of blue emission from inside the cells clearly suggests the presence of either intact SNDs or disassembled CDs. Notably, control cell imaging experiments with only CDs (dose = 60 µg/mL) reveal similar diffuse blue emission uniformly distributed throughout the cells after 4 h of incubation (Figure 3.9(iii)). This observation supports the fact that SNDs may undergo disassembly inside the cellular environment to yield free CDs after internalization via endocytosis *[38]*.

However, cells incubated with SNDs for 24 h show relatively brighter blue fluorescence along with some localized punctate fluorescence at the cell membrane as well as inside the cytosol (Figure 3.9(iv), magenta arrows). Further, the endocytosis-mediated internalization process was performed with LNDs and we observed an endocytic intermediate during endocytosis of a LND through the cell membrane of BHK-21 cell incubated for 24 h Figure 3.9(v). The mechanism of cellular uptake has been shown to be influenced by the size of the internalized NPs *[39]*. Therefore, our findings clearly suggest the time- and size-dependent endocytosis-mediated internalization of these SNDs through the cell membrane.
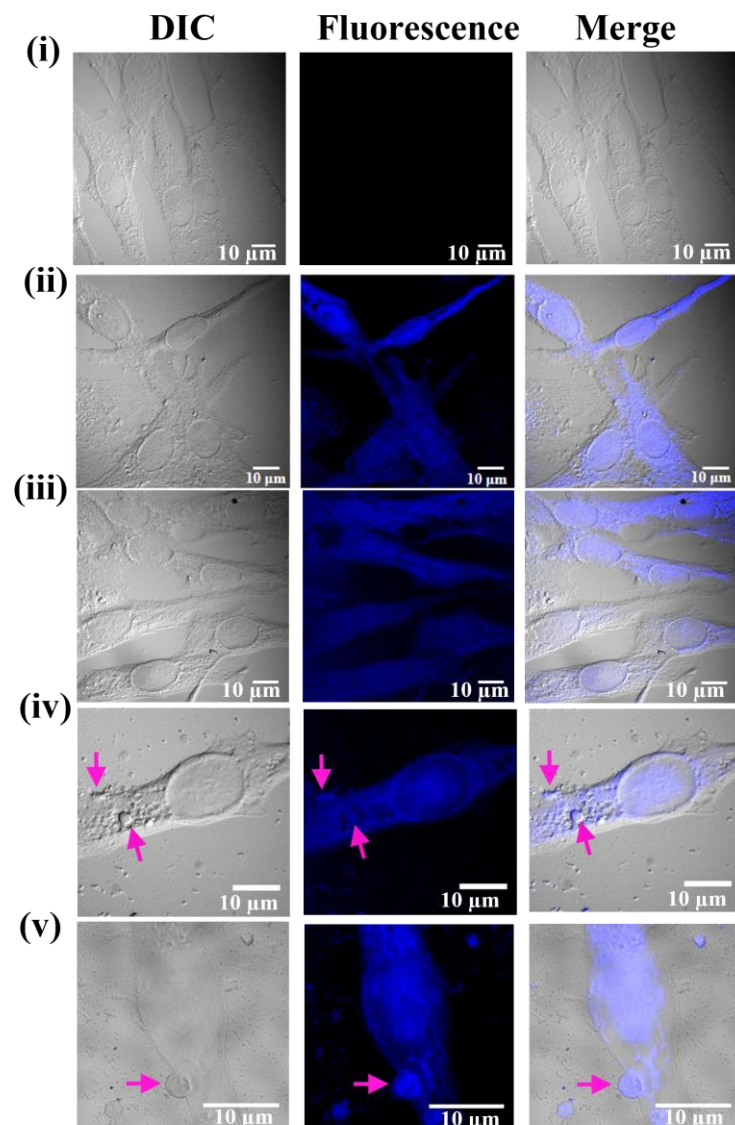
Figure 3.9. Confocal microscopy images (DIC, fluorescence, merge) of (i) BHK-21 cells and (ii) SNDs in BHK-21 cells at 4 h of incubation, (iii) SNDs in BHK-21 cells at 24 h of incubation, and (iv) LNDs in BHK-21 cells at 24 h of incubation showing an endocytic intermediate. Images were captured at 100X magnification. (Saini *et al. ACS Appl. Nano Mater.* **2020**, *3*, 5826-5837)

To address the stability of internalized SNDs, time-dependent cellular uptake experiments with EtBr-loaded SNDs were performed. Figure 3.10A shows the confocal images (20X objective) of BHK-21 cells incubated with EtBr-loaded SNDs for 24 h. The DIC image displays the presence of healthy cells and blue channel reveals diffused blue fluorescence uniformly distributed throughout the cells along with red channel reveals distinct highly intense red fluorescence from the cell nucleus even after 24 h of incubation. The merged image of blue and red channels reveals distinct magenta fluorescence from the nucleus and blue fluorescence from the cytosol. These findings can be explained by considering disassembly of internalized SNDs inside late endosomes/lysosomes. The released CDs distribute themselves nonspecifically throughout the cellular compartment and released EtBr further binds with nucleic acid *[38]*. To justify this hypothesis, we have performed cellular uptake experiments with EtBr-loaded SNDs at 4 h of incubation (Figure 3.10B). The fluorescence signal in the blue channel appears weak and diffuse in nature, interesting results have been observed in the red channel (Figure 3.10B). While the bright red fluorescence originates mainly from the nucleoli of the nucleus bind with ribosomal-RNA (rRNA), the red signal from the cytosol is diffuse in nature *[40]*. Therefore, the presence of EtBr in the cytosol even after 4 h of incubation unambiguously suggests the disassembly of internalized SNDs inside the cellular compartment after endocytosis. More importantly, localized punctate red fluorescence is clearly visible at the cell membrane originates from intact EtBr-loaded SNDs after 4 h of incubation (Figure 3.10B & C).
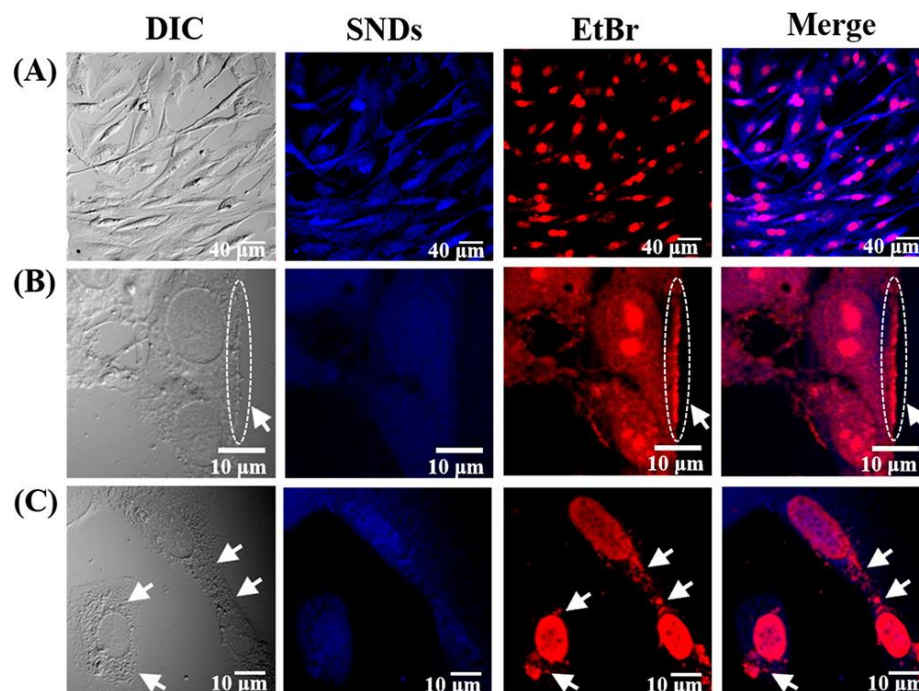
Figure 3.10. Confocal microscopy images of EtBr-loaded SNDs in BHK-21 cells (A) after 24 h of incubation at 20X magnification, (B) after 4 h of incubation at 100X magnification, and (C) after 24 h of incubation at 100X magnification. (Saini *et al. ACS Appl. Nano Mater.* **2020**, *3*, 5826-5837)

However, no such punctate blue fluorescence has been observed in the blue channel due to luminescence quenching of SNDs by EtBr (Figure 3.10B & C). Our findings not only indicate endocytosis mediated cell internalization of EtBr-loaded SNDs but also reveal specific labeling of cell nucleus with loaded EtBr.

On the basis of our findings, we propose a tentative model for the time- and size-dependent cellular uptake of bare and EtBr-loaded SNDs (Scheme 3.1). At the initial stage, the smaller sized NDs easily internalized within the cell via endocytosis, and subsequent disassembly occurs due to the lower acidic pH of late endosomes/lysosomes with release of free CDs and EtBr in the cytosol *[38]*. The released EtBr dyes subsequently bind with

the nucleic acid inside the cell nucleus. However, the endocytosis process for relatively larger sized SNDs is slow, and few intact larger sized SNDs inside the endosome survive even after 24 h of incubation (Scheme 3.1).
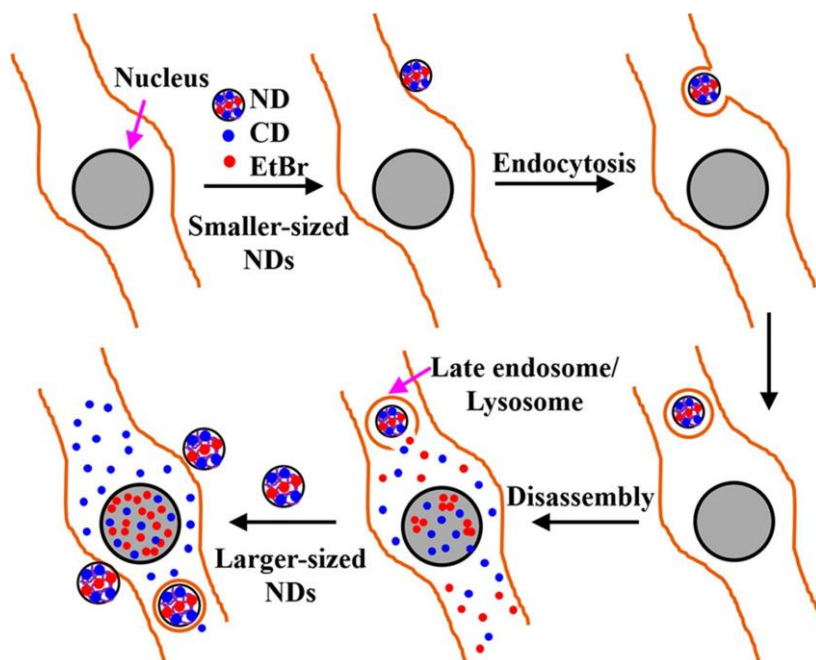
Scheme 3.1. Schematic illustration of cellular uptake of NDs and subsequent subcellular distribution of NDs (intact assembly), CDs (blue dots), and EtBr (red dots) inside a BHK-21 Cell. (Saini *et al. ACS Appl. Nano Mater.* **2020**, *3*, 5826-5837)

Taken together, our findings highlight the potential of these luminescent NDs toward various theranostic applications. Particularly, their biocompatible nature along with well-defined robust structure and stimuli-responsive structural disassembly makes these NDs as ideal nanocarriers for targeted delivery of a wild range of therapeutics in the form of small ligands, growth factors, antibodies, antigens, and specific drugs. These cargo-loaded NDs can be administered through different parenteral delivery routes such as intramuscular, intravenous, intrathecal, intraparenchymal,

intracerebral, and intranasal delivery directly to the targeted site to circumvent anatomical barriers or blood−brain barrier for the treatment of several neurological disorders such as Alzheimer's disease, multiple sclerosis, Parkinson's disease, or solid tumors referred to as neuroblastoma or glioblastoma. Further studies are underway to explore the loading and stimuli-responsive release as well as delivery profiles of various therapeutic drugs using these biocompatible NDs.

3.3. Conclusions

The present study illustrates the potential application of biocompatible inherently luminescent coacervate NDs toward cell imaging and pH-triggered intracellular disassembly characteristics. It has been observed that the self-assembly between negatively charged 2.7 ± 0.3 nm sized CDs and cationic polymer PDADMAC leads to the formation of spherical NDs. The size distribution and stability of these NDs are found to be influenced by equilibration time, pH, and ionic strength of the aqueous medium. Two differently sized NDs have been fabricated in this study, namely, SNDs and LNDs upon equilibrating the binary mixture for 1 and 18 h at room temperature, respectively. While these NDs are stable in the pH range of 6−12, the stability decreases sharply below pH 5. Similarly, disassembly has also been observed in high ionic strength medium. Using UV−vis and CLSM measurements, we have further demonstrated preferential sequestration of various organic dyes and anticancer drug DOX inside the membrane-less porous structure of these NDs. The MTT assay on BHK-21 cell line reveals the biocompatible nature of the present SNDs with cell viability of 82.4% at a dose of 230 μg/ mL upon 24 h of incubation. We have utilized their inherent PL characteristics toward cell imaging application. In addition, using EtBr-loaded SNDs, we have successfully demonstrated intracellular trafficking and pH-triggered disassembly of

SNDs in the cytosol. Our findings reveal endocytosis mediated internalization of SNDs and subsequent disassembly at the lower acidic pH (<5.5) of late endosomes/lysosomes. The present study highlights the potential of these inherently luminescent NDs in various theranostic applications as an active material for luminescent marker as well as nanocarrier and may have practical implications toward stimuli-responsive therapeutic drug delivery.

Note: This is copyrighted material from permission of the American Chemical Society.

3.4. References

1. Li Y., Wang Y., Huang G., Gao J. (2018), Cooperativity principles in self-assembled nanomedicine, Chem. Rev., 118(11), 5359–5391. (DOI:10.1021/acs.chemrev.8b00195)

2. Zhao L., Xing Y., Wang R., Yu F., Yu F. (2020), Self-assembled nanomaterials for enhanced phototherapy of cancer, ACS Appl. Bio Mater., 3(1), 86–106. (DOI:10.1021/acsabm.9b00843)

3. Nam J., Ha Y. S., Hwang S., Lee W., Song J., Yoo J., et al. (2013), pH-responsive gold nanoparticles-in-liposome hybrid nanostructures for enhanced systemic tumor delivery, Nanoscale, 5(21), 10175. (DOI:10.1039/c3nr03698g)

4. Discher B. M., Won Y-Y., Ege D. S., Lee JC-M., Bates F. S., Discher D. E., et al. (1999), Polymersomes: Tough vesicles made from diblock copolymers, Science, 284(5417), 1143–1146. (DOI:10.1126/science.284.5417.1143)

5. Liu Y., He J., Yang K., Yi C., Liu Y., Nie L., et al. (2015), Folding up of gold nanoparticle strings into plasmonic vesicles for enhanced

photoacoustic imaging, Angew. Chem. Int. Ed., 54(52), 15809–15812. (DOI:10.1002/anie.201508616)

6. Medina S. H., El-Sayed M. E. H. (2009), Dendrimers as carriers for delivery of chemotherapeutic agents, Chem. Rev., 109(7), 3141–3157. (DOI:10.1021/cr900174j)

7. Yuk H., Lu B., Zhao X. (2019), Hydrogel bioelectronics, Chem. Soc. Rev., 48(6), 1642–1667. (DOI:10.1039/C8CS00595H)

8. Horcajada P., Gref R., Baati T., Allan P. K., Maurin G., Couvreur P., et al. (2012), Metal–organic frameworks in biomedicine, Chem. Rev., 112(2), 1232–1268. (DOI:10.1021/cr200256v)

9. Kamaly N., Yameen B., Wu J., Farokhzad O. C. (2016), Degradable controlled-release polymers and polymeric nanoparticles: Mechanisms of controlling drug release, Chem. Rev., 116(4), 2602–2663. (DOI:10.1021/acs.chemrev.5b00346)

10. Buddingh' B. C., van Hest J. C. M. (2017), Artificial cells: Synthetic compartments with life-like functionality and adaptivity, Acc. Chem. Res., 50(4), 769–777. (DOI:10.1021/acs.accounts.6b00512)

11. Pattni B. S., Chupin V. V., Torchilin V. P. (2015), New Developments in liposomal drug delivery, Chem. Rev., 115(19), 10938–10966. (DOI:10.1021/acs.chemrev.5b00046)

12. Dora. Tang T-Y., van Swaay D., deMello A., Ross Anderson J. L., Mann S. (2015), In vitro gene expression within membrane-free coacervate protocells, Chem. Commun., 51(57), 11429–11432. (DOI:10.1039/C5CC04220H)

13. Wang S., Chen Y., Wang S., Li P., Mirkin C. A., Farha O. K. (2019), DNA-functionalized metal–organic framework nanoparticles for intracellular delivery of proteins, J. Am. Chem. Soc., 141(6), 2215–2219. (DOI:10.1021/jacs.8b12705)

14. Frankel E. A., Bevilacqua P. C., Keating C. D. (2016), Polyamine/nucleotide coacervates provide strong compartmentalization of Mg^{2+}, nucleotides, and RNA, Langmuir, 32(8), 2041–2049. (DOI:10.1021/acs.langmuir.5b04462)

15. Williams D. S., Koga S., Hak C. R. C., Majrekar A., Patil A. J., Perriman A. W., et al. (2012), Polymer/nucleotide droplets as bio-inspired functional micro-compartments, Soft Matter, 8(22), 6004. (DOI:10.1039/c2sm25184a)

16. Martin N., Li M., Mann S. (2016), Selective uptake and refolding of globular proteins in coacervate microdroplets, Langmuir, 32(23), 5881–5889. (DOI:10.1021/acs.langmuir.6b01271)

17. Nishida K., Tamura A., Yui N. (2018), pH-responsive coacervate droplets formed from acid-labile methylated polyrotaxanes as an injectable protein carrier, Biomacromolecules, 19(6), 2238–2247. (DOI:10.1021/acs.biomac.8b00301)

18. Lv K., Perriman A. W., Mann S. (2015), Photocatalytic multiphase micro-droplet reactors based on complex coacervation, Chem. Commun., 51(41), 8600–8602. (DOI:10.1039/C5CC01914A)

19. Drobot B., Iglesias-Artola J. M., Le Vay K., Mayr V., Kar M., Kreysing M., et al. (2018), Compartmentalized RNA catalysis in membrane-free coacervate protocells, Nat. Commun., 9(1), 3643. (DOI:10.1038/s41467-018-06072-w)

20. Crosby J., Treadwell T., Hammerton M., Vasilakis K., Crump M. P., Williams D. S., et al. (2012), Stabilization and enhanced reactivity of actinorhodin polyketide synthase minimal complex in polymer–nucleotide coacervate droplets, Chem. Commun., 48(97), 11832. (DOI:10.1039/c2cc36533b)

21. Love C., Steinkühler J., Gonzales D. T., Yandrapalli N., Robinson T., Dimova R., et al. (2020), Reversible pH-responsive coacervate formation in lipid vesicles activates dormant enzymatic reactions, Angew. Chem. Int. Ed., 59(15), 5950–5957. (DOI:10.1002/anie.201914893)

22. Qiao Y., Li M., Qiu D., Mann S. (2019), Response-retaliation behavior in synthetic protocell communities, Angew. Chem. Int. Ed., 58(49), 17758–17763. (DOI:10.1002/anie.201909313)

23. Koga S., Williams D. S., Perriman A. W., Mann S. (2011), Peptide–nucleotide microdroplets as a step towards a membrane-free protocell model, Nat. Chem., 3(9), 720–724. (DOI:10.1038/nchem.1110)

24. Douliez J-P., Martin N., Gaillard C., Beneyton T., Baret J-C., Mann S., et al. (2017), Catanionic coacervate droplets as a surfactant-based membrane-free protocell model, Angew. Chem. Int. Ed., 56(44), 13689–13693. (DOI:10.1002/anie.201707139)

25. van Swaay D., Tang T-Y. D., Mann S., de Mello A. (2015), Microfluidic formation of membrane-free aqueous coacervate droplets in water, Angew. Chem. Int. Ed., 54(29), 8398–8401. (DOI:10.1002/anie.201502886)

26. Priftis D., Leon L., Song Z., Perry S. L., Margossian K. O., Tropnikova A., et al. (2015), Self-assembly of α-helical polypeptides driven by complex coacervation, Angew. Chem. Int. Ed., 54(38), 11128–11132. (DOI:10.1002/anie.201504861)

27. Priftis D., Xia X., Margossian K. O., Perry S. L., Leon L., Qin J., et al. (2014), Ternary, tunable polyelectrolyte complex fluids driven by complex coacervation, Macromolecules, 47(9), 3076–3085. (DOI:10.1021/ma500245j)

28. Priftis D., Tirrell M. (2012), Phase behaviour and complex coacervation of aqueous polypeptide solutions, Soft Matter, 8(36), 9396–9405. (DOI:10.1039/C2SM25604E)

29. Cruz M. A., Morris D. L., Swanson J. P., Kundu M., Mankoci S. G., Leeper T. C., et al. (2018), Efficient protein encapsulation within thermoresponsive coacervate-forming biodegradable polyesters, ACS Macro Lett., 7(4), 477–481. (DOI:10.1021/acsmacrolett.8b00118)

30. Li J., Wang B., Zhang H., Yu J. (2019), Carbon dots-in-matrix boosting intriguing luminescence properties and applications, Small, 15(32), 1805504. (DOI:10.1002/smll.201805504)

31. Bhattacharya A., Chatterjee S., Prajapati R., Mukherjee T. K. (2015), Size-dependent penetration of carbon dots inside the ferritin nanocages: evidence for the quantum confinement effect in carbon dots, Phys. Chem. Chem. Phys., 17(19), 12833–12840. (DOI:10.1039/C5CP00543D)

32. Singh S., Vaishnav J. K., Mukherjee T. K. (2020), Quantum dot-based hybrid coacervate nanodroplets for ultrasensitive detection of Hg^{2+}, ACS Appl. Nano Mater., 3(4), 3604–3612. (DOI:10.1021/acsanm.0c00317)

33. Vaishnav J. K., Mukherjee T. K. (2019), Highly photostable and two-photon active quantum dot–polymer multicolor hybrid coacervate droplets, Langmuir, 35(36), 11764–11773. (DOI:10.1021/acs.langmuir.9b01783)

34. Vaishnav J. K., Mukherjee T. K. (2019), Surfactant-induced self-assembly of CdTe quantum dots into multicolor luminescent hybrid vesicles, Langmuir, 35(19), 6409–6420. (DOI:10.1021/acs.langmuir.9b00357)

35. Bhattacharya A., Mukherjee T. K. (2017), Synergistic enhancement of electron-accepting and -donating ability of nonconjugated polymer nanodot in micellar environment, Langmuir, 33(51), 14718–14727. (DOI:10.1021/acs.langmuir.7b04030)

36. Black K. A., Priftis D., Perry S. L., Yip J., Byun W. Y., Tirrell M. (2014), Protein encapsulation via polypeptide complex coacervation, ACS Macro Lett., 3(10), 1088–1091. (DOI:10.1021/mz500529v)

37. Izumrudov V. A., Zhiryakova M. V., Goulko A. A. (2002), Ethidium bromide as a promising probe for studying DNA interaction with cationic amphiphiles and stability of the resulting complexes, Langmuir, 18(26), 10348–10356. (DOI:10.1021/la020592u)

38. Wong P. T., Choi S. K. (2015), Mechanisms of drug release in nanotherapeutic delivery systems, Chem. Rev., 115(9), 3388–3432. (DOI:10.1021/cr5004634)

39. Panja P., Jana N. R. (2020), Arginine-terminated nanoparticles of <10 nm size for direct membrane penetration and protein delivery for straight access to cytosol and nucleus, J. Phys. Chem. Lett., 11(6), 2363–2368. (DOI:10.1021/acs.jpclett.0c00176)

40. Li X., Gorle A. K., Ainsworth T. D., Heimann K., Woodward C. E., Grant Collins J., et al. (2015), RNA and DNA binding of inert oligonuclear ruthenium(II) complexes in live eukaryotic cells, Dalton Trans., 44(8), 3594–3603. (DOI:10.1039/C4DT02575J)

Chapter 4

Specific Loading and In Vitro Controlled Release of a Ru-Based Hydrophobically Encapsulated Model Anticancer Drug inside Nanoassemblies toward Stimuli-Responsive Drug Delivery

4.1. Introduction

In the present-day scenario, designing and utilization of multifunctional nanocarriers are at high demand due to its importance for the solubilization and target-specific delivery of hydrophobic therapeutic drugs inside various cellular compartments with better therapeutic efficacy *[1–5]*. To circumvent these challenges, various nanoscale drug-delivery systems such as liposomes *[6, 7]*, hybrid vesicles *[8, 9]*, polymeric micelles (PMs) based on amphiphilic block copolymers *[10, 11]*, polymersomes *[12]*, dendrimer nanoparticles (NPs) *[13]*, polymeric NPs *[14]*, hydrogels *[15]*, and metal-organic frameworks (MOFs) *[16]* have been developed for the efficient delivery of various therapeutically active hydrophobic drugs at the target site *[6–22]*. Among these, conventional phospholipid-based liposomes with structural diversity have been extensively utilized as a model drug-delivery vehicle for the in vivo delivery of various hydrophobic, hydrophilic, and amphiphilic drugs because of their well characterized and simple cell-membrane-mimicking lipid-bilayer structures *[6, 7, 17]*. Most of the above-mentioned nanocarriers possesses complex and time-consuming synthetic procedure along with poor drug-loading capability, short in vivo retention time, leakage, and uncontrolled burst release of the loaded drug. In this context, membrane-free coacervates offer unique advantages over other nanocarriers via facile synthetic route and preferential sequestration of a wide range of hydrophilic/hydrophobic compounds, including biological macromolecules and inorganic NPs *[13, 22–30]*. Till date, various groups have fabricated different types of nanocarriers for efficient loading and delivery of wide range of therapeutic drugs to their target sites but it is highly desirable to have a systematic and comparative study of the loading and release efficiency of a given therapeutic drug inside different nanocarriers. This kind of comparative

study will not only help to understand the inherent physicochemical properties of various nanocarriers but also provide valuable information for optimization of their in vivo performances. The aim of the present study is to systematically investigate the photophysical properties of a model anticancer drug, [(p-cymene)Ru(curcuminato)Cl] (Ru-Cur), inside various nano-assemblies, such as micelles (cationic, neutral, and anionic), liposomes (SUV, GUV, and MLV), and coacervates (CD- and ATP-based), using various spectroscopic and microscopic techniques and explore their pH-responsive controlled release mechanism. However, the solubility of this hydrophobic Ru-Cur in the cellular environment is a major concern for their effective delivery at the target sites. Although the antitumor activity of this drug toward various tumor cell lines has been well documented, the controlled and sustained delivery of this hydrophobic drug to its target organelle inside an aqueous cellular environment is a challenging task and has not been explored yet. To the best of our knowledge, this is the first comprehensive study to quantitatively compare the loading efficiency of Ru-Cur inside various self-assembled nanocarriers and demonstrate the in vitro pH-responsive controlled- and sustained-release mechanism.

4.2. Results and discussion

The structure and mass of synthesized Ru-Cur was characterized by ^{1}H NMR and ESI-MS (Figure 4.1B & C). The molar concentration of Ru-Cur was kept constant at 5 μM throughout the present study, and all of the aqueous solutions were equilibrated for 1 h before any spectroscopic and microscopic measurements.
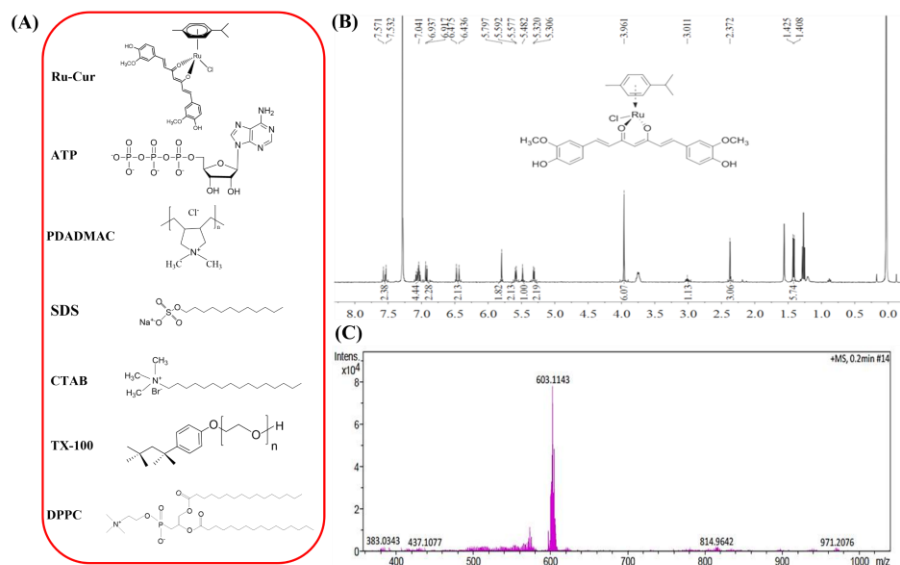
Figure 4.1. (A) Chemical structures of various molecules used in the present study. (B) ^{1}H NMR spectrum of synthesized Ru-Cur in CDCl$_3$. (C) ESI mass spectrum of Ru-Cur in MeOH. (Saini *et al. ACS Appl. Nano Mater.* **2021**, *4*, 2037-2051)

4.2.1. Interaction of Ru-Cur with micelles. Photophysical aspects in micellar assemblies.

The photophysical aspects of Ru-Cur have been explored inside three distinct charged micellar systems, namely cationic CTAB, neutral TX-100, and anionic SDS micelles in the aqueous media using fluorescence spectroscopy. In water, Ru-Cur shows a broad structureless absorption band centered at 413 nm with a fwhm value of 154 nm. The absorption band gets narrower (fwhm = 100, 111, and 130 nm for CTAB, TX-100, and SDS, respectively) with an increase in absorbance near the critical micelle concentration (CMC) of all three surfactants (Figure 4.2A).

The absorption band shifts to 418, 422, and 441 nm in the presence of 1 mM CTAB, 0.24 mM TX-100, and 8 mM SDS with two distinct shoulders, respectively (Figure 4.2A). These spectral changes at or near the CMC of

the respective surfactants indicate the association of Ru-Cur with the micellar pseudophase *[31, 32]*. Next, we explored the interaction mechanism and fluorescence properties of Ru-Cur via monitoring the evolution of the fluorescence spectrum of Ru-Cur as a function of the surfactant concentrations. The fluorescence intensity of non-fluorescent Ru-Cur gradually increases with an increase in the concentrations of all three different surfactants upon excitation at 425 nm and the fluorescence maximum of Ru-Cur appears at 503 nm in the presence of 1 mM CTAB and 0.24 mM TX 100 micelles, the same appears at 538 nm in the presence of 8 mM SDS micelles (Figures 4.2B). Figure 4.2C displays the photographs of Ru-Cur associated with green fluorescence signal in the presence of different concentrations of surfactants (top panel-CTAB; middle panel-TX-100; lower panel-SDS). Further, we plotted the enhancement factor (I/I_0) against surfactant concentrations and a sudden jump at respective CMC's of CTAB and TX-100 was observed (Figure 4.2D).

On the other hand, no such sudden jump in the value of I/I_0 has been observed in the presence of SDS. The saturated values of I/I_0 of Ru-Cur in the presence of CTAB, TX-100, and SDS are estimated to be 109, 145, and 23, respectively (Figure 4.2D). The present Ru-Cur complex is a neutral hydrophobic molecule and shows no noticeable fluorescence in water. The drastic enhancement in the fluorescence intensity at the CMCs of CTAB and TX-100 along with 5 and 9 nm red shifts in the absorption maximum of Ru-Cur, respectively, indicates strong ground-state hydrophobic association. Notably, a similar enhancement of the fluorescence in the presence of micelles has been reported earlier for curcumin due to the suppression of nonradiative decay channels upon association with the micellar phase *[31, 33]*. But the significant different findings have been observed in case of negatively charged SDS micelles.
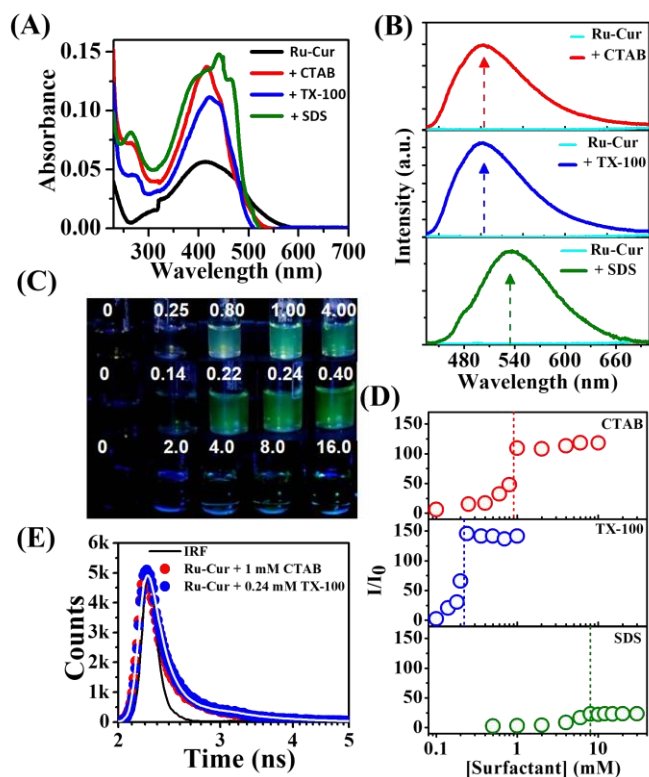
Figure 4.2. Changes in the (A) absorption and (B) fluorescence spectra of 5 µM Ru-Cur in the presence of 1 mM CTAB, 0.24 mM TX-100, and 8 mM SDS. (C) UV-light (λ_{ex} = 365 nm) photographs of aqueous solutions of Ru-Cur in the presence of different concentrations of surfactants (top panel, CTAB; middle panel, TX 100; lower panel, SDS). (D) Plot of the enhancement factor against surfactant concentrations. (E) Fluorescence lifetime decay traces (λ_{ex} = 405 nm) and fitted decay parameters of Ru-Cur in the presence of 1 mM CTAB and 0.24 mM TX-100. (Saini *et al. ACS Appl. Nano Mater.* **2021**, *4*, 2037-2051)

The 28 nm shift in the absorption maximum may be originated because of a strong and specific association between the Ru-Cur and SDS micelles while the insignificant fluorescence enhancement suggests the association of Ru-Cur with the less hydrophobic Stern layer of the SDS

micelles. We have further estimated the equilibrium partition coefficient of Ru-Cur inside the CTAB and TX-100 micelles using a UV−vis spectrophotometer. The estimated partition coefficients are 3.2 ± 0.3 and 6.5 ± 0.4 for CTAB and TX-100 micelles, respectively. This further justifies the higher binding affinity of Ru-Cur toward the more hydrophobic micellar core of TX-100 micelles. Next, we performed time-resolved fluorescence lifetime experiments by using diode of 405 nm. The lifetime decay curve of Ru-Cur in water overlaps with the IRF. The fluorescence decay of Ru-Cur in the presence of 1 mM CTAB and 0.24 mM TX-100 shows biexponential lifetime decay profile with mean lifetime of 0.11 ns and 0.14 ns (Figure 4.2E). The lifetime components correspond to CTAB are 0.07 ns (92%) and 0.59 ns (8%) and with TX-100 are 0.09 ns (93%) and 0.76 ns (7%) (Table 4.1). This multi-exponential decay kinetics signify the heterogeneous distribution of Ru-Cur inside the micellar nanoassemblies of CTAB and TX-100. Similar multiexponential decay kinetics in micellar media were reported earlier for curcumin and Ru-based complexes because of the presence of various radiative decay channels *[31, 33, 34]*.

Table 4.1. Fitted fluorescence decay parameters of Ru-Cur in the presence of 1 mM CTAB and 0.24 mM TX-100.

Sample	τ_1 **(ns)**	a_1	τ_2 **(ns)**	a_1	$<\tau>$ **(ns)**	χ^2
Ru-Cur + 1 mM CTAB	0.07	0.92	0.59	0.08	0.11	1.22
Ru-Cur + 0.24 mM TX-100	0.09	0.93	0.76	0.07	0.14	1.21

CLSM. Figure 4.3A shows the confocal image of only Ru-Cur with no detectable fluorescence signal. However, uniformly distributed localized fluorescence spots have been observed for micellized encapsulated Ru-Cur inside 1 mM CTAB and 0.24 mM TX-100 (Figure 4.3B, C). In contrast, the confocal image of Ru-Cur in the presence of 8 mM SDS reveals a different scenario.
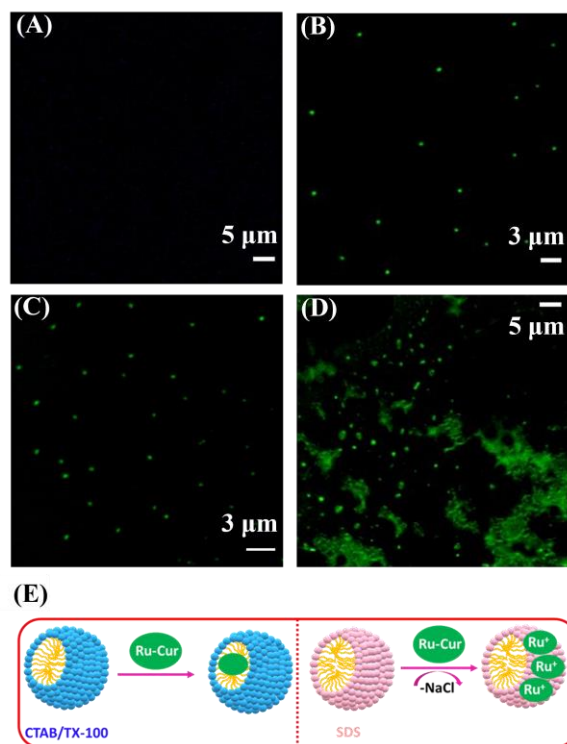
Figure 4.3. Confocal images of (A) Ru-Cur, (B) Ru-Cur with 1 mM CTAB, (C) Ru-Cur with 0.24 mM TX-100, and (D) Ru-Cur with 8 mM SDS. (E) Illustration of the association mechanism of Ru-Cur with different micelles. (Saini *et al. ACS Appl. Nano Mater.* **2021**, *4*, 2037-2051)

Figure 4.3D displays the fluorescence signal from the nanocomposites of Ru-Cur and SDS mainly originates from random aggregates with very few localized fluorescence spots. These strikingly different fluorescence characteristics in the steady-state and confocal

fluorescence measurements indicate an altered mode of interactions between Ru-Cur and negatively charged SDS micelles. Here it is important to note that the presence of excess Na^+ ions at the surface of SDS micelles results in dechlorination of chloride ligands from the Ru-Cur complex (Figure 4.3E). As a consequence of this dechlorination process, the neutral Ru-Cur converts to positively charged species and binds electrostatically with the negatively charged Stern layer of SDS micelles. This leads to the intermicellar aggregation of Ru-Cur- adsorbed SDS micelles.

4.2.2. Interaction of Ru-Cur with liposomes. Photophysical aspects in liposomes.
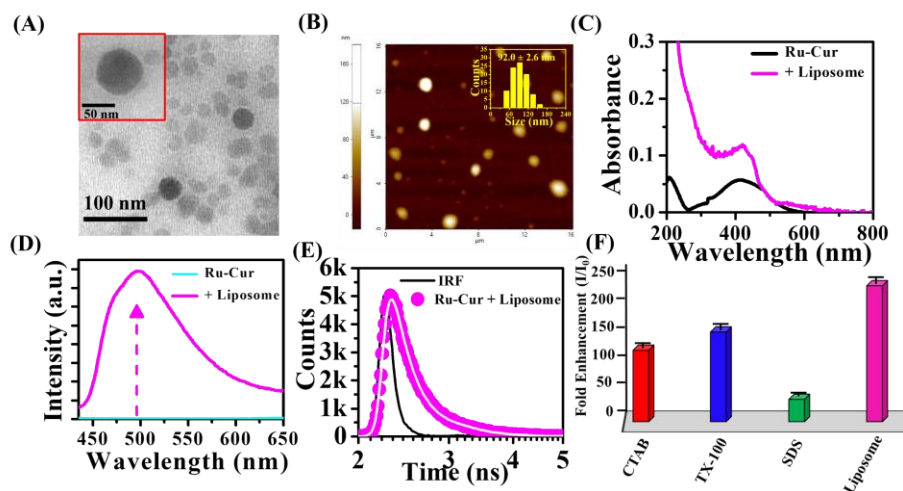
Figure 4.4. (A) HR-TEM, and (B) AFM images of SUV of DPPC. Size distribution histogram of liposomes with their mean size generated by AFM height profile. (C) Absorption, and (D) fluorescence spectra of 5 μM Ru-Cur in the absence and presence of liposomes. (E) Fluorescence decay trace (λ_{ex} =405 nm) of Ru-Cur in the presence of liposome. (F) Fluorescence enhancement factors of 5 Mm Ru-Cur in the presence of 1 mM CTAB, 0.24 mM TX-100, 8 mM SDS, and liposomes upon 1 h of incubation. (Saini *et al. ACS Appl. Nano Mater.* **2021**, *4*, 2037-2051)

Next, we explored the photophysical properties of Ru Cur in the presence of zwitterionic DPPC liposomes. Figure 4.4A and 4.4B shows the HR-TEM and AFM images of uniform spherical liposomes with sizes in the range of 30−140 nm. The estimated partition coefficient of Ru-Cur inside the SUV of the DPPC liposome is 19.3 ± 0.8, which is reasonably higher than that estimated for CTAB and TX-100 micellar systems. The absorption maximum of Ru-Cur shifts from 413 to 423 nm (Figure 4.4C) whereas the fluorescence emission (Figure 4.4D) and fluorescence lifetime (Figure 4.4E) gets enhanced upon excitation in the presence of liposomes. The fluorescence enhancement factor (I/I_0) is estimated to be 219, which is significantly higher than those estimated for the micellar systems (Figure 4.4F) and the fitted parameters reveal an average lifetime of 0.22 ns with lifetime components of 0.14 ns (78%) and 0.50 ns (22%) (Table 4.2).
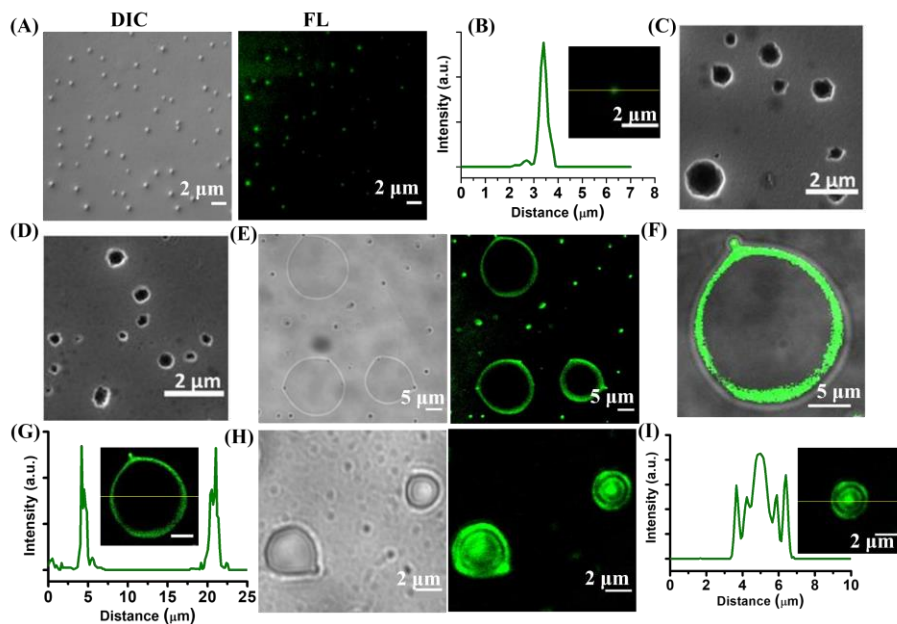
Figure 4.5. Confocal images (A, E, F, and H) and representative line profiles (B, G, and I) of encapsulated Ru-Cur inside the SUV, GUV, and

MLV. FESEM images of (C) GUV, and (D) MLV. (Saini *et al. ACS Appl. Nano Mater.* **2021**, *4*, 2037-2051)

The significantly enhanced fluorescence of liposome-encapsulated Ru-Cur arises as a consequence of the more hydrophobic character of the lipid bilayer compared to that of the simple surfactant-based micellar systems. A similar kind of fluorescence enhancement due to hydrophobic encapsulation of a ruthenium polypyridine complex inside the liposomal matrix has been reported recently *[35]*.

Table 4.2. Fitted fluorescence decay parameters of Ru-Cur in the presence of liposome.

Sample	τ_1 (ns)	a_1	τ_2 (ns)	a_1	$<\tau>$ (ns)	χ^2
Ru-Cur + Liposomes	0.14	0.78	0.50	0.22	0.22	1.05

CLSM. To further establish localization of Ru-Cur at the hydrophobic lipid bilayer of DPPC liposomes, we directly visualized the individual nanocomposites under confocal microscopy. Figure 4.5A displays the confocal images of a Ru-Cur-encapsulated SUV of DPPC. The DIC image of SUV shows the presence of well-dispersed spherical liposomes while the fluorescence image in the green channel reveals distinct diffraction-limited localized fluorescent spots that are colocalized with the spherical SUV of DPPC. The line profile of the selected diffraction-limited fluorescent spot reveals a single sharp peak that signifies the SUV nature of these liposomes (Figure 4.5B). For easy visualization of Ru-Cur inside lipid bilayer, we prepared a GUV and a MLV of DPPC lipids. The morphologies and mean sizes (GUV: 1074 ± 50 and MLV: 831 ± 38 nm) of the fabricated GUV and MLV were characterized using FESEM measurements (Figure 4.5C & D). Figure 4.5E displays the DIC confocal images of well dispersed spherical

Ru-Cur sequestered GUV while the fluorescence image reveals distinct ring-shaped green fluorescent structures. Moreover, the merge image reveals that green fluorescence appears exclusively from the surface of the GUV, signifying the specific binding of Ru-Cur at the hydrophobic lipid bilayer of a GUV (Figure 4.5F). The line profile of the selected fluorescent GUV reveals the presence of two peaks, which is the characteristic of a ring-shaped structure (Figure 4.5G). To check that the present drug can also selectively associate with the multiple hydrophobic lipid bilayer of MLV, we performed confocal imaging with a Ru-Cur-equilibrated MLV of DPPC. The confocal images of a Ru-Cur-encapsulated MLV reveal the presence of uniform onion-like multilamellar architectures with concentric fluorescent rings which signifies that Ru-Cur can selectively bind with the hydrophobic lipid bilayers of MLV (Figures 4.5H). The line profile of the selected fluorescent MLV reveals the characteristics of two concentric rings (Figure 4.5I). Further, no significant alteration of the ζ potentials of liposomes (SUV, GUV, and MLV) was observed upon the loading of neutral Ru-Cur (Table 4.3). Together, confocal measurements of the aqueous dispersions of Ru-Cur with various liposomal structures reveal selective localization of Ru-Cur at the hydrophobic lipid bilayer of liposomes.

Table 4.3. Changes in the ζ-potentials of SUV, GUV, and MLV upon Loading of Ru-Cur.

	Empty liposomes			Ru-Cur loaded liposomes		
	SUV	GUV	MLV	SUV	GUV	MLV
ζ-potential (mV)	-3.1 ± 0.4	-3.9 ± 0.6	-4.2 ± 0.2	-3.5 ± 0.3	-4.3 ± 0.4	-4.4 ± 0.5

4.2.3. Interaction of Ru-Cur with coacervate nano-droplets. Photophysical aspects in nanodroplets.

We have fabricated two different types of coacervate nanodroplets, namely, CD and ATP nanodroplets, in the presence of the cationic polyelectrolyte PDADMAC *[24]*. While the fabricated CD nanodroplets exhibit highly stable and inherent blue luminescence because of the presence of blue-emitting CDs, the ATP nanodroplets exhibit no intrinsic fluorescence.
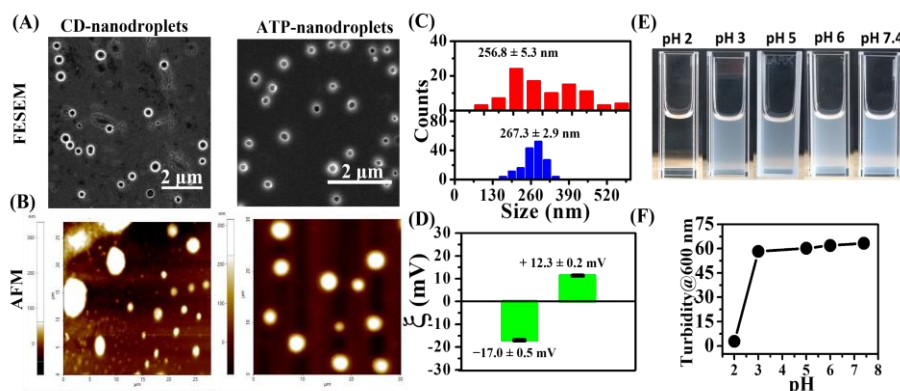
Figure 4.6. (A) FESEM, and (B) AFM images of CD and ATP nanodroplets. (C) Size distribution histograms of CD and ATP nanodroplets estimated from the AFM height profiles. (D) ζ potentials of CD and ATP nanodroplets. (E) Daylight photographs of aqueous dispersions of ATP nanodroplets ([ATP] = 0.066 mM and [PDADMAC] = 0.2 mM) at different pH values. (F) Changes in the turbidity at 600 nm as a function of the solution pH of ATP nanodroplets. (Saini *et al. ACS Appl. Nano Mater.* **2021**, *4*, 2037-2051)

Therefore, CD nanodroplets provide an added advantage for in vitro and in vivo bioimaging applications as an inherent optical marker for direct spatiotemporal visualization. However, for the quantitative estimation of the loading and release profile, we utilized ATP nanodroplets because the absorption and luminescence of CD interfere with the fluorescence signal

of the loaded Ru-Cur. The fabricated coacervate nanodroplets were characterized using FESEM, AFM, and ζ-potential measurements. The FESEM and AFM images of both CD and ATP system reveal well-dispersed spherical nano-droplets having mean sizes of 256.8 ± 5.3 and 267.3 ± 2.9 nm along with coalescence phenomena (Figure 4.6A, B, & C). The estimated ζ potentials are -17.0 ± 0.5 and $+12.3 \pm 0.2$ mV for CD and ATP nanodroplets, respectively (Figure 4.6D). Further, we explored the colloidal stability of ATP nanodroplets as a function of the solution pH in the range between 7.4 and 2 by monitoring the turbidity of the aqueous dispersions of nanodroplets. Figure 4.6E displays the daylight photographs of aqueous dispersions of ATP nanodroplets at different pH values. While the aqueous dispersions remain opaque in the pH range of 7.4−3, they suddenly turn clear isotropic at pH 2. Similarly, turbidity measurements at different pH values reveal a sudden drop of the turbidity at pH 2 (Figure 4.6F). These findings suggest the pH-responsive structural disassembly of ATP nanodroplets, and complete disassembly occurs at a pH value of 2.

Next, we explored the interactions of Ru-Cur with ATP nanodroplets using UV−vis and fluorescence spectroscopy. Ru-Cur in the presence of ATP nanodroplets shows a broad structureless absorption band centered at 428 nm with a red shift of 15 nm suggests the association of Ru-Cur with the coacervate phase whereas the 399-fold enhanced fluorescence emission appears at 537 nm upon excitation at 425 nm, which is even higher than that estimated for the liposomal system (Figure 4.7A, B, & C). The highly intense visible green fluorescence from coacervate-associated Ru-Cur is clearly evident upon UV illumination at 365 nm (Figure 4.7C-inset). Moreover, the estimated equilibrium partition coefficient of Ru-Cur inside these ATP nanodroplets is found to be 76.6 ± 0.8, These findings not only reveal a strong association of Ru-Cur with the coacervate phase but also

indicate a more hydrophobic microenvironment inside these coacervate nano-droplets. The fluorescence lifetime of Ru-Cur drastically increases to 0.98 ns with lifetime components of 0.84 ns (69%) and 1.28 ns (31%) (Figure 4.7D & table 4.4).

Table 4.4. Fitted fluorescence decay parameters of Ru-Cur in the presence of ATP-nanodroplets.

Sample	τ_1 (ns)	a_1	τ_2 (ns)	a_1	$<\tau>$ (ns)	χ^2
Ru-Cur + Nanodroplets	0.84	0.69	1.28	0.31	0.98	1.30

Here it is important to note that the fluorescence maximum of Ru-Cur appears at 537 nm, which is significantly red-shifted compared to that in CTAB, TX-100, and liposomes. However, the peak position closely matches that in SDS micelles. This observation can be explained by considering the presence of a significant amount of bound water inside the microenvironment of these liquid nano-droplets. This argument gains support from an earlier study with the solvatochromic dye Nile Red, where it has been shown that the interior of ATP nanodroplets is significantly more polar than DMSO but less hydrophilic than bulk water *[24]*.
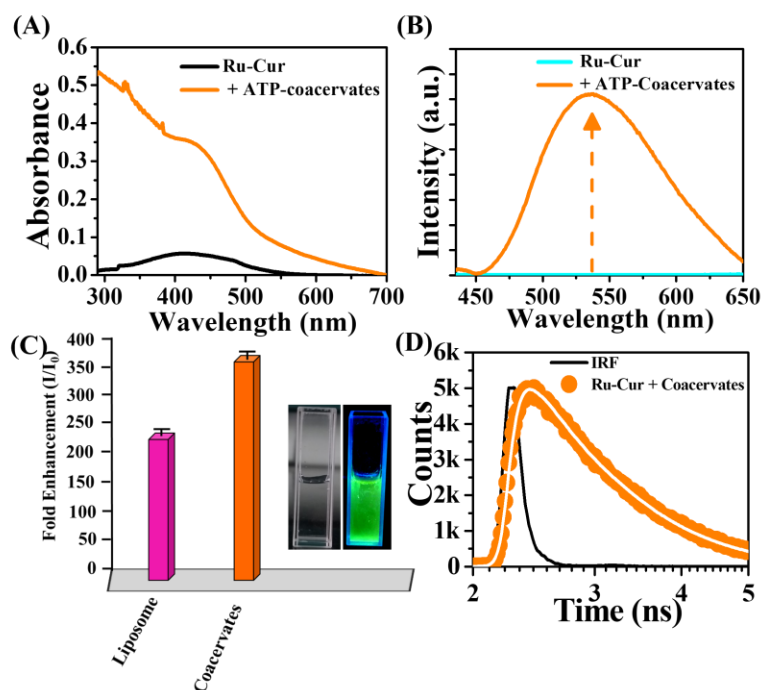
Figure 4.7. (A) Absorption, and (B) fluorescence spectra of 5 µM Ru-Cur in the absence and presence of ATP nanodroplets. (C) Fluorescence enhancement factors of Ru-Cur in the presence of liposomes and ATP nanodroplets. The inset shows the daylight and UV-light ($\lambda_{ex} = 365$ nm) photographs of Ru-Cur aqueous dispersions in the presence of ATP nanodroplets. (D) Fluorescence decay trace ($\lambda_{ex} = 405$ nm) of Ru-Cur in the presence of ATP-nanodroplets. (Saini *et al. ACS Appl. Nano Mater.* **2021**, *4*, 2037-2051)

CLSM. Next, we performed confocal fluorescence imaging measurements to determine the location of the hydrophobically encapsulated Ru-Cur inside the coacervate phase. Figure 4.8A & B displays well-dispersed intact spherical morphologies of both droplets with blue fluorescence exclusively comes from the CD-embedded coacervate nanodroplets (top panel) along with uniform green signal (top & bottom

panel). These observations clearly signify uniform and homogeneous loading of Ru-Cur inside the nanodroplets. Moreover, the morphology and size of the Ru-Cur-loaded CD nanodroplets remain unaltered but the sizes of the Ru-Cur-loaded ATP coacervates increases (721 ± 13 nm) compare to bare coacervates, which may be due to the swelling and enhanced coalescence events (Figure 4.8C).
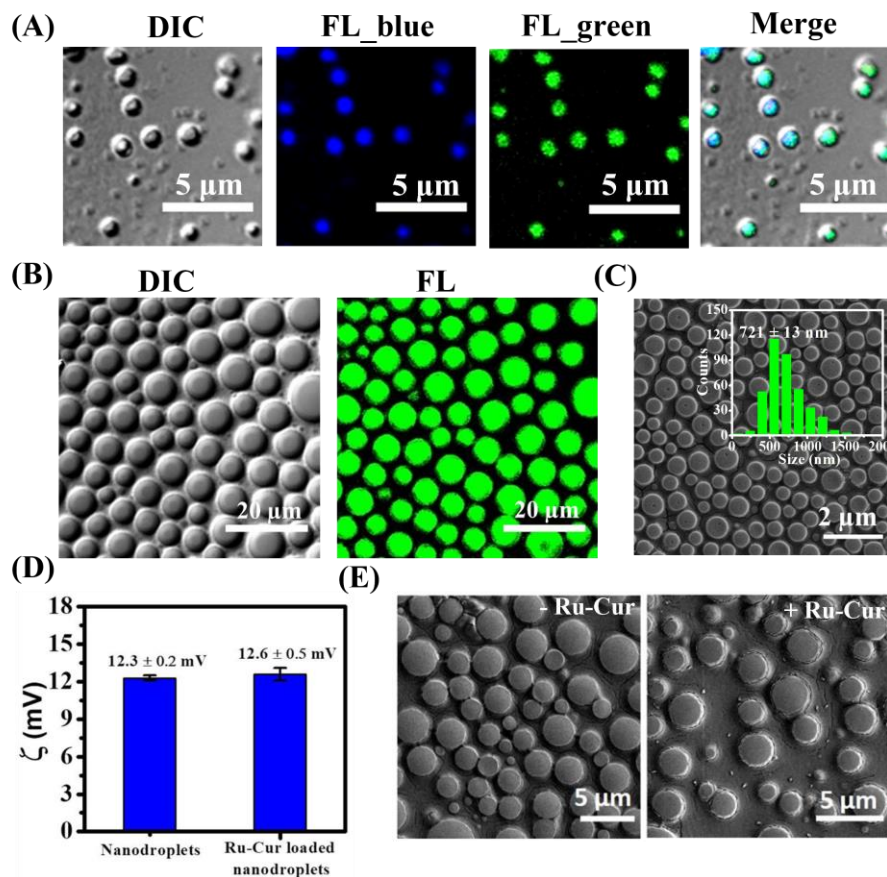
Figure 4.8. Confocal images of an encapsulated Ru-Cur inside (A) CD, and (B) ATP nanodroplets. (C) FESEM image of Ru-Cur loaded ATP-nanodroplets at pH 7.4. The inset shows the size distribution histogram. (D) The estimated ζ-potentials of ATP-nanodroplets in the absence and presence of Ru-Cur at pH 7.4. (E) FESEM images of ATP-nanodroplets in

the absence and presence of Ru-Cur over a period of 7-days. (Saini *et al.*
ACS Appl. Nano Mater. **2021**, *4*, 2037-2051)

Here, it is important to note that swelling and deswelling phenomena
are common characteristics of self-assembled nanoassemblies including
liquid nanodroplets and depend on various factors such as the loading
content, charge density of loaded molecules, ionic strength, pH, and
temperature *[36]*. Notably, the ζ potential of nanodroplets remains
unchanged upon sequestration of Ru-Cur (Figure 4.8D). Moreover, the
morphology and stability of these ATP nanodroplets remain unaltered in the
absence and presence of Ru-Cur over a period of 7 days (Figure 4.8E). Next,
we quantitatively estimated the pH- and temperature-dependent in vitro
controlled-release profiles of the loaded Ru-Cur inside liposomes and
coacervates to illustrate the fundamental release mechanism.

**4.2.4. Controlled release of Ru-Cur from liposomes and coacervates.
Loading and release profiles in liposomes and coacervates**

To determine the stability of Ru-Cur-loaded nanoassemblies, we monitored
the time-dependent changes in the fluorescence signal of Ru-Cur-loaded
nano-assemblies (TX-100 micelles, SUV, and ATP nanodroplets) at pH 7.4
and 25 °C over a period of 7 days. It was observed that the fluorescence
intensity of encapsulated Ru-Cur gradually decreases over time, and shows
a total loss of 28, 14, and 6% in intensity through micelles, liposomes, and
nanodroplets over a period of 7 days (Figure 4.9A). These findings clearly
highlight the structural stability of Ru-Cur-loaded liposomes and ATP
nanodroplets over conventional TX-100 micelles. To further substantiate
this argument, we performed drug leakage assay at pH 7.4 and 37 °C and
drug leakage is found to be maximum for TX-100 micelles (31%), followed
by liposomes (9%) and ATP nanodroplets (5%) over a period of 120 h
(Figure 4.9B). Therefore, the loading and subsequent controlled release of

Ru-Cur was investigated inside SUV and ATP nanodroplets at pH 7.4, 6.5, 6.0, and 5 (Figure 4.9C).
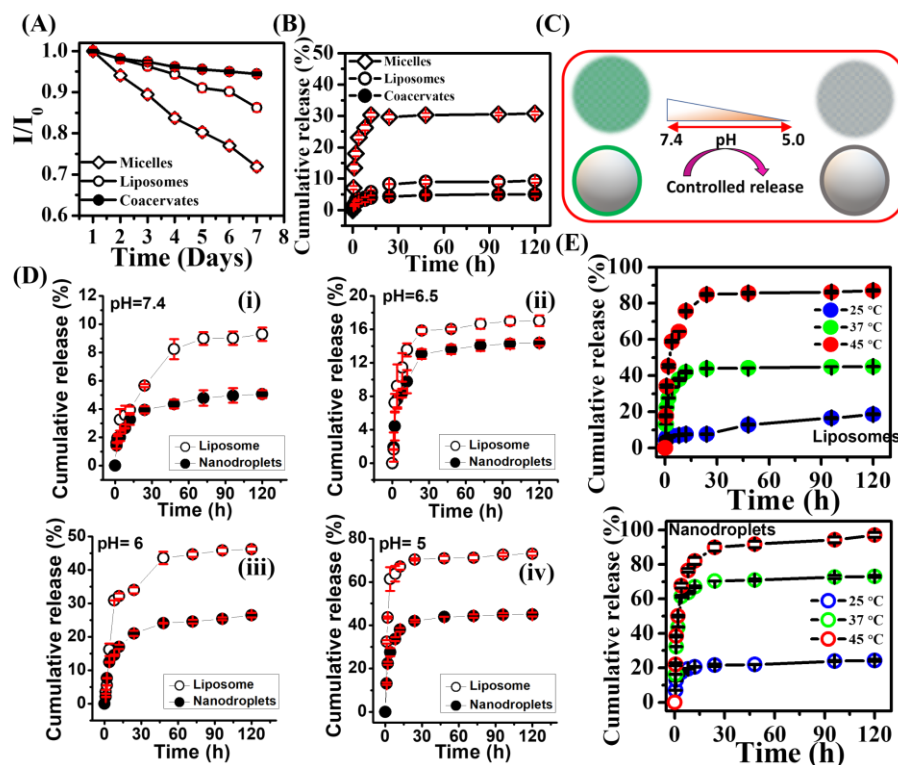
Figure 4.9. Changes in the fluorescence intensity of Ru-Cur loaded nano-assemblies over a period of 7-days at 25 °C in pH 7.4 aqueous medium. (B) Drug leakage assay of Ru-Cur loaded TX-100 micelles, liposomes and ATP-nanodroplets at 37 °C in pH 7.4 PBS. (C) Schematic representation of the pH-responsive release of Ru-Cur from liposome and ATP nanodroplet. (D) In vitro release profiles of Ru-Cur from liposomes and ATP nanodroplets at pH values of (i) 7.4, (ii) 6.5, (iii) 6.0, and (iv) 5.0. (E) Temperature-dependent release profiles of Ru-Cur loaded ATP-nanodroplets and liposomes in pH 5.0 PBS. (Saini *et al. ACS Appl. Nano Mater.* **2021**, *4*, 2037-2051)

These pH values were selected by keeping in view of the physiological pH of normal tissue and blood (pH 7.4), extracellular pH of

the tumor cell (pH 6.5), and intracellular pH of the endosome/lysosome (pH 6−5). The loading content and encapsulation efficiency of Ru-Cur in SUV of DPPC were estimated to be 9.5 and 92.1%, respectively. In contrast, the estimated loading content and encapsulation efficiency in ATP nanodroplets revealed significantly higher values of 31.2 and 99.6%, respectively. Notably, these estimated values exceed most of earlier-reported figures for different delivery vehicles such as liposomes, PMs, polymer NPs, MOFs, and coacervates for various cargos. At the physiological pH of 7.4, the release profiles reveal very low cumulative releases of 9 and 5% over a 120-h period for SUV and coacervates, respectively. While the cumulative releases at pH 6.5 reach 17 and 14.4%, the same at pH 6 reach 46.2 and 26.5% for SUV and coacervates, respectively (Figure 4.9D). Notably, the cumulative releases increase sharply at pH 5 for both systems and saturate at values of 73 and 45% for the SUV and coacervates, respectively (Figure 4.9C). More importantly, the release rate of Ru-Cur in coacervates is appreciably slower compared to that in DPPC liposomes, signifying a more controlled and sustained release mechanism in coacervates (Figure 4.9D).

Next, to determine the effect of temperature, we investigated the release profiles at 25, 37, and 45 °C in pH 5 PBS (Figure 4.9E). While the cumulative release at 25 °C shows a saturation value of 19%, it increases to 45 and 87% at an equilibration temperature of 37 and 45 °C, respectively along with similar trend in case of liposomes (Figure 4.9E). We believe that this thermal deswelling process triggers the release of encapsulated Ru-Cur from ATP nanodroplets. On the other hand, the enhanced release of Ru-Cur from DPPC liposome at higher temperature can be explained by considering temperature-induced gel-to-liquid crystalline phase transition ($T_m \sim 42$ °C), which enhances the fluidity of the lipid bilayer *[37]*. Recently, we

demonstrated that the structural stability of the CD nanodroplets decreases rapidly below pH 5 as a consequence of protonation of the surface carboxylate groups of CDs (ζ-potential at pH 4.5 = +15.4 ± 0.7 mV) and subsequent weak electrostatic interaction with the positively charged PDADMAC *[38]*. On the other hand, the reported pK_a values of ATP are 6.5 and 4 for secondary phosphate and amino groups, respectively, and it is expected that ATP molecules inside the nanodroplets will undergo partial protonation at a pH value of ≤6.5 *[23–25]*.

To know the pH-dependent colloidal stability of Ru-Cur-loaded ATP- nanodroplets, we monitored the changes in the turbidity of an aqueous dispersion of Ru-Cur-loaded nanodroplets as a function of the solution pH (Figure 4.10A). Notably, the turbidity remains unaltered in the pH range 6-3 but disappears completely at a pH value of 2, which is similar to that observed earlier for unloaded ATP nano-droplets (Figure 4.10A). Further, AFM measurements reveal the intact and spherical morphology of unloaded ATP nano-droplets at pH 5 (Figure 10B). Therefore, the downward trend observed at lower acidic pH (6−3) in the case of Ru-Cur-loaded nanodroplets suggests partial disassembly due to the protonation of ATP molecules inside the swelled nanodroplets. To substantiate this argument, we directly visualized the morphology and luminescence behavior of ATP nanodroplets at pH 5 under AFM and confocal microscopy (Figure 4.10C & D). AFM and confocal images clearly reveal partial disassembled and structural distorted polymeric network of these coacervates at pH 5 along with green background signal of released Ru-Cur (Figure 4.10C & D). On the other hand, the phosphate groups of DPPC lipids at lower acidic pH (~5) undergo protonation due to the acid− base equilibrium, which triggers liposome fusion and the subsequent release of the bilayer-trapped Ru-Cur *[39]*. To gain further insight into the pH-dependent release mechanism, we

used a comprehensive semiempirical mathematical model to analyze our experimental release profile data.
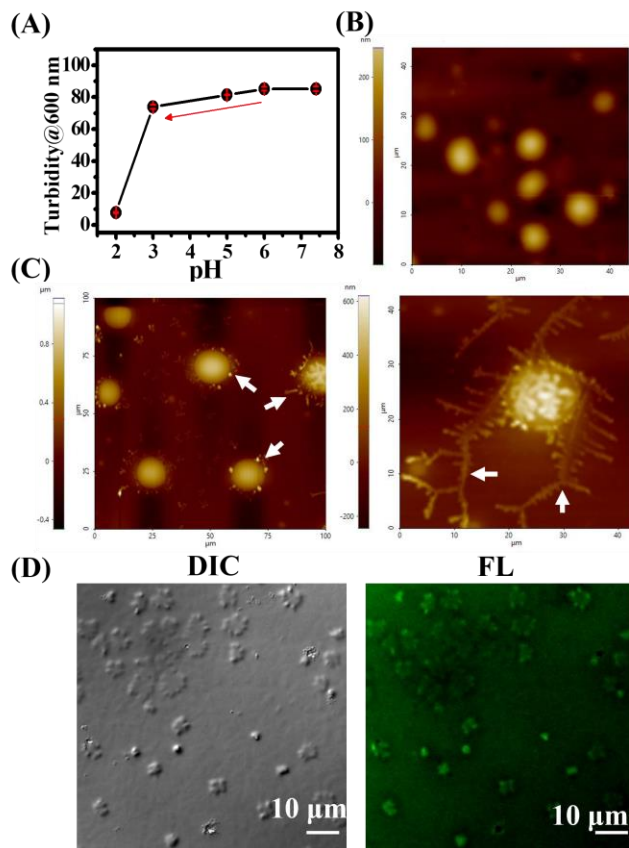
Figure 4.10. (A) Changes in the turbidity of Ru-Cur-loaded ATP nanodroplets at 600 nm as a function of the solution pH. The red arrow indicates the downward trend of the turbidity in the pH range of 6–3. (B) AFM image of unloaded ATP-nanodroplets at pH 5. (C) AFM, and (D) confocal images of Ru-Cur-loaded ATP nanodroplets at pH 5. The white arrows in the AFM images indicate partially disassembled nanodroplets. (Saini *et al. ACS Appl. Nano Mater.* **2021**, *4*, 2037-2051)

4.2.5. Mechanism of release from ATP nanodroplets

The knowledge of the in vitro release mechanism of an encapsulated drug from nanocarriers provides various useful structural and kinetic parameters

for their in vivo applications inside cellular environments. Therefore, we analyzed the experimental release profiles of Ru-Cur-loaded ATP coacervates with a semiempirical power law mathematical model developed by Siepmann and Peppas for the polymeric matrix *[40]*, which can be expressed according to the following equations:

$$\frac{M_t}{M_\infty} = kt^n \tag{1}$$

$$\log\left(\frac{M_t}{M_\infty}\right) = \log k + n \log t \tag{2}$$

where M_t and M_∞ are the absolute cumulative drug release amounts at time t and infinity, respectively. The parameter k is a constant, depends on the structural and geometric properties of the nanocarrier, and signifies the rate of release. The parameter n is the release exponent and determines the release mechanism. Here, it should be noted that, for accurate determination of the release mechanism, one should use the release curve where $M_t/M_\infty < 0.6$ *[40, 41]*.
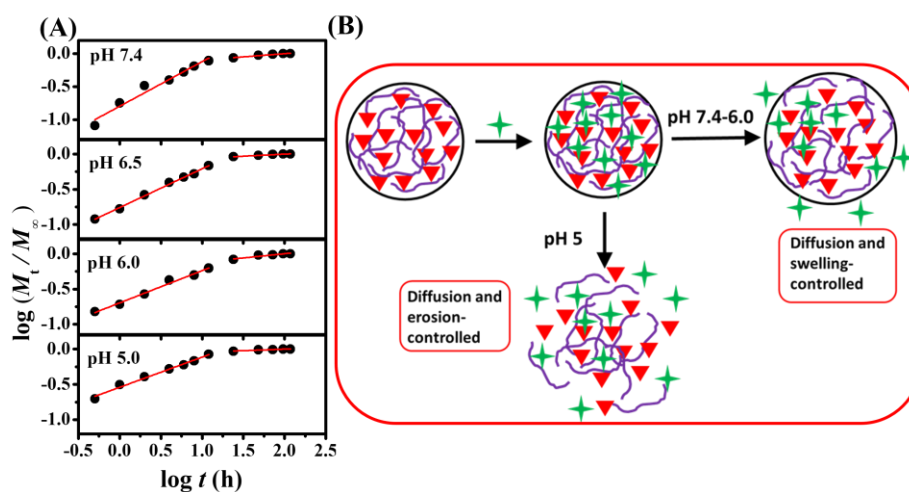
Figure 4.11. (A) Plot of log (M_t /M_∞) against log t for Ru-Cur loaded ATP-nanodroplets at different pH values. (B) Schematic illustration of pH-

dependent release mechanisms for Ru-Cur-loaded ATP nanodroplets. (Saini *et al. ACS Appl. Nano Mater.* **2021**, *4*, 2037-2051)

For spherical nanocarriers, depending on the value of *n*, one can have four distinct release mechanisms, namely, Fickian diffusion-controlled ($n = 0.43$), swelling-controlled ($n = 0.85$), diffusion- and swelling-controlled ($0.43 < n < 0.85$), and anomalous transport or diffusion- and erosion-controlled ($n < 0.43$) transport *[10, 41]*. The experimental data were fitted separately in two-time intervals of the release profile, namely, $0.5-12$ and $24-120$ h (Figure 4.11A). The fitted parameters from the first-time interval were used to understand the release mechanism and tabulated in Table 4.5. It is evident that the *n* values for pH 7.4, 6.5, and 6.0 are >0.43 but less than 0.85, suggesting that the release of Ru-Cur occurs via diffusion- and swelling-controlled mechanisms through the membrane-free nanostructure of ATP nanodroplets.

Table 4.5. Fitted Parameters for the Drug Release Profile in the Time Interval of $0.5-12$ h.

pH	*n*	*k*	Correlation coefficient (*R*)	Pearson's r	Mechanism
7.4	0.677	0.159	0.956	0.983	diffusion and swelling
6.5	0.550	0.174	0.996	0.998	
6.0	0.457	0.200	0.986	0.994	
5.0	0.427	0.287	0.986	0.994	Diffusion and erosion

However, the estimated value of n at pH 5 is 0.427, indicating that the release of Ru-Cur is dominated by a diffusion- and erosion-controlled mechanism. This mechanism corroborates with our observation of a partially disassembled architecture of Ru-Cur- loaded ATP nanodroplets at pH 5. On the other hand, the value of k increases from 0.159 to 0.200 with a decrease in the pH value from 7.4 to 6 (Table 4.5). This signifies that the Ru-Cur release rate from the coacervate phase increases with a decrease in the pH value. This can be explained by considering the facile release of the loaded Ru-Cur from the coacervate phase due to swelling of the liquid nanodroplets and a subsequent relaxed structure at lower acidic pH (Figure 4.11A). This swelling of the coacervates at lower acidic pH is caused by partial protonation of the ATP molecules by H_3O^+. Notably, k increases appreciably to a value of 0.287 at pH 5, indicating more relaxed and open structures of these ATP nanodroplets due to the protonation-induced erosion of these nanoassemblies (Figure 4.11B). Therefore, our present study reveals that the semiempirical power law model can successfully account for the present in vitro release profiles of Ru-Cur from self-assembled ATP nanodroplets. The present findings not only provide a fundamental understanding of the specific loading and release profiles of Ru-Cur from various nanoassemblies but also illustrate the potential of coacervate nanodroplets as pH-responsive nanocarriers for the controlled and sustained delivery of anticancer cargos.

4.3. Conclusions

In summary, we have illustrated the potential of self-assembled coacervates toward the controlled and sustained release of hydrophobically encapsulated model anticancer drug Ru-Cur. Moreover, the physicochemical properties of an encapsulated drug inside various

nanoassemblies have been quantitatively compared using spectroscopic and microscopic techniques. It has been observed that the unique membrane-free architecture of coacervates provides an ideal microenvironment for the efficient entrapment of the hydrophobic drug Ru-Cur. Notably, the encapsulated drug shows several 100-fold enhancements in its intrinsic green fluorescence upon association with a hydrophobic microenvironment of coacervates. This unprecedented fluorescence enhancement of a hydrophobically encapsulated Ru-Cur may find tremendous importance in bioimaging applications as an optical marker. Confocal imaging of individual nanoassemblies reveals the uniform distribution of a hydrophobically encapsulated Ru-Cur without any unnecessary morphological changes in the nanoassemblies. Finally, the pH-responsive controlled release of a hydrophobically encapsulated Ru-Cur has been quantitatively compared for liposomes and coacervates at 37 °C in the pH range of 7.4−5. It has been observed that the coacervate encapsulated Ru-Cur complexes undergo controlled and sustained release compared to that from conventional liposome nanocarriers. The experimental release profiles have been quantitatively analyzed using a semiempirical power law model. While the fitted parameters reveal a diffusion- and swelling-controlled drug release mechanism in the pH range of 7.4−6, the drug release at pH 5 proceeds via a diffusion- and erosion-controlled mechanism. Our present findings illustrate the fundamental loading and in vitro release mechanism of a hydrophobically encapsulated therapeutically active Ru-Cur drug inside the coacervates and pave the way for their utilization toward controlled and sustained drug delivery inside the cellular compartments.

4.4. References

1. Ikoba U., Peng H., Li H., Miller C., Yu C., Wang Q. (2015), Nanocarriers in therapy of infectious and inflammatory diseases, Nanoscale, 7(10), 4291–4305. (DOI:10.1039/C4NR07682F)

2. Wong P. T., Choi S. K. (2015), Mechanisms of drug release in nanotherapeutic delivery systems, Chem. Rev., 115(9), 3388–3432. (DOI:10.1021/cr5004634)

3. Scicluna M. C., Vella-Zarb L. (2020), Evolution of nanocarrier drug-delivery systems and recent advancements in covalent organic framework–drug systems, ACS Appl. Nano Mater., 3(4), 3097–3115. (DOI:10.1021/acsanm.9b02603)

4. Su Y., Xie Z., Kim G. B., Dong C., Yang J. (2015), Design strategies and applications of circulating cell-mediated drug delivery systems, ACS Biomater. Sci. Eng., 1(4), 201–217. (DOI:10.1021/ab500179h)

5. Yang G., Liu Y., Wang H., Wilson R., Hui Y., Yu L., et al. (2019), Bioinspired core–shell nanoparticles for hydrophobic drug delivery, Angew. Chem. Int. Ed., 58(40), 14357–14364. (DOI:10.1002/anie.201908357)

6. Pattni B. S., Chupin V. V., Torchilin V. P. (2015), New developments in liposomal drug delivery, Chem. Rev., 115(19), 10938–10966. (DOI:10.1021/acs.chemrev.5b00046)

7. Sawant R. R., Torchilin V. P. (2010), Liposomes as 'smart' pharmaceutical nanocarriers, Soft Matter, 6(17), 4026. (DOI:10.1039/b923535n)

8. Tripathy N., Ahmad R., Ko H. A., Khang G., Hahn Y-B. (2015), Enhanced anticancer potency using an acid-responsive ZnO-incorporated liposomal drug-delivery system, Nanoscale, 7(9), 4088–4096. (DOI:10.1039/C4NR06979J)

9. Yao C., Wang P., Li X., Hu X., Hou J., Wang L., et al. (2016), Near-infrared-triggered azobenzene-liposome/up conversion nanoparticle hybrid vesicles for remotely controlled drug delivery to overcome cancer multidrug resistance, Adv. Mater., 28(42), 9341–9348. (DOI:10.1002/adma.201503799)

10. Xu M., Zhang C. Y., Wu J., Zhou H., Bai R., Shen Z., et al. (2019), PEG-detachable polymeric micelles self-assembled from amphiphilic copolymers for tumor-acidity-triggered drug delivery and controlled release, ACS Appl. Mater. Interfaces, 11(6), 5701–5713. (DOI:10.1021/acsami.8b13059)

11. Nasongkla N., Bey E., Ren J., Ai H., Khemtong C., Guthi J. S., et al. (2006), Multifunctional polymeric micelles as cancer-targeted, MRI-ultrasensitive drug delivery systems, Nano Lett., 6(11), 2427–2430. (DOI:10.1021/nl061412u)

12. Meng F., Zhong Z., Feijen J. (2009), Stimuli-responsive polymersomes for programmed drug delivery, Biomacromolecules, 10(2), 197–209. (DOI:10.1021/bm801127d)

13. Medina S. H., El-Sayed M. E. H. (2009), Dendrimers as carriers for delivery of chemotherapeutic agents, Chem. Rev., 109(7), 3141–3157. (DOI:10.1021/cr900174j)

14. Nicolas J., Mura S., Brambilla D., Mackiewicz N., Couvreur P. (2013), Design, functionalization strategies and biomedical applications of targeted biodegradable/biocompatible polymer-based nanocarriers for drug delivery, Chem. Soc. Rev., 42(3), 1147–1235. (DOI:10.1039/C2CS35265F)

15. Rossi F., Castiglione F., Salvalaglio M., Ferro M., Moioli M., Mauri E., et al. (2017), On the parallelism between the mechanisms behind chromatography and drug delivery: the role of interactions with a

stationary phase, Phys. Chem. Chem. Phys., 19(18), 11518–11528. (DOI:10.1039/C7CP00832E)

16. Shang W., Peng L., Guo P., Hui H., Yang X., Tian J. (2020), Metal–Organic frameworks as a theranostic nanoplatform for combinatorial chemo-photothermal therapy adapted to different administration, ACS Biomater. Sci. Eng., 6(2), 1008–1016. (DOI:10.1021/acsbiomaterials.9b01075)

17. Li Y., Cong H., Wang S., Yu B., Shen Y. (2020), Liposomes modified with bio-substances for cancer treatment, Biomater. Sci., 8(23), 6442–6468. (DOI:10.1039/D0BM01531H)

18. Liu G-Y., Li M., Zhu C-S., Jin Q., Zhang Z-C., Ji J. (2014), Charge-conversional and pH-sensitive PEGylated polymeric micelles as efficient nanocarriers for drug delivery: Charge-conversional and pH-sensitive PEGylated polymeric, Macromol. Biosci., 14(9), 1280–1290. (DOI:10.1002/mabi.201400162)

19. Su J., Chen F., Cryns V. L., Messersmith P. B. (2011), Catechol polymers for pH-responsive, targeted drug delivery to cancer cells, J. Am. Chem. Soc., 133(31), 11850–11853. (DOI:10.1021/ja203077x)

20. Senthilkumar T., Zhou L., Gu Q., Liu L., Lv F., Wang S. (2018), Conjugated polymer nanoparticles with appended photo-responsive units for controlled drug delivery, release, and imaging, Angew. Chem. Int. Ed., 57(40), 13114–13119. (DOI:10.1002/anie.201807158)

21. Raemdonck K., Naeye B., Buyens K., Vandenbroucke R. E., Høgset A., Demeester J., et al. (2009), Biodegradable dextran nanogels for RNA interference: Focusing on endosomal escape and intracellular siRNA delivery, Adv. Funct. Mater., 19(9), 1406–1415. (DOI:10.1002/adfm.200801795)

22. Keating C. D. (2012), Aqueous phase separation as a possible route to compartmentalization of biological molecules, Acc. Chem. Res., 45(12), 2114–2124. (DOI:10.1021/ar200294y)

23. Frankel E. A., Bevilacqua P. C., Keating C. D. (2016), Polyamine/nucleotide coacervates provide strong compartmentalization of Mg^{2+}, nucleotides, and RNA, Langmuir, 32(8), 2041–2049. (DOI:10.1021/acs.langmuir.5b04462)

24. Williams D. S., Koga S., Hak C. R. C., Majrekar A., Patil A. J., Perriman A. W., et al. (2012), Polymer/nucleotide droplets as bio-inspired functional micro-compartments, Soft Matter, 8(22), 6004. (DOI:10.1039/c2sm25184a)

25. Koga S., Williams D. S., Perriman A. W., Mann S. (2011), Peptide–nucleotide microdroplets as a step towards a membrane-free protocell model, Nat. Chem., 3(9), 720–724. (DOI:10.1038/nchem.1110)

26. Dora Tang T-Y., Rohaida Che Hak C., Thompson A. J., Kuimova M. K., Williams D. S., Perriman A. W., et al. (2014), Fatty acid membrane assembly on coacervate microdroplets as a step towards a hybrid protocell model, Nat. Chem., 6(6), 527–533. (DOI:10.1038/nchem.1921)

27. van Swaay D., Tang T-Y. D., Mann S., de Mello A. (2015), Microfluidic formation of membrane-free aqueous coacervate droplets in water, Angew. Chem. Int. Ed., 54(29), 8398–8401. (DOI:10.1002/anie.201502886)

28. Priftis D., Leon L., Song Z., Perry S. L., Margossian K. O., Tropnikova A., et al. (2015), Self-assembly of α-helical polypeptides driven by complex coacervation, Angew. Chem. Int. Ed., 54(38), 11128–11132. (DOI:10.1002/anie.201504861)

29. Priftis D., Tirrell M. (2012), Phase behaviour and complex coacervation of aqueous polypeptide solutions, Soft Matter, 8(36), 9396–9405. (DOI:10.1039/C2SM25604E)

30. Priftis D., Xia X., Margossian K. O., Perry S. L., Leon L., Qin J., et al. (2014), Ternary, tunable polyelectrolyte complex fluids driven by complex coacervation, Macromolecules, 47(9), 3076–3085. (DOI:10.1021/ma500245j)

31. Adhikary R., Carlson P. J., Kee T. W., Petrich J. W. (2010), Excited-state intramolecular hydrogen atom transfer of curcumin in surfactant micelles, J. Phys. Chem. B, 114(8), 2997–3004. (DOI:10.1021/jp9101527)

32. Mukherjee T. K., Ahuja P., Koner A. L., Datta A. (2005), ESPT of 2-(2'-Pyridyl)benzimidazole at the micelle−water interface: Selective enhancement and slow dynamics with sodium dodecyl sulfate, J. Phys. Chem. B, 109(25), 12567–12573. (DOI:10.1021/jp051574z)

33. Mandal S., Banerjee C., Ghosh S., Kuchlyan J., Sarkar N. (2013), Modulation of the photophysical properties of curcumin in nonionic surfactant (Tween-20) forming micelles and niosomes: A comparative study of different microenvironments, J. Phys. Chem. B, 117(23), 6957–6968. (DOI:10.1021/jp403724g)

34. Renfrew A. K., Bryce N. S., Hambley T. W. (2013), Delivery and release of curcumin by a hypoxia-activated cobalt chaperone: a XANES and FLIM study, Chem. Sci., 4(9), 3731. (DOI:10.1039/c3sc51530c)

35. Shen J., Kim H-C., Wolfram J., Mu C., Zhang W., Liu H., et al. (2017), A liposome encapsulated ruthenium polypyridine complex as a theranostic platform for triple-negative breast cancer, Nano Lett., 17(5), 2913–2920. (DOI:10.1021/acs.nanolett.7b00132)

36. Schuurmans C. C. L., Abbadessa A., Bengtson M. A., Pletikapic G., Eral H. B., Koenderink G., et al. (2018), Complex coacervation-based loading and tunable release of a cationic protein from monodisperse glycosaminoglycan microgels, Soft Matter, 14(30), 6327–6341. (DOI:10.1039/C8SM00686E)

37. Moussa Z., Chebl M., Patra D. (2017), Interaction of curcumin with 1,2-dioctadecanoyl-sn-glycero-3-phosphocholine liposomes: Intercalation of rhamnolipids enhances membrane fluidity, permeability and stability of drug molecule, Colloids Surf. B: Biointerfaces, 149, 30–37. (DOI:10.1016/j.colsurfb.2016.10.002)

38. Saini B., Singh R. R., Nayak D., Mukherjee T. K. (2020), Biocompatible pH-Responsive luminescent coacervate nanodroplets from carbon dots and poly(diallyldimethylammonium chloride) toward theranostic applications, ACS Appl. Nano Mater., 3(6), 5826–5837. (DOI:10.1021/acsanm.0c00995)

39. Petelska A. D., Naumowicz M., Figaszewski Z. A. (2006), The interfacial tension of the lipid membrane formed from lipid–cholesterol and lipid–lipid systems, CBB, 44(2), 205–212. (DOI:10.1385/CBB:44:2:205)

40. Siepmann J. (2001), Modeling of drug release from delivery systems based on hydroxypropyl methylcellulose (HPMC), Adv. Drug Deliv. Rev., 48(2–3), 139–157. (DOI:10.1016/S0169-409X(01)00112-0)

41. Li Y., Li H., Wei M., Lu J., Jin L. (2009), pH-Responsive composite based on prednisone-block copolymer micelle intercalated inorganic layered matrix: Structure and in vitro drug release, Chem. Eng. J., 151(1–3), 359–366. (DOI:10.1016/j.cej.2009.03.049)

Chapter 5

> ## *Nanocatalysis under Nanoconfinement: A Metal-Free Hybrid Coacervate Nanodroplet as a Catalytic Nanoreactor for Efficient Redox Reactions*

Chapter 5

5.1. Introduction

Nature uses nanoconfinement phenomenon to drive various biochemical transformations in a highly regulated and efficient manner by modulating their chemical reactivity and surface chemistry *[1, 2]*. The concept of compartmentalization of catalysts and substrates at one place finds tremendous importance in fundamental and industrial applications as it accelerates the reaction kinetics with high conversion yields, altered selectivity and energetics along with drive the incompatible reactions to completion efficiently *[3, 4]*. In recent years, designing of artificial synthetic nanoreactors for large-scale catalytic transformations has gained significant attention with the aim to mimic the highly efficient enzymatic reactions in confined cellular environments. But the scope of synthetic nanoreactors toward a diverse range of chemical transformations is limited by their inherent structural constraints such as fixed cavity sizes, limited catalytic centers along with the restricted scope for free diffusion of substrates and products. Therefore, the facile synthetic procedure with non-harsh experimental conditions and reusability of the catalytic nanoreactor for multiple cycles is highly desirable.

In this context, various artificial catalytic nanoreactors such as porous zeolite based nanoreactors *[5, 6]*, mesoporous silica NPs *[7]*, polymeric hydrogels *[8]*, yolk−shell NPs *[9]*, carbon nanotubes *[10]*, hollow carbon spheres *[11]*, mesoporous carbon-organosilica NPs *[12]*, metal nanocages *[13]*, synthetic coordination cages *[14]* water microdroplets *[15]*, covalent organic frameworks *[16]*, and metal organic frameworks *[17]* have been fabricated and utilized to drive a diverse range of catalytic transformations. Among them, coacervate droplets have been utilize more often as a friendly host for enzymatic reactions due to its facile synthesis in an aqueous

medium *[18–23]*. Most of the coacervates provide fundamental insights into the mechanism and dynamics of enzymatic catalysis inside the coacervates, very less is known about the hybrid coacervates with embedded catalytic units as a catalytic nanoreactor for chemical conversions. Moreover, most of the previous studies on selective hydrogenation of various nitroarenes are mainly limited on metal NP-based catalysts *[24–28]*.Our aim in the present study is to utilize a unique metal-free carbon dot (CD)-embedded hybrid coacervate ND as a catalytic nanoreactor to illustrate the role of confinement on catalytic transformations. Luminescent CDs are embedded inside these NDs and electrostatically associated with the positively charged polyelectrolyte poly(diallyldimethylammonium chloride) (PDADMAC). To the best of our knowledge, this is the first example of metal-free catalytic hydrogenation of nitroarenes using 2.5 nm-sized spherical CD.

5.2. Results and discussion

5.2.1. Synthesis and characterization of CDs and coacervate NDs

The hydrothermally synthesized CDs were characterized using UV−vis and PL spectroscopy, AFM, FTIR, PXRD, and Raman spectroscopy (discussed in chapter 3). The XPS survey spectrum shows the presence of carbon (55.0%), oxygen (31.4%), and nitrogen (13.6%) (Figure 5.1A). The deconvoluted XPS spectra of C1s reveal the presence of various functional groups such as C=C/C−C (284.6 eV), C− O/C−N (286.0 eV), and C=O (287.6 eV) (Figure 5.1B). Similarly, the deconvoluted O1s spectra confirm the presence of C=O (533.2 eV) and C−O−C (531.3 eV) functional groups (Figure 5.1C). The peaks at 400.0 and 401.8 eV can be observed in the deconvoluted N 1s spectra of CDs and indicate the presence of C=N and N−H groups, respectively (Figure 5.1D). The TEM image reveal the presence of well-dispersed spherical CDs in the size range of 2.1−4.6 nm

(Figure 5.1E & F) along with a characteristic d-spacing of 0.34 nm (Figures 5.1G).
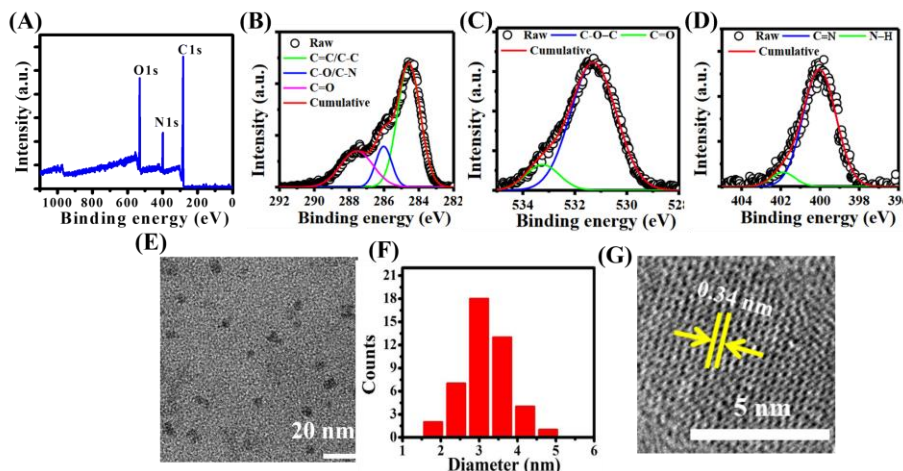
Figure 5.1. (A) XPS survey spectrum of CDs. Deconvoluted XPS spectra of (B) C1s, (C) O1s, and (D) N1s. (E) HR-TEM image, (F) size distribution histogram. (G) Lattice fringes of CDs. (Saini *et al. ACS Appl. Mater. Interfaces* **2021**, *13*, 51117-51131)

Further, coacervate NDs with embedded CDs were fabricated by mixing as-synthesized CDs with PDADMAC in pH 10 aqueous medium and equilibrated this binary mixture for 12 h under constant stirring (Figure 5.2A). The TEM image reveals the formation of well-dispersed uniform spherical NDs with sizes in the range of 210−450 nm (Figure 5.2B). We have reported that the ζ-potential value of free CDs decreases from −31.3 ± 1.8 mV to −17.0 ± 0.5 mV upon ND formation in the presence of positively charged PDADMAC due to partial surface passivation of negatively charged functional groups of CDs by positively charged PDADMAC via electrostatic association (discussed in chapter 3). To further substantiate this argument, we performed two sets of experiments. In the first set of experiment, negatively charged CDs were replaced with negatively charged MSA-capped CdTe QDs (170 nM) with mean size of 2.7 ± 0.1 nm and ζ-

potential of −25.1 ± 1.3 mV (Figures 5.2C, D, & E). FESEM and CLSM measurements reveal the formation of well-dispersed inherently luminescent spherical NDs with a mean size of 410 ± 15 nm (Figures 5.2F, G, & H).
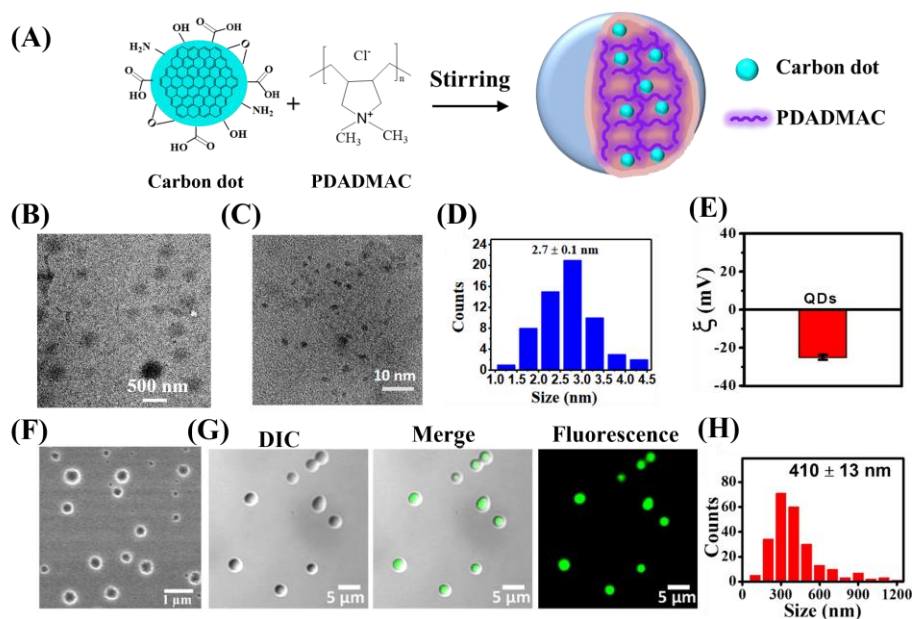
Figure 5.2. (A) Schematic illustration of the fabrication of CD-embedded NDs from CDs and PDADMAC. (B) TEM image of NDs. (C) TEM image, (D) size distribution histogram, and (E) ζ-potential of QDs. (F) FESEM, and (G) confocal images of QD-embedded NDs. (H) Size distribution histogram of NDs with mean size. (Saini *et al. ACS Appl. Mater. Interfaces* **2021**, *13*, 51117-51131)

In the another set of experiment, the positively charged PDADMAC was replaced with the positively charged poly-L-lysine (PLys-166.7 μM) polyelectrolyte and characterized using CLSM (Figure 5.3A). The presence of spherical and luminescent NDs is clearly evident from the CLSM image. Taken together, these findings unambiguously establish the universality of

our approach for the fabrication of hybrid NDs via electrostatic association between oppositely charged inorganic NPs and polyelectrolytes.

Next, we performed CLSM to explore the luminescence properties of an individual ND. Figure 5.3B shows the DIC image of well-dispersed individual spherical NDs and the merged image displays the distinct blue emission originating exclusively from the interior of these NDs indicating that the luminescent CDs are embedded inside the membrane-free architecture of these NDs. Notably, the intensity line profile reveals that the blue emission appears homogeneously throughout the NDs (Figure 5.3C), suggesting the uniform distribution of luminescent CDs inside these NDs *[29–32]*.
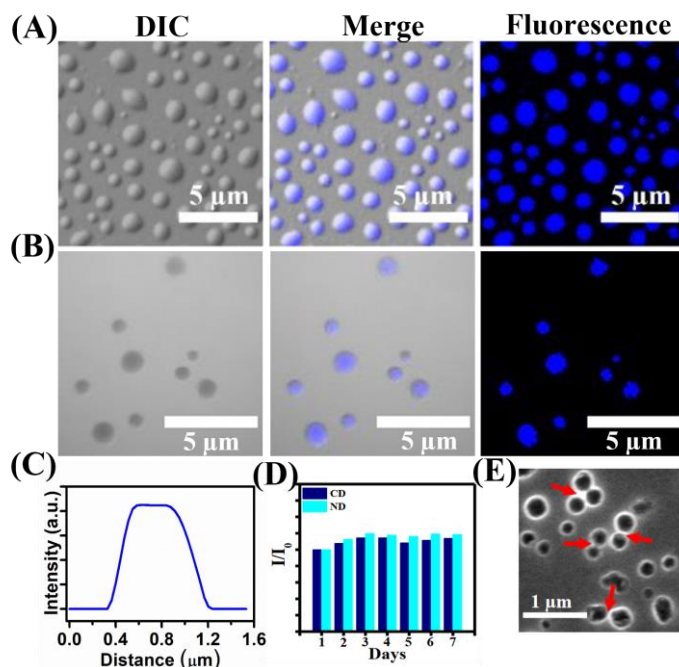
Figure 5.3. Confocal microscopy images of NDs fabricated from CDs and (A) PLys, and (B) PDADMAC. (C) Intensity line profile of NDs. (D) Changes in the PL intensity of aqueous dispersion of CDs and NDs as a function of time. (E) FESEM image of NDs showing coalescence phenomenon. Red arrows indicate representative coalescence

intermediates. (Saini *et al. ACS Appl. Mater. Interfaces* **2021**, *13*, 51117-51131)

Importantly, the physicochemical and optoelectronic properties of embedded CDs do not change significantly as compared to that of free CDs and is found to be quite stable over a period of 7 days (Figure 5.3D). These NDs also display spontaneous coalescence or fusion phenomenon of liquid droplets (Figure 5.3E). Taken together, all these findings unambiguously indicate the uniform distribution of luminescent CDs inside the coacervate NDs. Next, we aimed to explore the catalytic efficacy of CD-embedded NDs toward model catalytic conversions. For this, we have selected two model redox hydrogenation reactions, namely, 4-NP to 4- aminophenol (4-AP) and 4-NA to 4-aminoaniline (4-AA), in the presence of excess NaBH$_4$.

5.2.2. Catalytic conversion of nitroarenes to arylamines

To investigate the role of compartmentalization and subsequent confinement on the catalytic performance of CD-embedded NDs, we first loaded 4-NP and 4-NA inside the NDs and utilized after the removal of free substrates from the aqueous bulk phase. The estimated equilibrium partition coefficients of 4-NP and 4-NA inside the NDs were found to be 56.0 ± 1.8 and 50.2 ± 2.5, respectively. These high values of partition coefficients indicate preferential sequestration of both the nitroarenes inside the coacervate phase. Afterwards, the morphological stabilities of nitroarene-loaded NDs were accessed using FESEM measurements indicating the unperturbed morphology of sequestrated NDs (Figure 5.4A). First, we have examined the efficacy of bare CDs to drive the catalytic conversion of 4-NP to 4-AP in the presence of excess NaBH$_4$ in the aqueous medium by monitoring the time-dependent changes in the UV−vis absorption spectrum. A distinct absorption peak at 400 nm corresponds to 4-nitrophenolate ions appears upon addition of 2 mM NaBH$_4$ into the aqueous solution of 20 μM

4-NP (Figure 5.4B). The kinetics was monitored after the addition of CDs (1 µg/ mL) and the overall spectrum along with the absorbance at 400 nm remains unchanged even after 60 min (Figure 5.4B), indicating the lack of any catalytic activity of isolated bare CDs. Also, the similar results were obtained with another substrate 4-NA (Figure 5.4C).
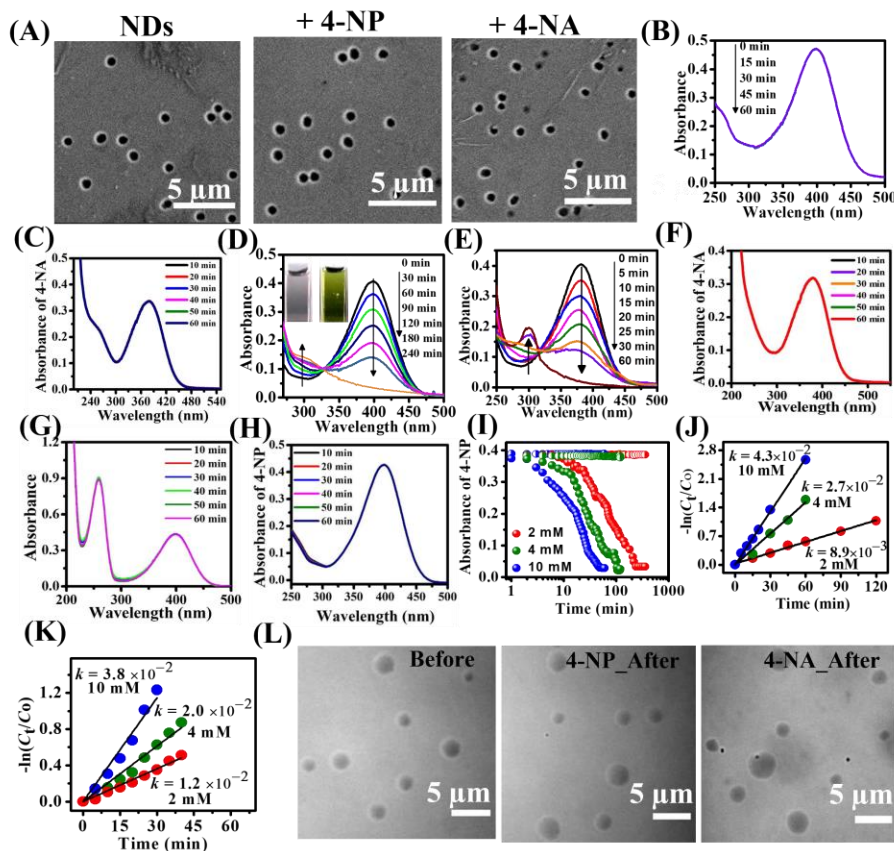
Figure 5.4. (A) FESEM images of NDs in the absence and presence of 20 µM 4-NP and 4-NA. Time-dependent UV–vis spectral changes of 20 µM 4-NP with (B) 2 mM, and (C) 10 mM NaBH$_4$ in the presence of CD. Time-dependent UV–vis spectral changes of (D) 20 µM 4-NP with 2 mM NaBH$_4$, and (E) 20 µM 4-NA by 10 mM NaBH$_4$ in the presence of CD-embedded NDs. The inset shows the color change from dark yellow to colorless after complete conversion. Time-dependent UV-vis spectra of (F) 4-NA-loaded

(20 μM) NDs in the absence of $NaBH_4$, (G) 4-NP-loaded (20 μM) ATP NDs with 10 mM $NaBH_4$, and (H) 20 μM 4-NP with 10 mM $NaBH_4$ in the presence of binary mixture of CDs and PDADMAC (0.25 μM) for a duration of 1 h. (I) Changes in absorbance (400 nm) of 20 μM 4-NP with different concentrations of $NaBH_4$ (red: 2 mM; green: 4 mM; and blue: 10 mM) in the presence of CDs (half-filled circle) and CD-embedded NDs (solid filled circle). Plot of $-\ln(C_t/C_0)$ vs reaction time for the reduction of 20 μM (I) 4-NP and (J) 4-NA by different concentrations of $NaBH_4$ (red: 2 mM; green: 4 mM; and blue: 10 mM) in the presence of CD-embedded NDs. (L) Confocal DIC images of CD-embedded NDs before and after the reduction reaction of 20 μM 4-NP and 4-NA in the presence of 10 mM $NaBH_4$. All the measurements were performed at 298 K in pH 10 aqueous medium. (Saini *et al. ACS Appl. Mater. Interfaces* **2021**, *13*, 51117-51131)

However, in case of 4-NP-loaded NDs, absorbance at 400 nm decreases gradually over time with a concomitant appearance of a new peak at 300 nm after the addition of 2 mM $NaBH_4$ (Figure 5.4D). The new absorption peak at 300 nm can be assigned to 4-AP and an isosbestic point at 327 nm indicates stoichiometric conversion of 4- NP to 4-AP inside the NDs *[24, 33]*. The inset of figure 5.4D shows a visible color change of the reaction mixture from dark yellow to colorless upon completion of the reaction. On the other hand, a new absorption peak at 300 nm has been observed due to the formation of 4-AA while utilizing 4-NA-loaded NDs and a distinct absorption peak correspond to 4-NA at 379 nm decreases gradually as a function of reaction time in the presence of 10 mM $NaBH_4$ (Figure 5.4E). Moreover, Control experiments in the absence of either $NaBH_4$ or CDs (ATP NDs) reveal no such spectral changes (Figures 5.4F & G). The mean size and the zeta potential of ATP NDs are estimated to be 270.5 ± 3.4 nm and $+12.0 \pm 0.5$ mV, respectively *[32]*. It has been observed

that simple ATP NDs without embedded CDs failed to initiate any detectable spectral changes, suggesting the essential role of CDs to drive these redox conversions (Figure 5.4G). Moreover, it has been observed that a simple binary mixture of CDs and PDADMAC at lower concentration of the polyelectrolyte, which lacks any spherical NDs, could not drive the catalytic conversion of 4-NP to 4-AP in the presence of excess $NaBH_4$ (Figure 5.4H). Taken together, the observed spectral changes of nitroarenes inside the NDs highlight the catalytic role of embedded CDs in the presence of excess $NaBH_4$.

Notably, it has been observed that the reaction kinetics is strongly dependent on the concentrations of $NaBH_4$ used and the observed decrease in absorbance is faster for higher concentrations of $NaBH_4$ (Figure 5.4I). No noticeable changes in the absorbance have been observed in the presence of isolated bare CDs at 2, 4, 10 mM $NaBH_4$ concentration (Figure 5.4I). The presence of finite induction time is also evident, which varies with the concentrations of $NaBH_4$. A similar induction time has been observed previously for different metal NP catalysts *[27, 28, 34]*. Figure 5.4J displays the linear plots of $-\ln(C_t/C_0)$ versus reaction time (*t*) ($R^2 = 0.9984$) for different concentrations of $NaBH_4$ for the reduction of 4-NP, which suggest pseudo-first-order reaction kinetics. The estimated apparent rate constants (k_{app}) increase from a value of 8.9×10^{-3} to 4.3×10^{-2} min^{-1} upon increasing the $NaBH_4$ concentration from 2 to 10 mM, respectively (Figure 5.4J). Similarly, the estimated k_{app} for the reduction of 20 μM 4-NA by 2, 4, and 10 mM $NaBH_4$ inside the NDs (CD = 2 μg/mL) is found to be 1.2×10^{-2}, 2.0×10^{-2}, and 3.8×10^{-2} min^{-1}, respectively (Figure 5.4K). Moreover, the structural stability of individual NDs after the completion of the redox conversions were captured by confocal DIC images indicating the intact spherical morphology and unaltered mean size of NDs (Figure 5.4L).

Previous studies showed that the reductive hydrogenation of nitroarenes by NaBH$_4$ on the surface of metal NPs follow LH mechanism according to which the increase in the concentration of nitroarenes leads to the decrease in the rate and conversion yield of the catalytic transformation *[24–26, 28, 34, 35]*. This happens due to the competitive adsorption between both the reactants to occupy the surface of the nanocatalyst, and at a high concentration of nitroarenes. To verify the reaction mechanism inside the NDs, we performed the catalytic conversions as a function of concentrations of 4-NP and catalyst. It is found that the concentrations of 4-NP have profound effects on the extent and kinetics of the redox hydrogenation reaction at a fixed concentration of NaBH$_4$ (10 mM) and catalyst (1 µg/mL) (Figure 5.5A & B). The k_{app} and conversion yield (%) decrease from a value of 8×10^{-2} to 2×10^{-2} min^{-1} and 94.2 to 78.2% upon increasing the 4-NP concentration from 5 to 60 µM, respectively (Figure 5.5B & C). Interestingly, at a very high concentration of 4-NP (200 µM), no noticeable change in the absorbance at 400 nm has been observed, indicating the lack of any catalytic conversion due to the complete surface coverage of CDs by 4-NP, which limits the surface adsorption of BH$_4^-$. Figure 5.5C shows the decrease in the k_{app} with 4-NP concentrations and this nonlinear decrease in the rate constant is also accompanied with an increase in the induction time (Figure 5.5A). These findings suggest that the catalytic conversion of 4-NP to 4-AP by excess NaBH$_4$ inside the NDs follows the classical LH mechanism. Further, we examined the catalytic conversion at different

catalyst doses (effective [CD]=1, 2, and 4 µg/mL) by varying the concentrations of NDs (Figure 5.5D & E).
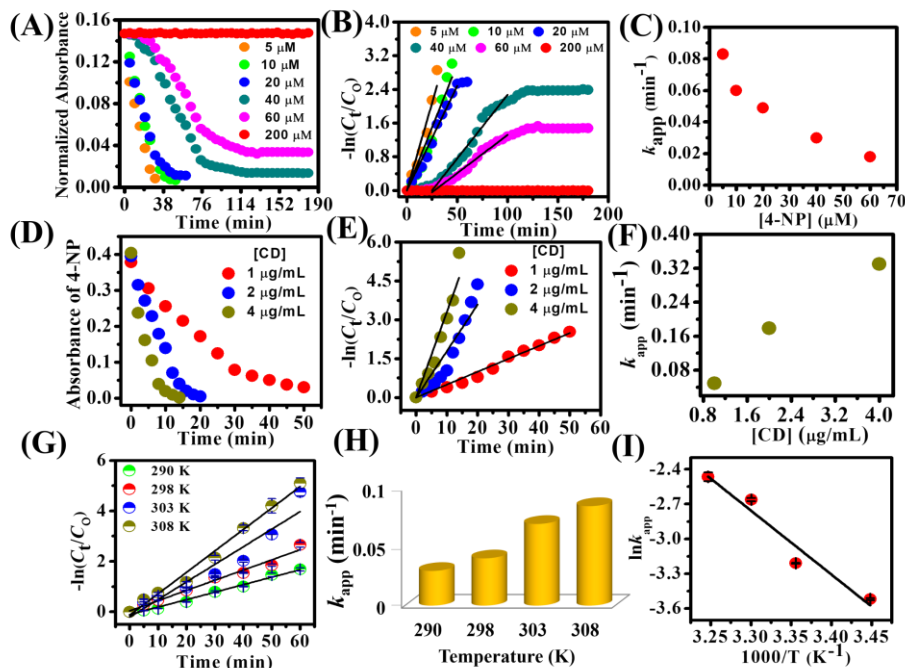
Figure 5.5. (A) Normalized absorbance (λ = 400 nm) and (B) plot of $-\ln(C_t/C_0)$ vs reaction time for the reduction of different concentrations of 4-NP (5, 10, 20, 40, 60, and 200 µM) by 10 mM NaBH$_4$ in the presence of CD-embedded NDs at 298 K. (C) Changes in the k_{app} as a function of 4-NP concentrations (5, 10, 20, 40, and 60 µM) in the presence of 10 mM NaBH$_4$ inside the CD-embedded NDs at 298 K. (D) Changes in the absorbance (λ = 400 nm), (E) plot of $-\ln(C_t/C_0)$ vs reaction time, and (F) changes in the k_{app} as a function of embedded CD concentrations of 1, 2, and 4 µg/mL for the reduction of 20 µM 4-NPs by 10 mM NaBH$_4$ at 298 K. (G) Plot of $-\ln(C_t/C_0)$ vs reaction time and (H) variation of k_{app} as a function of temperatures (290, 298, 303, and 308 K), and (I) Arrhenius plot of $\ln(k_{app})$ against 1000/T for the reduction of 20 µM 4-NP by 10 mM NaBH$_4$ inside

the CD-embedded NDs. (Saini *et al. ACS Appl. Mater. Interfaces* **2021**, *13*, 51117-51131)

It is evident that the catalytic conversion of 4-NP to 4-AP becomes faster in the presence of higher concentrations of CDs. The estimated k_{app} is found to be 5×10^{-2}, 1.8×10^{-1}, and 3.3×10^{-1} min^{-1} in the presence of 1, 2, and 4 µg/mL CDs, respectively (Figure 5.5F). It is expected as the available surface area of the catalyst increases with the increase in the catalyst dose, which facilitates surface adsorption of both the reactants and results in faster reaction kinetics. In order to estimate various thermodynamic parameters, we performed reductive hydrogenation inside the NDs at four different temperatures of 290, 298, 303, and 308 K. It should be noted that the structure and morphology of the NDs remain intact in this temperature range *[32]*. It is observed that the rate of catalytic conversion and estimated k_{app} (from 3.0×10^{-2} to 8.5×10^{-2} min^{-1}) values increases upon increasing the reaction temperature from 290 to 308 K (Figure 5.5G & H). This observation can be explained by considering enhancement in the collisional frequency of both the reactants with the surface for CDs inside the NDs, which facilitates surface adsorption and subsequent catalytic hydrogenation. The Arrhenius plot between ln(k_{app}) versus 1/T reveals an activation energy ($E_{a,kapp}$) of 45.8 kJ mol^{-1} (Figure 5.5I). In general, the activation energy of the redox hydrogenation of 4-NP varies from ~20−50 kJ mol^{-1} in the presence of different nanocatalysts *[24, 25, 35]*.
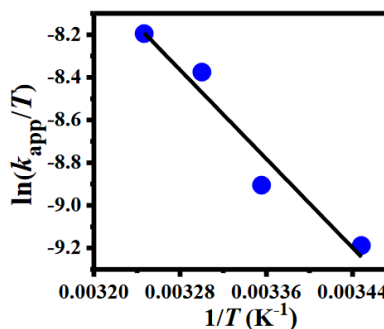
Figure 5.6. Plot of ln (k_{app}/T) against 1/T for the reduction of 4-NP-loaded (20 μM) NDs in the presence of 10 mM NaBH$_4$. (Saini *et al. ACS Appl. Mater. Interfaces* **2021**, *13*, 51117-51131)

The changes in the enthalpy (ΔH) and entropy (ΔS) of activation were estimated from the Eyring equation by plotting ln(k_{app}/T) versus 1/T (Figure 5.6.). The estimated values of ΔH and ΔS for the present system are 43.3 kJ mol^{-1} and −140 J mol^{-1} K^{-1}, respectively (Table 5.1). Notably, the associated Gibbs free energy (ΔG) increases from a value of 83.90 to 86.43 kJ mol^{-1} upon increasing the reaction temperature from 290 to 308 K, respectively. Similar changes in the thermodynamic parameters have been observed previously in the presence of other nanocatalysts *[24–28, 33–40]*.

Table 5.1. Thermodynamic parameters for catalytic reduction of 4-NP-loaded (20 μM) NDs in the presence of 10 mM NaBH$_4$ at different temperatures.

T (K)	k_{app} x 10^{-3} (min^{-1})	E_a (kJ/mol)	A x 10^6	ΔH (kJ/mol)	ΔS (J/mol K)	ΔG (kJ/mol)
290	3.0					83.90
298	4.0					85.02
303	7.0	45.8	4.98	43.3	-140.0	85.72
308	8.5					86.42

5.2.3. Product isolation, recyclability, and spatiotemporal control

In the present study, we have isolated and characterized both the hydrogenated products 4-AP and 4-AA using NMR and mass spectrometry techniques. After the completion of the reaction, the coacervate phase was separated from the bulk aqueous phase via centrifugation (10,000 rpm, 30 min). Figure 5.6A shows the DIC images of coacervate phase showing well-dispersed intact spherical NDs along with the aqueous bulk phase of the supernatant with no NDs. In the present system, 4-AP can either diffuse out of the NDs or it can trap inside the coacervate phase. To know the exact

location of 4-AP, we recorded the UV−vis spectrum of coacervate phase as well as the bulk aqueous phase separately. The UV−vis spectrum of the supernatant shows no peak while a distinct absorption peak at 300 nm corresponding to 4-AP is clearly visible in the UV−vis absorption spectrum of the coacervate phase suggesting that the product 4-AP remains inside the NDs after the completion of the reaction (Figure 5.6B).

Further, we use solvent extraction method to isolate the hydrogenated products and the aqueous and ethylacetate phases were collected separately. Figure 5.7A shows the DIC image of the intact regenerated NDs in coacervate phase after the solvent extraction.
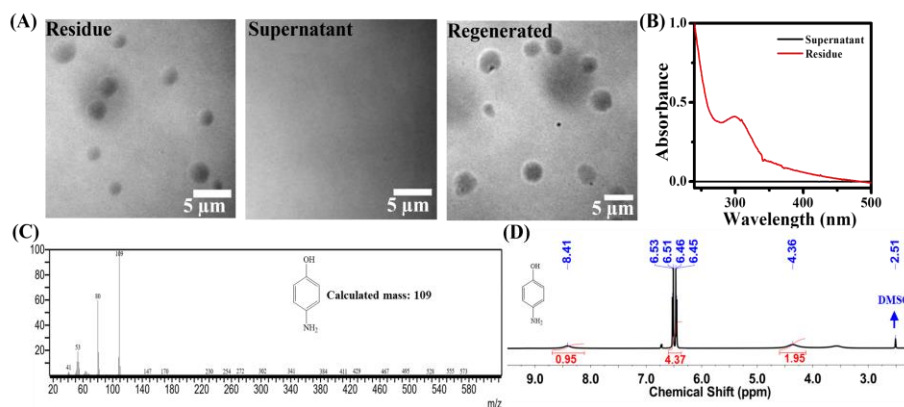
Figure 5.7. (A) Confocal DIC images of NDs in the residue, supernatant, and regenerated solution after centrifugation of the reaction mixture and solvent extraction. (B) UV-vis spectra of supernatant, and coacervate phase after centrifugation of the reaction mixture. (C) GC-MS and ^{1}H NMR (DMSO-d_6) spectra of 4-AP. (Saini *et al. ACS Appl. Mater. Interfaces* **2021**, *13*, 51117-51131)

The products 4-AP and 4-AA were collected from the ethylacetate phase and subjected to structural characterization using GC−MS and ^{1}H NMR techniques. The GC−MS spectrum of 4-AP reveals a molecular ion peak at m/z of 109 while ^{1}H NMR spectrum reveals three peaks with

chemical shift (δ) values of 4.36, 6.45−6.53, and 8.41 ppm correspond to the amino, benzylic, and phenolic −OH protons, respectively (Figure 5.7C & D). Similarly, the product 4-AA was confirmed using GC−MS and ^{1}H NMR (Figures 5.8A & B). Next, we checked the recyclability of the present NDs till six consecutive cycles using regenerated NDs after the solvent extraction step. For this, NDs were first prepared and then subjected for the subsequent reductive hydrogenation of 20 μM 4-NP by 10 mM NaBH$_4$. The conversion yield (%) and k_{app} estimated for the first cycle are found to be 98.9% and 0.18 min^{-1}, respectively. Figure 5.8C shows the estimated conversion yield (%) and k_{app} values of each cycle and both the parameters remain unaltered over six consecutive cycles of reuse. These findings indicate that the present NDs can be recycled over several consecutive runs without any compromise on their catalytic efficacy. In order to demonstrate the spatiotemporal control over reaction kinetics, we utilized the characteristic coalescence phenomenon of self-assembled soft materials including liposomes, vesicles, and droplets *[29–32]*. For this purpose, we utilized two different coacervate populations, namely, CD-embedded NDs and ATP-containing NDs *[32]*.
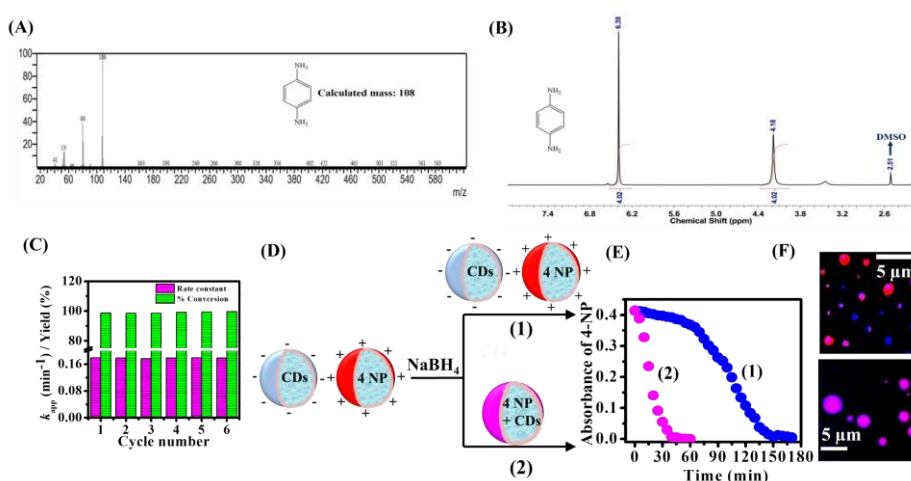
Figure 5.8. (A) GC-MS, and (B) ^{1}H NMR (DMSO-d^6) spectrum of the product 4-AA. (C) Recyclability test of CD-embedded NDs ([CD] = 2 μg/mL) toward the reduction of 20 μM 4-NP by 10 mM NaBH$_4$ at 298 K. (D) Schematic illustration of coalescence between CD-embedded NDs (blue) and 4-NP-loaded ATP NDs (red). (E) Changes in the absorbance (λ = 400 nm) of 20 μM 4-NP by 10 mM NaBH$_4$ for (1) instant mixing and (2) pre-equilibrated coacervate populations. (F) Confocal merge images of CD-embedded NDs (blue) and Rh 6G-loaded ATP NDs (red) for (1) instant mixing and (2) pre-equilibrated mixture. (Saini *et al. ACS Appl. Mater. Interfaces* **2021**, *13*, 51117-51131)

ATP NDs were first loaded with 20 μM 4-NP and mixed with equal volume of CD-embedded hybrid NDs (Figure 5.8D). The hydrogenation reaction was initiated by adding 10 mM NaBH$_4$ into the mixed populations of coacervates. Further, the kinetics was monitored at 400 nm in two-time regimes, just after the mixing of ATP NDs with hybrid NDs and after equilibrating the mixed coacervate phase for 12 h (Figure 5.8D). Here, it is important to note that the hydrogenation reaction can only be possible once the CD-embedded NDs fuse with the 4-NP-loaded ATP NDs in the presence of excess NaBH$_4$. Figure 5.8E displays the changes in the absorbance at 400 nm as a function of reaction time where pre-equilibration of the two populations of coacervates leads to a faster completion within 40 min (k_{app}=0.11 min^{-1}) compared to the instant mixing that completes in 150 min (k_{app}=0.05 min^{-1}). Pre-equilibrating the mixed populations of oppositely charged coacervates for 12 h results in a steady-state condition where most of the oppositely charged coacervates are already fused with each other signifying the time dependent coalescence. In contrast, instant mixing results in a nonequilibrium state where coalescence between two populations of coacervates takes place in a time-dependent manner. To

support our experimental findings, we have captured the time-dependent confocal images of mixed populations of coacervates (Figure 5.8F). ATP NDs were first labeled with Rh 6G dye, and mixed with the blue-emitting CD-embedded NDs. Figure 5.8F shows the merged confocal image for the instant mixing sample reveals individual red and blue-emitting coacervates along with very few magenta signals from fused coacervates while the merged image for the pre-equilibrated sample displays majority of magenta-emitting fused coacervates which strongly support our experimental findings.

5.2.4. Mechanism of redox hydrogenation

Our findings reveal that the embedded CDs inside the NDs act as catalytic centers for the reductive hydrogenation of nitroarenes. In bulk aqueous medium, both CDs and nitroarenes have negative charges in the presence of excess NaBH$_4$, and as a consequence of electrostatic repulsion, no appreciable adsorption of nitroarenes and BH$_4^-$ takes place at the surface of CDs. However, the alteration of surface charge density of CDs inside the NDs and the compartmentalization effect favors the adsorption of nitroarenes and BH$_4^-$ at the surface of CDs. To further substantiate this argument, we performed catalytic reduction of 4-NP with bare CDs in the presence of NaBH$_4$ by increasing the concentrations of reactants and the catalyst by 10 times in the absence and presence of 10% (w/v) PEG as a molecular crowder. It is evident that increasing the concentrations of the reactant and the catalyst in the absence and presence of 10% (w/v) PEG has no effect on the feasibility of the redox transformation (Figure 5.9A & B), indicating that a simple increase in the local concentrations of the substrate and the catalyst due to compartmentalization is not enough to drive the catalytic conversion.

Previously, it has been proposed that BH_4^- transfers hydride (H^-) ions on the surface of NPs, and reduction of surface-adsorbed nitroarenes takes place via the involvement of these adsorbed H^- ions *[24–28, 33–36]*. Moreover, it is known that metal NPs act as electron mediators between BH_4^- and nitroarenes for the hydrogenation of nitroarenes. Similarly, the catalytic activity of the present CD-embedded NDs could be due to the generation of active hydrogen species via the reactions of excess BH_4^- with the surface of CDs.
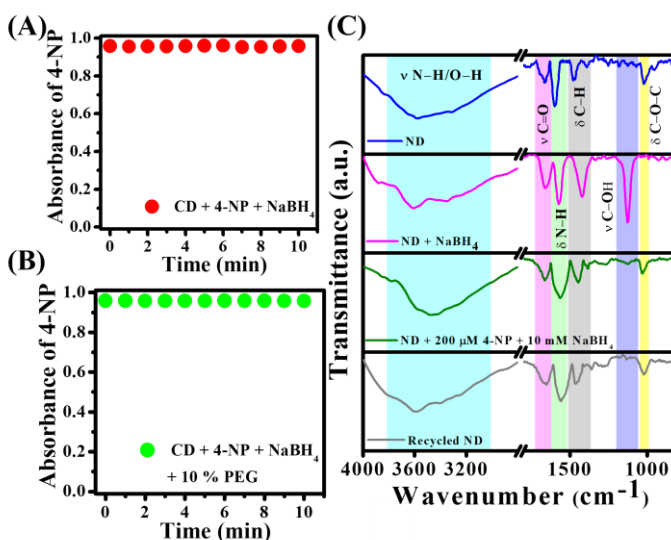
Figure 5.9. Changes in absorbance (400 nm) of 200 μM 4-NP with 0.06 mg/mL CDs and 25 mM NaBH₄ in the (A) absence and, (B) presence of 10% PEG. (C) FTIR spectra of CD-embedded NDs in the absence and presence of 200 μM 4-NP upon addition of 10 mM NaBH₄ along with the FTIR spectrum of recycled (first cycle) NDs. (Saini *et al. ACS Appl. Mater. Interfaces* **2021**, *13*, 51117-51131)

The efficient transfer of these active hydrogen species along with electrons to the surface-adsorbed 4-NP molecules can finally reduce the nitro groups to amino groups. In order to elucidate the role of BH_4^- in the present system, we recorded the FTIR spectra of NDs in the absence and

presence of excess $NaBH_4$. The FTIR spectrum of NDs shows multiple characteristic peaks at 3449, 1652, 1569, 1426, and 1045 cm^{-1}, which can be assigned to the $-N-H/-O-H$ stretching, $-C=O$ stretching, $-N-H$ bending, $-C-H$ bending, and $-C-O-C$ bending from epoxy groups, respectively (Figure 5.9B). Notably, significant changes have been observed in the FTIR spectrum of NDs in the presence of 10 mM $NaBH_4$. A new sharp peak at 1125 cm^{-1} appears in the presence of $NaBH_4$, which can be assigned to the stretching vibration of $-C-O$ functional groups *[41]*. The peak at 3440 cm^{-1} due to the stretching vibration of $-N-H/- O-H$ functional groups get broaden with enhancement in intensity in the presence of $NaBH_4$. Moreover, a noticeable spectral shift in the stretching frequency of carbonyl groups from 1652 to 1658 cm^{-1} has been observed in the presence of $NaBH_4$. Previously, it has been reported that carbonyls and epoxy functional groups on the surface of CDs get reduced to alcohols in the presence of $NaBH_4$ *[41–44]*. It is evident from the FTIR spectrum that the peak due to the epoxy groups on the NDs disappears in the presence of $NaBH_4$ (Figure 5.9C). Therefore, the new peak at 1125 cm^{-1} due to the $-C-O$ functional groups originate from the reduced CDs (r-CDs), where carbonyl and epoxy groups reduced to hydroxyl groups. Notably, the deconvoluted XPS spectra of O 1s in CDs further confirm the conversion of epoxy moieties to hydroxyl groups in the presence of $NaBH_4$ (Figure 5.10A & B). These hydroxyl groups of rCDs are the active species for the present redox hydrogenation of nitroarenes inside the NDs. Moreover, we recorded the FTIR spectrum of NDs loaded with 200 µM 4-NP in the presence of excess $NaBH_4$ (10 mM) (Figure 5.10C). The absence of any characteristic peak at 1125 cm^{-1} from the $-C-O$ moieties of surface hydroxyl groups unambiguously indicate complete surface coverage of CDs by 4-NP at high concentration, which limits the surface adsorption of $NaBH_4$. Further, the

involvement and catalytic role of reactive surface hydroxyl groups of r-CDs on the reaction mechanism have been confirmed by recording the FTIR spectrum of the regenerated NDs after the first and sixth cycles (Figures 5.9C).
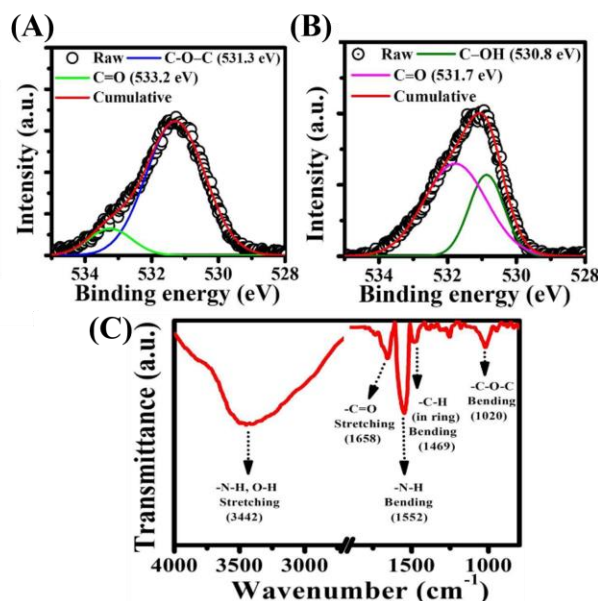
Figure 5.10. Deconvoluted XPS spectra of O1s in CDs in the (A) absence and, (B) presence of NaBH$_4$. (Saini *et al. ACS Appl. Mater. Interfaces* **2021**, *13*, 51117-51131)

The FTIR spectra of the recycled NDs after the first and sixth cycles reveal no signature peak at 1125 cm^{-1} from the −C−O moieties of surface hydroxyl groups, signifying that all the surface hydroxyl groups are oxidized to epoxy functional groups upon completion of the redox catalysis. Moreover, the characteristic peak of epoxy groups at 1045 cm^{-1} reappears after the completion of redox conversions. Taken together, our present findings strongly substantiate that the reactive hydroxyl groups of r-CDs inside the NDs are the active species for the selective reduction of nitro groups to amino groups (Scheme 5.1.). This finding is unique and distinct

from the earlier reported metal NP-catalyzed redox hydrogenation of nitroarenes, where simple H$^-$ ions take part in the reaction.
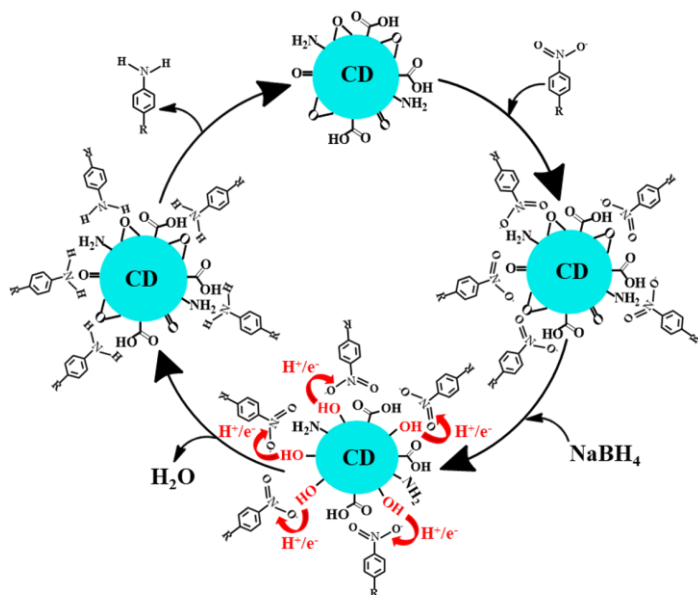
Scheme 5.1. Schematic illustration of redox hydrogenation of nitroarenes in the presence of NaBH$_4$ inside the NDs via the formation of reactive hydroxyl groups on the surface of CDs. (Saini *et al. ACS Appl. Mater. Interfaces* **2021**, *13*, 51117-51131)

5.3. Conclusions

In the present study, we have demonstrated a proof of concept for the nanocatalysis under nanoconfinement by studying the model redox hydrogenation of nitroarenes using metal free CD-embedded coacervate NDs. The fabricated CD-embedded coacervate NDs with unique physicochemical properties have been utilized as confined catalytic nanoreactors to drive redox hydrogenation of nitroarenes in the presence of excess NaBH$_4$. While isolated bare CDs failed to catalyze the hydrogenation reaction, the membraneless robust architecture of NDs provides an ideal microenvironment to drive the incompatible reaction in

the confined space by modulating the surface charge density and effective concentrations of reactants. Our findings revealed that these NDs can be recycled over several consecutive cycles without any compromise on the rate and conversion yield of the hydrogenation reaction. Moreover, we have successfully demonstrated spatiotemporal control over the kinetics of the redox hydrogenation by compartmentalization of the substrate and catalyst using mixed populations of coacervate droplets. The mechanism of redox hydrogenation is found to follow the classical LH model inside the NDs via the generation of reactive surface hydroxyl groups, and the rate of the reaction is found to be influenced by the concentrations of the substrate, NaBH$_4$, and the catalyst. The catalytic activity of the present NDs can be ascribed to the synergistic effect between the modulation of surface charge density of individual CDs and nanoconfinement effect inside the spherical NDs.

Note: This is copyrighted material from permission of the American Chemical Society.

5.4. References

1. Küchler A., Yoshimoto M., Luginbühl S., Mavelli F., Walde P. (2016), Enzymatic reactions in confined environments, Nat. Nanotechnol., 11(5), 409–420. (DOI:10.1038/nnano.2016.54)

2. Stroberg W., Schnell S. (2018), Do cellular condensates accelerate biochemical reactions? Lessons from microdroplet chemistry, Biophys. J., 115(1), 3–8. (DOI:10.1016/j.bpj.2018.05.023)

3. Gao C., Lyu F., Yin Y. (2021), Encapsulated metal nanoparticles for catalysis, Chem. Rev., 121(2), 834–881. (DOI:10.1021/acs.chemrev.0c00237)

4. Mahmoud M. A., Saira F., El-Sayed M. A. (2010), Experimental evidence for the nanocage effect in catalysis with hollow nanoparticles, Nano Lett., 10(9), 3764–3769. (DOI:10.1021/nl102497u)

5. Vogt E. T. C., Weckhuysen B. M. (2015), Fluid catalytic cracking: recent developments on the grand old lady of zeolite catalysis, Chem. Soc. Rev., 44(20), 7342–7370. (DOI:10.1039/C5CS00376H)

6. Wang N., Sun Q., Zhang T., Mayoral A., Li L., Zhou X., et al. (2021), Impregnating subnanometer metallic nanocatalysts into self-pillared zeolite nanosheets, J. Am. Chem. Soc., 143(18), 6905–6914. (DOI:10.1021/jacs.1c00578)

7. Zhao J., Jian R., Wang Y., Yang B., Zhao D., Shen C., et al. (2021), Mesoporous silica as sorbents and enzymatic nanoreactors for microbial membrane proteomics, ACS Appl. Mater. Interfaces, 13(10), 11571–11578. (DOI:10.1021/acsami.0c19528)

8. Martí-Centelles R., Rubio-Magnieto J., Escuder B. (2020), A minimalistic catalytically-active cell mimetic made of a supramolecular hydrogel encapsulated into a polymersome, Chem. Commun., 56(92), 14487–14490. (DOI:10.1039/D0CC04941G)

9. Zhao X., Liu X., Yi C., Li J., Su Y., Guo M. (2020), Palladium nanoparticles embedded in yolk–shell N-doped carbon nanosphere@Void@SnO_2 composite nanoparticles for the photocatalytic reduction of 4-nitrophenol, ACS Appl. Nano Mater., 3(7), 6574–6583. (DOI:10.1021/acsanm.0c01038)

10. Xiao J., Pan X., Guo S., Ren P., Bao X. (2015), Toward fundamentals of confined catalysis in carbon nanotubes, J. Am. Chem. Soc., 137(1), 477–482. (DOI:10.1021/ja511498s)

11. Dong C., Yu Q., Ye R., Su P., Liu J., Wang G. (2020), Hollow carbon sphere nanoreactors loaded with PdCu nanoparticles: Void-confinement effects in liquid-phase hydrogenations, Angew. Chem. Int. Ed., 59(42), 18374–18379. (DOI:10.1002/anie.202007297)

12. Yang T., Wei L., Jing L., Liang J., Zhang X., Tang M., et al. (2017), Dumbbell-shaped bi-component mesoporous Janus solid nanoparticles for biphasic interface catalysis, Angew. Chem. Int. Ed., 56(29), 8459–8463. (DOI:10.1002/anie.201701640)

13. Sun J., Cao C., Chen J., Zhao W., Tang Q., Jiang B., et al. (2020), Bowl-like nanoreactors composed of packed gold nanoparticles surrounded with silica nanosheets for a photothermally enhancing enzymatic reaction, ACS Appl. Nano Mater., 3(11), 11465–11473. (DOI:10.1021/acsanm.0c02580)

14. Bhattacharyya S., Ali S. R., Venkateswarulu M., Howlader P., Zangrando E., De M., et al. (2020), Self-assembled Pd_{12} coordination cage as photoregulated oxidase-like nanozyme, J. Am. Chem. Soc., 142(44), 18981–18989. (DOI:10.1021/jacs.0c09567)

15. Lee J. K., Samanta D., Nam H. G., Zare R. N. (2019), Micrometer-sized water droplets induce spontaneous reduction, J. Am. Chem. Soc., 141(27), 10585–10589. (DOI:10.1021/jacs.9b03227)

16. Sasmal H. S., Bag S., Chandra B., Majumder P., Kuiry H., Karak S., et al. (2021), Heterogeneous C–H functionalization in water via porous covalent organic framework nanofilms: A case of catalytic sphere transmutation, J. Am. Chem. Soc., 143(22), 8426–8436. (DOI:10.1021/jacs.1c02425)

17. Li G., Zhao S., Zhang Y., Tang Z. (2018), Metal-organic frameworks encapsulating active nanoparticles as emerging composites for

catalysis: Recent progress and perspectives, Adv. Mater., 30(51), 1800702. (DOI:10.1002/adma.201800702)

18. Koga S., Williams D. S., Perriman A. W., Mann S. (2011), Peptide–nucleotide microdroplets as a step towards a membrane-free protocell model, Nature Chem, 3(9), 720–724. (DOI:10.1038/nchem.1110)

19. Crosby J., Treadwell T., Hammerton M., Vasilakis K., Crump M. P., Williams D. S., et al. (2012), Stabilization and enhanced reactivity of actinorhodin polyketide synthase minimal complex in polymer–nucleotide coacervate droplets, Chem. Commun., 48(97), 11832. (DOI:10.1039/c2cc36533b)

20. Qiao Y., Li M., Booth R., Mann S. (2017), Predatory behaviour in synthetic protocell communities, Nat. Chem., 9(2), 110–119. (DOI:10.1038/nchem.2617)

21. Qiao Y., Li M., Qiu D., Mann S. (2019), Response-retaliation behavior in synthetic protocell communities, Angew. Chem. Int. Ed., 58(49), 17758–17763. (DOI:10.1002/anie.201909313)

22. Love C., Steinkühler J., Gonzales D. T., Yandrapalli N., Robinson T., Dimova R., et al. (2020), Reversible pH-responsive coacervate formation in lipid vesicles activates dormant enzymatic reactions, Angew. Chem. Int. Ed., 59(15), 5950–5957. (DOI:10.1002/anie.201914893)

23. Drobot B., Iglesias-Artola J. M., Le Vay K., Mayr V., Kar M., Kreysing M., et al. (2018), Compartmentalized RNA catalysis in membrane-free coacervate protocells, Nat. Commun., 9(1), 3643. (DOI:10.1038/s41467-018-06072-w)

24. Aditya T., Pal A., Pal T. (2015), Nitroarene reduction: a trusted model reaction to test nanoparticle catalysts, Chem. Commun., 51(46), 9410–9431. (DOI:10.1039/C5CC01131K)

25. Zhao P., Feng X., Huang D., Yang G., Astruc D. (2015), Basic concepts and recent advances in nitrophenol reduction by gold- and other transition metal nanoparticles, Coord. Chem. Rev., 287, 114–136. (DOI:10.1016/j.ccr.2015.01.002)

26. Ansar S. M., Kitchens C. L. (2016), Impact of gold nanoparticle stabilizing ligands on the colloidal catalytic reduction of 4-nitrophenol, ACS Catal., 6(8), 5553–5560. (DOI:10.1021/acscatal.6b00635)

27. Wunder S., Lu Y., Albrecht M., Ballauff M. (2011), Catalytic activity of faceted gold nanoparticles studied by a model reaction: Evidence for substrate-induced surface restructuring, ACS Catal., 1(8), 908–916. (DOI:10.1021/cs200208a)

28. Roy S., Rao A., Devatha G., Pillai PP. (2017), Revealing the role of electrostatics in gold-nanoparticle-catalyzed reduction of charged substrates, ACS Catal., 7(10), 7141–7145. (DOI:10.1021/acscatal.7b02292)

29. Vaishnav J. K., Mukherjee T. K. (2019), Highly photostable and two-photon active quantum dot–polymer multicolor hybrid coacervate droplets, Langmuir, 35(36), 11764–11773. (DOI:10.1021/acs.langmuir.9b01783)

30. Singh S., Vaishnav J. K., Mukherjee T. K. (2020), Quantum dot-based hybrid coacervate nanodroplets for ultrasensitive detection of Hg^{2+}, ACS Appl. Nano Mater., 3(4), 3604–3612. (DOI:10.1021/acsanm.0c00317)

31. Saini B., Singh R. R., Nayak D., Mukherjee T. K. (2020), Biocompatible pH-responsive luminescent coacervate nanodroplets from carbon dots and poly(diallyldimethylammonium chloride)

toward theranostic applications, ACS Appl. Nano Mater., 3(6), 5826–5837. (DOI:10.1021/acsanm.0c00995)

32. Saini B., Singh R., Mukhopadhyay S., Mukherjee T. K. (2021), Specific loading and in vitro controlled release of a Ru-based hydrophobically encapsulated model anticancer drug inside nanoassemblies toward stimuli-responsive drug delivery, ACS Appl. Nano Mater., 4(2), 2037–2051. (DOI:10.1021/acsanm.0c03356)

33. Pradhan N., Pal A., Pal T. (2002), Silver nanoparticle catalyzed reduction of aromatic nitro compounds, Colloids Surf. A: Physicochem. Eng. Asp., 196(2–3), 247–257. (DOI:10.1016/S0927-7757(01)01040-8)

34. Strachan J., Barnett C., Masters A. F., Maschmeyer T. (2020), 4-Nitrophenol reduction: Probing the putative mechanism of the model reaction, ACS Catal., 10(10), 5516–5521. (DOI:10.1021/acscatal.0c00725)

35. Hervés P., Pérez-Lorenzo M., Liz-Marzán L. M., Dzubiella J., Lu Y., Ballauff M. (2012), Catalysis by metallic nanoparticles in aqueous solution: model reactions, Chem. Soc. Rev., 41(17), 5577. (DOI:10.1039/c2cs35029g)

36. Lawrence R. L., Scola B., Li Y., Lim C-K., Liu Y., Prasad P. N., et al. (2016), Remote optically controlled modulation of catalytic Properties of nanoparticles through reconfiguration of the inorganic/organic interface, ACS Nano, 10(10), 9470–9477. (DOI:10.1021/acsnano.6b04555)

37. Kong X., Sun Z., Chen M., Chen C., Chen Q. (2013), Metal-free catalytic reduction of 4-nitrophenol to 4-aminophenol by N-doped graphene, Energy Environ. Sci., 6(11), 3260. (DOI:10.1039/c3ee40918j)

38. Liu J., Yan X., Wang L., Kong L., Jian P. (2017), Three-dimensional nitrogen-doped graphene foam as metal-free catalyst for the hydrogenation reduction of p-nitrophenol, J. Colloid Interface Sci., 497, 102–107. (DOI:10.1016/j.jcis.2017.02.065)

39. Liu H., Wang H., Qian Y., Zhuang J., Hu L., Chen Q., et al. (2019), Nitrogen-doped graphene quantum dots as metal-free photocatalysts for near-infrared enhanced reduction of 4-nitrophenol, ACS Appl. Nano Mater., 2(11), 7043–7050. (DOI:10.1021/acsanm.9b01549)

40. Wang Z., Su R., Wang D., Shi J., Wang J-X., Pu Y., et al. (2017), Sulfurized graphene as efficient metal-free catalysts for reduction of 4-nitrophenol to 4-aminophenol, Ind. Eng. Chem. Res., 56(46), 13610–13617. (DOI:10.1021/acs.iecr.7b03217)

41. Zhuo Y., Zhong D., Miao H., Yang X. (2015), Reduced carbon dots employed for synthesizing metal nanoclusters and nanoparticles, RSC Adv., 5(41), 32669–32674. (DOI:10.1039/C5RA02598B)

42. Zheng H., Wang Q., Long Y., Zhang H., Huang X., Zhu R. (2011), Enhancing the luminescence of carbon dots with a reduction pathway, Chem. Commun., 47(38), 10650. (DOI:10.1039/c1cc14741b)

43. Wang X., Long Y., Wang Q., Zhang H., Huang X., Zhu R., et al. (2013), Reduced state carbon dots as both reductant and stabilizer for the synthesis of gold nanoparticles, Carbon, 64, 499–506. (DOI:10.1016/j.carbon.2013.07.104)

44. Long L., Wu Q., Chao Q., Dong Y., Wu L., Zhang Q., et al. (2020), Surface-state-mediated interfacial charge dynamics between carbon dots and ZnO toward highly promoting photocatalytic activity, J. Chem. Phys., 153(4), 044708. (DOI:10.1063/5.0011474)

Chapter 6

Synthetic Protocell as Efficient Bioreactor: Enzymatic Superactivity and Ultrasensitive Glucose Sensing in Urine

Chapter 6

6.1. Introduction

Enzymes drive various complex tandem metabolic reactions efficiently inside the confined, crowded, and heterogeneous cellular environments by modulating the physicochemical properties and activities of various biomacromolecules *[1]*. Therefore, it is essential to understand the mechanistic pathway of enzymatic reactions under confined cellular environments. Recent in vitro studies have highlighted the role of crowding on the formation of compartmentalized membraneless biocondensates via soft protein-protein interactions which acts as a host and accelerate a wide range of complex metabolic processes *[2–5]*. To understand the catalytic transformations under confinement, various artificial bioreactors such as liposomes *[6]*, microemulsions *[7]*, polymersomes *[8]*, polymeric capsules *[9]*, metal−organic frameworks (MOFs) *[10, 11]*, covalent organic frameworks (COFs) *[12]*, hydrogels *[13]*, and deoxyribonucleic acid (DNA) nanostructures *[14]* have been developed. These robust architectures not only stabilize the native conformations of enzymes and protect them from harmful external conditions such as acidic pH, temperature, protease digestion, and denaturation, but also enhance the enzymatic activity via stabilization of the active site, modulation of chemical activity, and enhanced mass transport. Moreover, these earlier studies delineate the importance of enzyme immobilization for efficient multienzymatic cascade reactions, the scope of synthetic bioreactors toward a diverse range of metabolic transformations is limited by their inherent structural constrains such as fixed pore or cavity sizes, limited scope for free diffusion, and complex synthetic routes with harsh experimental conditions.

In this context, membraneless synthetic liquid droplets with facile fabrication methodology, and large aqueous void space to accommodate a wide variety of biomolecules find tremendous importance in drug delivery

[15–18], catalysis *[19–21]*, and sensing *[22, 23]* along with high interest in protocell research as model artificial synthetic cells *[24, 25]*. In the recent past, various functional coacervate droplets have been fabricated and utilized as scaffolds for a wide range of biochemical transformations, demonstrated the role of mass action and Michaelis constant (K_m) *[19, 26–32]*. Despite these efforts, pharmaceutically important bienzymatic GOx/HRP cascade reactions have not been investigated within synthetic droplets and very little is known about the impact of immobilization on the Michaelis−Menten kinetic parameters of this important model enzymatic transformation.

Moreover, in different type of enzymatic/nanozymatic/hybrid bioreactors, accurate and reliable glucose sensing has gain tremendous importance, because of its physiological relevance. Here, in the present study, our first aim is to fabricate a synthetic condensate as a catalytic bioreactor and to illustrate the role of confinement on the enzymatic activity. Secondly, by using droplet-immobilized GOx/HRP cascade pair, we want to develop a facile glucose sensing assay. As a result, we have immobilized GOx/HRP cascade pair inside the droplets (GOx/HRP@Droplet) with high encapsulation efficiency and retention time for the fast, selective, reliable, cost-effective, user-friendly, recyclable, and ultrasensitive detection of glucose.

6.2. Results and discussion

6.2.1. Droplet preparation and characterization

Droplets were prepared by equilibrating 8 μM ATP with 25 μM PDADMAC solution in pH 7.4 phosphate buffer with constant stirring for 1 h at RT and characterized using CLSM, TEM, and FESEM measurements (Figure 6.1A). Figure 6.1B displays the DIC, TEM, and FESEM images of well-dispersed spherical droplets. Moreover, the speed of stirring of the

aqueous mixture during the mixing of aqueous ATP solution with aqueous PDADMAC solution has a profound effect on the size distribution, as well on the morphology of droplets (Figure 6.1C).
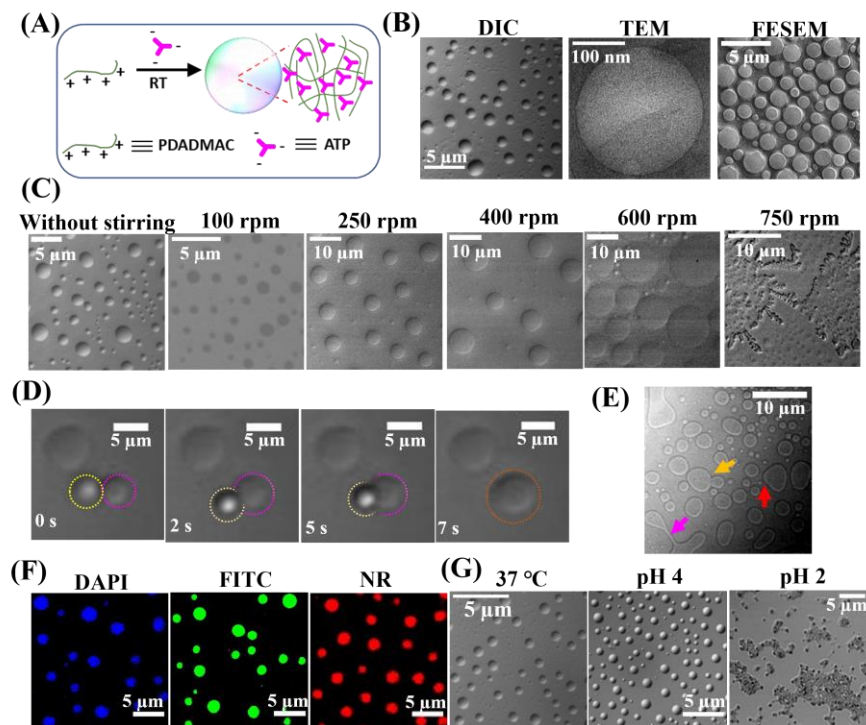
Figure 6.1. (A) Schematic illustration of the preparation of droplets from ATP and PDADMAC. (B) Confocal DIC, TEM, and FESEM images of droplet. (C) DIC images of droplets fabricated from ATP and PDADMAC binary mixtures at different stirring speeds. (D) Time-lapse confocal DIC images of droplets showing fusion over a period of 7 s. (E) Confocal DIC image of droplets showing fusion (yellow arrow), dripping (pink arrow), and surface wetting (red arrow). (F) Confocal fluorescence images of DAPI-, FITC-, and NR-sequestered droplets. (G) DIC images showing the stability of droplets at 37 °C and at pH 4.0 and 2.0. (Saini *et al. ACS Appl. Mater. Interfaces* **2022**, *14*, 53462-53474)

While an inhomogeneous size distribution of droplets has been observed without any stirring, the formation of ruptured droplets is evident at a high stirring speed of 750 rpm. In the present study, we have used an optimum stirring speed of 250 rpm to obtain relatively uniform size (1.1−5.5 μm) and morphology of droplets along with a ζ-potential of 12.3 ± 0.2 mV (Figure 6.1C) *[18]*. Moreover, these droplets exhibit liquidlike properties, such as fusion, dripping, and surface wetting (Figures 6.1D & E), similar to other reported synthetic and biomolecular condensates *[2–4, 33]*. Next, we used three differently charged organic dyes, namely, DAPI (positively charged), FITC (negatively charged), and NR (neutral), to explore the sequestration behavior. Figure 6.1F shows the CLSM images of DAPI-, FITC-, and NR-sequestered droplets with characteristic blue, green, and red emission indicating the membraneless architecture of these droplets facilitates preferential sequestration of organic dyes, irrespective of their surface charges. Subsequently, figure 6.1G displays the stability of these droplets at physiological temperature of 37 °C and at different pH (stable pH range: 3−12) indicating that the disassembly occurs at lower acidic pH of 2, because of the disruption of electrostatic interactions as a consequence of protonation of ATP *[18]*.

6.2.2. Enzyme sequestration and stability assay

The fabricated stable membraneless droplets were utilized as scaffold for selective sequestration of HRP, GOx, and HRP/GOx cascade pair separately (Figure 6.2A). All the experiments were performed with 25 pM initial concentrations of HRP and GOx, because, at higher concentrations, the enzymatic kinetics were too fast to monitor using UV-vis spectroscopy. The estimated EE is found to be 99.1% ± 0.3%, 98.9% ± 0.2%, and 99.3% ± 0.4%/99.1% ± 0.3% for HRP (HRP@Droplet), GOx (GOx@Droplet), and GOx/HRP pair (GOx/HRP@ Droplet), respectively suggesting high affinity

of enzymes toward the confined microenvironment of droplets (Figure 6.2B). Notably, no significant effect on EE has been observed by changing the composition of droplet due to the changes in the physicochemical properties of droplets (Table 6.1). To visualize the presence of both enzymes inside the droplet matrix under CLSM, we loaded individual droplets with fluorescently labeled GOx (FITC-labeled) and HRP (RBITC-labeled).

Table 6.1. Effect of droplet composition on the EE of GOx and HRP.

Droplet Composition	Encapsulation Efficiency (%)	
	GOx	HRP
8.0 µM ATP and 1.0 µM PDADMAC	95.2 ± 0.4	94.7 ± 0.7
8.0 µM ATP and 8.0 µM PDADMAC	96.6 ± 0.3	95.1 ± 0.8
8.0 µM ATP and 16.0 µM PDADMAC	97.3 ± 0.6	97.1 ± 0.2
8.0 µM ATP and 25.0 µM PDADMAC	98.6 ± 0.7	98.2 ± 0.4
8.0 µM ATP and 50.0 µM PDADMAC	99.3 ± 0.4	99.1 ± 0.3

(A)

GOx@Droplet
EE = 98.9 ± 0.2

HRP@Droplet
EE = 99.1 ± 0.3

GOx-HRP@Droplet
EE = 99.3 ± 0.4/99.1 ± 0.3

(B) DIC FITC-GOx RBITC-HRP Merged

(C) Leakage (%) HRP GOx
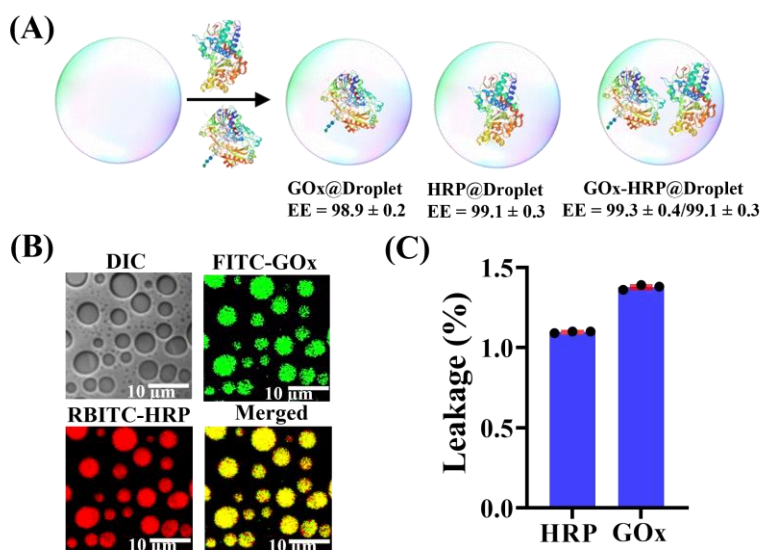
Figure 6.2. (A) Schematics showing the sequestration of HRP, GOx, and HRP/GOx cascade pair inside the droplets along with their EE (%). (B) Confocal images of droplets after the sequestration of FITC-labeled GOx (green channel), and RBITC-labeled HRP (red channel). (C) Enzyme leakage (%) assays of HRP@Droplet and GOx@Droplet over a period of 48 h at 37 °C. The data represent the mean ± standard error in measurement (s.e.m.) from three independent experiments. (Saini *et al. ACS Appl. Mater. Interfaces* **2022**, *14*, 53462-53474)

Figure 6.2B displays the DIC image of stable well-dispersed intact spherical droplets of GOx/ HRP@Droplet. Importantly, the fluorescence images in the green and red channels display distinct green and red emission originating exclusively from the interior of these droplets (Figure 6.2B). The uniform yellow signal from the merged image substantiates the presence of both FITC-labeled GOx and RBITC-labeled HRP inside the GOx/HRP@Droplets. Next, we estimated the extent of enzyme leakage (%) at 37 °C which reveals that only 1.09% and 1.38% of GOx or HRP were released from GOx@Droplet and HRP@Droplet, respectively over a period of 48 h. (Figure 6.2C).

6.2.3. Peroxidase activity inside the droplet

We tested the peroxidase activity of sequestered HRP in the presence of different substrates, namely, TMB, OPD, ABTS, and H_2O_2 at 37 °C in pH 4.0 acetate buffer. Peroxidase activity of free HRP and HRP@Droplet with TMB as substrate reveals that the absorbance at 650 nm due to oxidized TMB (ox-TMB) increases linearly with time, as a function of the TMB concentration upon addition of 8 mM H_2O_2 (Figure 6.3A & B). The apparent rate of change of absorbance in droplet phase is significantly higher, relative to that in a bulk medium. Next, we performed detailed kinetic analyses by varying the concentration of substrates by keeping the

H_2O_2 concentration fixed at 8 mM using the classical Michaelis−Menten model to quantitatively evaluate various kinetic parameters. Figure 6.3C shows the plot of initial reaction rate versus the molar concentrations of TMB reveals a typical Michaelis−Menten behavior in a bulk aqueous medium. Similar Michaelis−Menten plots have also been observed for HRP@Droplet (Figure 6.3D), suggesting that HRP follows similar mechanistic pathways in the droplet phase. The estimated kinetic parameters for different substrates are tabulated in Table 6.2 after fitting the Michaelis−Menten plots. The K_m for TMB is found to be 0.5 mM for free HRP, which matches well with the earlier reports *[34]*. Notably, the K_m of TMB remains almost unaltered (K_m = 0.4 mM) for HRP@Droplet, indicating that the affinity between small substrate like TMB toward HRP remains unperturbed inside the droplet phase. Similarly, K_m for other substrates remains almost unaltered inside the droplet phase (Figure 6.3E, F, G & Table 6.2). In contrast, a drastic enhancement in the k_{cat} value has been observed for HRP@Droplet ($4.0 \times 10^5 \, s^{-1}$), compared to the free HRP ($4.0 \times 10^3 \, s^{-1}$) in bulk (Figure 6.3H, & Table 6.2). This 100-fold increase in the k_{cat} value is unprecedented in the literature.

Table 6.2. Michaelis-Menten parameters of HRP for different substrates.

Substrate	Buffer				Droplet			
	V_{max}	K_m	k_{cat}	k_{cat}/K_m	V_{max}	K_m	k_{cat}	k_{cat}/K_m
	$(M \, s^{-1})$	(mM)	(s^{-1})	$(mM^{-1}s^{-1})$	$(M \, s^{-1})$	(mM)	(s^{-1})	$(mM^{-1}s^{-1})$
TMB	1.0×10^{-7}	0.5	4.0×10^3	8.0×10^3	1.0×10^{-5}	0.4	4.0×10^5	2.7×10^5
OPD	7.3×10^{-7}	0.4	3.0×10^4	7.5×10^4	5.0×10^{-6}	0.2	2.0×10^5	1.0×10^6
ABTS	1.0×10^{-7}	0.4	4.0×10^3	1.0×10^4	2.2×10^{-6}	0.4	8.8×10^4	2.2×10^5
H_2O_2	8.8×10^{-8}	3.4	3.5×10^3	1.0×10^3	5.7×10^{-6}	2.4	2.3×10^5	1.0×10^5

The inset of figure 6.3C & D shows the daylight photographs of free HRP (pale blue) and HRP@Droplet (distinct blue color in ∼5 s) reveals the formation of ox-TMB upon the addition of 1 mM TMB in the presence of

8 mM H_2O_2, suggesting the enhanced peroxidase activity inside the droplet phase, compared to the bulk aqueous medium.
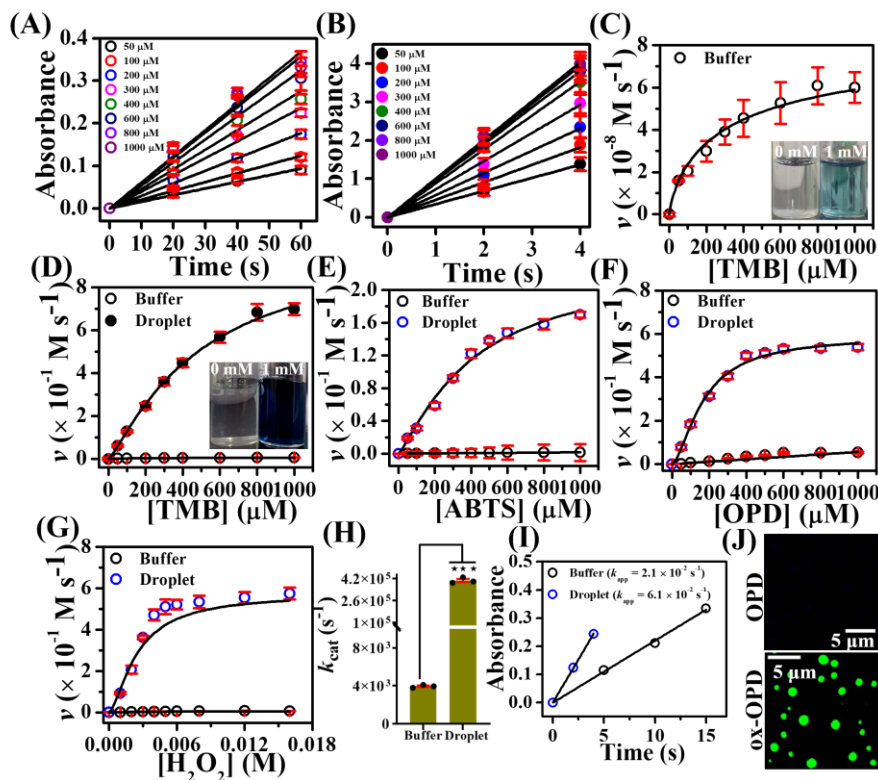
Figure 6.3. Plots of absorbance (λ_{abs} = 650 nm) versus time as a function of TMB concentrations in the (A) absence and (B) presence of droplets in pH 4 acetate buffer at 37 °C. Michaelis−Menten plots of HRP as a function of TMB concentration in the (C) absence and (D) presence of droplets in pH 4.0 acetate buffer at 37 °C. The inset of figure C and D shows the daylight photographs of free HRP in bulk aqueous medium, and of HRP@Droplet in the absence and presence of 1 mM TMB upon addition of 8 mM H_2O_2. Michaelis-Menten plots of HRP as a function of (E) ABTS, (F) OPD, and (G) H_2O_2 concentrations in pH 4 acetate buffer at 37 °C. (H) Comparison of the k_{cat} values in the buffer and droplet. The data represent the mean ± s.e.m. for three independent experiments. Statistical significance was assessed by a two-tailed, unpaired Student's t-test with the three-asterisk

symbol (***) representing a P value of <0.001 (8 × 10−8). (I) Linearized plots of absorbance (λ = 650 nm) of ox-TMB as a function of time in buffer (50-fold molar excess) and droplet in the presence of HRP. (J) Confocal fluorescence images of droplets before and after the formation of ox-OPD. (Saini *et al. ACS Appl. Mater. Interfaces* **2022**, *14*, 53462-53474)

Next, we examined whether the enhanced activity observed inside the droplet phase is solely due to higher local concentrations of enzymes and substrates, or combination of other critical factors. For this, we monitored the reaction kinetics with a 50-fold molar excess of HRP, TMB, and H_2O_2 in bulk aqueous buffer. The estimated apparent rate constant shows a value of 2.1×10^{-2} M^1 s^{-1}, which is 3-fold lower than that in droplets (Figure 6.3I) suggesting that simple mass action is not the sole reason behind the remarkable enhancement observed in the enzymatic rate inside the droplet. To authenticate that the observed peroxidase reaction occurs exclusively inside the droplet phase and not at the outer surface or bulk medium, we visualized the fluorescence signals (λ_{em} = 525 nm) of oxidized OPD (ox-OPD) using CLSM after the completion of the enzymatic reaction. For this, we used unlabeled HRP to specifically monitor the fluorescence signal of the oxidized product. Remarkably, distinct green emission appears exclusively from the interior of these droplets, suggesting the formation of ox-OPD inside the droplet phase (Figure 6.3J).

6.2.4. Alteration in the secondary structure of sequestered enzymes

The enhanced activity observed for HRP@Droplet could be due to conformational reorganization of sequestered enzymes as immobilization of enzymes often leads to alteration in their secondary structure, which has direct impact on their activity. To know the conformational perturbation of HRP@Droplet, we observed the CD spectral changes in the far-UV and Soret region. Figure 6.4A shows the far-UV CD spectrum of HRP in

aqueous medium at pH 4.0 with two minima at 208 and 222 nm, suggesting an α-helix rich secondary structure *[33]*. However, the CD spectrum of HRP@Droplet exhibits a single sharp minimum at 226 nm (Figure 6.4A).
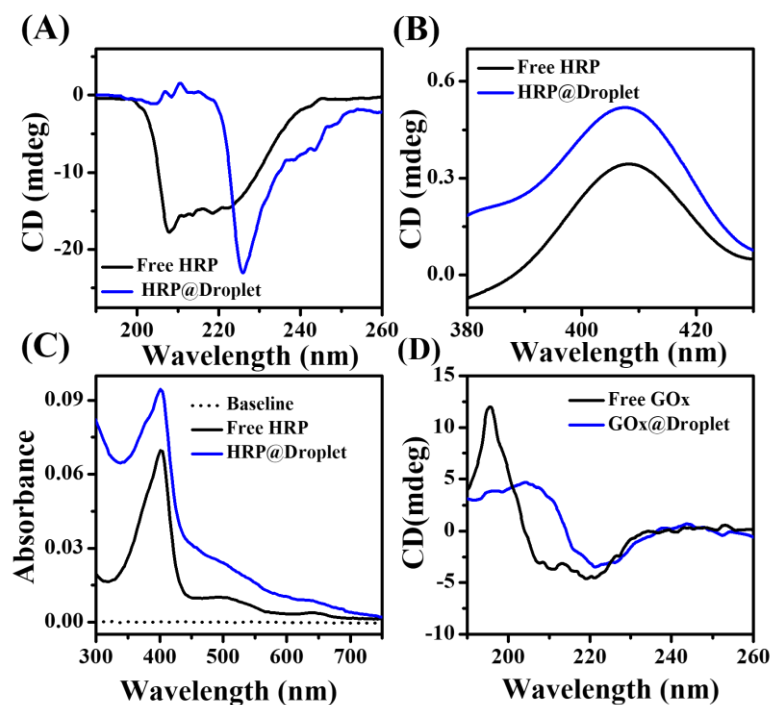
Figure 6.4. Changes in the (A) far-UV and (B) Soret region CD spectra of HRP at pH 4.0 inside the droplet. (C) UV-vis absorption spectra of HRP at pH 4.0 in buffer and droplet. (D) Far-UV CD spectra of GOx at pH 7.4 in buffer and droplets. All the measurements were performed at 37 °C. (Saini *et al. ACS Appl. Mater. Interfaces* **2022**, *14*, 53462-53474)

These spectral changes clearly indicate a substantial amount of conformational alteration of sequestered HRP inside the scaffold as a consequence of combination of several factors. First, specific interactions such as electrostatic, hydrophobic, hydrogen bonding, and/or van der Waals interactions of sequestered HRP with the constituents of droplet may significantly modulate the secondary structure of enzyme. Second,

significant amount of confinement inside the droplets may also leads to severe protein-protein interactions, which perturb the native secondary structure of sequestered enzymes. Third, the hydrophobic microenvironment of the droplet may also influence the effective solvation shell of the native enzymes. To know the influence of these effects on the conformation of the active site of HRP, we recorded the CD spectra of HRP in Soret region and UV-vis absorption spectra. Interestingly, both the CD intensity in the Soret region and the UV-vis absorbance at 401 nm increase appreciably inside the scaffold (Figures 6.4B & C), suggesting higher integrity of the active heme pocket of sequestered HRP. Similar conformational changes were observed with sequestered GOx (Figure 6.4D). Taken together, our findings highlight the scaffold-induced alteration of secondary structure of sequestered enzymes possibly via the involvement of various effects including multivalent scaffold-enzyme interactions, protein-protein interactions, and/or modulation of the effective solvation shell of the enzymes.

6.2.5. Cascade activity, stability, and recyclability

The GOx/HRP cascade reaction is one of the most extensively studied model enzymatic reactions, because of its well-established reaction mechanism and tremendous application in clinical diagnosis. This pair catalyzes the oxidation of glucose by GOx in the presence of O_2 to produce H_2O_2, which is subsequently utilized by HRP to oxidize organic or inorganic substrates by releasing H_2O (Figure 6.5A). In order to examine the efficiency and selectivity of cascade reaction inside the droplets, we first sequestered both the enzymes inside the droplet before adding other substrates (Figure 6.5A). Figure 6.5B displays the changes in the absorbance of ox-TMB at 650 nm as a function of reaction time in bulk and droplet phase in pH 6.0 phosphate buffer after the addition of 1 mM glucose.

It is evident that the rate of change of absorbance is much faster inside the droplet phase compared to that in a bulk medium signifies that the multienzymatic cascade reaction is very feasible inside the droplet. The inset of figure 6.5B shows the daylight photographs of instantly turned blue droplet solution (within 5 s) after the cascade reaction along with unaltered spherical morphology of the droplet as shown in DIC image. The apparent rate constant (k_{app}) shows 51-fold enhancement and increases from a value of 1.6×10^{-4} s^{-1} in bulk aqueous medium to a value of 8.2×10^{-3} s^{-1} inside the droplet, which is unprecedented in the literature (Figure 6.5C). Notably, complete inhibition of the formation of ox-TMB has been observed in the absence of any one of the constituents (Figure 6.5D), signifying the cascade nature of the reaction. Moreover, the sequestered GOx/HRP pair exhibits excellent selectivity toward glucose inside the droplet (Figure 6.5E).
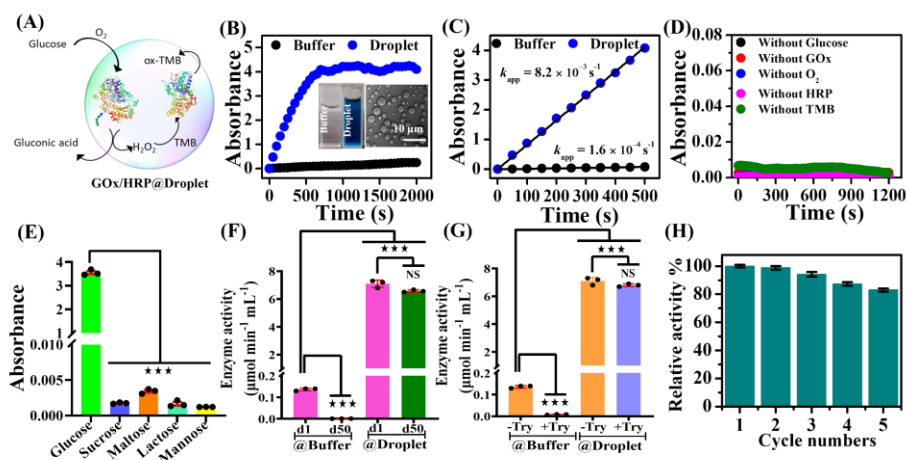
Figure 6.5. (A) Schematic representation of the GOx/HRP cascade reaction inside the droplet with TMB as substrate. (B) Changes in the absorbance (λ = 650 nm) and (C) linearized plots of absorbance (λ = 650 nm) of ox-TMB as a function of time for GOx/HRP cascade reaction in buffer and droplets at 37 °C. The inset shows the photographs of aqueous solutions before and after the cascade reaction. (D) Plot of absorbance (λ = 650 nm) versus time

for GOx/HRP cascade reaction in the absence of either glucose, GOx, O_2, HRP, or TMB. (E) Selectivity test of GOx/HRP@Droplet toward glucose. (F) Comparison of activities of free and sequestered enzymes for day 1 (magenta bars) and day 50 (green bars). (G) Comparison of activities of free and sequestered enzymes before (orange bar) and after (violet bar) trypsin digestion. (H) Recyclability test of GOx/HRP@Droplet over five cycles. The data represent the mean ± s.e.m. for three independent experiments. Statistical significance was assessed by a two-tailed, unpaired Student's t-test with (***) P value < 0.001 and not significant (NS; P = 0.84). All the measurements were performed in pH 6.0 phosphate buffer. (Saini *et al. ACS Appl. Mater. Interfaces* **2022**, *14*, 53462-53474)

In order to know the structural and functional stability of sequestered enzymes, we explored the stability of sequestered enzymes inside the droplets as a function of various experimental conditions. To know the effect of aging on the functional aspects of sequestered enzymes, we compared the enzymatic activity of GOx/HRP cascade pair in bulk solution and within the droplets upon 50 days of storage (Figure 6.5F). Meanwhile, a 99.2% decrease in the cascade activity of free enzymes has been observed upon 50 days of storage, and a negligible loss (4.7%) of activity has been noticed for sequestered enzymes inside the droplet during the same period of time. Further, to examine the biological stability of the GOx/HRP@Droplet against protease, we utilized trypsin digestion assay.

Comparison of the enzymatic activity of GOx/HRP pair before and after trypsin digestion reveals 93% loss of the initial activity of free GOx/HRP pair. In contrast, GOx/HRP@Droplet exhibits high resistance to trypsin digestion with >90% retention of its initial activity (Figure 6.5G), suggesting scaffold-induced protection of the active enzymes inside the droplet. All these findings clearly substantiate the fact that the sequestered

enzymes retain their structural and functional integrity within the droplets for several days. These observations are physiologically relevant as biomolecular condensates concentrate and store various biomacromolecules and provide potential mechanism by which cells can regulate metabolic reactions temporally and spatially. Next, to test the reusability of GOx/HRP@Droplet, we performed recyclability assay for five consecutive cycles (Figure 6.5H). It is evident that GOx/HRP@Droplet can retain 83% of its initial activity even after five repeated cycles, indicating the structural integrity of the composite cascade pair.

6.2.6. Glucose sensing in solution, filter paper, and urine samples

In order to check applicability toward sensitivity and practicability of GOx/HRP@Droplet as an efficient glucose sensor, we tested the glucose sensing ability of the composite first in solution. Figure 6.6A shows the changes in the absorbance (λ_{max}= 650 nm) of ox-TMB as a function of time over a broad range of glucose concentrations (0−100 μM). Notably, the absorbance follows a linear trend as a function of glucose concentrations in the range of 0−100 μM and even at lower concentrations (0.1−0.5 μM) (Figure 6.6B, & inset). The limit of detection (LOD, S/N = 3) is estimated from the linear slope and found to be 228 nM, which is superior to most of the earlier reported enzymatic bioreactors. These spectral changes are accompanied by a gradual color change of the aqueous mixture from colorless to deep blue upon increasing the glucose concentrations within 5 s, indicating the fast and highly sensitive colorimetric response of the composite GOx/HRP@Droplet system toward glucose sensing in solution. (Figure 6.6C, upper panel). Next, we checked the performance of composite on a solid support. For this, we first deposited the aqueous composite material on Whatman filter paper and did quick drying at 37 °C followed by soaking the composite-loaded filter paper in different concentrations of

glucose solutions. Figure 6.6C (lower panel) shows the daylight photographs of the dried papers from colorless to deep blue reveal glucose dose dependent color change as has been observed in the solution phase whereas no colorimetric change has been observed with same concentrations of bare GOx/HRP-loaded filter paper (Figure 6.6D). These findings clearly authenticate that the GOx/ HRP@Droplet is much more effective toward ultrasensitive glucose sensing on solid paper, compared to its bare counterpart, as a consequence of spatial confinement, altered conformations of active enzymes, mass action, and barrierless diffusion inside the liquidlike microenvironment of droplets.

Figure 6.6. (A) Changes in the absorbance ($\lambda = 650$ nm) of ox-TMB as a function of time with different concentrations (0−100 µM) of glucose in pH 6.0 phosphate buffer. (B) Linearized plot of absorbance at 650 nm of ox-TMB as a function of glucose concentrations in pH 6.0 phosphate buffer. The inset shows the linearized plot at lower concentrations of glucose. (C) Photographs of colorimetric response of aqueous mixtures (upper panel) and filter papers (lower panel) upon increase in the concentrations of glucose in pH 6.0 phosphate buffer. (D) Photograph of bare GOx/HRP-loaded filter paper. (E) Schematics showing the glucose sensing in spiked urine samples in solution and filter paper using GOx/HRP@ Droplet. (F) Changes in the UV-vis absorption spectra of the unspiked and spiked urine

samples in the presence of GOx/HRP@Droplet composite. (G) Comparison of the colorimetric response of commercial strips and GOx/HRP@Droplet-loaded filter papers in the absence and presence of glucose. (Saini *et al. ACS Appl. Mater. Interfaces* **2022**, *14*, 53462-53474)

Next, we tested the efficacy of our composite GOx/HRP@Droplet system in spiked urine samples with different concentrations of glucose (Figure 6.6E). Although self-monitoring of blood glucose is currently the preferred method, noninvasive portable urine glucose meters find medical importance in diabetes screening tests. We collected urine samples from normal healthy volunteers and spiked it with different concentrations (0.2 and 0.5 mM) of glucose after centrifugation. Notably, the composite shows no UV-vis peak at 650 nm for the unspiked urine sample, signifies the undetectable amounts of glucose in normal urine samples (Figure 6.6F). However, a prominent peak appears at 650 nm correspond to ox-TMB in the presence of 0.2 mM and 0.5 mM glucose in the spiked sample. Next, we compared the sensitivity of the filter paper loaded GOx/HRP@Droplet composite with the commercial urine glucose testing strip toward colorimetric glucose sensing. The color of the commercial strip changes from light blue to dark brown upon increasing the glucose concentration from 0 to 0.5 mM, while the color of the GOx/HRP@Droplet-loaded filter paper changes from white to dark blue under similar experimental conditions (Figure 6.6G). Moreover, it has been observed that the colorimetric response of droplet-loaded filter paper toward spiked urine sample remains unaltered even after 7-days of storage at room temperature (Figure 6.6H). After considering the cost of all the chemicals used, the estimated cost our filter paper-based composite sensor is found to be ∼2.0 rupee/strip, which is less than the commercially available urinalysis test strip (∼5.6 rupee/strip). Therefore, the response, sensitivity, and cost of our

present enzymatic composite material are superior to the commercial glucose testing strip and may find future prospects in the pharmaceutical industry. In addition, the performance of our filter paper loaded with composite material is superior to most of the earlier reported urine glucose sensing systems, in terms of its intrinsic noninvasive nature, facile cost-effective fabrication, fast colorimetric response, durability, and easy self-handling *[35–38]*.

6.3. Conclusions

In summary, we have developed a robust, stable, and cost-effective integrated bioplatform using GOx/HRP cascade pair and synthetic membraneless droplet for ultrasensitive glucose sensing in urine. The present biocomposite material exhibits high encapsulation efficiency (≥99%), low leakage (<1.5%), enhanced biological stability, and superior activity compared to the earlier reported enzymatic bioreactors. A remarkable enhancement (6.7−100-fold) in the k_{cat} values has been observed for HRP@Droplet relative to the bulk aqueous phase. The enhanced activity has been taken into account by considering increased local concentrations of the enzyme and substrate, along with conformational alteration of the active enzyme. The bienzymatic cascade reaction with GOx/HRP@Droplet composite reveals a 51-fold enhancement in the apparent activity, relative to the bulk aqueous phase. This enhanced activity is stable against aging and protease digestion, indicating the protective environment of these liquidlike scaffolds. Moreover, we have shown that these droplets can be recycled over several consecutive runs without any significant loss of enzymatic activity. Using GOx/HRP@Droplet composite, we have demonstrated fast (5 s), reliable, and selective colorimetric sensing of glucose in solution and solid support with a LOD of 228 nM, which is the lowest reported value for enzymatic bioreactors until date. Finally, we have

illustrated that our present composite senses the glucose level in a spiked urine sample, even in the presence of other interfering chemicals, which outperforms the commercial glucose sensing strip, in terms of sensitivity and colorimetric response. Our present study not only highlights the tremendous potential of biomimetic synthetic condensates to regulate the enzymatic activity inside their aqueous micro-environment, but also illustrates their vast scope in biosensing and pharmaceutical applications.

Note: This is copyrighted material from permission of the American Chemical Society.

6.4. References

1. Minton A. P. (2006), How can biochemical reactions within cells differ from those in test tubes?, J. Cell Sci., 119(14), 2863–2869. (DOI:10.1242/jcs.03063)

2. Ray S., Singh N., Kumar R., Patel K., Pandey S., Datta D., et al. (2020), α-Synuclein aggregation nucleates through liquid–liquid phase separation, Nat. Chem., 12(8), 705–716. (DOI:10.1038/s41557-020-0465-9)

3. Poudyal M., Patel K., Sawner A. S., Gadhe L., Kadu P., Datta D., et al. (2022), Liquid condensate is a common state of proteins and polypeptides at the regime of high intermolecular interactions, Biophysics, preprint. (DOI:10.1101/2021.12.31.474648)

4. Patel C. K., Singh S., Saini B., Mukherjee T. K. (2022), Macromolecular crowding-induced unusual liquid–liquid phase separation of human serum albumin via soft protein–protein interactions, J. Phys. Chem. Lett., 13(16), 3636–3644. (DOI:10.1021/acs.jpclett.2c00307)

5. O'Flynn B. G., Mittag T. (2021), The role of liquid–liquid phase separation in regulating enzyme activity, Curr. Opin. Cell Biol., 69, 70–79. (DOI:10.1016/j.ceb.2020.12.012)

6. Miele Y., Jones S. J., Rossi F., Beales P. A., Taylor A. F. (2022), Collective behavior of urease pH clocks in nano- and microvesicles controlled by fast ammonia transport, J. Phys. Chem. Lett., 13(8), 1979–1984. (DOI:10.1021/acs.jpclett.2c00069)

7. Weitz M., Kim J., Kapsner K., Winfree E., Franco E., Simmel F. C. (2014), Diversity in the dynamical behaviour of a compartmentalized programmable biochemical oscillator, Nat. Chem., 6(4), 295–302. (DOI:10.1038/nchem.1869)

8. Peters R. J. R. W., Marguet M., Marais S., Fraaije M. W., van Hest J. C. M., Lecommandoux S. (2014), Cascade reactions in multicompartmentalized polymersomes, Angew. Chem. Int. Ed., 53(1), 146–150. (DOI:10.1002/anie.201308141)

9. Parthasarathy R. V., Martin C. R. (1994), Synthesis of polymeric microcapsule arrays and their use for enzyme immobilization, Nature, 369(6478), 298–301. (DOI:10.1038/369298a0)

10. Greifenstein R., Ballweg T., Hashem T., Gottwald E., Achauer D., Kirschhöfer F., et al. (2022), MOF hosted enzymes for continuous flow catalysis in aqueous and organic solvents, Angew. Chem. Int. Ed., 134(18) (DOI:10.1002/ange.202117144)

11. Liang W., Xu H., Carraro F., Maddigan N. K., Li Q., Bell S. G., et al. (2019), Enhanced activity of enzymes encapsulated in hydrophilic metal–organic frameworks, J. Am. Chem. Soc., 141(6), 2348–2355. (DOI:10.1021/jacs.8b10302)

12. Chao H., Zhou Z., He W., Li M., Yuan X., Su P., et al. (2022), Template-free in situ encapsulation of enzymes in hollow covalent

organic framework capsules for the electrochemical analysis of biomarkers, ACS Appl. Mater. Interfaces, 14(18), 20641–20651. (DOI:10.1021/acsami.2c01357)

13. Sakamoto Y., Suehiro F., Akiba I., Nishimura T. (2022), Supramolecular shear-thinning glycopeptide hydrogels for injectable enzyme prodrug therapy applications, Langmuir, 38(18), 5883–5890. (DOI:10.1021/acs.langmuir.2c00504)

14. Zhao Z., Fu J., Dhakal S., Johnson-Buck A., Liu M., Zhang T., et al. (2016), Nanocaged enzymes with enhanced catalytic activity and increased stability against protease digestion, Nat. Commun., 7(1), 10619. (DOI:10.1038/ncomms10619)

15. Chu H., Gao J., Chen C-W., Huard J., Wang Y. (2011), Injectable fibroblast growth factor-2 coacervate for persistent angiogenesis, Proc. Natl. Acad. Sci. U.S.A., 108(33), 13444–13449. (DOI:10.1073/pnas.1110121108)

16. Guo H., Song S., Dai T., Sun K., Zhou G., Li M., et al. (2020), Near-infrared fluorescent and magnetic resonance dual-imaging coacervate nanoprobes for trypsin mapping and targeted payload delivery of malignant tumors, ACS Appl. Mater. Interfaces, 12(15), 17302–17313. (DOI:10.1021/acsami.0c03433)

17. Saini B., Singh R. R., Nayak D., Mukherjee T. K. (2020), Biocompatible pH-responsive luminescent coacervate nanodroplets from carbon Dots and poly(diallyldimethylammonium chloride) toward theranostic applications, ACS Appl. Nano Mater., 3(6), 5826–5837. (DOI:10.1021/acsanm.0c00995)

18. Saini B., Singh R., Mukhopadhyay S., Mukherjee T. K. (2021), Specific loading and in vitro controlled release of a Ru-based hydrophobically encapsulated model anticancer drug inside

nanoassemblies toward stimuli-responsive drug delivery, ACS Appl. Nano Mater., 4(2), 2037–2051. (DOI:10.1021/acsanm.0c03356)

19. Peeples W., Rosen M. K. (2021), Mechanistic dissection of increased enzymatic rate in a phase-separated compartment, Nat. Chem. Biol., 17(6), 693–702. (DOI:10.1038/s41589-021-00801-x)

20. Saini B., Singh S., Mukherjee T. K. (2021), Nanocatalysis under Nanoconfinement: A Metal-Free Hybrid Coacervate Nanodroplet as a Catalytic Nanoreactor for Efficient Redox and Photocatalytic Reactions, ACS Appl. Mater. Interfaces, 13(43), 51117–51131. (DOI:10.1021/acsami.1c17106)

21. Singh S., Rao C., Nandi C. K., Mukherjee T. K. (2022), Quantum dot-embedded hybrid photocatalytic nanoreactors for visible light photocatalysis and dye degradation, ACS Appl. Nano Mater., 5(5), 7427–7439. (DOI:10.1021/acsanm.2c01446)

22. Sureka H. V., Obermeyer A. C., Flores R. J., Olsen B. D. (2019), Catalytic biosensors from complex coacervate core micelle (C3M) Thin Films, ACS Appl. Mater. Interfaces, 11(35), 32354–32365. (DOI:10.1021/acsami.9b08478)

23. Singh S., Vaishnav J. K., Mukherjee T. K. (2020), Quantum dot-based hybrid coacervate nanodroplets for ultrasensitive detection of Hg^{2+}, ACS Appl. Nano Mater., 3(4), 3604–3612. (DOI:10.1021/acsanm.0c00317)

24. Dora Tang T-Y., Rohaida Che Hak C., Thompson A. J., Kuimova M. K., Williams D. S., Perriman A. W., et al. (2014), Fatty acid membrane assembly on coacervate microdroplets as a step towards a hybrid protocell model, Nat. Chem., 6(6), 527–533. (DOI:10.1038/nchem.1921)

25. van Stevendaal M. H. M. E., Vasiukas L., Yewdall N. A., Mason A. F., van Hest J. C. M. (2021), Engineering of biocompatible coacervate-based synthetic cells, ACS Appl. Mater. Interfaces, 13(7), 7879–7889. (DOI:10.1021/acsami.0c19052)

26. Koga S., Williams D. S., Perriman A. W., Mann S. (2011), Peptide–nucleotide microdroplets as a step towards a membrane-free protocell model, Nat. Chem., 3(9), 720–724. (DOI:10.1038/nchem.1110)

27. Dewey D. C., Strulson C. A., Cacace D. N., Bevilacqua P. C., Keating C. D. (2014), Bioreactor droplets from liposome-stabilized all-aqueous emulsions, Nat. Commun., 5(1), 4670. (DOI:10.1038/ncomms5670)

28. Crosby J., Treadwell T., Hammerton M., Vasilakis K., Crump M. P., Williams DS., et al. (2012), Stabilization and enhanced reactivity of actinorhodin polyketide synthase minimal complex in polymer–nucleotide coacervate droplets, Chem. Commun., 48(97), 11832. (DOI:10.1039/c2cc36533b)

29. Qiao Y., Li M., Booth R., Mann S. (2017), Predatory behaviour in synthetic protocell communities, Nat. Chem., 9(2), 110–119. (DOI:10.1038/nchem.2617)

30. Qiao Y., Li M., Qiu D., Mann S. (2019), Response-retaliation behavior in synthetic protocell communities, Angew. Chem. Int. Ed., 58(49), 17758–17763. (DOI:10.1002/anie.201909313)

31. Love C., Steinkühler J., Gonzales D. T., Yandrapalli N., Robinson T., Dimova R., et al. (2020), Reversible pH-responsive coacervate formation in lipid vesicles activates dormant enzymatic reactions, Angew. Chem. Int. Ed., 59(15), 5950–5957. (DOI:10.1002/anie.201914893)

32. Drobot B., Iglesias-Artola J. M., Le Vay K., Mayr V., Kar M., Kreysing M., et al. (2018), Compartmentalised RNA catalysis in membrane-free coacervate protocells, Nat. Commun., 9(1), 3643. (DOI:10.1038/s41467-018-06072-w)

33. Saini B., Mukherjee T. K. (2022), Biomolecular condensate regulates enzymatic activity under crowded milieu: Synchronization of liquid-liquid phase separation and enzymatic transformation, Biochemistry, preprint. (DOI:10.1101/2022.06.16.496378)

34. Gao L., Zhuang J., Nie L., Zhang J., Zhang Y., Gu N., et al. (2007), Intrinsic peroxidase-like activity of ferromagnetic nanoparticles, Nat. Nanotech., 2(9), 577–583. (DOI:10.1038/nnano.2007.260)

35. Yao Y., Zhang C. (2016), A novel screen-printed microfluidic paper-based electrochemical device for detection of glucose and uric acid in urine, Biomed. Microdevices, 18(5), 92. (DOI:10.1007/s10544-016-0115-6)

36. Karim Md. N., Anderson S. R., Singh S., Ramanathan R., Bansal V. (2018), Nanostructured silver fabric as a free-standing NanoZyme for colorimetric detection of glucose in urine, Biosens. Bioelectron., 110, 8–15. (DOI:10.1016/j.bios.2018.03.025)

37. Su L., Feng J., Zhou X., Ren C., Li H., Chen X. (2012), Colorimetric detection of urine glucose Based $ZnFe_2O_4$ magnetic nanoparticles, Anal. Chem., 84(13), 5753–5758. (DOI:10.1021/ac300939z)

38. Zhang Z., Chen Z., Cheng F., Zhang Y., Chen L. (2017), Highly sensitive on-site detection of glucose in human urine with naked eye based on enzymatic-like reaction mediated etching of gold nanorods, Biosens. Bioelectron., 89, 932–936. (DOI:10.1016/j.bios.2016.09.090)

Chapter 7

Biomolecular Condensates Regulate Enzymatic Activity under a Crowded Milieu: Synchronization of Liquid−Liquid Phase Separation and Enzymatic Transformation

7.1. Introduction

The cellular interior is highly crowded ($\sim$200−400 g/L) by various biomacromolecules which occupy $\sim$40% of its volume [1]. How the complex and heterogeneous cellular environment governs various complex biochemical reactions efficiently is a fundamental question in cell physiology that has not been understood yet. The effect of crowding on enzymatic activity is complex and difficult to forecast. Some enzymes show enhanced activity by considering crowding induced conformational changes of the enzymes and excluded volume effect [2, 3] in the presence of crowders. On the other hand, some enzymes display reduced or unaltered catalytic rates due to the significant diffusion barriers of enzymes and substrates along with product inhibition in a highly crowded environment [4–12]. Moreover, crowding may also influence the magnitude of K_m by either lowering [5, 6, 13, 14] or increasing [15, 16] its value compared to that in dilute buffer conditions. These contrasting effects of macromolecular crowding on the kinetic parameters indicate the complex role of macromolecular crowding on the enzymatic reactions.

Generally, the enhancement in catalytic activity was accounted by considering stabilization of active conformation of enzymes via excluded volume effect and modulation of soft protein-protein interactions via weak nonspecific chemical interactions under a crowded milieu [17–19]. Notably, macromolecular crowding also induce the liquid−liquid phase separation (LLPS) of many disease-associated proteins containing intrinsically disordered regions (IDRs) with low complexity domains (LCDs) in their amino acid sequence [20–24]. It is important to mention that most of the earlier studies on enzymatic kinetics in a crowded milieu have focused solely on the kinetic aspects, while the influence of inert crowders on the physicochemical properties of enzymes is highly

overlooked. The primary objective of the present study is to thoroughly probe the physicochemical properties of two well-known model enzymes HRP and GOx before and after the enzymatic transformations in the absence and presence of inert polymeric (PEG 8000, dextran 70, Ficoll 400) and protein crowders (BSA). The HRP/GOx pair catalyzes the oxidation of glucose by GOx in the presence of oxygen (O_2) to produce hydrogen peroxide (H_2O_2), which is subsequently utilized by HRP to oxidize organic or inorganic substrates by releasing H_2O (Scheme 1).
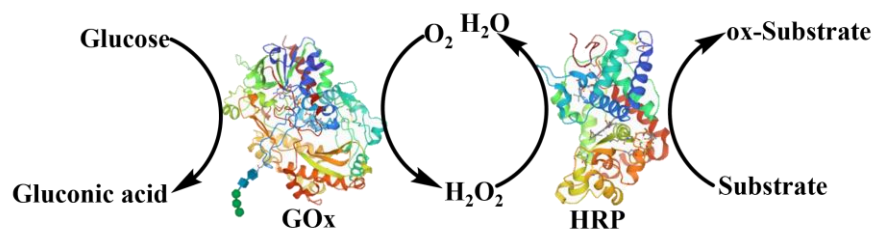
Scheme 7.1. *Schematics of enzymatic reactions.* (Saini *et al. J. Phys. Chem. B* **2023**, *127*, 180-193)

7.2. Results and discussion

7.2.1. Macromolecular crowding induces LLPS of HRP and GOx

The aqueous solutions of 0.5 μM HRP and GOx in the absence and presence of crowders remain isotropic in nature and no visible turbidity appears within 2 days of incubation at 37 °C (Figure 7.1A). However, the aqueous solution of GOx in the presence of 10% PEG shows visible turbidity after 3 days of incubation at 37 °C. Surprisingly, both enzymes in the presence of 10% PEG 8000 at 37 °C display uniform spherical assemblies as revealed from DIC images (Figure 7.1B). No such assemblies are observed in the absence of PEG and enzymes (Figure 7.1C), indicating the active role of crowders behind the formation of these spherical assemblies. Next, to visualize clearly under CLSM, HRP and GOx were first labeled with RBITC and FITC, respectively. Figure 7.1D displays the CLSM images of

RBITC-labeled HRP and FITC-labeled GOx in the presence of 10% unlabeled PEG, confirm the presence of enzymes inside these assemblies. Notably, fluorescent labeling does not perturb the formation and morphologies of these assemblies as revealed by 10 and 100% labeled enzymes (Figure 7.1E).
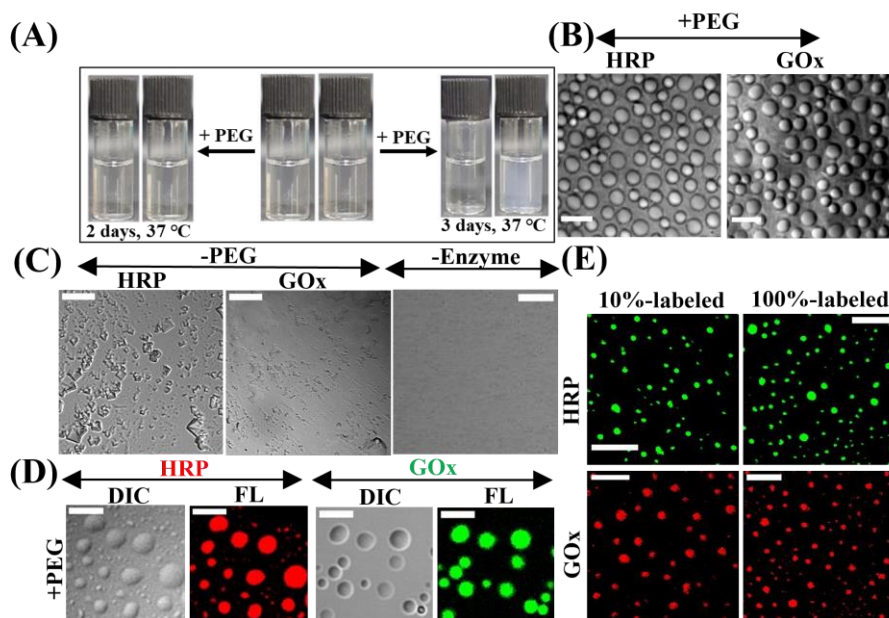
Figure 7.1. (A) Daylight photographs of aqueous solutions of HRP and GOx in the absence and presence of 10% PEG in pH 4.0 acetate buffer. DIC images of HRP and GOx in the (B) presence and (C) absence of 10% PEG and enzymes. (D) Confocal images of RBITC-labeled HRP and FITC-labeled GOx droplets in 10% PEG. (E) CLSM images of droplets in the presence of 10% PEG with 10%- and 100%-labeled enzymes. The scale bars correspond to 5 μm. (Saini *et al. J. Phys. Chem. B* **2023**, *127*, 180-193)

Interestingly, these assemblies also display the liquid-like characteristics such as fusion, dripping, and surface wetting (Figure 7.2A) *[23–28].* Similar droplet formation has also been observed in the presence of 12.5% Ficoll 400, 10% dextran 70, and 20 mg/mL BSA, suggesting a

general crowding effect (Figure 7.2B). Moreover, FESEM measurement also confirms the formation of similar droplets in the presence of polymeric crowders without any structural distortion over a period of 15 days (Figure 7.2C & D).

To know the homotypic (only enzymes are involved) or heterotypic (both enzyme and crowder are involved) LLPS behavior of enzymes, we utilized fluorescently labeled PEG (RBITC-labeled mPEG-NH$_2$, MW 5000) and BSA (RBITC-labeled) with unlabeled enzymes. Figure 7.2E shows that both PEG and BSA are excluded from the phase-separated droplets of HRP and GOx as revealed from their background fluorescent signals and also authenticate the spontaneous homotypic LLPS of HRP and GOx in the presence of inert crowders.
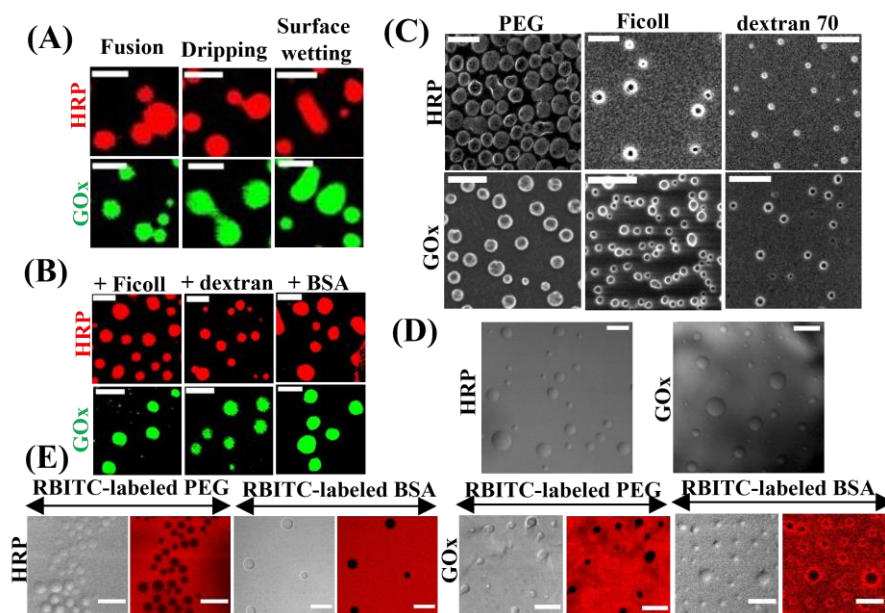
Figure 7.2. (A) Confocal images showing fusion, dripping, and surface wetting phenomena for HRP and GOx droplets. (B) Confocal images of droplets in 12.5% Ficoll, 10% dextran, and 20 mg/mL BSA. (C) FESEM images of HRP and GOx droplets in the presence of polymeric crowders.

(D) Confocal DIC images showing the stability of droplets HRP, and GOx over a period of 15 days. (E) Confocal images of droplets in RBITC-labeled mPEG-NH$_2$ and RBITC-labeled BSA. (Saini *et al. J. Phys. Chem. B* **2023**, *127*, 180-193)

Next, we examine the physicochemical properties of these phase-separated droplets as a function of incubation time (5, 15, 30, and 60 min) at 37 °C. Figure 7.3A shows the CLSM images of formation of well-dispersed HRP and GOx droplets irrespective of the incubation time. However, droplets become homogeneous in size upon an increase in the incubation time due to spontaneous fusion events and after 60 min of incubation, droplets of both the enzymes exhibit uniform size distribution (Figure 7.3A). Importantly, no droplet formation was observed at lower concentrations of crowders, indicating the critical role of crowders to induce LLPS (Figure 7.3B). In general, proteins having IDRs with LCDs in their amino acid sequence exhibit spontaneous LLPS beyond a critical concentration in the absence or presence of macromolecular crowders *[23–32]*. However, recent findings revealed that the presence of IDRs with LCDs is not an essential requirement for biomacromolecules to undergo LLPS *[27, 28]*. To know the LCDs and IDRs of both enzymes, we used sequence prediction algorithms, namely, SMART and IUPred2, respectively. While SMART analysis of GOx sequence reveals three LCDs (residues 4−17, 47−61, and 363−371), IUPred2 disorder prediction algorithm predicts around six short disorder regions (residues 127−130, 192−204, 222−226, 237−243, 287−291, and 359−360) (Figure 7.3C). However, neither LCDs nor any disorder regions are predicted for HRP (Figure 7.3D), suggesting that the presence of LCDs and/or IDRs is not an essential prerequisite for LLPS. Next, we explored the molecular origin of

these intermolecular protein-protein interactions under the crowded environment.
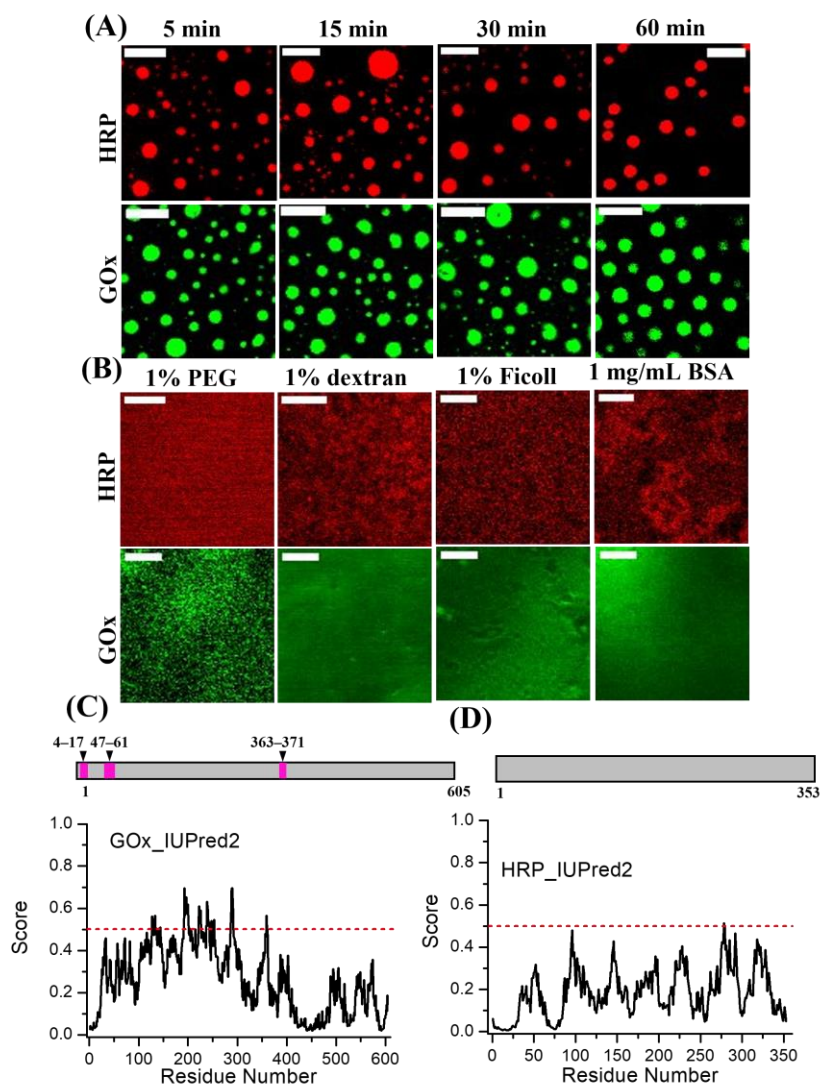
Figure 7.3. (A) Confocal images of RBITC-labeled HRP and FITC-labeled GOx droplets in the presence of 10% PEG as a function of incubation time. (B) Confocal images showing absence of any droplets in the presence of 1% PEG, 1% dextran, 1% Ficoll, and 1 mg/mL BSA. The scale bars correspond to 5 μm. Predictive algorithm showing

LCDs and IDRs of (C) GOx, and (D) HRP. (Saini *et al. J. Phys. Chem. B* **2023**, *127*, 180-193)

7.2.2. Nature of intermolecular interactions

7.2.2.1. Effect of temperature and pH

To decipher the precise role of various multivalent interactions, we studied the droplet formation pathways of HRP and GOx as a function of temperature, pH, and ionic strength under CLSM and FESEM in the presence of 10% PEG. Depending on the nature of intermolecular interactions, LLPS of biomacromolecules exhibits either upper critical solution temperature (UCST) *[27]* or lower critical solution temperature (LCST) *[26]* or both *[32]*. Figure 7.4A shows the CLSM and FESEM images of feasibility of both the enzymes undergo LLPS in the presence of 10% PEG in the range of 4−90 °C. It has been observed that droplets of both the enzymes are stable in the temperature range of 4−80 °C; however, droplet formation is completely inhibited at 90 °C suggesting that LLPS of both the enzymes follow UCST profile. The observed UCST profiles indicate a dominant role of enthalpically driven intermolecular interactions over the entropy of mixing as described previously by the Flory−Huggins theory *[33, 34]*. Next, the feasibility of LLPS of both the enzymes in the presence of 10% PEG is investigated as a function of solution pH in the range of 4.0−10.0 (Figure 7.4B). HRP in the presence of 10% PEG forms well-dispersed droplets in the pH range of 4.0−9.0; however, droplet formation is inhibited at pH 10.0. In contrast, droplets of GOx are stable in the pH range of 7.4−9.0; however, they disintegrate at pH values of 4.0 and 10.0 (Figures 7.4B).

These findings indicate the active role of charged residues of HRP and GOx behind the droplet formation mechanism by considering their pI values of 8.8 and 4.2, respectively *[35]*. In addition, we believe that pH-

dependent alteration in the secondary structures of enzymes may also contributes to the overall stability of these liquid-like droplets.
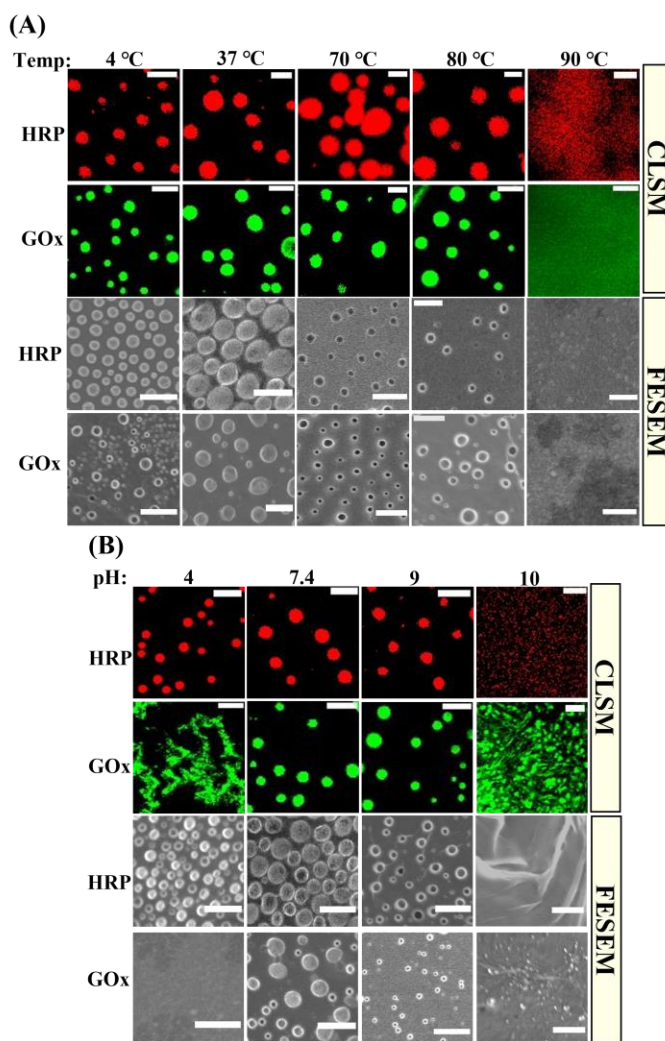
Figure 7.4. Confocal and FESEM images showing the stability of RBITC-labeled HRP and FITC-labeled GOx droplets as a function of (A) temperature, (B) pH. The scale bars correspond to 5 μm. (Saini *et al. J. Phys. Chem. B* **2023**, *127*, 180-193)

7.2.2.2. Effect of salt and aliphatic alcohol

Intermolecular protein-protein interactions can be modulated to a great extent by varying the concentrations of salts and aliphatic alcohols. Next, we tested the feasibility of LLPS in the presence of 10% PEG upon the addition of varying concentrations of a neutral salt, sodium chloride (NaCl), chaotropic salt, sodium thiocyanate (NaSCN), and aliphatic alcohol, 1,6-hexanediol.
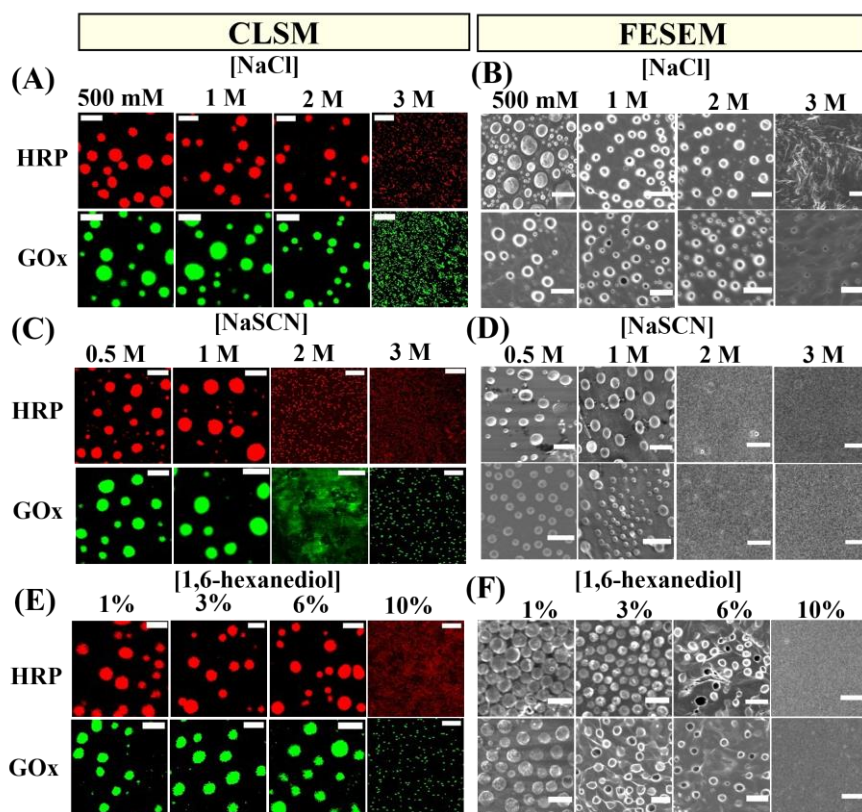
Figure 7.5. Confocal and FESEM images showing the stability of RBITC-labeled HRP and FITC-labeled GOx droplets as a function of (A, B) NaCl concentrations, (C, D) NaSCN concentrations, and (E, F) 1,6- hexanediol concentrations. The scale bars correspond to 5 μm. (Saini *et al. J. Phys. Chem. B* **2023**, *127*, 180-193)

Droplets of both the enzymes are found to be stable upto a NaCl concentration of 2 M (Figures 7.5A & B). However, droplet formation is completely inhibited in the presence of 3 M NaCl for both the enzymes, indicating the key role of electrostatic intermolecular interactions behind the LLPS of both the enzymes *[25–27, 29, 31, 32]*. To know whether any hydrophobic protein-protein interactions play any role in the observed LLPS of HRP and GOx, we varied the concentrations of NaSCN and 1,6-hexanediol, which are known to disrupt hydrophobic protein-protein interactions *[25, 27, 31]*. Droplets of both enzymes remain intact upto 1 M of NaSCN; however, droplet formation is inhibited completely at and beyond 2 M of NaSCN (Figures 7.5C & D).

Similarly, droplets of both enzymes remain intact in the presence of 1−6% of 1,6−hexanediol; however, they disintegrate completely at 10% of 1,6−hexanediol (Figures 7.5E & F). These findings authenticate the active role of hydrophobic protein-protein interactions behind the observed LLPS of HRP and GOx in the presence of crowders. Taken together, our findings illustrate that the droplet formation of both enzymes via LLPS is primarily driven by multivalent electrostatic as well as hydrophobic intermolecular interactions between short patches of polypeptide chains. Moreover, the present findings reveal that macromolecular crowding effectively favors these soft protein-protein interactions and drives the LLPS under the physiological conditions.

7.2.3. Alteration of secondary structures of enzymes

To know the conformational perturbation of HRP and GOx in the presence of crowders, we performed circular dichroism (CD) measurements in the absence and presence of 10% PEG. The far-UV CD spectrum of HRP at pH 4.0 displays two minima at 208 and 222 nm, suggesting an α-helical rich secondary structure (Figure 7.6A). The spectrum of HRP at pH 4.0 differs

slightly from that at pH 7.4 with decrease in ellipticity at 222 nm (Figure 4A, dotted line), indicating pH-dependent conformation change. Importantly, a distinct red shift of 4 nm with an increase in ellipticity at 222 nm has been observed in the presence of PEG. Similarly, the CD spectrum at the Soret region and UV−vis spectrum of HRP in the presence of PEG display a prominent red shift of 3 and 15 nm, respectively, compared to that in the aqueous buffer (Figure 7.6B & C). These spectral change of HRP upon crowding indicates more compact secondary structure and higher integrity of the heme pocket *[36]*. In contrast, the ellipticity of GOx at 222 nm decreases slightly upon crowding (Figure 7.6D), suggesting a subtle conformational change of GOx. Therefore, these findings clearly authenticate the altered secondary structures of phase separated enzymes under the crowded environment relative to that in the aqueous buffer.
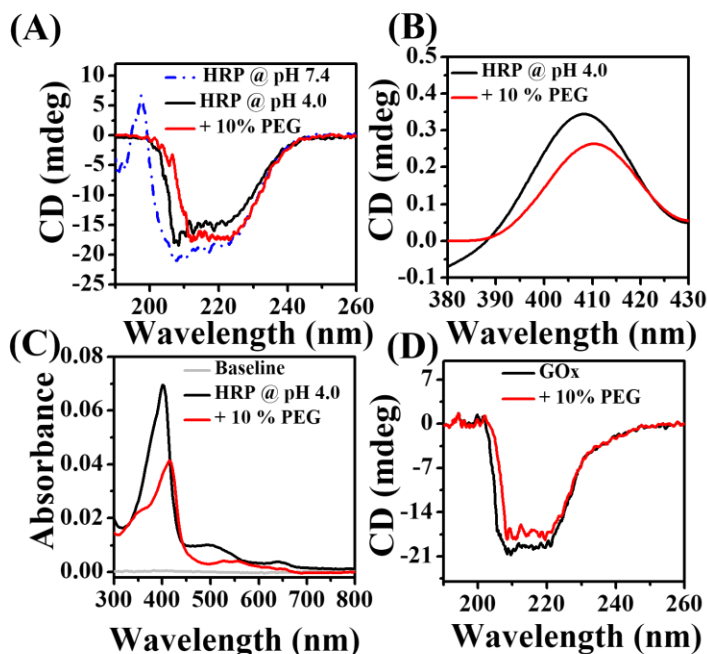
Figure 7.6. Effect of 10% PEG on (A) far-UV CD, (B) Soret region CD, and (C) UV−vis absorption spectra of 0.5 μM HRP. (D) Changes in the far-

UV CD spectra of 0.5 µM GOx in the presence of 10% PEG. (Saini *et al. J. Phys. Chem. B* **2023**, *127*, 180-193)

Next, we seek to address how these conformationally altered phase separated enzymes in a crowded milieu drive their respective catalytic transformations. Here it is important to mention that the present study is first of its kind to demonstrate the detailed kinetic aspects of enzymatic transformations considering the phase separation in a crowded milieu, which is completely ignored in earlier reports.

7.2.4. Effect of LLPS on the enzymatic kinetics

For all the kinetic experiments, we kept the enzyme concentration fixed at 25 pM as at high concentration (0.5 µM), the enzymatic transformations were too fast to monitor in the crowded environments. Control experiments with 25 pM of enzymes reveal similar kinds of LLPS in the presence of 10% PEG (Figure 7.7A). However, the sizes of droplets are smaller than that observed with 0.5 µM of enzymes. Nevertheless, we have observed phase separation in a broad concentration range of both the enzymes, indicating their high tendency toward LLPS under macromolecular crowding. The kinetics of HRP and GOx catalyzed reactions were monitored using a UV−vis spectrophotometer at their optimum pH values of 4.0 and 7.4, respectively (Figure 7.7B). We mainly monitored the enzymatic transformations before and after the phase separation of HRP and GOx in the presence of different crowders such as 10% PEG 8000, 10% dextran 70, 12.5% Ficoll 400, and 20 mg/mL BSA. Moreover, the feasibility of GOx/HRP cascade reaction was investigated in the presence of 10% PEG and 20 mg/mL BSA after their phase separation using different substrates such as TMB, OPD, and ABTS.

7.2.4.1. Enzymatic Kinetics before Phase Separation
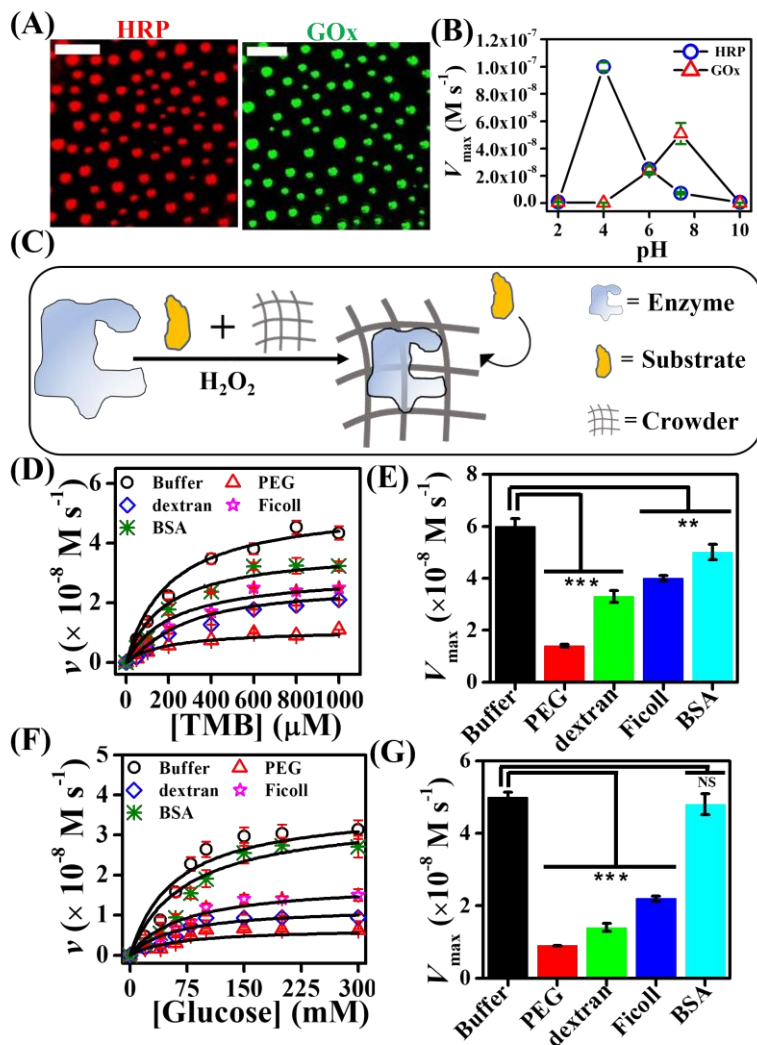
Figure 7.7. (A) CLSM images of RBITC-labeled HRP, and FITC- labeled GOx in the presence of 10% PEG at 37 °C with an enzyme concentration of 25 pM. The scale bars correspond to 5 μm. (B) Plot of V_{max} versus pH for HRP and GOx catalyzed reactions at 37 °C. (C) Illustration of enzymatic reaction in the presence of substrates and crowder. The effect of different crowders on the (D) Michaelis−Menten plots of HRP, (E) V_{max} values of HRP, (F) Michaelis−Menten plots of GOx, and (F) V_{max} values of GOx. The data represent the mean ± SEM for three (n = 3) independent experiments. Statistical significance was assessed by a two-tailed, unpaired Student's t-

test with ***, P value < 0.001; **, P value < 0.01; and not significant (NS), P > 0.05. (Saini *et al. J. Phys. Chem. B* **2023**, *127*, 180-193)

Initially, we tested the influence of various crowders on the individual enzymatic kinetics of HRP and GOx just after their addition in pH 4.0 and 7.4 aqueous buffers, respectively (Figure 7.7C). HRP catalyzed reactions were monitored using TMB as a substrate by recording the changes in the absorbance at 650 nm as a function of reaction time. The enzymatic rate of 25 pM HRP in the presence of 8.8 mM H_2O_2 in the aqueous acetate buffer (pH 4.0) at 37 °C follows a typical Michaelis−Menten plot as a function of TMB concentrations (Figure 7.7D). Notably, the rate decreases drastically in the presence of different crowders as revealed from the Michaelis−Menten plots (Figure 7.7D). The observed rate is the lowest in 10% PEG followed by 10% dextran, 12.5% Ficoll, and 20 mg/mL BSA.

These data were fitted with the Michaelis−Menten equation to obtain maximum velocity (V_{max}) and Michaelis constant (K_m). The calculated V_{max} values for different crowders are compared in Figure 7.7E. It is evident that V_{max} decreases in the presence of crowders and more so in the presence of polymeric crowders. Previously, it has been shown that macromolecular crowding slowdown enzymatic kinetics significantly *[4–10, 12, 37, 38]*.

Moreover, it is known that polymeric crowders increase the viscosity of the solution more compared to the protein crowders and as a result the rate of the diffusion-controlled reactions slowdown significantly in the presence of polymeric crowders *[38]*. The estimated K_m and turnover numbers (k_{cat}) are tabulated in Table 7.1.

Table 7.1. Michaelis-Menten parameters estimated instantly in different solutions.

	K_m (mM)		k_{cat} (s^{-1})	
	HRP	GOx	HRP	GOx
buffer	0.30 ± 0.06	101.0 ± 5.2	$(2.4 \pm 0.07) \times 10^3$	$(2.0 \pm 0.01) \times 10^3$
10% PEG	0.30 ± 0.05	83.3 ± 2.3	$(5.6 \pm 0.5) \times 10^2$	$(3.7 \pm 0.1) \times 10^2$
10% dextran	0.60 ± 0.05	88.0 ± 1.2	$(1.3 \pm 0.07) \times 10^3$	$(5.6 \pm 0.8) \times 10^2$
12.5% Ficoll	0.40 ± 0.03	84.4 ± 1.6	$(1.6 \pm 0.1) \times 10^3$	$(8.8 \pm 0.7) \times 10^2$
20 mg/mL BSA	0.40 ± 0.07	84.0 ± 2.1	$(2.0 \pm 0.04) \times 10^3$	$(1.9 \pm 0.1) \times 10^3$

While the K_m of TMB remains unaltered in the presence of PEG, a noticeable increase has been observed in the presence of dextran, Ficoll, and BSA. The estimated K_m values are in good agreement with the previous report [39]. On the other hand, k_{cat} decreases from a value of 2.4×10^3 in buffer to 5.6×10^2, 1.3×10^3, 1.6×10^3, and 2.0×10^3 s^{-1} in the presence of 10% PEG, 10% dextran, 12.5% Ficoll, and 20 mg/mL BSA, respectively. Similar trends have been observed for GOx kinetics with glucose as a substrate in the presence of different crowders (Figures 7.7F). The V_{max} decreases significantly in the presence of polymeric crowders compared to that in the aqueous buffer (Figure 7.7G). Moreover, a noticeable decrease in the K_m value of glucose has been observed in the presence of crowders (Table 7.1). The estimated K_m values are in good agreement with the previous report [40]. The lower values of K_m in the presence of crowders indicate higher binding affinity of glucose possibly due to the altered conformation of GOx in the crowded environments. While the estimated k_{cat} of GOx decreases remarkably in the presence of polymeric crowders, it remains almost unaltered in the presence of 20 mg/mL BSA. Taken together, our findings reveal that the enzymatic kinetics of HRP and GOx slowdown appreciably in the crowded environment, similar to the previous

reports *[4–10, 12, 37, 38]*. Notably, these observations are valid only when the enzymatic reactions are monitored instantly after the addition of enzymes in the crowded environment. However, these enzymes can simultaneously undergo LLPS during the course of these transformations and hence the present framework is not an ideal platform to explore the effect of macromolecular crowding. To know the overall impact of crowding on the enzymatic kinetics, we next bifurcated the complete process into two independent events, namely, LLPS followed by enzymatic transformations.

7.2.4.2. Enzymatic kinetics after phase separation

Here, we first allowed the enzymes to undergo LLPS in the presence of crowders. Enzymes were incubated in the aqueous buffers in the presence of crowders at 37 °C for 1 h to have a homogeneous growth of phase separated droplets. Subsequently, enzymatic reactions were monitored instantly after the addition of substrates (Figure 7.8A). The absorbance at 650 nm was monitored as a function of reaction time in the absence and presence of crowders. Reactions with phase separated droplets of HRP exhibit crowder-dependent variation in the rate. Interestingly, the enzymatic rate increases appreciably compared to that in the aqueous buffer for all the crowders (Figure 7.8B). The observed enhancement is crowder-dependent and maximum enhancement has been observed in the presence of 20 mg/mL BSA, whereas polymeric crowders show comparatively lower extent of enhancement. Similar enhancement in the enzymatic rates of phase separated GOx has been observed in the presence of different crowders (Figures 7.8C). The estimated V_{max} values are compared in Figure 7.8D. The V_{max} value of HRP and GOx increases by a factor of 62- and 14.3-times, respectively, in the presence of BSA relative to that in the aqueous buffer.

Figure 7.8. (A) Schematic illustration showing the enzymatic reaction after the LLPS in the presence of crowder. (B) Michaelis-Menten plots of HRP as a function of TMB concentrations in the absence and presence of different crowders after the LLPS in pH 4.0 acetate buffer at 37 °C. (C) Michaelis-Menten plots of GOx as a function of glucose concentrations in the absence and presence of different crowders after the LLPS in pH 7.4 PBS at 37 °C. (D) Estimated V_{max} values of HRP and GOx in the absence and presence of 10% PEG, 10% dextran, 12.5% Ficoll, and 20 mg/mL BSA. (E) Estimated V_{max} values of HRP in the presence of 1% PEG, 1% dextran, 1% Ficoll, and 1 mg/mL BSA. The data represent the mean ± SEM for three (n = 3) independent experiments. (Saini *et al. J. Phys. Chem. B* **2023**, *127*, 180-193)

However, much lower extent (2.0- to 6.4-fold for HRP and 1.8- to 4.0-fold for GOx) of enhancement has been observed in the presence of polymeric crowders. The observed enhancement in the enzymatic rates could be due to the formation of phase separated droplet in the presence of crowders. In order to establish this argument, we performed enzymatic assays under the same experimental conditions with lower concentrations of crowders where no droplet formation was observed earlier. Control experiments reveal a decrease in the V_{max} values compared to that in the aqueous buffer in the presence of 1% PEG, 1% dextran, 1% Ficoll, and 1 mg/mL BSA (Figure 7.8E). Therefore, the unusual enhancement in the enzymatic rates of HRP and GOx arises primarily due to the formation of phase-separated droplets in the presence of crowders. On the other hand, the lower rates observed in the presence of polymeric crowder for both enzymes

compared to that in protein crowder could be due to slow diffusion and lower extent of substrate partitioning in the viscous polymeric solutions.
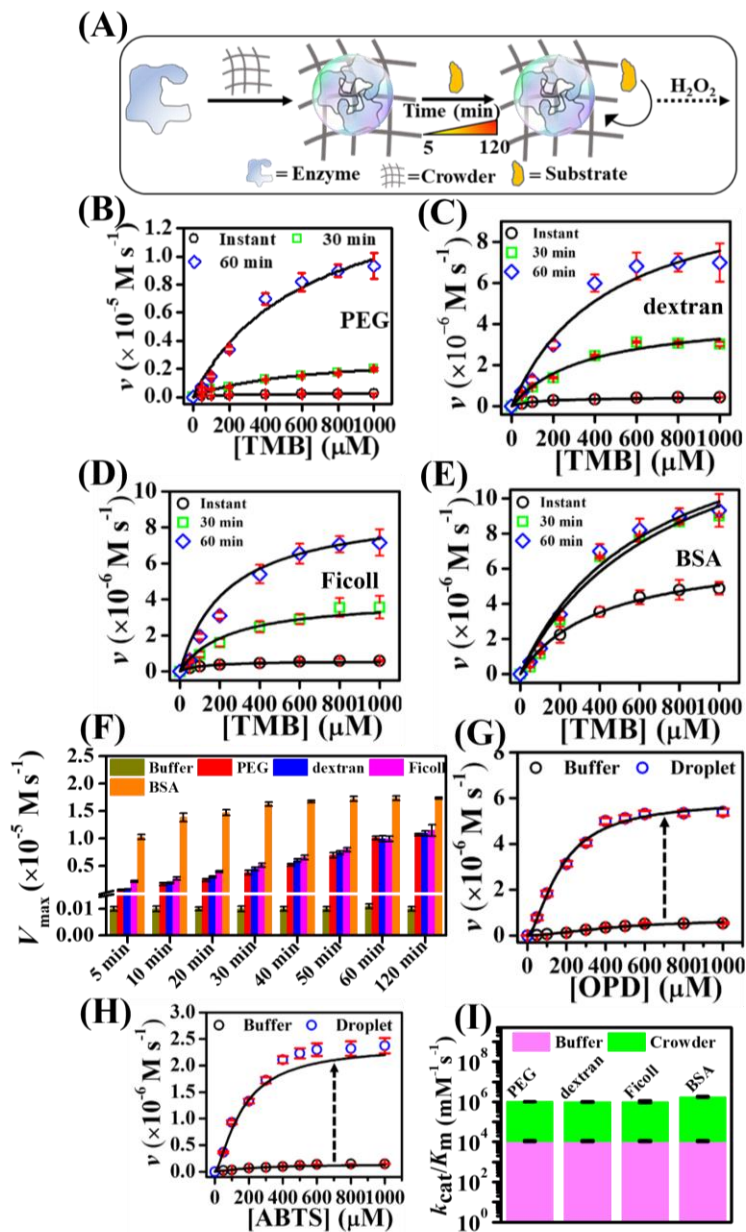
Figure 7.9. (A) Illustration of enzymatic reaction after the LLPS of enzyme in a time-dependent manner. Michaelis−Menten plots of HRP as a function of TMB concentrations at different time intervals after the LLPS in (B) 10%

PEG, (C) 10% dextran, (D) 12.5% Ficoll, and (E) 20 mg/mL BSA. (F) Estimated V_{max} values of HRP in the absence and presence of various crowders at different time-intervals after the LLPS. Michaelis-Menten plots of HRP as a function of (G) OPD, and (H) ABTS concentrations in the absence and presence of 10% PEG at 37 °C in pH 4.0 acetate buffer. (I) Plot of k_{cat}/K_m values of HRP in buffer and different crowders. (Saini *et al. J. Phys. Chem. B* **2023**, *127*, 180-193)

To establish this possibility, we performed time-dependent kinetic assays with phase-separated HRP in the presence of different crowders. It should be noted that the reaction catalyzed by HRP provides a unique opportunity to test the effect of diffusion and substrate partitioning into the phase-separated droplets in a time-dependent manner as the reaction requires additional oxidant, H_2O_2, which is essential to initiate the catalytic transformation (Figure 7.9A). HRP catalyzed reactions were followed after the addition of TMB and initiated just after the addition of 8.8 mM H_2O_2 at a desire time interval (5−120 min). Surprisingly, the enzymatic rate of HRP in the presence of 10% PEG increases remarkably in a time-dependent manner as revealed from the Michaelis−Menten plots (Figure 7.9B).

Similar time-dependent enhancement in the enzymatic rate has also been observed in the presence of dextran, Ficoll, and BSA as crowders (Figures 7.9C, D, & E). Reactions monitored after 5 min of incubation of TMB with phase-separated droplets show 7-, 8-, 22-, and 100- fold enhancement in the V_{max} value relative to that in the aqueous buffer in the presence of PEG, dextran, Ficoll, and BSA, respectively (Figure 7.9F). While a gradual increase in the V_{max} value has been observed in the presence of different crowders in a time-dependent manner, the V_{max} of HRP in the aqueous buffer under the same experimental conditions remains constant at 1×10^{-7} M s^{-1}. Notably, the kinetics of HRP in 20 mg/mL BSA differs from

those in polymeric crowders in two aspects. First, a sharp increase in the V_{max} value has been observed for reaction monitored instantly after the addition of TMB and H_2O_2 in the presence of 20 mg/mL BSA. Second, the V_{max} of HRP in 20 mg/mL BSA saturates faster (within 30 min) than that in other polymeric crowders (within 60 min). Similar enhancement in the enzymatic rate of HRP has also been observed with OPD and ABTS as substrates in the presence of 10% PEG upon 60 min of incubation (Figures 7.9G & H). The saturated values of k_{cat} and K_m for TMB are summarized in Table 7.2.

Table 7.2. Saturated Michaelis-Menten parameters for HRP after the LLPS.

	K_m (mM)	k_{cat} (s^{-1})
buffer	0.50 ± 0.02	$(4.4 \pm 0.2) \times 10^3$
10% PEG	0.40 ± 0.03	$(4.0 \pm 0.6) \times 10^5$
10% dextran	0.50 ± 0.07	$(4.0 \pm 0.3) \times 10^5$
12.5% Ficoll	0.40 ± 0.04	$(4.0 \pm 0.2) \times 10^5$
20 mg/mL BSA	0.40 ± 0.06	$(7.2 \pm 0.2) \times 10^5$

It is evident that the K_m of TMB in the presence of different crowders remains almost unchanged relative to that estimated in the aqueous buffer under similar experimental conditions. Remarkably, the k_{cat} for TMB increases by 164-fold in the presence of 20 mg/mL BSA. The saturated value of catalytic efficiency (k_{cat}/K_m) of HRP increases by 114-, 91-, 114-, and 205-fold relative to the bulk aqueous phase in the presence of 10% PEG, 10% dextran, 12.5% Ficoll, and 20 mg/mL BSA, respectively (Figure 7.9I).

The observed differences in the kinetic parameters for polymeric and protein crowders clearly indicate the critical role of diffusion and partitioning of TMB inside the phase-separated droplets in crowded

polymeric solutions. The aqueous polymeric solutions being more viscous compared to the aqueous BSA solution provide additional diffusion barriers *[38]*. Moreover, it has been reported previously that TMB can specifically bind with polymeric crowders via the hydrophobic interactions *[41]*. Therefore, the lower enzymatic rates in polymeric crowders could also be due to specific hydrophobic interactions of TMB with polymers.
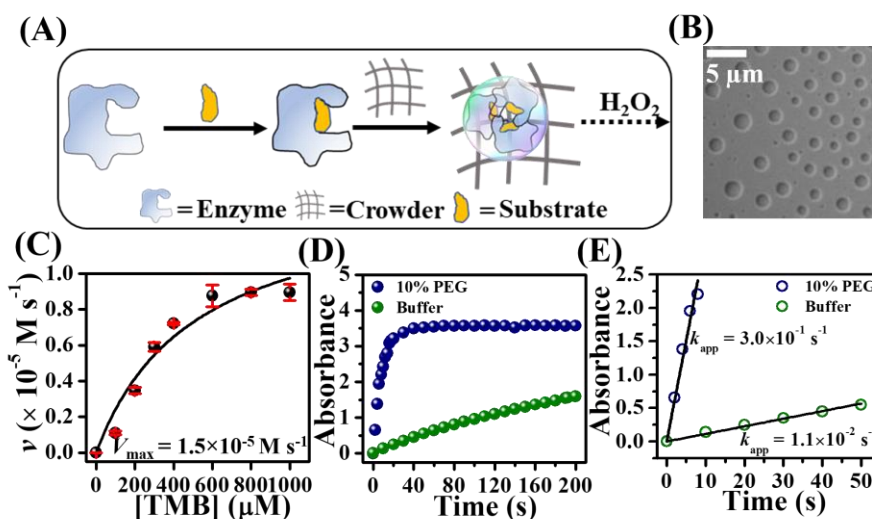
Figure 7.10. (A) Schematic illustration of enzymatic reaction after the LLPS of substrate-bound enzyme in the presence of 10% PEG. (B) Confocal DIC image of TMB-bound HRP in the presence of 10% PEG. (C) Michaelis−Menten plot after the LLPS of TMB-bound HRP. The data represent the mean ± SEM for three (n = 3) independent experiments. Changes in the (D) absorbance (λ = 650 nm) of ox-TMB and (E) k_{app} of HRP in buffer with100-fold molar excess of enzymes and substrates along with those obtained in the presence of 10% PEG with 1X concentrations. (Saini *et al. J. Phys. Chem. B* **2023**, *127*, 180-193)

To further substantiate these arguments, we performed a control experiment with TMB-bound HRP after its LLPS in the presence of crowders (Figure 7.10A). Importantly, TMB-bound HRP exhibits a similar

kind of LLPS in the presence of 10% PEG as revealed from confocal DIC image (Figure 7.10B). A kinetic experiment with TMB-bound HRP after the LLPS in 10% PEG reveals a saturated V_{max} value of 1.5×10^{-5} M s^{-1} (Figure 7.10C). This high value of V_{max} obtained instantly after the phase separation of TMB-bound HRP suggests that the time-dependent changes observed earlier in the HRP kinetics originate exclusively from the slow diffusion and substrate partitioning inside the droplets in a crowded environment. Taken together, our findings clearly indicate the critical role of diffusion and substrate partitioning on the enzymatic kinetics in a crowded milieu with phase-separated droplets. These findings suggest that LLPS has a tremendous influence on the enzymatic activity of HRP. In particular, the enhanced activity of phase-separated enzymes could be due to a combination of several factors. Among these, conformational change of the phase-separated enzyme is an important factor as revealed from our CD measurements. Second, the high local concentrations (mass action) of enzymes and substrates inside the phase-separated droplets can also accelerate the enzymatic kinetics. A control experiment with a 100-fold molar excess of HRP and substrates in the aqueous buffer reveals that the observed enhancement is not solely due to a simple mass action mechanism (Figure 7.10D & E).

Third, the confinement induced enhancement in the activities of bound water and substrates may also contribute positively to the overall enzymatic kinetics. Previously, it has been shown that confinement can significantly influence the feasibility, kinetics, and efficacy of a wide range of chemical transformations *[42, 43]*. Therefore, the remarkable enhancement in the catalytic efficiency of phase separated enzymes originates due to a combined effect of altered conformation of the active enzymes, mass action, and confinement induced enhanced activities of

water and substrates inside the phase separated droplets. Finally, we seek to address the feasibility of GOx/HRP cascade reaction after their respective phase separation in the presence of 10% PEG and 20 mg/mL BSA (Figure 7.11A). CLSM measurements reveal spontaneous coalescence between HRP and GOx droplets upon mixing their phase-separated solution in the presence of 10% PEG (Figure 7.11B). The uniform yellow signal appears exclusively from the interior of these droplets as a consequence of spontaneous fusion of red-emitting RBITC-labeled HRP droplets and green emitting FITC-labeled GOx droplets. This observation can be explained by considering the isoelectric point (*p*I) of HRP (8.8) and GOx (4.2) *[35]*. It is expected that the droplet formed by HRP at pH 4.0 will have a net positive charge, whereas droplet formed by GOx at pH 7.0 will bear a net negative charge. Upon mixing, these oppositely charged droplets of GOx and HRP fuse spontaneously to yield droplets having both GOx and HRP. The cascade reaction was initiated after the addition of glucose into the reaction mixture. dehydrogenase in the presence of 10% PEG in pH 7.4 PBS. The scale bars correspond to 5 μm.

The reactions were monitored by observing the time-dependent formation of oxidized products of TMB, OPD, and ABTS. In buffer, the apparent rate constant (k_{app}) of the cascade reaction with TMB as substrate is estimated to be 3.0×10^{-3} s^{-1}, which increases to 9.5×10^{-2} and 1.2×10^{-1} s^{-1} in the presence of 10% PEG and 20 mg/mL BSA, respectively (Figure 7.11 C & D). This 32- and 40-fold enhancement in the k_{app} value of the GOx/HRP cascade reaction in the presence of crowders is unprecedented in the literature and indicates the active role of phase-separated droplets on the cascade activity in a crowded milieu. Notably, much lower extent of enhancement has been observed for OPD (7.0- and 9.0-fold) and ABTS (5.3- and 6.0-fold) as substrates in the presence of both

PEG and BSA (Figure 7.11C & D). This contrasting behavior of substrate specificity could be either due to substrate-dependent alteration of the stability of fused droplets or due to the intrinsic physicochemical properties of substrates. However, the morphologies of fused droplets remain unaltered after the cascade reactions (Figure 7.11 E), indicating that the droplets are stable in the presence of different substrates during the reactions.
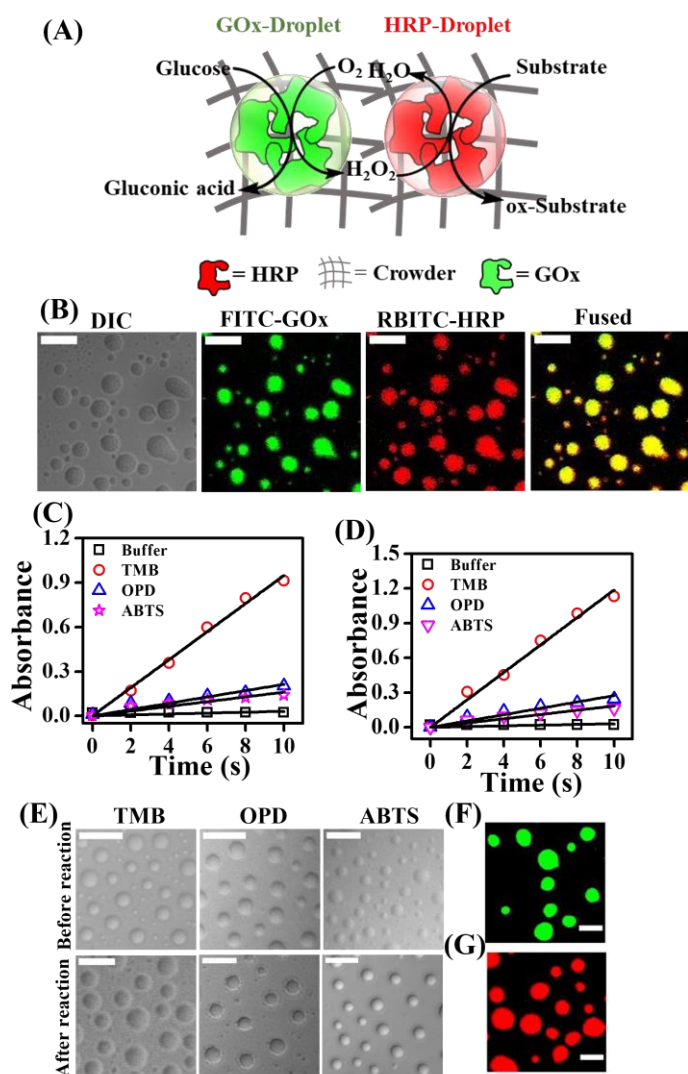
Figure 7.11. (A) Illustration of GOx/HRP cascade reaction in a crowded environment. (B) Confocal images showing the spontaneous coalescence between FITC-labeled GOx droplets and RBITC-labeled HRP droplets. Linearized plots of absorbance of oxidized substrates (TMB, OPD, and ABTS) for GOx/HRP cascade reactions in the absence and presence of (C) 10% PEG and (D) 20 mg/mL BSA. (E) Confocal DIC images of droplets before and after the cascade reactions with different substrates. CLSM images of (F) FITC-labeled trypsin, and (G) RBITC-labeled alcohol dehydrogenase. (Saini *et al. J. Phys. Chem. B* **2023**, *127*, 180-193)

In contrast, the physicochemical properties of these substrates differ significantly from each other. The substrate TMB, being more hydrophobic than OPD and ABTS is expected to partition preferentially inside the droplets containing both HRP and GOx *[41]*. In addition, the hydrophobicity of fused droplets containing both GOx and HRP is comparatively higher than the individual droplets of GOx and HRP due to the macromolecular crowding from both the enzymes. On the other hand, hydrophilic substrates OPD and ABTS prefer to remain in the bulk aqueous phase, which lowers their partition coefficient. Therefore, our findings reveal that the physicochemical properties of phase-separated droplets and substrates dictate the specificity and selectivity of the enzymatic cascade reactions under heterogeneous and crowded environments. Finally, control experiments with two other enzymes, namely, trypsin and alcohol dehydrogenase, reveal a similar crowding induced spontaneous LLPS phenomenon (Figure 7.11 F), suggesting the generality of this physiologically relevant unique event in regulating the efficacy of complex biocatalytic reactions under heterogeneous and crowded environments. Based on our findings, we propose a mechanistic model where enzymatic transformations can take place via three main competing pathways in a

crowded environment (Scheme 2). We believe that spatiotemporal regulation of these pathways determines the fate of enzymatic transformations in a crowded environment. In pathway 1, enzymes bind with substrates in a diffusion-controlled manner under the crowded environment and subsequently transform into products with reduced efficiency relative to that in the aqueous buffer. Most of the earlier reported enzymatic kinetics follow this pathway, where reactions were monitored just after the addition of enzymes into the reaction mixture in the presence of crowders.

Scheme 7.2. Illustration of competing pathways for enzymatic reactions under the crowded environment. (Saini *et al. J. Phys. Chem. B* **2023**, *127*, 180-193)
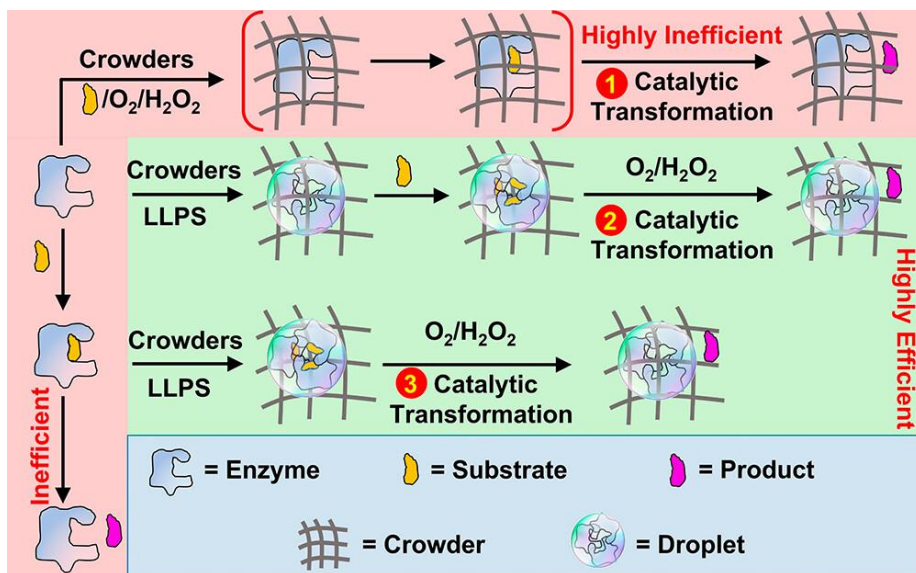
The present study is first of its kind to discover the presence of two other competing pathways in the presence of macromolecular crowders. In pathway 2, enzymes first undergo spontaneous LLPS in the presence of crowders via the formation of liquid- like droplets (Scheme 2). Subsequently, substrate binding via time-dependent partitioning into these phase-separated droplets leads to enzyme-substrate adducts. These

substrate-bound phase-separated enzymes ultimately undergo catalytic transformations in the presence of oxidants. Notably, the enzymatic activity enhances appreciably in pathway 2 in a time-dependent manner. In pathway 3, substrate-bound enzymes first undergo LLPS in the presence of crowders to yield liquid-like droplets. These phase-separated substrate-bound enzymes take part in the catalytic transformations in the presence of oxidants without any diffusion and partitioning barriers for substrates. Pathway 3 shows maximum enhancement in the enzymatic activity in the presence of crowders relative to that in the aqueous buffer and other pathways (Scheme 2). Therefore, our present study is one of its kind to illustrate the complex interplay of LLPS and enzymatic transformations under the crowded environment. While significant hindrance in the enzymatic activity has been observed before the LLPS of enzymes, remarkable enhancement has been observed in the catalytic activity after the LLPS of enzymes. The enhanced activity is due to a combined effect of conformational alteration of active enzymes, mass action, and confinement-induced alteration in the activities of water and substrates. In the physiological context, we believe that nature must utilize this spatiotemporal synchronization of LLPS, substrate binding, and enzymatic transformation in a highly regulated manner to tune the efficiency of various parallel and tandem complex metabolic reactions under the highly crowded environments. Notably, recent studies have highlighted the critical role of LLPS as a common mechanism underlying regulation of enzyme activity in cells *[44, 45]*.

7.3. Conclusions

In summary, we have discovered a unique and unprecedented phenomenon of LLPS of biologically active enzymes under the crowded environments. It has been shown that macromolecular crowding induces homotypic LLPS

of HRP and GOx via enthalpically controlled electrostatic as well as hydrophobic intermolecular interactions. We have illustrated the active role of phase-separated droplets behind the crowding induced enhancement of enzymatic activity under physiological conditions. Our mechanistic model represents the first proof of concept example of enhanced enzymatic activity and selectivity inside the phase-separated droplets under a crowded milieu. The enhanced activities inside the phase-separated droplets have been explained by considering conformational change of the active enzymes, mass action, and confinement induced alteration of the activity of surrounding water and substrates. The present discovery of phase-separation-induced active regulation of enzymatic activity and selectivity opens the door of a new avenue in biocatalysis with a vast scope in industrial applications.

Note: This is copyrighted material from permission of the American Chemical Society.

7.4. References

1.   Zhou H-X., Rivas G., Minton A. P. (2008), Macromolecular Crowding and Confinement: Biochemical, Biophysical, and Potential Physiological Consequences, Annu. Rev. Biophys., 37(1), 375–397. (DOI:10.1146/annurev.biophys.37.032807.125817)

2.   Norris M. G. S., Malys N. (2011), What is the true enzyme kinetics in the biological system? An investigation of macromolecular crowding effect upon enzyme kinetics of glucose-6-phosphate dehydrogenase, Biochem. Biophys. Res. Commun., 405(3), 388–392. (DOI:10.1016/j.bbrc.2011.01.037)

3. Totani K., Ihara Y., Matsuo I., Ito Y. (2008), Effects of macromolecular crowding on glycoprotein processing enzymes, J. Am. Chem. Soc., 130(6), 2101–2107. (DOI:10.1021/ja077570k)

4. Asaad N., Engberts J. B. F. N. (2003), Cytosol-mimetic chemistry: Kinetics of the trypsin-catalyzed hydrolysis of p- nitrophenyl acetate upon addition of polyethylene glycol and N-tert-butyl acetoacetamide, J. Am. Chem. Soc., 125(23), 6874–6875. (DOI:10.1021/ja034298f)

5. Poggi C. G., Slade K. M. (2015), Macromolecular crowding and the steady-state kinetics of malate dehydrogenase, Biochem., 54(2), 260–267. (DOI:10.1021/bi5011255)

6. Schneider S. H., Lockwood S. P., Hargreaves D. I., Slade D. J., LoConte M. A., Logan B. E., et al. (2015), Slowed diffusion and excluded volume both contribute to the effects of macromolecular crowding on alcohol dehydrogenase steady-state kinetics, Biochem., 54(38), 5898–5906. (DOI:10.1021/acs.biochem.5b00533)

7. Wilcox X. E., Ariola A., Jackson J. R., Slade K. M. (2020), Overlap concentration and the effect of macromolecular crowding on citrate synthase activity, Biochem., 59(18), 1737–1746. (DOI:10.1021/acs.biochem.0c00073)

8. Pastor I., Pitulice L., Balcells C., Vilaseca E., Madurga S., Isvoran A., et al. (2014), Effect of crowding by dextrans in enzymatic reactions, Biophys. Chem., 185, 8–13. (DOI:10.1016/j.bpc.2013.10.006)

9. Pavlovic M., Plucinski A., Zhang J., Antonietti M., Zeininger L., Schmidt B. V. K . J. (2020), Cascade kinetics in an enzyme-loaded aqueous two-phase system, Langmuir, 36(6), 1401–1408. (DOI:10.1021/acs.langmuir.0c00186)

10. Isabel Pastor L. P. (2013), Influence of macromolecular crowding on the oxidation of ABTS by hydrogen peroxide catalyzed by HRP, J

Biocatal. Biotransformation, 02(01) (DOI:10.4172/2324-9099.1000107)

11. Vöpel T., Makhatadze G. I. (2012), Enzyme activity in the crowded milieu, PLoS ONE, 7(6), e39418. (DOI:10.1371/journal.pone.0039418)

12. Pastor I., Vilaseca E., Madurga S., Garcés J. L., Cascante M., Mas F. (2011), Effect of crowding by dextrans on the hydrolysis of N -succinyl- L -phenyl-Ala- p -nitroanilide catalyzed by α-chymotrypsin, J. Phys. Chem. B, 115(5), 1115–1121. (DOI:10.1021/jp105296c)

13. Jiang M., Guo Z. (2007), Effects of macromolecular crowding on the intrinsic catalytic efficiency and structure of enterobactin-specific isochorismate synthase, J. Am. Chem. Soc., 129(4), 730–731. (DOI:10.1021/ja065064+)

14. Totani K., Ihara Y., Matsuo I., Ito Y. (2008), Effects of macromolecular crowding on glycoprotein processing enzymes, J. Am. Chem. Soc., 130(6), 2101–2107. (DOI:10.1021/ja077570k)

15. Aumiller W. M., Davis B. W., Hatzakis E., Keating C. D. (2014), Interactions of macromolecular crowding agents and cosolutes with small-molecule substrates: Effect on horseradish peroxidase activity with two different substrates, J. Phys. Chem. B, 118(36), 10624–10632. (DOI:10.1021/jp506594f)

16. Pastor I., Pitulice L., Balcells C., Vilaseca E., Madurga S., Isvoran A., et al. (2014), Effect of crowding by Dextrans in enzymatic reactions, Biophys. Chem., 185, 8–13. (DOI:10.1016/j.bpc.2013.10.006)

17. Benton L. A., Smith A. E., Young G. B., Pielak G. J. (2012), Unexpected effects of macromolecular crowding on protein stability, Biochem., 51(49), 9773–9775. (DOI:10.1021/bi300909q)

18. Sarkar M., Lu J., Pielak G. J. (2014), Protein crowder charge and protein stability, Biochem., 53(10), 1601–1606. (DOI:10.1021/bi4016346)

19. Kim Y. C., Mittal J. (2013), Crowding induced entropy-enthalpy compensation in protein association equilibria, Phys. Rev. Lett., 110(20), 208102. (DOI:10.1103/PhysRevLett.110.208102)

20. Molliex A., Temirov J., Lee J., Coughlin M., Kanagaraj A. P., Kim H. J., et al. (2015), Phase Separation by low complexity domains promotes stress granule assembly and drives pathological fibrillization, Cell, 163(1), 123–133. (DOI:10.1016/j.cell.2015.09.015)

21. Wegmann S., Eftekharzadeh B., Tepper K., Zoltowska K. M., Bennett R. E., Dujardin S., et al. (2018), Tau protein liquid–liquid phase separation can initiate tau aggregation, EMBO J., 37(7) (DOI:10.15252/embj.201798049)

22. Ambadipudi S., Biernat J., Riedel D., Mandelkow E., Zweckstetter M. (2017), Liquid–liquid phase separation of the microtubule-binding repeats of the Alzheimer-related protein Tau, Nat. Commun., 8(1), 275. (DOI:10.1038/s41467-017-00480-0)

23. Protter D. S. W., Rao B. S., Van Treeck B., Lin Y., Mizoue L., Rosen MK., et al. (2018), Intrinsically disordered regions can contribute promiscuous interactions to RNP granule assembly, Cell Rep., 22(6), 1401–1412. (DOI:10.1016/j.celrep.2018.01.036)

24. Ray S., Singh N., Kumar R., Patel K., Pandey S., Datta D., et al. (2020), α-Synuclein aggregation nucleates through liquid–liquid phase separation, Nat. Chem., 12(8), 705–716. (DOI:10.1038/s41557-020-0465-9)

25. Wegmann S., Eftekharzadeh B., Tepper K., Zoltowska K. M., Bennett R. E., Dujardin S., et al. (2018), Tau protein liquid–liquid phase separation can initiate tau aggregation, EMBO J., 37(7) (DOI:10.15252/embj.201798049)

26. Ambadipudi S., Biernat J., Riedel D., Mandelkow E., Zweckstetter M. (2017), Liquid–liquid phase separation of the microtubule-binding repeats of the Alzheimer-related protein Tau, Nat. Commun., 8(1), 275. (DOI:10.1038/s41467-017-00480-0)

27. Patel C. K., Singh S., Saini B., Mukherjee T. K. (2022), Macromolecular crowding-induced unusual liquid–liquid phase separation of human serum albumin via soft protein–protein interactions, J. Phys. Chem. Lett., 13(16), 3636–3644. (DOI:10.1021/acs.jpclett.2c00307)

28. Poudyal M., Patel K., Sawner A. S., Gadhe L., Kadu P., Datta D., et al. (2022), Liquid condensate is a common state of proteins and polypeptides at the regime of high intermolecular interactions, Biophysics, preprint. (DOI:10.1101/2021.12.31.474648)

29. Molliex A., Temirov J., Lee J., Coughlin M., Kanagaraj A. P., Kim H. J., et al. (2015), Phase separation by low complexity domains promotes stress granule assembly and drives pathological fibrillization, Cell, 163(1), 123–133. (DOI:10.1016/j.cell.2015.09.015)

30. Wang J., Choi J-M., Holehouse A. S., Lee H. O., Zhang X., Jahnel M., et al. (2018), A molecular grammar governing the driving forces for phase separation of prion-like RNA binding proteins, Cell, 174(3), 688-699.e16. (DOI:10.1016/j.cell.2018.06.006)

31. Krainer G., Welsh T. J., Joseph J. A., Espinosa J. R., Wittmann S., de Csilléry E., et al. (2021), Reentrant liquid condensate phase of proteins

is stabilized by hydrophobic and non-ionic interactions, Nat. Commun., 12(1), 1085. (DOI:10.1038/s41467-021-21181-9)

32. Dogra P., Joshi A., Majumdar A., Mukhopadhyay S. (2019), Intermolecular charge-transfer modulates liquid–liquid phase separation and liquid-to-solid maturation of an intrinsically disordered pH-responsive domain, J. Am. Chem. Soc., 141(51), 20380–20389. (DOI:10.1021/jacs.9b10892)

33. Flory P. J. (1942), Thermodynamics of High Polymer Solutions, J. Chem. Phys., 10(1), 51–61. (DOI:10.1063/1.1723621)

34. Huggins M. L. (1942), Some properties of dolutions of long-chain compounds., J. Phys. Chem., 46(1), 151–158. (DOI:10.1021/j150415a018)

35. Zhao Z., Fu J., Dhakal S., Johnson-Buck A., Liu M., Zhang T., et al. (2016), Nanocaged enzymes with enhanced catalytic activity and increased stability against protease digestion, Nat. Commun., 7(1), 10619. (DOI:10.1038/ncomms10619)

36. Haddad R. E., Gazeau S., Pécaut J., Marchon J-C., Medforth C. J., Shelnutt J. A. (2003), Origin of the red shifts in the optical absorption bands of nonplanar tetraalkylporphyrins, J. Am. Chem. Soc., 125(5), 1253–1268. (DOI:10.1021/ja0280933)

37. Aumiller W. M., Davis B. W., Hashemian N., Maranas C., Armaou A., Keating C. D. (2014), Coupled enzyme reactions performed in heterogeneous reaction media: Experiments and modeling for glucose oxidase and horseradish peroxidase in a PEG/Citrate aqueous two-phase system, J. Phys. Chem. B, 118(9), 2506–2517. (DOI:10.1021/jp501126v)

38. Derham B. K., Harding J. J. (2006), The effect of the presence of globular proteins and elongated polymers on enzyme activity,

Biochim. Biophys. Acta (BBA) – Proteins Proteom., 1764(6), 1000–1006. (DOI:10.1016/j.bbapap.2006.01.005)

39. Gao L., Zhuang J., Nie L., Zhang J., Zhang Y., Gu N., et al. (2007), Intrinsic peroxidase-like activity of ferromagnetic nanoparticles, Nat. Nanotechol., 2(9), 577–583. (DOI:10.1038/nnano.2007.260)

40. Holland J. T., Lau C., Brozik S., Atanassov P., Banta S. (2011), Engineering of glucose oxidase for direct electron transfer via site-specific gold nanoparticle conjugation, J. Am. Chem. Soc., 133(48), 19262–19265. (DOI:10.1021/ja2071237)

41. Aumiller W. M., Davis B. W., Hatzakis E., Keating C. D. (2014), Interactions of macromolecular crowding agents and cosolutes with small-molecule substrates: Effect on horseradish peroxidase activity with two different substrates, J. Phys. Chem. B, 118(36), 10624–10632. (DOI:10.1021/jp506594f)

42. Küchler A., Yoshimoto M., Luginbühl S., Mavelli F., Walde P. (2016), Enzymatic reactions in confined environments, Nat. Nanotechnol., 11(5), 409–420. (DOI:10.1038/nnano.2016.54)

43. Saini B., Singh S., Mukherjee T. K. (2021), Nanocatalysis under Nanoconfinement: A metal-free hybrid coacervate nanodroplet as a catalytic nanoreactor for efficient redox and photocatalytic reactions, ACS Appl. Mater. Interfaces, 13(43), 51117–51131. (DOI:10.1021/acsami.1c17106)

44. O'Flynn B. G., Mittag T. (2021), The role of liquid–liquid phase separation in regulating enzyme activity, Curr. Opin. Cell Biol., 69, 70–79. (DOI:10.1016/j.ceb.2020.12.012)

45. Peeples W., Rosen M. K. (2021), Mechanistic dissection of increased enzymatic rate in a phase-separated compartment, Nat. Chem. Biol., 17(6), 693–702. (DOI:10.1038/s41589-021-00801-x)

Chapter 8

Conclusions and Future Scope

Chapter 8

8.1. Conclusions

The development of various types of multifunctional self-assembled systems such as hybrid liposomes, polymersomes, plasmonic vesicles, dendrimer nanoparticles, hydrogels, metal-organic frameworks, polymeric nanoparticles and coacervates have gained immense attention on account of their potential applications in different fields. Among them, synthetic coacervates as an artificial cell have attracted a lot of attention due to their inherent membrane-free structure and preferential sequestration of a wide range of foreign molecules. Here, in this thesis, we have formulated three different classes of coacervates, namely synthetic organic coacervates, synthetic hybrid coacervates, and biomolecular condensates and finally utilized them for sensing, catalysis, and biomedical applications.

The unique class of biocompatible luminescent synthetic hybrid metal-free coacervates from carbon dots (CDs) and poly(diallyldimethylammonium chloride) (PDADMAC) in an aqueous medium have been employed for theranostic applications. Subsequently, the physicochemical properties of synthetic ATP-coacervates have been compared with different nanoassemblies like micelles, and liposomes to understand the target-specific delivery of hydrophobic drugs via nanocarriers.

Moreover, the demand of synthetic hybrid coacervates as a nanoreactor or bioreactor in various technology related fields is increasing continuously due to the availability of multiple catalytic centers in confined region and free diffusion of substrates/products. Here in this thesis, the mechanistic insights and reaction rates of various catalytic transformations such as redox catalysis and enzyme catalysis have been examined inside the confined environment of synthetic coacervates (CD- or ATP-coacervates).

Furthermore, the liquid-liquid phase separation (LLPS) or biomolecular condensates of biologically active enzymes have been explored in the presence of various macromolecular crowders. In addition, the mechanistic insights and enzymatic reaction rates inside these biomolecular condensates have been examined. The next segment discusses the chapter-wise conclusion of the entire work of this thesis.

In chapter three, the physicochemical properties of biocompatible inherently luminescent coacervate NDs along with their potential application toward cell imaging and pH-triggered intracellular disassembly characteristics have been explored. The self-assembly between negatively charged CDs and cationic polymer PDADMAC leads to two different sizes of NDs namely, SNDs and LNDs upon equilibration for 1 and 18 h at room temperature, respectively. These NDs are found to be stable over a broad range of pH, and ionic strength of the medium. In addition, the preferential sequestration of various organic dyes and anticancer drug DOX inside the membrane-less NDs have been demonstrated. Furthermore, the MTT assay reveals 82.4% biocompatibility of the present SNDs upon 24 h of incubation. Finally, the intracellular trafficking and pH-triggered disassembly of EtBr-loaded SNDs reveal endocytosis mediated internalization of SNDs and subsequent disassembly at the lower acidic pH of late endosomes/lysosomes. This study highlights the potential of these luminescent NDs as luminescent marker as well as nanocarrier.

In chapter four, the physicochemical properties and in vitro release mechanism of an encapsulated hydrophobic Ru-Cur drug have been compared inside various nanoassemblies. The uniformly encapsulated drug inside ATP-coacervates shows several 100-fold enhancements in its intrinsic green fluorescence upon association with a hydrophobic

microenvironment of coacervates which open its way for bioimaging applications as an optical marker. Finally, the coacervate encapsulated Ru-Cur complex shows controlled and sustained release compared to conventional liposome at 37 °C in the pH range of 7.4–5. These findings exemplify its importance toward controlled and sustained drug delivery inside the cellular compartments.

In chapter five, redox hydrogenation reaction of nitroarenes in the presence of excess $NaBH_4$ have been examined inside metal-free CD-embedded coacervate NDs as a catalytic nanoreactors. It has been observed that the isolated bare CDs failed to catalyze the hydrogenation reaction whereas synthetic hybrid NDs provides an ideal microenvironment to drive the incompatible reaction. In addition, NDs showed excellent recyclability over several consecutive cycles without any loss in rate and conversion yield of the hydrogenation reaction. Moreover, the spatiotemporal control over the redox reaction kinetics using mixed populations of coacervate droplets have been demonstrated. Finally, the mechanism of redox hydrogenation reaction is found to follow the classical LH model inside the NDs and this enhanced activity can be assigned due to the synergistic effect between the modulation of surface charge density of individual CDs and nanoconfinement effect inside the spherical NDs.

In chapter six, a robust, stable, and cost-effective integrated bioplatform from synthetic membrane-less coacervates with GOx/HRP cascade pair have been designed and thereafter utilized for ultrasensitive glucose sensing in urine. High encapsulation efficiency (≥99%), low leakage (<1.5%), enhanced biological stability, and superior activity compared to the earlier reported enzymatic bioreactors have been observed with the present system. In addition, (6.7–100)-fold and 51-fold

enhancement in catalytic activity has been observed with HRP@Droplet and GOx/HRP@Droplet composite relative to the bulk aqueous phase, respectively. Moreover, this enhanced activity is stable against aging and protease digestion, indicating the protective environment of these liquid-like scaffolds and can be recycled over several consecutive cycles without any significant loss in enzymatic activity. A fast (5 s), reliable, and selective colorimetric sensing of glucose in solution and solid support with LOD of 228 nM has been observed with GOx/HRP@Droplet composite. Finally, the present system was utilized to sense glucose level in spiked urine sample and it performed well in terms of sensitivity and colorimetric response compared to commercial glucose sensing strip. This study illustrates the vast scope of synthetic coacervates in biosensing and pharmaceutical applications.

In chapter seven, the LLPS or biomolecular condensates of biologically active enzymes (HRP & GOx) have been discovered in the presence of various macromolecular crowders. The LLPS of enzymes is found to be homotypic in nature induced by enthalpically controlled electrostatic as well as hydrophobic intermolecular interactions. More importantly, this study is the first proof of concept example to demonstrate the enhanced enzymatic activity and selectivity inside the phase-separated biomolecular condensates under a crowded milieu. The enhanced activities inside the phase-separated droplets have been explained by considering conformational change of the active enzymes, mass action, and confinement induced alteration of the activity of surrounding water and substrates. This present discovery opens the door of a new avenue in biocatalysis with a vast scope in industrial applications.

8.2. Scope for future work

The present thesis shows the physicochemical properties of three different classes of self-assembled coacervate droplets and explains their potential toward catalysis, sensing, and biomedical applications. In chapter 3, the fabrication of biocompatible luminescent coacervates from CD and PDADMAC has been demonstrated for theranostic application. These luminescent droplets can be utilized further as biocompatible targeted drug delivery vehicles after suitable functionalization. For this, the functional groups present on the surface of CD should be modified or conjugated by targeted functional groups like folic acid, methotrexate, amino acids, peptides, lysozyme, hemoglobin, DNA, aptamer, antibody, genes vitamin B1, glucose etc. Thereafter, the modified CDs should be mixed with PDADMAC to obtain targeted hybrid coacervates which will further expand their applicability in biosensing, cell imaging, targeted delivery, and photothermal therapy (PTT). In addition, NIR-emissive CDs-PDADMAC coacervates will show dual benefits and can be employed simultaneously for drug delivery and PTT.

In chapter 4, the physicochemical properties of ATP-coacervates have been found to be superior compared to other nanoassemblies such as micelles and liposomes. Here, the size of ATP-coacervates was found to be very large due to the continuous coalescence phenomenon and membrane-less feature of coacervates droplets which subjects them to fuse easily with each other. Therefore, it is important to fabricate long-standing stable coacervates by novel preparation method to enhance the stability of coacervates. One of the strategies to enhance the stability of coacervates is by proper organization of lipid bilayers onto the surface of coacervate droplets which will restrict the coalescence phenomenon and favor controlled and stimulated release.

In chapter 5 and 6, the potential of metal-free coacervate droplets have been examined toward redox and enzyme catalysis. The applicability of reported systems can be further extended for other chemical transformations such as dehydration reactions (esterification, etherification, dithioacetalization, condensation, alkene/ketene/nitrile formation), non-dehydration reactions (oxidation, reduction, aromatic substitution, C-C/C-H functionalization, cross coupling, olefin metathesis, asymmetric synthesis, click reactions), and heterocycles formation. In addition, the integrated bioplatform composed from GOx/HRP@Droplet has been utilized for rapid and real-time glucose detection in spiked urine samples. In extension of this study, a programmable nanoreactors for stochastic sensing (PNRSS) can be developed through the integration of coacervates and artificial intelligence algorithm that can be further applied in pharmacokinetics or drug screening. Subsequently, there is a need of development for optical computation analytical device to read out the exact optical measurements leading to the detection of biochemicals, pathogenic proteins, disease specific genes, organic and pharmaceutical pollutants. It will be beneficial in the commercial production and consumer approval of coacervate-based biosensors.

Further in chapter 7, the fundamental mechanism behind the LLPS of HRP and GOx enzymes has been illustrated. Also, the influence of macromolecular crowders on the enzymatic activity has been exemplified. Various enzymes are utilized for multifarious direction in various domains such as food, agriculture, cosmetic, analytics, and pharmaceutical industries. Therefore, it is important to examine the kinetic and mechanistic aspects of enzymatic reactions involving a wide range of biologically active enzymes including renin, invertase, cellulase, trypsin, alcohol dehydrogenase, amylase, protease, lipase, carbohydrase, zymase, lipase,

dextranase, penicillin amylase, phtase in the absence or the presence of macromolecular crowders.

Over all, we believe the findings of this thesis may be useful to understand and explore the functional aspects of various synthetic as well as biomolecular condensates toward a diverse range of applications in various field.